Numerical prediction of cavitation erosion

Saira Freda Pineda Rondon

Numéro d'ordre : 2017 LYSEC31

THÈSE de DOCTORAT DE L'UNIVERSITÉ DE LYON
Opérée au sein de l'École centrale de Lyon

École Doctorale 162

Mécanique, Énergétique, Génie Civil et Acoustique

Spécialité : Mécanique des fluides

Saira Freda PINEDA RONDON

Numerical prediction of cavitation erosion

Devant le jury composé de :

M. FARHAT	Professeur École Polytechnique Fédérale de Lausanne	Rapporteur
E. GONCALVES	Professeur École Nationale Supérieure de Mécanique et d'Aérotechnique	Rapporteur
R. FORTES-PATELLA	Professeur Université de Grenoble	Examinatrice
M. LANCE	Professeur École Centrale de Lyon France	Directeur
S. AUBERT	Professeur École Centrale de Lyon France	Co-directeur
J.-C. MARONGIU	Docteur ANDRITZ HYDRO France	Encadrant

Acknowledgements

I had the opportunity to work and discuss with many interesting people and I am grateful to everyone who contributed directly and indirectly to this thesis.

I would like to thank the members of the jury: Regiane Fortes-Patella and the "rapporteurs" Mohamed Farhat and Eric Goncalves da Silva for their evaluation and their constructive remarks.

This work was an European Project involving the Ecole centrale de Lyon, INSA Lyon and ANDRITZ Hydro, so I would like to thank all the partners involved.

It was an honor to work with Prof. Michel LANCE and Prof. Stéphane AUBERT who were my supervisors, their ideas and literature suggestions were very useful and appreciated. In particularly, I thank Prof. Stéphane AUBERT for his support and his constructive lessons in several aspects of my PhD subject. Also, I thank Prof. Alain COMBESCURE for being available for discussions.

It was an excellent opportunity to work in collaboration with the R&D department of ANDRITZ Hydro. I thank Etienne PARKINSON and Jean-Christophe MARONGIU, my co-supervisor, for having offered me this opportunity. In particular, I thank sincerely Jean-Christophe for his help about technical aspects (like SPH) but also because he was always available for discussing any aspect of my thesis project. I thank my colleagues from Lyon: Hervé for his help in coding C++ and Gilles-Alexis for his help in SPH. I thank also my colleagues from Vevey: Magdalena, Martin, Hélène, Nicolas R., Nicolas G., Dorothée, Steven, Pascal, Cyril and Florent.

A big thank-you to the other thesis students from the PREDHYMA project: Wiebke, Jorge and Guillaume, for their contribution to develop our willingness to help each other. Also, I thank the other thesis students from LMFA at Ecole centrale de Lyon: Annabelle, Xu, Feng Gao, Quentin, Slatko, Johannes, Gerardo, Emmanuel, Victor, Paolo, Julisa, Thomas, Valdo, Franck and Ludo.

To start a PhD project is an interesting and intense phase, specially arriving from a different country (Venezuela). In that case, understanding the new culture and learning another language could be overwhelming sometimes. Luckily I met friends that helped to learn the language and to discover the region that has become my home. In particular, I thank José Luis, Eli, Sam, Fede, Dania, Pierre, Yuri, Miguelangel, Shagid, Céline and Romain.

Agradezco a mis padres y mi hermano por su apoyo incondicional en todas mis decisiones. Gracias mamá, papá y Alfredo. Un gros merci Nicolas pour ton soutien chaque jour de ma vie.

Abstract

Hydraulic turbines can experience cavitation, which is a phenomenon occurring when vapor bubbles collapse in the vicinity of the machine's surface. This phenomenon can lead to negative consequences, such as erosion, that affect the machine's performance.

The compression of a non-condensable gas bubble in water is simulated with the Smoothed Particle Hydrodynamics method following the Arbitrary Lagrange Euler approach (SPH-ALE), where a compressible and multiphase model has been developed. The model solves the mass, momentum and energy conservation equations of the Euler system using the Stiffened Gas EOS for water and the ideal gas EOS for the non-condensable gas inside the bubble. Both phases are modeled as compressible and the phase change is not considered.

The meshless feature of the SPH-ALE method allows the calculation of multiphase flows where the interface is sharply defined. For cavitation applications, where the Mach number reaches values of 0.5, the distribution of particles must be corrected, which is achieved by the ALE feature. The compressible model was validated through mono-dimensional configurations, such as shock tube test cases for monophase and multiphase flows.

The bubble compression close to the wall has been addressed as the fundamental mechanism producing damage. Its general behavior is characterized by the formation of a water jet and by the collapse of the bubble by itself. The phenomenon is analyzed by considering the major parameters that govern the bubble collapse dynamics, such as the initial distance between the bubble center and the wall (H_0), the bubble size (R_0), and the collapse driven pressure ratio (p_w/p_b). It is shown that the intensity of the collapse depends mainly on the pressure ratio between the liquid and the bubble (p_w/p_b). As well, four indicators, such as the pressure at the wall, the impulse, the water-hammer pressure and the water jet velocity, are used to determine the loading. This analysis gives that the bubble initially located at a distance lower than $H_0/R_0 = 2$ presents high potential to cause damage.

In order to predict the damage due to the bubble collapse, the solid mechanics is analyzed through fluid-structure interaction simulations. It is obtained that the material reacts to the hydraulic loads by having compression and traction zones, suggesting that a fatigue mechanism drives the damage phenomenon. Additionally, it is found that the highest stresses are located below the material surface, indicating that this zone may reach plastic deformation. Key words: cavitation, bubble collapse, numerical simulation, SPH-ALE, material erosion.

Résumé

La cavitation peut avoir lieu dans les turbines hydrauliques. Ce phénomène se produit lorsque les bulles de vapeur s'effondrent à proximité de la surface de la machine. Ceci entraîne des conséquences négatives, telles que l'érosion, affectant ainsi les performances de la machine.

L'effondrement d'une bulle de gaz non-condensable dans l'eau est simulé en utilisant la méthode sans maillage SPH-ALE, qui intègre un modèle pour simuler les écoulements compressibles et multiphases. Le modèle résout les équations de conservation de masse, de quantité de mouvement et d'énergie du système d'Euler, en utilisant l'équation d'état de Stiffened Gas pour l'eau et l'équation d'état de gaz parfait pour le gaz non-condensable à líntérieur de la bulle. Les deux phases sont modélisées comme compressibles et le changement de phase n'est pas considéré.

La caractéristique sans maillage de la méthode SPH-ALE permet le calcul des écoulements diphasiques où l'interface est nettement définie. Pour les applications de cavitation, où le nombre de Mach atteint des valeurs de 0.5, la distribution de particules doit être corrigée. Cela est réalisé grâce à la fonctionnalité ALE. Le modèle compressible a été validé à l'aide de configurations monodimensionnelles, comme le cas du tube à choc pour des écoulements monophase et multiphases.

L'effondrement de la bulle près dúne paroi a été abordé comme le mécanisme fondamental qui produit des dégâts. Son comportement général se caractérise par la formation d'un micro jet d'eau et par l'effondrement de la bulle sur elle-même. Le phénomène est analysé en tenant compte des principaux paramètres qui le régissent, comme la distance initiale entre le centre de la bulle et la paroi (H_0), la taille de la bulle (R_0) et le taux de pression qui entraîne l'effondrement (p_w/p_b). Il est démontré que l'intensité de l'effondrement dépend principalement du rapport de pression entre le liquide et la bulle (p_w/p_b). De plus, quatre indicateurs, comme la pression en paroi, l'impulsion, la pression du coup de bélier et la vitesse du micro jet d'eau, servent à déterminer le chargement. Cette analyse indique qu'une bulle initialement située à une distance inférieure à $H_0/R_0 = 2$ présente un haut potentiel d'endommagement.

Afin de prédire cet endommagement, la mécanique du solide est analysée à l'aide de simulations d'interaction fluide-structure. On obtient que le matériau réagit aux charges hydrauliques en ayant des zones de compression et de traction. Ceci suggère qu'un mécanisme de fatigue entraîne le phénomène d'endommagement. En plus, on constate que les contraintes les plus importantes sont situées sous la surface du matériau, indiquant que cette zone peut être sujette à une déformation plastique. Mots clés: cavitation, effondremment de bulle, simulation numérique, SPH-ALE, érosion de matériau.

Contents

List of Figures

List of Tables

Notation: Greek characters

Δv	variation of flow velocity
Δs	change of entropy
Δt	time step
Δt_{CFL}	time step calculated with CFL condition
Δt_{xi}	characteristic size
Ω	computational domain
$\partial\Omega$	boundary of the computational domain
∂D	boundary of the kernel support
Ξ	dynamic viscosity
α	limiter function for the MUSCL scheme
β	numerical parameter for correction in compressible SPH-ALE
η	enthalpy per mass unit
ϵ_x	normal strain component on x-direction
ϵ_y	normal strain component on y-direction
ϵ_z	normal strain component on z-direction
γ_{xy}	shear strain component on xy-plane
γ	ratio of specific heats (c_p/c_v)
κ	constant related to the kernel function
λ	eigenvalue
μ	wave speed
ν	specific volume
ω	integration weight, particle volume
ω^{∂}	area of the surface element, integration weight for the discretized surface integral
ω_T	angular velocity of the turbine
ρ	density
ρ_0	reference density for the Tait EOS

ρ_{liq}	liquid density
ρ_w	initial liquid water density
ρ_L	left density in Riemann solver
ρ_R	right density in Riemann solver
ρ^*	star density in Riemann solver
σ_x	normal stress component on x-direction
σ_y	normal stress component on y-direction
σ_z	normal stress component on z-direction
τ_{xy}	shear stress component on xy-plane
θ	compressibility of a fluid
$\mathbf{\Lambda}$	Lagrange multipliers. Vector that contains the fluid pressure value
$\mathbf{\Phi}$	vector of conservative variables
$\boldsymbol{\tau}$	viscous shear stress tensor

Notation: Latin characters

$\mathbb{D}$	mass diffusivity
$\mathbb{R}$	Real numbers
$\mathfrak{R}$	universal gas constant ($8.31451[J/(molK)]$)
$\mathfrak{M}$	molecular weight
A_I	transversal area of the jet
B_2	width of the bucket
D	SPH kernel support
D_1	Pelton wheel diameter
E	total energy per mass unit
H_0	distance from the bubble center and the wall
K_{CFL}	Courant-Friedriech-Levy (CFL) coefficient
L	characteristic length
Ma	Mach number
Pe	Peclet number
Re	Reynolds number
R	radius of the bubble
$\dot{R}$	velocity of the bubble interface
$\ddot{R}$	acceleration of the bubble interface
R_0	initial radius of the bubble
R_G	particular gas constant
R_∞	cut-off distance for Rayleigh equation in 2D
$S_{tension}$	surface tension
T	temperature
V	volume of the bubble
V_0	initial volume of the bubble
V_T	turbine velocity

V_I	jet velocity at the injector outlet
W	smoothing kernel function
X_C	position of the bubble centroide
X_0	initial position of the bubble
a	scalar variable per mass unit
c	speed of sound
c_0	reference speed of sound for the Tait EOS
c_c	speed of sound for correction in compressible SPH-ALE
c_{gas}	speed of sound for gas
c_{liq}	speed of sound for liquid
C_p	specific heat at constant pressure
C_v	specific heat at constant volume
c_w	initial speed of sound for liquid water
c_{wp}	speed of wave propagation in the domain
c_L	left speed of sound in Riemann solver
c_R	right speed of sound in Riemann solver
d	distance between the injector and the bucket
d_I	jet diameter created by the injector
e	internal energy per mass unit
h	smoothing length
m	mass
$\dot{m}$	material mass loss rate
p	static pressure
p_∞	stiffened constant pressure for the Stiffened Gas EOS
p_0	reference pressure for the Tait EOS
p_{amb}	pressure far away from the bubble
p_b	initial bubble gas pressure
p_{cavity}	pressure inside the internal cavity
p_c	pressure field for correction in compressible SPH-ALE
p_v	saturation pressure
p_w	initial liquid water pressure
p_{wh}	water-hammer pressure
p_L	left pressure in Riemann solver
p_R	right pressure in Riemann solver

p^*	star pressure in Riemann solver
q	heat transfer per mass unit
q_c	heat sources
r	radial direction
s	entropy per mass unit
t	time
t_1	time of a fluid particle to go from the injector to the bucket
t_2	time of a fluid particle spent inside the bucket
t_c	collapse time from Rayleigh equation
u	x-component of the velocity vector $\mathbf{v}$
u_k	velocity in the direction of interest x_k
u_0	x-component of the ALE velocity vector $\mathbf{v}_0$
u_L	left normal velocity in Riemann solver
u_R	right normal velocity in Riemann solver
u_r	radial component of the velocity in cylindrical and spherical coordinates
u^*	star normal velocity in Riemann solver
v	y-component of the velocity vector $\mathbf{v}$
v_0	y-component of the ALE velocity vector $\mathbf{v}_0$
v_d	velocity of the lower part of the bubble
v_j	velocity of the re-entrant jet during bubble collapse
v_L	left tangential velocity in Riemann solver
v_R	right tangential velocity in Riemann solver
w	z-component of the velocity vector $\mathbf{v}$
w_0	z-component of the ALE velocity vector $\mathbf{v}_0$
x	space coordinate
x_k	direction of interest
y	space coordinate
z	space coordinate
$\mathbf{A}$	matrix coefficient for the primitive variable system
$\mathbf{B}$	matrix coefficient for the primitive variable system
$\mathbf{F}$	ALE flux tensor
$\mathbf{F}_C$	convective flux tensor
$\mathbf{F}_D$	diffusive flux tensor
$\mathbf{F}_\nu$	viscous flux tensor

$\mathbf{G}_f$	vector of fluid pressure information of elements along the fluid-solid interface
$\mathbf{I}$	unit tensor
$\mathbf{M}_f$	matrix containing fluid information of elements along the fluid-solid interface
$\mathbf{M}_s$	diagonal matrix related to the degrees of freedom of the system
$\mathbf{S_e}$	vector of external forces
$\mathbf{S_T}$	vector of source terms
$\mathbf{L}_f$	matrix operator
$\mathbf{L}_p$	matrix of surface area information of elements along the fluid-solid interface
$\mathbf{L}_s$	matrix operator
$\mathbf{L}$	vector of left eigenvectors
$\mathbf{R}$	vector of right eigenvectors
$\mathbf{W}$	vector of primitive variables
$\mathbf{a}_s$	acceleration vector of the solid domain
$\mathbf{a}$	column vector
$\mathbf{b}$	column vector
$\mathbf{b}_i$	vector of closed box error
$\mathbf{f}_s^{ext}$	external forces of the solid domain
$\mathbf{f}_s^{int}$	internal forces of the solid domain
$\mathbf{n}_k$	direction of interest
$\dot{\mathbf{q}}$	heat flux vector
$\mathbf{u}_s$	displacement vector of the solid domain
$\mathbf{v}$	velocity vector
$\mathbf{v}_0$	ALE particle velocity vector
$\mathbf{v}_f$	velocity vector of the solid elements in the outward-pointing normal direction
$\mathbf{v}_s$	velocity vector of the solid domain
$\mathbf{v}_w$	velocity vector of the solid boundary
$\mathbf{x}$	coordinate vector, position

Chapter 1

Introduction

1.1 Motivation

This thesis addresses the study of cavitation erosion in Pelton turbines. Specifically, it focuses on the prediction of material response to cavitation in flow regions where unsteady cavitation pockets exist.

Cavitation is the formation of vapor bubbles in a liquid flow due to local low pressures. The initial bubble growth phase is developed in the low pressure regions, or in high velocity regions. Later, cavitation bubbles are transported by the flow arriving to zones of higher pressure. There, they collapse. When the collapses occur repeatedly close to a solid boundary, they may induce wear and erosion.

The cavitation bubble collapse is characterized by high pressure amplitudes produced on relatively small sizes (e.g. micrometers) and within short characteristic times (e.g. microseconds). These pressure amplitudes are the consequences of pressure waves emitted during the collapse of one or several cavitation bubbles. Then, if the bubble collapse is produced near a wall, it can generate pressure signals. At some moments, these pressure signals can be compared to the yield stress of common materials (e.g. aluminum and steel), representing thus a threat on the material integrity.

As it was brought out, cavitation erosion involves fluid flow and material properties. On the fluid side, cavitation erosion depends on the magnitude of the cavitating flow, which is defined in terms of the frequency and intensity of the collapses. On the material side, it depends on material properties, which govern the response to the cavitating flow. Hence,

the actual damage will be the result of the relation between the cavitation intensity and the material strength.

It is well known that cavitation can have detrimental consequences in rotating machines. Strong variations of pressure may induce bubble collapse generating damage on solid surfaces. So, it threats the structural integrity and declines the machine's efficiency. Understanding the unsteady nature of gas pockets is very important for the prediction of erosion because it is their frequent collapse that causes damages to hydraulic components.

Since this work is in the frame of hydraulic turbines, specifically it is related to Pelton turbines, a presentation of this type of turbine is needed. Pelton turbines are impulsive turbines that are used for high head (e.g. 200 to 2000 m) and low flow rates (e.g. 0.05 to 30 $[m^3/s]$). Its operative system consists of water jets impinging on the Pelton buckets to transform the kinetic energy of water to mechanical energy and thus, to produce electric energy. For illustration, representations of Pelton turbines are shown in Fig. 1.1. It is observed a Pelton turbine prototype of horizontal shaft and a general view of the flow (in blue) in a Pelton turbine wheel obtained by numerical simulations.

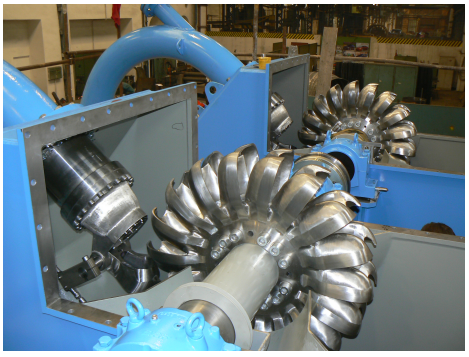

(a) Pelton turbine of horizontal shaft [35]. Detail of the water injector and wheel on the left

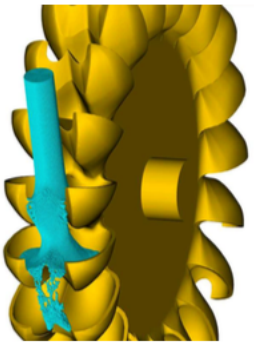

(b) General view of the flow in a Pelton turbine wheel. Numerical simulations using SPH method from Marongiu [62]

FIGURE 1.1: Different representations of a Pelton turbine: prototype and numerical simulation

In general, this type of turbine presents an acceptable efficiency, around 92%. However, some improvements are desirable. In this context, a better comprehension of the fluid flow and its perturbations, such as erosion due to cavitation, is required in order to improve its conception and optimization.

Because of the small characteristic dimensions (i.e. size and time), a numerical approach seems suitable for studying this physical phenomenon. In this context, in order to simulate

the fluid flow, this thesis follows a numerical approach using the Smoothed Particle Hydrodynamics method considering the Arbitrary Lagrangian Eulerian description, which is called SPH-ALE. Historically, SPH-ALE has been used in ANDRITZ Hydro S.A. to simulate the flow behavior inside Pelton turbines ([62], [68], [54]). The flow inside a Pelton turbine is mainly dominated by free surface flow, so the messless feature and the Lagrangian description of SPH-ALE represent an interesting advantage to model it.

In SPH, two different strategies have been followed to model fluids. Firstly, we mention the weakly compressible SPH (WC-SPH) method, which is a density based method where pressure is modeled using an equation of state (EOS). This method is divided in two branches: the classical WC-SPH from Monaghan [64] and the WC-SPH from Vila [105]. The major difference between them lies on the strategy to treat the equations. The classical WC-SPH from Monaghan adds an artificial viscosity into the momentum equation in order to guarantee its conservation and to stabilize the method [64]. On the other side, the WC-SPH from Vila [105] uses the Riemann solver to compute numerical fluxes adding a decentered discretization in space in order to stabilize the method. Secondly, we have the incompressible SPH (I-SPH) method, which is a pressure-based method where incompressibility is achieved solving a Poisson solver for the computation of pressure [16]. In these two strategies, i.e. weakly compressible and incompressible SPH, the fluid dynamic has been described using the Navier-Stokes equation system of conservation of mass and momentum. Thus, the energy equation is not solved.

This approach fits for large physical applications such as the modeling of fluid flow inside a hydro-machine, the free surface flow of Newtonian and non-Newtonian fluids, shallow-water experiences, mono-phase and multiphase flows. However, in this work, we are interested in the simulation of the cavitation phenomenon and its impact on the material, where the interaction between liquid and gas is mandatory in order to properly model the pressure waves that characterize this physical phenomenon. Therefore, compressibility effects are important and must be taken into consideration. In these cases the temperature is involved and thus the solution of the energy equation is mandatory.

Hence, a fully compressible model in SPH-ALE has been developed throughout this thesis to solve the hydrodynamic equations describing the conservation of mass, momentum and energy ([76], [77]). This numerical implementation was required because a proper representation of the bubble collapse phenomenon is the first step towards the prediction of cavitation erosion.

Regarding the material response, the pressure profile generated on the solid surface is usually considered in order to predict the material reaction. An approach taken quite often is to represent this pressure pulse as a synthetic load in order to use it as input in solid simulations. But, a more complete way to address the problem is considering the flexible solid and the fluid domain. In this case, the fluid and the solid domains are solved together, giving the possibility to analyze the solid response due to the actual pressure signals emitted by the flow behavior. The latter approach is followed in this work.

The solid domain is solved through the finite element method implemented in the research solver EUROPLEXUS, which is developed by The French Office of Atomic Energy (Commissariat à l'Énergie Atomique) and the European Commission Joint Research Centre. Meanwhile, the fluid domain is solved through the in-house solver developed by ANDRITZ Hydro S.A., called ASPHODEL. It uses the SPH-ALE method, in which modifications have been implemented along this work in order to model the bubble collapse. The coupling solver to connect the fluid and the solid solvers was done in parallel by another doctoral thesis also involved in the frame of the present project.

1.2 PREDHYMA Project

This thesis is enclosed in a project called PREDHYMA (*Prediction of Erosion Damages in Hydraulic Machines*). PREDHYMA is an European project belonging to the Marie-Curie European Industrial Doctorates program. It assembles two universities (INSA Lyon and École Centrale de Lyon) and the company ANDRITZ Hydro S.A. This company is a global supplier of electro-mechanical systems and services for hydropower plants, as well as one of the leaders in the world market for hydraulic power generation.

The main motivation of ANDRITZ Hydro S.A. in developing this project is because the hydraulic turbines can experience severe wear during operation due to adverse flow conditions and poor quality water. So, facing the turbine damage induces maintenance costs, losses in power production and it could increase the risk of accidents in the facilities. Under this situation, turbine manufacturers and hydropower plants operators are interested in extending overhaul periods by reducing the intensity of the erosion and protecting the turbine components with appropriate surface treatments.

In this context, the PREDHYMA project aims at developing predictive tools addressing damaging mechanisms encountered during Pelton turbine operations.

The program is composed by four thesis projects: the hydro abrasive erosion, the wear by the impact of gravels and stones, the droplets impact erosion and the cavitation erosion. A short description of each phenomenon is given below.

The hydro abrasive erosion is the material wear caused by the impact of small sediments traveling in the water flow. The gravel and stones impacts produce another erosion mechanism, which happens when relatively large stones hit the turbine components. This impact usually produces fracture of the turbine components. The droplet impact erosion is caused by the impact of high-speed water droplets on the components, producing, similarly to cavitation, high-pressure pulses. Finally, the cavitation erosion is the material wear caused by the impact of several pressure waves of high amplitude emitted during the bubble compression near a solid. This subject represents the core of the present research work.

1.3 Objectives

The main objective of this thesis is the prediction of the material response due to cavitation loading. In order to achieve it, two sub-objectives are set-up.

First, we address the fluid flow side. In this context, it is developed a two-phase model, in the SPH-ALE method, able to treat fully compressible fluids in order to correctly simulate the compression of a non-condensable gas bubble and estimate the pressure loads when it collapses near a solid wall. The SPH-ALE method enables the calculation points to move and adapt themselves to the flow interface and to the solid geometry, giving an interesting approach to treat two-phase flows in which the interface is sharply and always defined. So, special mesh treatments, such as mesh refining, near the interface zone are not needed. The model needs to deal with a proper algorithm to correct the particle motion because the pure Lagrange motion of SPH particles is not adequate for compressible flows with Mach number larger than 0.1. For this type of application, where cavitation flow is involved, the Mach number reaches values of 0.5 and in the validation process Mach number values of 0.6 were reported. In this regard, the ALE feature of the scheme is exploited.

Second, an insight towards the erosion by cavitation is addressed by conducting fluid-structure interaction simulations. The coupling algorithm plays as a link between the fluid and the solid domains using the fluid pressure as an input for its calculations. In the system of hydrodynamic equations considered (i.e. conservation equations of mass, momentum and total energy), the pressure depends on the density and the internal energy. In this regard, some modifications must be done in order to adapt the coupling algorithm that was developed for solving a barotropic system (i.e. pressure depends only on density).

1.4 Outline of this document

The present document is organized as follows.

Chapter 2 presents a description of the cavitation phenomenon and the cavitation erosion. It includes the description of bubble dynamics and physical aspects usually considered in cavitation analyses, like compressibility, mass transfer, viscosity and surface tension effects. It also discusses the erosion process, the material response and some examples of cavitation erosion in Pelton turbines. Chapter 3 presents thermodynamic considerations on the physical model involved in non-condensable gas bubble dynamics and compressible regimes.

The numerical model is addressed in Chapter 4, where the governing equations are presented. The SPH method is described with emphasis in the Arbitrary Lagrange Euler approach. Then, the computation of the numerical fluxes is detailed by describing the Riemann problem and the solution developed in this work. Next, the correction method for the compressible SPH-ALE is given. Finally, the multiphase flow model is presented followed by a discussion regarding the validation cases.

In Chapter 5, it is presented the numerical simulations related to the non-condensable gas bubble compression in a free field and near a rigid surface. Corresponding analyses in order to understand the non-condensable gas bubble dynamics in the presence of neighboring surfaces are discussed. Next, in Chapter 6, the fluid-structure interaction approach is described, making emphasis on the coupling algorithm and the material properties. Corresponding analysis is taken up to estimate the material response due to hydrodynamics loads. In the end, in Chapter 7, conclusions are given and further perspectives are discussed.

Chapter 2

Cavitation and cavitation erosion

In this chapter, an introduction to cavitation and cavitation erosion is presented. Cavitation occurs when a liquid in a continuous medium breaks down under very low pressures [25], [94], generating a phase change, the formation of vapor bubbles and vapor pockets [1], [6].

Cavitation involves the development of several types of vapor structures, such as attached cavities, travelling bubbles, vortical cavities and bubble clouds. These vapor structures appear in liquid flow due to a drop in the local pressure below a critical value, which is usually close to the vapor pressure [45]. These structures are created from cavitation nuclei. Typically, it is about gas microbubbles contained in the liquid. If a nucleus is subject to pressure lower than its critical pressure, it will grow into a macroscopic bubble. Eventually, the bubble will collapse when it is transported by the liquid flow into regions of higher pressure. If the collapse occurs near a wall, the resulting high amplitude and small duration impulsive loads may cause local damage. The critical pressure is defined as the particular value of the pressure below which no equilibrium is possible. This critical value varies with nuclei size. Chahine et al. [45] have shown that for initial nuclei sizes of 10 μm the critical pressure is close to the vapor pressure. The consideration of the nuclei size distribution in the liquid is important for an accurate cavitation inception prediction. However the cavitation inception is not part of the present thesis, because in the current state of knowledge at ANDRITZ Hydro S.A. the most important point, at the beginning of this work, was how a non-condensable gas bubble can damage a solid and not how it is formed.

Cavitation can be present in several industrial systems, like the hydraulic and aeronautical one, but also in the medical domain. For example, the lithostropy techniques use pressure waves to break up stones formed in the kidney [6], [100]. In the case of hydraulic machines, the innovative designs demand to have particular flow conditions such as higher rotating speed or higher water head, increasing thus the cavitation risk. Following this idea, cavitation represents an important challenge in the design and operation of hydraulic machines. Hence, there is a big interest in understanding it better to avoid negative effects, such as low efficiency, noise, vibration and erosion of solid surfaces.

2.1 Cavitation phenomenon

Chahine in [45] defines cavitation as the growth and intense collapse of bubble nuclei in a liquid when it is exposed to large pressure variations. In a practical manner, cavitation is identified as either the visual appearance of cavities in the absence of air injection and heat input, or the acoustical emission of repeated sound produced by these cavities. Sound emission usually occurs earlier than visual identification. It happens at lower speeds and/or higher local pressures because microscopic bubbles can experience very strong dynamics and emit pressure impulses before they can be visible.

It is often assumed that cavitation occurs when the local pressure in the liquid drops below its vapor pressure at the given temperature. This assumption comes from the phase diagram of a substance, i.e. the curves which separate solid, liquid, and vapor phases of the substance at different temperatures (see Fig. 2.1).

As the liquid pressure decreases sufficiently, a part of the liquid changes its phase suddenly. The fluid goes from the liquid phase to the vapor phase. Thermodynamically speaking, this phenomenon can occur due to two physical phenomena: cavitation and boiling. These two phenomena are explained by Saurel in [90] as follows. Cavitation in a liquid is a phase change phenomenon due to a pressure drop driven by acoustic waves generating gas cavities. When liquid pressure is lower than the saturation one at the local temperature, phase change happens. Actually, during a pressure drop, the liquid temperature varies weakly and at low pressure it becomes hot with respect to the saturation temperature, this latter being highly dependent of pressure. Boiling is another phase transition phenomenon produced by a heating process in a liquid, usually by heat

conduction from a hot wall. The heating increases the liquid temperature and when it becomes greater than the saturation temperature at local pressure phase change appears.

From this, cavitation in a liquid can occur by reducing the pressure at approximately constant temperature. Cavitation thus appears similar to boiling, except that the driving mechanism is not due to a temperature change but to a pressure change, generally controlled by the flow dynamics [25].

These two phenomena can been observed in the phase diagram shown in Fig 2.1. Considering a fluid like water, the curve from the triple point to the critical point separates the liquid and vapor phases. Passing through that curve produces a reversible transformation under static conditions of the fluid at vapor pressure p_v, which is function of temperature T.

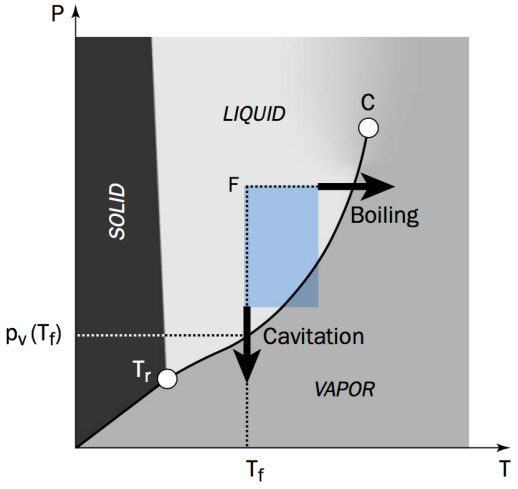

FIGURE 2.1: Phase diagram of water. The curve that joins the triple point (T_r) to the critical point (C) is the vapor pressure curve [25].

Two steps can be distinguished during the first instants of cavitation, also known as nucleation of vapor cavities in a homogeneous liquid. The first aspect is represented by the breakdown or void creation. Then, the second aspect corresponds to the filling of this void with vapor.

In the present work, the cavitation inception or nucleation is not considered; the interest is in the vapor cavity dynamics. Following this line, a brief explanation of different ways of cavitation development is presented in the next section.

2.1.1 Types of cavitation

Cavitation can take a variety of forms depending on geometry, hydrodynamic conditions and liquid quality. In turbomachines, these forms are classified in patterns that can be divided in three groups as cavitation develops from inception [25].

2.1.1.1 Cavitation of isolated bubbles

Traveling bubble cavitation is favored by the presence of microbubbles, which depend on water quality [25], [45]. Bubbles are developed in low pressure regions as a result of the rapid growth of air nuclei present in the liquid. Next, they are carried along the flow (see Fig 2.2). Eventually, they implode when the flow has moved them to higher pressure regions. In general, the bubble development is mainly controlled by the pressure distribution and the liquid nuclei content.

In practice, bubble cavitation can be observed over the blades of hydraulic machinery when working at high velocity or when the local pressure drops due to operation conditions. For example, it can be seen at the outlet of Francis turbine models and at the inlet of centrifugal pumps near their design point [25].

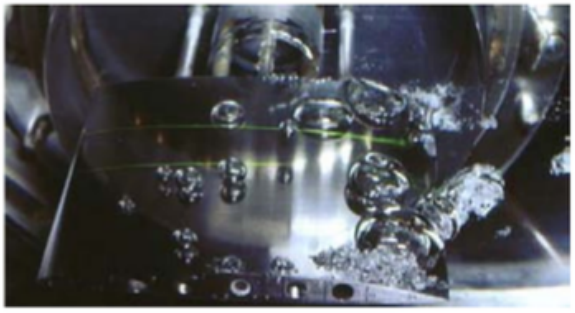

FIGURE 2.2: Isolated bubble cavitation on a hydrofoil. Flow is from left to right [25]

According to Franc in [25] when bubbles explode on the upper side of the hydrofoil there is almost no slip between the bubbles and the liquid. Usually, the difference between the bubble and liquid velocities does not exceed 10%.

2.1.1.2 Attached or sheet cavities

This type of cavitation appears in low-pressure zones, generally on the depression zone of a profile, for example in low-pressure sides of blades and hydrofoils. As the pressure

decreases or the fluid velocity increases, a small cavity attached to a hydrofoil will extend and grow. Depending on the length of the attached cavity, this cavitation pattern is classified in partial cavity or supercavity. It is known as a partial cavity if the cavity length finishes on the cavitator wall (see Fig. 2.3(a)). On contrary if the cavity close inside the liquid, downstream of the cavitator, it is known as supercavity (see Fig. 2.3(b)) [25].

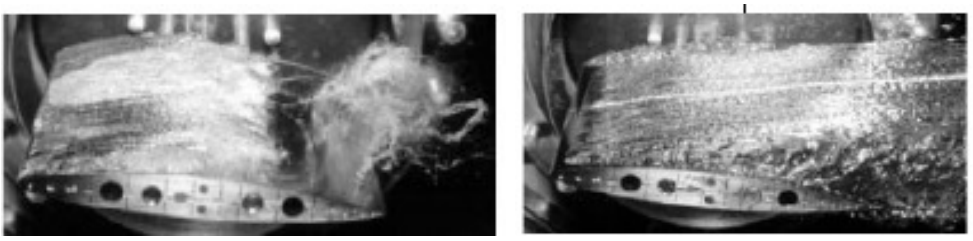

(a) Attached partial cavitation pocket on a profile (b) Supercavitation pocket on a profile

FIGURE 2.3: Cavitation due to attached cavities [25]

Partial cavity

Partial cavities usually develop in regions of separated flow. They are found in two main practical situations, either on the upperside of hydrofoils and blades or in internal flows, such as Venturi nozzles [25].

In general, there are two types of behavior of partial cavitation. When cavities are rather short and thin, the length of the cavity is constant and the flow is stable on the whole. On contrary, when the cavities are thicker, they become unstable and their length is variable because of the cavity shedding.

For thicker cavities, as the pressure inside the cavity decreases, a particular dynamics is developed in their closure. The curvature of the surrounding streamlines tends to be directed towards the cavity generating a re-entrant jet which carries a small quantity of the liquid inside the cavity [25]. This configuration is not steady and depends on the re-entrant flow rate, the jet may arrive to the front section of the cavity. The jet may also tear off a part of the cavity. This detached part is broken into smaller vapor structures such as bubbles. These smaller vapor structures are convected downstream where they collapse [28]. Then, the part of the pocket that remains attached to the profile develops again and the cycle is repeated [1]. This process is mainly controlled by inertia and it can be either random or periodic [25].

This type of cavitation is generally associated with flow separation near the leading edge. Cavity closure is usually more unstable than cavity detachment because the fluctuations at closure are accompanied by the shedding of vapor clouds. An example of this type of cavitation is taken from the work of Grekula [28]. Fig. 2.4 shows the starting cavitation at the suction side of a blade of a Kaplan model turbine. It is observed two attached sheet cavities at the leading edge of different sizes and another one closer to the hub. It is also observed relatively large cavitating vortices that break off from the small sheet cavity attached to the leading edge.

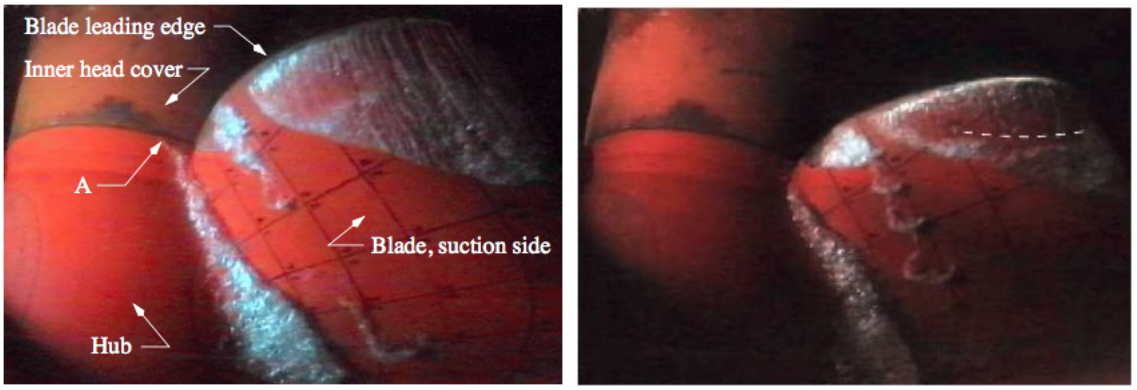

(a) Cavitation starts from the join between the rotating hub and the stationary inner head cover as shown at A. The flow is from above.

(b) Attached sheet cavity on the suction side of a Kaplan turbine. Two partial cavitation sheets are observed at the leading edge and one sheet closer to the hub. Relatively large cavitating vortices broken off from the small sheet cavity attached to the leading edge. The trace of a re-entrant jet front in the large sheet cavity has been marked with a white dashed curve.

FIGURE 2.4: Sheet cavities in a Kaplan turbine [28].

Supercavity

A small cavity attached to a hydrofoil that extends becomes a supercavity when it stops closing on the body wall but inside the liquid, downstream of the hydrofoil. It is formed behind small size bodies and it usually happens for very high relative velocities between the liquid and the body [25].

As the cavity pressure is lower than the surrounding pressure, the liquid tends to penetrate into the cavity forming a re-entrant jet in the closure region. This region is unstable and presents two main regimes. There is the re-entrant jet that tends to confine the gas and vapor mixture inside the cavity, and at the same time, there is an emission of vortices that take off gas and vapor from the cavity. This phenomenon stimulates the vaporization at the cavity interface. Vaporization usually happens at the front part of

the cavity and it regularly feeds the cavity with vapor and compensates the amount of vapor released at the rear.

The wake of a cavity is the region just downstream of the attached cavity. There, the flow contains many bubbles, which are released from the cavity and appear more or less entrapped in the core of alternating vortices. This region is always highly turbulent due to the instability of the cavity closure.

2.1.1.3 Cavitating vortices

Rotational structures generate zones of strong vorticity that can create low-pressure regions inside the liquid itself. Such pressure drops can be very intense [25] generating noise and vibrations [104].

In a simple form, a cavitating tip vortex is just a tube of vapor of approximately constant diameter [104] as it is shown in Fig. 2.5(b).

In a practical approach, cavitation vortices can occur at the pump suction [67], in tip vortices of wings and in propeller blades [104]. Fig. 2.5(a) comes from the work of Nagara et al. [67] and shows the flow structure of the vortex occurring in a pump suction intake. They showed that the mean velocity and the swirl flow at the lower part of the pump inlet causes the submerged vortex cavitation. They also showed that some increment in the swirl flow strength increases the vortex diameter and intensity. For the propeller blades, Van Wijngaarden et al. [104] report that the cavitating tip cavity (see Fig. 2.5(b)) varies in diameter due to changes in tip loading as the propeller goes through the wake peak of the ship. Thus, pressure pulses at the blade are generated by the acceleration and deceleration of the cavitating core. They state that the tubular cavity is very sensitive to perturbations, highlighting that cavitating vortices show break-ups and even local cloud formation.

To conclude, it can be highlighted that whatever the type of cavitation, its occurrence is strongly dependent on the minimum pressure in the flow. As well, during the cavitation development, it has been shown that breaking vapor structures containing bubbles are present for the three cavitation patterns (e.g. isolated bubbles, sheet cavities and cavitating vortices).

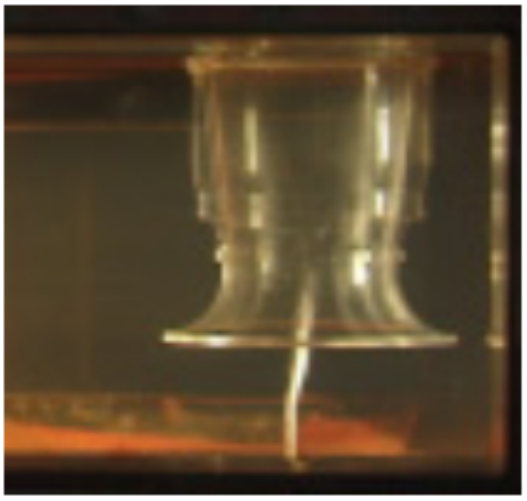

(a) Submerged vortex cavitation in the inlet part of a pump [67]

(b) Cavitating tip vortices on a propeller in open water [104]

FIGURE 2.5: Cavitating vortices

2.1.2 Dynamics of bubbles

In the current section, it is considered the dynamic evolution of a bubble surrounded by liquid whose pressure is uniform at infinity. This simple model can be used to explain the main features of many practical cases such as bubble collapse and bubble formation [25].

In terms of isolated bubble dynamics, the liquid motion induced by a spherical cavity in an infinite medium under uniform pressure was first considered by Besant in 1859 [25], [81]. Rayleigh in 1917 [81] developed theoretical formulations on the movement of an empty cavity in a incompressible and inviscid liquid, deriving his analytical formulation to interpret the phenomenon of bubble collapse. In 1948, Cole used the model of a spherical bubble containing gas and applied it to sub-marine explosions [25]. Plesset in 1949 [78] considered the case of bubble evolution, modifying the Rayleigh equation by including surface tension. Then in 1954, Plesset considered the general case adding the viscous effects [25], [79].

2.1.2.1 Rayleigh-Plesset equations

The Rayleigh-Plesset equation constitutes one of the basic equations when analyzing the bubble dynamics. In this frame some assumptions are taken. The liquid is considered incompressible, the gravity is neglected and the exchange of heat with the surrounding is neglected.

It is assumed that the bubble is filled with gas and vapor and that its content is constant. In a gas mixture, the partial pressure of a gas is the hypothetical pressure of that gas if it occupied alone the entire volume of the original mixture at the same temperature [8]. For the bubble, the partial pressure of vapor is the vapor pressure (p_v) at the liquid bulk temperature.

Fig. 2.6 shows the domain of interest. The liquid domain corresponds to $r \geq R(t)$ and since the domain presents a spherical symmetry only the radial evolution in time is considered. Hence, the functions to be determined are the velocity $u_r(r,t)$ and the pressure $p(r,t)$ induced within the liquid by the evolution of the bubble.

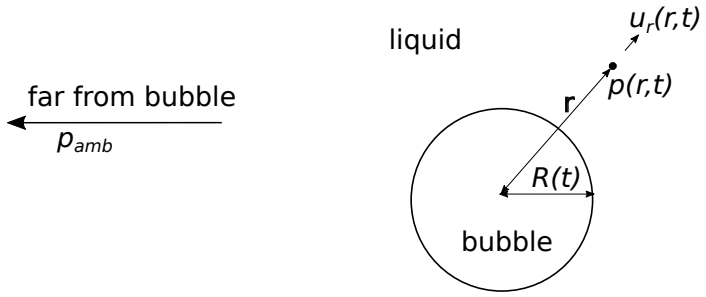

FIGURE 2.6: Scheme of a bubble in a infinite fluid

In the case of viscous liquid of dynamic viscosity Ξ, the normal stress (σ_{rr}) at the interface is given by [3], [25],

$$\sigma_{rr}(R,t) = -p(R,t) + 2\,\Xi\,\frac{\partial u_r}{\partial r}\Big|_{r=R}. \tag{2.1}$$

The balance of normal forces is given by

$$\sigma_{rr}(R,t) + p_v + p_g(t) - \frac{2S_{tension}}{R} = 0, \tag{2.2}$$

where $S_{tension}$ is the surface tension and it can be defied for a pure liquid as the "macroscopic manifestation of the intermolecular forces that tend to hold molecules together and prevent formation of large holes" [3]. Additionally, p_g stands for the partial pressure of the non-condensable gas inside the bubble. An expression for the

partial pressure can be obtained assuming an adiabatic transformation of this gas. Its instantaneous pressure is related to the initial pressure p_{g0} by the Eq. 2.3,

$$p_g(t) = p_{g0}\left[\frac{R_0}{R(t)}\right]^{3\gamma}, \tag{2.3}$$

where γ is the ratio of gas heat capacities.

Thus, the pressure on the interface is given by

$$p(R,t) = p_v + p_{g0}\left[\frac{R_0}{R(t)}\right]^{3\gamma} - \frac{2S_{tension}}{R} + 2\,\Xi\,\frac{\partial u_r}{\partial r}\Big|_{r=R}. \tag{2.4}$$

Far from the bubble the liquid is assumed at rest and the pressure p_{amb} is known.

The Rayleigh-Plesset equation is developed following the explication proposed by Brennen [3]. Due to spherical symmetry and by conservation of mass, the inverse-square law requires that the radially outward velocity $u_r(r,t)$ must be inversely proportional to the square of the distance from the origin (e.g. the center of the bubble), i.e.

$$u_r(r,t) = \frac{F(t)}{r^2}, \tag{2.5}$$

where $F(t)$ is some function of time.

The mass transfer through the interface is neglected, i.e. phase change is not considered, so the liquid velocity at the interface $u_r(R,t)$ is equal to the interface velocity $\dot{R} = \frac{dR}{dt}$. This expression gives a form to $F(t)$, i.e. $F(t) = \dot{R}R^2$, and therefore to $u_r(r,t)$, i.e.

$$u_r(r,t) = \dot{R}\frac{R^2}{r^2}. \tag{2.6}$$

Assuming a Newtonian liquid, the Navier-Stokes equation for motion in the r direction is [3]

$$\frac{\partial u_r}{\partial t} + u_r\frac{\partial u_r}{\partial r} = -\frac{1}{\rho}\frac{\partial p}{\partial r} + \frac{\Xi}{\rho}\left[\frac{1}{r^2}\frac{\partial}{\partial r}\left(r^2\frac{\partial u_r}{\partial r}\right) - \frac{2u_r}{r^2}\right]. \tag{2.7}$$

After substituting u_r (Eq. 2.6) in Eq. (2.7), the viscous term of the Navier-Stokes equation cancels. Thus, for a viscous and non-viscous fluid, the momentum equation is given by Eq. (2.8), i.e.

$$\frac{\partial u_r}{\partial t} + u_r \frac{\partial u_r}{\partial r} = -\frac{1}{\rho}\frac{\partial p}{\partial r}. \tag{2.8}$$

Continuing, the resulting expression is:

$$\ddot{R}\frac{R^2}{r^2} + 2\dot{R}^2\left[\frac{R}{r^2} - \frac{R^4}{r^5}\right] = -\frac{1}{\rho}\frac{\partial p}{\partial r}. \tag{2.9}$$

Integrating with respect to r, from r to $r \to \infty$, it is obtained:

$$\frac{p(r,t) - p_{amb}(t)}{\rho} = \ddot{R}\frac{R^2}{r} + 2\dot{R}^2\left[\frac{R}{r} - \frac{R^4}{4r^4}\right]. \tag{2.10}$$

On the interface $r = R$, Eq. (2.10) gives:

$$\frac{p(R,t) - p_{amb}(t)}{\rho} = R\ddot{R} + \frac{3}{2}\dot{R}^2. \tag{2.11}$$

Finally, with the expression in Eq. (2.4) for the pressure at the interface, and noting that $\frac{\partial u_r}{\partial r}\Big|_{r=R} = -\frac{2\dot{R}}{R}$, the equation of Rayleigh-Plesset is obtained [25]:

$$\rho\left[R\ddot{R} + \frac{3}{2}\dot{R}^2\right] = p_v - p_{amb}(t) + p_{g0}\left[\frac{R_0}{R}\right]^{3\gamma} - \frac{2S_{tension}}{R} - 4\,\Xi\frac{\dot{R}}{R}. \tag{2.12}$$

It is to notice that only the viscous contribution to the Rayleigh-Plesset equation comes from the balance of forces at the bubble surface.

Using this equation, it is possible to determine the temporal evolution of the radius R and consequently the pressure field in the liquid (Eq. 2.10) when $p_{amb}(t)$ is known. In most cases, the inertial forces are dominant and viscosity does not play a significant role. The surface tension is often secondary in the case of bubble collapse [25].

Rayleigh-Plesset equation in two dimensions

In some cases, two-dimensional configurations are used in order to simplify experimental situations. This is the case of Lohse et al. [60] that studied the jet formation during the impact on soft sand. Very soft sand is prepared in a fully not-compact state by letting gas bubbles through it. Then, a steel ball is dropped on the sand generating a granular jet into the air. In order to analyze this phenomenon, they performed 2D experiments of jet formation by letting fall a cylinder into this prepared sand. They confirmed the jet formation process. Although the jet is less pronounced than in 3D experiments, the whole physics is observed [60]. In this case, it is about a granular medium; nevertheless the authors found an analogy with water that allowed them to use the Rayleigh-Plesset equation in 2D for the analysis. Another case is reported by Oguz and Prosperetti in 1993 [71]. They analyzed several aspects of the growth and departure of bubbles from a submerged needle. Specifically, they remarked a situation similar to a radially collapsing cylinder (i.e. a two-dimensional sink) during the process by which the gas neck connecting the bubble to the needle collapses and releases the bubble. So, for this point of the analysis the Rayleigh-Plesset equation developed in 2D was used.

For developing the Rayleigh-Plesset equation in 2D the same steps presented previously in Section 2.1.2.1 are followed, except that in this case the cylindrical symmetry is considered. Hence, by conservation of mass, the radially outward velocity $u_r(r,t)$ must be inversely proportional to the distance from the origin. Also considering that the mass transfer is negligible through the interface, we have the radial velocity as,

$$u_r(r,t) = \dot{R}\frac{R}{r}, \tag{2.13}$$

which compares to Eq. (2.6).

Next, we consider only non-viscous flows. So, using the momentum equation (Eq. 2.8) and the radial velocity for two-dimensional cases (Eq. 2.13), we have:

$$\ddot{R}\frac{R}{r} + \dot{R}^2\left[\frac{1}{r} - \frac{R^2}{r^3}\right] = -\frac{1}{\rho}\frac{\partial p}{\partial r}, \tag{2.14}$$

which compares to Eq. (2.9).

As done in the previous case to obtain the Eq. (2.10), here the Eq. (2.14) is integrated with respect to r (from r to $r \to \infty$) to give the following expression,

$$\frac{p(r,t) - p_{amb}(t)}{\rho} = \left(\ddot{R}R + \dot{R}^2\right) \log\left(\frac{R_\infty}{r}\right) + \frac{\dot{R}^2}{2} R^2 \left(\frac{1}{R_\infty^2} - \frac{1}{r^2}\right). \tag{2.15}$$

It is important to mention that the logarithm appears after the integration and so, a cut-off distance R_∞ is used. This distance starts from the axis and represents an outer surface of radius R_∞ that delimits the zone at which the velocity in the fluid does not change.

To be compared to Eq. (2.11), it is taken that on the interface $r = R$, so Eq. (2.15) gives:

$$\left(\ddot{R}R + \dot{R}^2\right) \log\left(\frac{R}{R_\infty}\right) + \frac{\dot{R}^2}{2}\left(1 - \frac{R^2}{R_\infty^2}\right) = \frac{p_{amb}(t) - p(R,t)}{\rho}. \tag{2.16}$$

The expression for the pressure at the interface (Eq. 2.4) can again be used to take into account the pressure inside the bubble, the surface tension and the viscous effects.

Here, the Rayleigh-Plesset equation for two-dimensional configurations is presented as

$$\left(\ddot{R}R + \dot{R}^2\right) \log\left(\frac{R}{R_\infty}\right) + \frac{\dot{R}^2}{2}\left(1 - \frac{R^2}{R_\infty^2}\right) = \frac{p_{amb}(t) - p_v - p_{g0}\left[\frac{R_0}{R}\right]^{3\gamma} + \frac{2S_{tension}}{R} - 2\,\Xi\,\frac{\partial u_r}{\partial r}\Big|_{r=R}}{\rho}, \tag{2.17}$$

which compares to Eq. (2.12).

2.1.2.2 Compression of a non-condensable gas bubble inside an incompressible liquid

In this section, the effects of viscosity and surface tension are ignored. In addition, it is considered that the bubble is filled only with non-condensable gas, in other words, there is no vapor inside the bubble. The resulting model allows to describe the global features of the non-condensable gas bubble collapse for an almost inviscid liquid such as water. During the bubble compression, the radius tends to zero and the radial inwards motion tends to infinity. If the Rayleigh-Plesset equation (Eq. 2.12) is integrated following the previous assumptions, the velocity of the bubble surface is obtained.

To do so, the Rayleigh-Plesset equation is re-written as,

$$\frac{1}{2\dot{R}R^2}\frac{d}{dt}\left(\dot{R}^2R^3\right) = \frac{p_{g0}\left[\frac{R_0}{R}\right]^{3\gamma} - p_{amb}}{\rho} \tag{2.18}$$

$$\frac{d}{dt}\left(\dot{R}^2R^3\right) = 2\dot{R}R^2\left(\frac{p_{g0}\left[\frac{R_0}{R}\right]^{3\gamma} - p_{amb}}{\rho}\right). \tag{2.19}$$

$$\frac{d}{dt}\left(\dot{R}^2R^3\right) = 2\dot{R}R^2\left(\frac{p_{g0}}{\rho}\left[\frac{R_0}{R}\right]^{3\gamma}\right) - 2\dot{R}R^2\left(\frac{p_{amb}}{\rho}\right). \tag{2.20}$$

The above equation is integrated as follows,

$$\dot{R}^2R^3 = \frac{2p_{g0}R_0^{3\gamma}}{\rho}\int_0^t \dot{R}R^{(2-3\gamma)}dt - \frac{2p_{amb}}{\rho}\int_0^t \dot{R}R^2dt \tag{2.21}$$

$$\dot{R}^2R^3 = \frac{2p_{g0}R_0^{3\gamma}}{\rho(1-3\gamma)}\left(R^{(1-3\gamma)} - R_0^{(1-3\gamma)}\right) - \frac{2p_{amb}}{3\rho}\left(R^3 - R_0^3\right) \tag{2.22}$$

$$\dot{R}^2 = \frac{2}{\rho R^3}\left[\frac{p_{g0}R_0^{3\gamma}}{(1-3\gamma)}\left(R^{(1-3\gamma)} - R_0^{(1-3\gamma)}\right) - \frac{p_{amb}}{3}\left(R^3 - R_0^3\right)\right] \tag{2.23}$$

As $\dot{R}$ is negative during the compression, it is obtained

$$\dot{R} = \frac{dR}{dt} = -\sqrt{\frac{2}{\rho R^3}\left[\frac{p_{g0}R_0^{3\gamma}}{(1-3\gamma)}\left(R^{(1-3\gamma)} - R_0^{(1-3\gamma)}\right) - \frac{p_{amb}}{3}\left(R^3 - R_0^3\right)\right]}. \tag{2.24}$$

Measurements in several works ([25], [107], [9], [45]), present high values of interface velocity during the collapse. For example values of about 800 m/s depending on the ambient pressure have been reported. Such high velocity values, of the order of half of the speed of sound of water (e.g. 1500 m/s), indicate that liquid compressibility must be taken into account in the final stages of collapse.

Then, in order to find the characteristic time of collapse, the Rayleigh-Plesset equation should be solved numerically. Eq. 2.12 and Eq. 2.17 are solved for a spherical bubble and for a circular bubble (i.e. in two dimensions), respectively.

Pressure field during bubble compression

Regarding the pressure field, it has been mentioned in the literature ([25], [40]) that high pressure values close to the interface are reached during the collapse of a bubble. These high pressure values in the liquid generate a violent behavior during the non-condensable gas bubble collapse. Being interested on the pressure field inside the liquid, an analytic analysis is done thereafter. In this regard, the Rayleigh-Plesset equations for spherical (Eq. 2.12) and cylindrical (Eq. 2.17) configurations are considered.

- **Spherical configuration**

  For a spherical bubble, the pressure field $p(r,t)$ can be determined from the Eq. (2.10), in which $\ddot{R}$ is taken from the Rayleigh-Plesset equation (Eq. 2.12) with the previous assumptions (i.e. ignoring viscous and surface tension effects, and considering that the bubble is only filled with non-condensable gas). The corresponding expression for $\ddot{R}$ is given by,

$$\ddot{R} = \frac{1}{R}\left(\frac{p_{g0}\left[\frac{R_0}{R}\right]^{3\gamma} - p_{amb}}{\rho} - \frac{3}{2}\dot{R}^2\right). \tag{2.25}$$

  Including Eq. (2.25) in Eq. (2.10), an expression for the pressure field in the liquid is obtained, i.e.

$$\frac{p(r,t) - p_{amb}}{\rho} = \left(\frac{p_{g0}\left[\frac{R_0}{R}\right]^{3\gamma} - p_{amb}}{\rho} + \frac{1}{2}\dot{R}^2\right)\frac{R}{r} - \frac{\dot{R}^2}{2}\frac{R^4}{r^4}. \tag{2.26}$$

  It is to notice that for solving this expression, it is required to know the radius R and the interface velocity $\dot{R}$, which are calculated by integrating numerically the Rayleigh-Plesset equation (Eq. 2.12) with the same previous assumptions.

- **Cylindrical configuration**

  In the case of a cylindrical configuration, the expression for the pressure field in the liquid can be obtained following the same steps presented for the spherical shape. Eq. (2.15) is considered, in which $\ddot{R}$ comes from the Eq. (2.17). Ignoring viscous and surface tension effects, and considering that the bubble is only filled with

non-condensable gas, the expression for $\ddot{R}$ is given by,

$$\ddot{R} = \frac{1}{R}\left[\frac{\frac{p_{amb}-p_{g0}\left[\frac{R_0}{R}\right]^{3\gamma}}{\rho} - \frac{\dot{R}^2}{2}\left(1-\frac{R^2}{R_\infty^2}\right)}{\log\left(\frac{R}{R_\infty}\right)} - \dot{R}^2\right]. \tag{2.27}$$

Then, including Eq. (2.27) in Eq. (2.15), the pressure field in the liquid is obtained, i.e.

$$\frac{p(r,t)-p_{amb}}{\rho} = \left[\frac{\frac{p_{amb}-p_{g0}\left[\frac{R_0}{R}\right]^{3\gamma}}{\rho} - \frac{\dot{R}^2}{2}\left(1-\frac{R^2}{R_\infty^2}\right)}{\log\left(\frac{R}{R_\infty}\right)}\right]\log\left(\frac{R_\infty}{r}\right) + \frac{\dot{R}}{2}R^2\left(\frac{1}{R_\infty^2}-\frac{1}{r^2}\right) \tag{2.28}$$

Similarly to the spherical bubble case, for solving the pressure field is needed to know the radius R and the interface velocity $\dot{R}$, which are numerically calculated by integrating in time the Rayleigh-Plesset equation (Eq. 2.17).

Fig. 2.7 shows the behavior of the pressure in the liquid near the interface $p(r,t)$ for each configuration (i.e. 3D and 2D). It is used the Eq. 2.26 for the 3D configuration and the Eq. 2.28 for the 2D configuration. It exhibits the liquid pressure field at several instants during the compression. Each curve corresponds to a specific moment linked to bubble instantaneous radius, which here are expressed dimensionless, i.e. $R/R_0 = 0.9,\ 0.5,\ 0.3$ and 0.25.

In the present development the pressure from the non-condensable gas is considered as the only pressure contribution inside the bubble. The parameters used are shown in Table 2.1.

TABLE 2.1: Parameters used in the model to estimate the pressure in the liquid

Ambient pressure	$p_{amb}\ [MPa]$	10
Initial pressure of the non-condensable gas	$p_{g0}\ [MPa]$	0.1
Initial radius of the bubble	$R_0\ [m]$	0.010
Ratio of heat capacities	γ	1.4
Liquid density	$\rho\ [kg/m^3]$	1000

As illustrated in Fig. 2.7, the pressure in the liquid near the interface becomes higher than the ambient pressure over some time interval during the last stages of compression. Under adiabatic conditions, the pressure at the interface is $p_{g0}\left[\frac{R_0}{R}\right]^{3\gamma}$ and this term

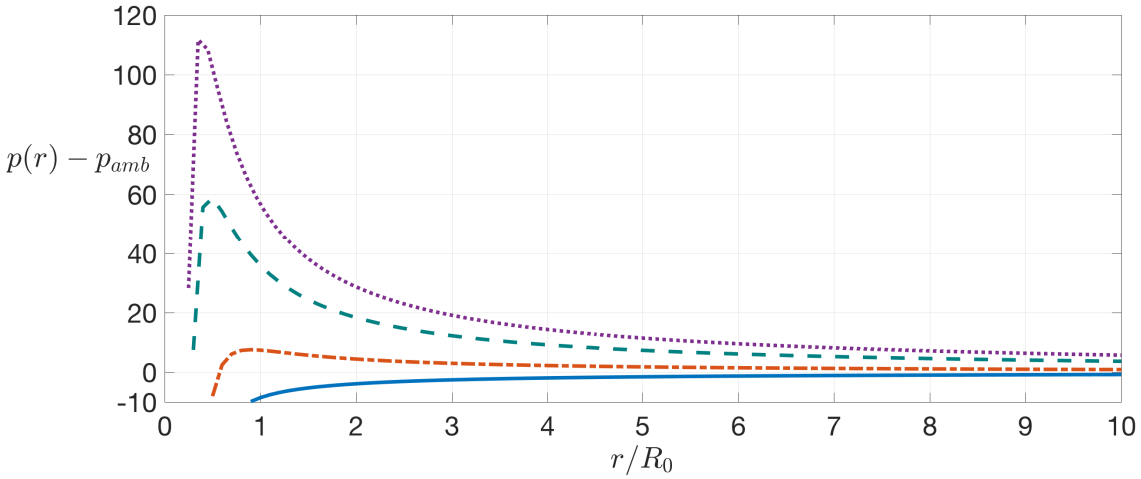

(a) Pressure in the liquid in 3D, using the Eq. 2.26

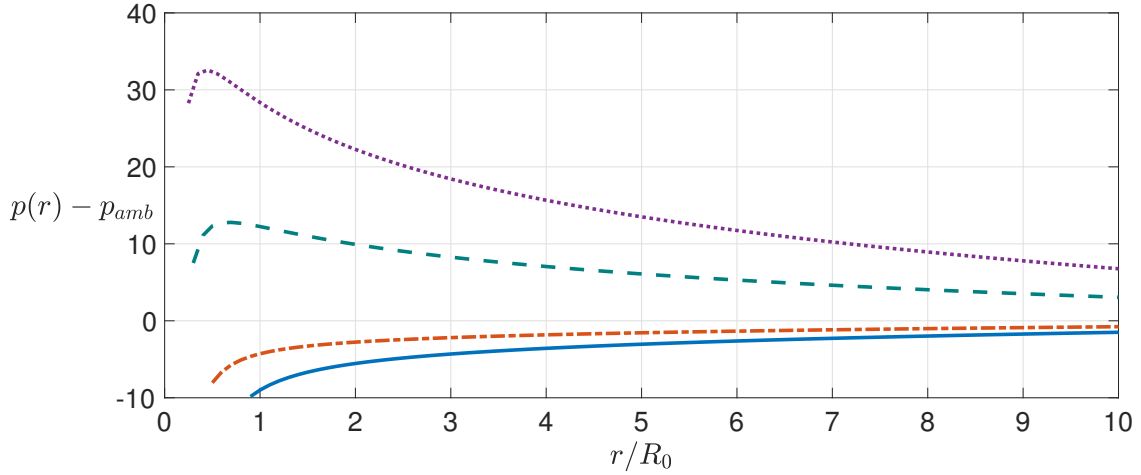

(b) Pressure in the liquid in 2D, using the Eq. 2.28

FIGURE 2.7: Pressure $[MPa]$ in the liquid as a function of the radial distance at different times corresponding to different bubble instantaneous radius. Blue solid line: $R/R_0 = 0.9$, red dashed-dotted line: $R/R_0 = 0.5$, green dashed line: $R/R_0 = 0.3$, violet dotted line: $R/R_0 = 0.25$

dominates the equations 2.26 in 3D and 2.28 in 2D in the last stages of compression, while the liquid pressure tends to the ambient pressure far away from the bubble.

The liquid pressure increases with the decrease of R/R_0. It is observed that this growth in the liquid pressure is faster close to the interface. So, high pressure values close to the bubble interface (i.e. $\frac{r}{R} \approx \frac{R}{R_0}$) are reached as the bubble size decreases.

The effect of the non-condensable gas on the liquid pressure field is observed at the bubble interface, i.e. at the lowest value of r/R_0 of each curve. It is not evident on the figure, but the pressure value of the liquid at the bubble-liquid interface is the same for both cases (i.e. 3D and 2D). This is because the term that quantifies the non-condesable

gas does not depend on the configuration. It depends on the radius evolution (i.e. $R(t)$) and here, both figures (Fig. 2.7(a) and Fig. 2.7(b)) present the same instantaneous radius R/R_0.

At early times, the liquid pressure increases from the low initial non-condensable gas bubble pressure to the ambient pressure (p_{amb}). As the non-condensable gas bubble is compressed, the bubble pressure increases, so that, as a consequence, the liquid pressure rises and eventually exceeds p_{amb}.

Because only pressure and inertia forces are taken into account, the pressure field is considered as the effect of inertia forces only. This liquid pressure behavior can be also explained as the result of the conservation of the liquid volume that tends to concentrate liquid motion to a smaller region [25]. This means that the liquid convergences into a region generating an increase of pressure. If we consider the divergence of the transport velocity of liquid, it is negative, then its volume decreases, and because the mass remains constant, its pressure increases.

So, the liquid pressure field presented in both configurations (3D and 2D) is a consequence of the velocity field generated by the bubble interface velocity ($\dot{R}$).

In summary, both 3D and 2D models present a liquid pressure field alike: near the interface the liquid pressure rises due to the non-condensable gas inside the bubble, and far away from the bubble the liquid pressure tends to p_{amb}. Of course there is a difference in the liquid pressure field linked to the dimensional approach (3D and 2D), which will be addressed in the next part.

It is observed that a 3D collapse presents pressure levels higher than the pressure levels in the 2D configuration. If we compare the pressure peak found near the bubble interface, it is noted one order of magnitude of difference between both configurations. This difference indicates that the use of the 2D model would underestimate the pressure peak at the bubble collapse.

After this peak and towards the growing direction of r/R_0, the pressure profile rapidly decreases in both cases. But the decreasing rate is also different for each configuration. To explain this behavior, both pressure field expressions (Eq. 2.26 and Eq. 2.28 for 3D and 2D models, respectively) are considered. There are two terms in the right-hand side of each expression. In the 3D model, the decreasing behavior is controlled by two functions, i.e. $1/r$ and $1/r^4$. These functions decrease faster than $log(1/r)$ and $1/r^2$

in the 2D configuration, explaining from a mathematically point of view the profile behavior. From a physical approach, the pressure decay rate may be attributed to the inverse-square law in 3D and to the inverse law in 2D. In 3D, the pressure field is governed by the inverse of the square of the distance and in 2D it is governed by the inverse of the distance, showing that the decay will be faster in 3D than in 2D configurations.

Although the amplitude value and the decreasing rate is affected by the 2D assumption, the liquid pressure tendency is comparable qualitatively in both configurations. So, the 2D assumption allows us to estimate the fluid dynamics during the non-condensable gas bubble compression.

2.1.2.3 Pressure waves during the bubble compression inside a compressible liquid

As our interest is to go towards the erosion caused by the cavitation phenomenon, an explanation of the pressure wave generated by the compression of a non-condensable gas bubble is given. Fig. 2.8 shows a sketch of two situations, it is shown the compression of an isolated bubble on the top of the figure, and the compression of a bubble near a solid surface on the bottom.

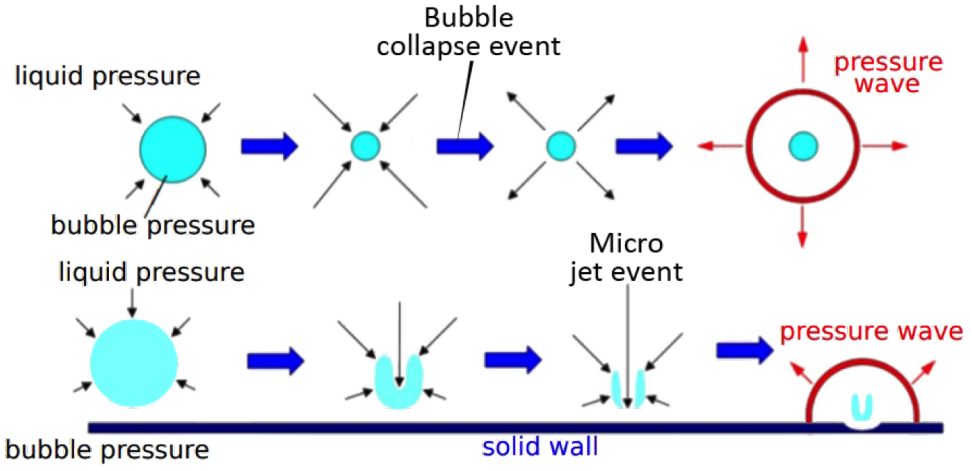

FIGURE 2.8: Bubble compression scheme. On top: bubble compression in free field. Bottom: bubble compression next to a solid boundary

The liquid compresses the bubble, causing that the non-condensable gas bubble is no longer able to support its structure because of its small internal pressure in comparison with the liquid pressure. In consequence, the bubble size decreases until its collapse, generating a pressure wave that propagates into the surrounding liquid. In other words,

before the "bubble collapse event" the liquid goes towards the non-condensable gas bubble, but after the "bubble collapse event" the liquid near the non-condensable gas bubble is pushed outwards by the pressure wave generated. This particular instant is highlighted on Fig. 2.8.

The compression of the non-condensable gas bubble near a wall shows different features. The solid wall boundary creates a geometrical asymmetry that causes the asymmetry shape of the bubble along the compression. The wall prevents the flow of filling the space between the bubble bottom and the wall. This generates a velocity difference between the upper side and the bottom side of the bubble, i.e. the upper side presents a higher velocity than the bottom side. Consequently, the farther side of the bubble with respect to the solid accelerates inward more rapidly than the opposite side, resulting in a micro jet that penetrates the bubble. Afterwards, the bubble collapses, generating a pressure wave that can damage structurally the material. It has been shown that the micro jet event also generates a pressure wave that propagates in the liquid ([26], [45], [40]). The "micro jet event" is highlighted on Fig. 2.8.

The later phenomenon has been studied experimentally highlighting additional features during the compression phase. For example, Vogel et al. [107] remarked a displacement of the bubble towards the solid wall when the bubble is initially located farther from the wall. This displacement is caused by the velocity difference between the upper and lower side of the bubble. The authors also observed a deformation of its shape, precisely the spherical bubble deforms into a ring as the compression is happening. Meanwhile, Fujikawa et al. [26] have studied the growth, collapse and rebound of a bubble close to a solid wall. Authors have observed that the bubble close to the solid wall emits a water jet towards the boundary in the final stages of collapse, then it rebounds. Authors describe that the bubble, during growth, becomes elongated in the direction parallel to the solid boundary, but as the bubble proceeds to collapse, it becomes elongated in the direction normal to the boundary and then approaches the boundary forming a water jet.

Additionally, estimations of the micro jet velocities were conducted, obtaining some orders of magnitudes. Values up to 100 m/s are reported from experimental works [107], and values in the range of 100 m/s to 800 m/s depending on the ambient pressure are obtained from numerical works ([45], [40]). Regarding pressure emissions during the collapse of bubbles attached to a rigid wall, it has been reported wall pressures of about 0.8 GPa [43] and 1GPa [4].

Sensitivity analysis has been done about the bubble collapse close to a boundary. It is considered a free surface boundary([56], [74], [112], [109], [101], [102]) and a rigid wall boundary ([39], [40], [45], [49], [113]). In all cases the boundary influences the bubble compression mechanism generating the physical conditions to develop a micro jet directed towards the boundary. Additionally, the effect of buoyancy has been studied by changing the inclination of the adjacent rigid wall with respect to the gravity direction [111]. In this case, a micro jet is also observed, however, some differences can be mentioned. For example, changing the inclination of the wall causes a distortion in the direction of the micro jet, i.e. the jet is not directed perpendicular towards the wall. Thus, the micro jet is formed and directed in a oblique direction with respect to the wall [111].

Furthermore, experimental ([5], [12]) and numerical [39] works indicate that multiple pressure peaks on the wall are registered during one bubble collapse event. Two major pressure peaks are usually identified, one corresponding to the impact of the micro jet and the other one from the pressure wave generated when the bubble collapses. The relative magnitudes of these two peaks depend on the ambient pressure and on the distance between the bubble and the wall. In some cases, the peak from the micro jet is higher, while in some other cases the one from the bubble collapse is higher.

Another typical configuration considered is the shock-induced collapse. It is the representation of a bubble that receives a high pressure wave generated by the collapse of neighbor bubbles. Results show that a jet forms in the direction of propagation of the wave and penetrates the bubble during collapse ([39], [75], [110], [43]). As a result of the propagation of this wave, high pressures are achieved for bubbles collapsing close to the wall, reporting values of about 0.7 GPa [43] and 1 GPa [39]. These wall pressure values are comparable with the ones obtained from a classical configuration, in which the bubble collapses due to an uniform pressure in the liquid higher than in the gas. The incoming shock retards the bubble collapse in comparison with the classical configuration [43]. Additionally, it is mentioned that as the pulse amplitude increases, the pressure on the wall also increases [39].

In conclusion, the high speed of the micro jet and the high pressure wave emissions cause large pressure amplitudes at the solid surface leading to material damage or erosion [9], [107]. Therefore, special interest is given to represent these two phenomena in the cavitation prediction. In this line, a brief description and some remarks on viscosity and

surface tension effects are presented, because they may affect the behavior of the micro jet and pressure waves under certain conditions.

2.1.2.4 Effect of viscosity on the bubble collapse

The effect of viscosity is studied due to its ability to damp out the perturbations in the flow field and consequently to affect the flow dynamics during the bubble collapse.

In the literature ([3], [25], [94], [2], [95], [58]) it is found that the collapse is slowed down by the viscosity. In general, for single bubble dynamics, viscosity plays a role for very small bubbles, i.e. bubbles having a radius of the order of 1 μm [3].

The influence of viscosity in the bubble collapse was also considered by Poritsky in 1952 and then by Shima and Fujiwara in 1980 [95]. They showed that viscosity retards the collapse. However, in the case of water this slow down is not large [25]. Likewise, in 1965, Ivany and Hammitt showed that the damping effect of viscosity does not play a significant role and thus it can be neglected for low viscous fluids like water [3], [94].

Later, in 2009, Johnsen and Colonius [40] analyzed the viscosity influence based on the Reynolds number (Re), which measures the ratio of inertial forces to the viscous forces. They calculated the Reynolds number considering the maximum jet velocity and the jet size (which is approximately $0.25R_0$) during compression and found out that the Reynolds number varies from 10^2 to 10^3 for bubbles of 10 μm. So, based on these values they conclude that viscosity does not influence the flow dynamics during the bubble collapse, because the inertial forces are 100 to 1000 times higher than the viscous forces.

In 2012, Lind et al. [59] have investigated the dynamics of multiple bubbles initially placed near a rigid boundary including the viscous effect. They considered two bubbles positioned along a vertical axis of symmetry, where one bubble is closest to wall. They analyzed their dynamics varying the Reynolds number. It was found that viscosity influences the dynamic interaction between these two bubbles for low Reynolds numbers (e.g. $Re = 2$). For example they remarked a difference in the time when the micro jet is formed. For inviscid flow, the micro jet is first developed in the upper bubble (i.e. the one that is farther from the boundary), but for viscous flow (e.g. $Re = 2$), the micro jet is first formed in the lower bubble (i.e. the one that is closer to the boundary), showing that this behavior is almost the opposite. They also reported that viscosity does not play a significant role for Reynolds numbers larger than 100. Therefore, viscosity effects are

relevant for applications involving very low Reynolds numbers, ergo where the inertial forces are not important.

Regarding the flow dynamics for cavitating flow, such as the cloud shedding behavior, the inertia effects mainly drive its collapse and in consequence viscosity effects are not significant. Nevertheless, special care might be taken into account when neglecting viscosity in flow where viscous separation could occur. So, a verification that the single-phase flow remains attached to the geometry at the same flow conditions is recommended [94].

Since we are interested in modeling the collapse of a non-condensable gas bubble, whose initial radius is about 10 $[mm]$ and it is located in water, an estimation of the Reynolds number can be done. So, considering the following values:

- the water kinematic viscosity at 20 $°C$ is $1 \cdot 10^{-6}[m^2/s]$ [108],
- the jet velocity is about half the water speed of sound [25] (i.e. $\frac{1500}{2}$ $[m/s]$) and
- the characteristic length corresponds to the jet size (i.e. 0.25 R_0 [40]),

the Reynolds number is: $Re = 2 \cdot 10^6$. This results highlights that the inertial forces dominate the dynamics during the bubble compression in the case that we are interested in.

To summarize, since the bubble compression is mainly driven by inertial forces and we consider machines (e.g. Pelton turbines) working with water, the effect of viscosity is neglected in the frame of this investigation.

2.1.2.5 Effect of surface tension on the bubble collapse

Concentrating our attention in the bubble dynamics, surface tension influences the whole bubble development. It has a significantly influence during the nucleation phase [3], [72], a stabilizing effect when instabilities are present [41], and a slightly acceleration effect during collapse [25]. It should be noted that instabilities exist, mainly but not only, during the bubble collapse [3]. Now, we examine in detail the compression phase and the range where this acceleration effect is significant.

In this regard, it is considered the Rayleigh-Plesset equation (Eq. 2.12), where the bubble is filled exclusively with non-condensable gas (there is no vapor inside the bubble) and only the surface tension term is considered, i.e.

$$\rho\left[R\ddot{R}+\frac{3}{2}\dot{R}^2\right]=p_g-p_{amb}(t)-\frac{2S_{tension}}{R}, \tag{2.29}$$

where p_g stands for the partial pressure of the gas inside the bubble, $S_{tension}$ is the surface tension and p_{amb} is the pressure far away from the bubble.

It is to notice that the viscous term are not considered.

Eq. (2.29) is integrated to obtain an expression for the interface velocity ($\dot{R}=dR/dt$). The resulting expression is given by [25], i.e.

$$\frac{dR}{dt}=-\left(\frac{2}{3}\left(\frac{p_{amb}-p_g}{\rho}\right)\left[\frac{R_0^3}{R^3}-1\right]+\frac{2S_{tension}}{\rho R_0}\frac{R_0^3}{R^3}\left[1-\frac{R^2}{R_0^2}\right]\right)^{1/2}, \tag{2.30}$$

where R_0 is the initial and maximum bubble radius.

The pressure and the surface tension term are compared to determine under which conditions the surface tension effect is important. Since we search to compare the influential terms, we take the ones involving the ratio R_0/R with the highest exponent. Then, it was shown by Franc in [25] that the surface tension effect is significant if:

$$\frac{2S_{tension}}{\rho R_0}>\frac{2}{3}\frac{p_{amb}-p_g}{\rho}. \tag{2.31}$$

Taking out R_0 from Eq. (2.31), we have an expression (Eq. 2.32) indicating the maximum bubble radius that is influenced by the surface tension for certain physical values, i.e.

$$R_0<\frac{3S_{tension}}{p_{amb}-p_g}. \tag{2.32}$$

Some physical values for water are taken to show the surface tension effect. Assuming 1 *bar* as pressure difference and knowing the water-air surface tension at 20 $°C$ (e.g. $S_{tension}=0.072\ N/m$), it is obtained a value of 2 μm for the maximum bubble radius. This small value is quite rare in hydraulic application [25]. Hence, the effect of surface tension is not significant in the case of bubble collapse in hydro-machines.

In summary, the surface tension does not influence the bubble dynamics in terms of our applications.

2.1.3 Considerations in the physical model of cavitating flows

Liquid compressibility and mass transfer are contemplated when studying the cavitation phenomenon. They allow investigating different aspects, such as the pressure wave propagation in micro-scale models when considering the liquid compressibility and the generation of vapor pockets when considering the mass transfer in macro-scale models. So, their explanation is relevant in order to define the physical model to be used during this work.

2.1.3.1 Liquid compressibility

Compressible flows are characterized by undergoing density variations due to a pressure field established. The compressibility of a fluid denoted by θ can be interpreted as the compression that suffers a small element of fluid of specific volume ν due to the increase of pressure p. So, compressibility is defined by [94],

$$\theta = -\frac{1}{\nu}\frac{d\nu}{dp}. \tag{2.33}$$

Since the volume is reduced, $d\nu$ is negative. Thus, a negative sign is added in the Eq. (2.33) because the compressibility of a substance cannot be negative [94]. This equation needs some attention, as the compression process may be not adiabatic. Therefore, the temperature in the fluid is considered and kept constant to obtain the isothermal compressibility, i.e.

$$\theta_T = -\frac{1}{\nu}\frac{\partial\nu}{\partial p}\Big|_T. \tag{2.34}$$

Similarly, for adiabatic and reversible processes (without any dissipation mechanisms) isentropic compressibility is expressed as,

$$\theta_s = -\frac{1}{\nu}\frac{\partial\nu}{\partial p}\Big|_s. \tag{2.35}$$

The Eq. (2.35) can be rewritten using the fluid density, ρ, as

$$\theta_s = \frac{1}{\rho}\frac{\partial \rho}{\partial p}\Big|_s. \tag{2.36}$$

For example in the physical problem of an air bubble collapsing in water, the water compressibility at standard conditions is about $5{\cdot}10^{-10}\ m^2/N$ while the air compressibility is about $10^{-5}\ m^2/N$. Although water compressibility is very low compared to air compressibility, all fluids should be treated as compressible substances in order to properly describe the propagation of waves.

This can be interpreted considering the speed of sound, which is the speed at which a pressure wave travels through a medium [8]. It is defined as

$$c^2 = \frac{\partial p}{\partial \rho}\Big|_s. \tag{2.37}$$

Therefore, a relation can be found between the isentropic compressibility and the speed of sound [94], i.e.

$$c^2 = \frac{1}{\rho \theta_s}, \tag{2.38}$$

showing that if compressibility is not taken into account, i.e. $\theta_s = 0$, a finite wave speed can not be defined as $c \to \infty$.

Another implication of liquid compressibility is shown considering the water-hammer phenomenon, where an initially moving liquid is instantaneously stopped. The sudden flow stagnation generates an upstream traveling wave. So, the water-hammer relation gives the pressure rise, Δp, linked to a conversion of kinetic energy to potential energy stored in the compressible liquid [85], i.e.

$$\Delta p = \rho c \Delta v, \tag{2.39}$$

where Δv is the variation of the flow velocity.

It is noted that for a proper estimation of the water-hammer pressure, the liquid speed of sound must be considered, and thus the liquid compressibility. Additionally, incompressible formulations does not allow the formation of pressure waves with finite

speed of sound (as $c \to \infty$) and so it does not allow to model the pressure difference created.

A link between the water-hammer phenomenon and the bubble dynamics can be done during the final stages of a bubble collapse near a wall, when the water micro-jet is developed. At that moment, the liquid at high velocity inside the jet meets the liquid at lower velocity, located between the bubble and the wall. From that instant on, it can be assumed that the kinetic energy of the liquid is transformed to elastic energy (i.e. a form of potential energy), thus releasing a pressure wave.

Supplementary information is given by Fuster et.al. [27], who studied the effect of liquid compressibility on the dynamics of a spherical cavitating bubble. Authors report that liquid compressibility effects are crucial in order to get accurate estimations of the internal pressures reached inside the bubble, as well as in the estimation of liquid pressure profiles after the bubble collapse. In addition, authors compare their numerical model that considers liquid compressibility against analytic models, like the Keller and Miksis model [44] that considers also liquid compressibility and the Rayleigh-Plesset model that does not. In conclusion they found out a difference of 5% in the collapse time.

In conclusion, during the compression and collapse phase, liquid compressibility must be considered. It allows taking into account the emission of pressure waves that are essential when studying cavitation erosion.

2.1.3.2 Mass transfer

Mass transfer mechanism, which is considered as an internal process inside the flow, is a physical process occurring under certain flow conditions. Sometimes this internal process happens in a time scale not negligible with respect to the time scale of the flow, so the internal process can be considered in the formulation. In some other situations, the time rate of the internal process can be negligible and therefore, the internal process is not taken into account in the formulation. So, in order to board the mass transfer subject, an internal process arising inside the flow is considered.

For that purpose, it is assumed a fluid flow without any dissipation mechanisms, which corresponds to the Euler equations of fluid dynamics. For any flow, the set of Euler equations requires an equation of state as a closure relation. For flows having a negligible internal process, an equation of state relating the thermodynamic variables such

as pressure, temperature and density is usually used. However, for flows having an internal process, an additional variable should be introduced in order to specify this non-equilibrium process.

This new variable is analyzed following a control volume approach. It is assumed that the new variable a is produced or modified due to thermodynamic or chemical process. For example, in cavitation, vapor is produced inside the control volume due to the phase transition process. Therefore, a can be taken as the volume fraction (i.e. the ratio between the vapor volume to the total volume, $\frac{V_v}{V_{tot}}$) or the mass fraction of vapor (i.e. the ratio of vapor mass to the total mass, $\frac{m_v}{m_{tot}}$).

Then, this process that occurs internally can be represented with the time rate change of a, i.e. $\left(\frac{da}{dt}\right)_{int.proc}$.

The addition of this new variable, a, requires an extra equation in the Euler system. It is a transport equation as the change of this new variable is influenced by the fluid flow [94]. Then, taking u_k as the velocity in the direction of interest x_k and writing the transport equation along this direction, the transport equation of a can be expressed as

$$\frac{\partial(\rho a)}{\partial t} + \frac{\partial(\rho a u_k)}{\partial x_k} = \rho \left(\frac{da}{dt}\right)_{int.proc}. \tag{2.40}$$

The right hand side term represents the time rate change of a inside the control volume due to internal processes, also called source term. The left hand side term corresponds to the change of variable a due to the net inflow into the control volume. Actually, this equation presents the same form as the transport equation for the void fraction usually used when modeling the phase transition, which is assumed to occur in a non-equilibrium process. This process is modeled by the definition of the source term.

Condensation and evaporation are good examples of flows with phase transition. Condensation process can be produced when a vapor at a given temperature is brought at a pressure higher than the vapor pressure at that certain temperature. This may happen along an isothermal compression path. So, as the vapor is compressed isothermally, it reaches its condensation pressure, which is the vapor pressure of the liquid phase of the same substance [63], then, the vapor condenses. For example, this phenomenon may occur during the compression of a vapor bubble. On the other hand, the evaporation process

is a metastable state that results due to a rapid expansion of a liquid flow [91], where the phase change takes place. This evaporation process is defined by a rate equation for cavitation and occurs during the growth phase of a vapor bubble.

The source term, on the right hand side of Eq. (2.40), is a defining parameter of several models. It is a function of the fluid properties and of the phase transition process. There exist several empirical models for evaporation and condensation that consider the flow as a homogeneous mixture. Among them we name the model of Kunz [48] that is based on the creation (m^+) and destruction (m^-) of liquid. We mention the model of Zwart based on the simplified Rayleigh-Plesset equation where their coefficients are calibrated empirically [65]. Likewise, there is the full cavitation model that is also based on the simplified Rayleigh-Plesset equation with empiric coefficients but considering the turbulent kinetic energy and the surface tension [36], [65]. There are also theoretical models, like the one proposed by Saurel et al. [91] that guarantees equilibrium conditions of equal temperatures and equal Gibss free energies during phase change, and the model proposed by Goncalves et al. [98] which assumes that the mass transfer is proportional to the divergence of the velocity. Additionally, there are phase change models that do not consider the flow as homogeneous mixture. Instead, they consider two pure fluid separated by a sharp interface like the one proposed by Lauer in [49]. In this model the rate of condensation and evaporation is taken from the kinetic theory of gases explained in Schrage [93].

In summary, the internal process is not considered in the formulation when the characteristic time of the internal process is much slower than the time scale of the flow. So, the internal process does not have the time necessary to take place within the flow time window, in consequence, the time rate of the internal process is negligible with respect to the time scale of the flow. On the other hand, when the time rate of the internal process is comparable to the time scale of the flow, the internal process cannot be negligible. In consequence, the internal process should be modeled by the use of transport equations and time dependent source terms.

Linking the process of mass transfer between vapor and liquid to the cavitation bubble phenomenon, a general overview of its development is addressed. During the bubble growth, there is an important mass transfer effect that leads its growth [3]. Later during the last stages of the compression phase, condensation is supposed to occur when the gas inside the bubble exceeds its condensation pressure. So, in order to estimate the

condensation effect with respect to the inertial effects, it is compared the collapse time against the time of mass diffusion in liquid through the bubble surface. To do so, the diffusion coefficient in liquids, D, is taken to be around $10^{-9}[m^2/s]$ [17]. To illustrate the physical significance of diffusion coefficient, it is considered the variable $\frac{z^2}{4Dt}$. When this variable equals the unity, the diffusion has happened, i.e. when z^2 equals $4Dt$, the diffusion has penetrated a distance z during the time t [17] .

So, it is considered a bubble of 100 $[\mu m]$ submerged in water whose density is $1000[kg/m^3]$ and the water pressure is $p_{amb} = 10^5[Pa]$. Using the Rayleigh equation for estimating the collapse time (Eq. 2.12) considering only non-condensable gas term and neglecting the surface tension and viscous term, it is obtained $1 \cdot 10^{-5}[s]$. Since condensation occurs in the last stages of compression, it is considered that the bubble's characteristic length z is $0.25R_0$, which corresponds to the bubble size when the micro jet impacts it [40]. Hence, the condensation time of a bubble having this characteristic length is given by $t = \frac{(0.25R_0)^2}{4D}$, so $t = 0.16[s]$.

Comparing these two times, it is evident that the condensation time is much shorter than the time of the bubble collapse.

In conclusion, the inertial effect are more important in comparison to the phase change effect during the final stages of the compression phase. So, mass transfer does not play a relevant role in the resulting pressure waves and jet dynamics, and in consequence, it is not modeled.

2.1.4 Numerical methods for modeling cavitation

A large variety of numerical methods for simulating cavitating flows have been found in the literature. Since cavitating flows involved several fluids such as liquid and vapor, special interest has been given to the treatment of the interface. For example we have the numerical models using level-sets techniques [7], [34] and volume-of-fluid (VOF) tracking [29]. High-order schemes, such as accurate WENO schemes [38], have been used as well to model two phase flows and compressible multi-fluids.

In particular, there is a distinction between the sharp discontinuity interface and the diffuse interface models. The first one is mostly used in Lagrangian schemes working with mesh misalignment or using meshless methods. It can be also developed in Eulerian schemes where the VOF or level-set model are used. The second type of methods considers

interfaces as numerically diffused zones. Diffuse interfaces correspond to artificial mixtures created by numerical diffusion, where the determination of thermodynamic variables is done following the multiphase flow theory. The challenge is to derive physically, mathematically and numerically consistent thermodynamic laws for the artificial mixture [92]. In addition, when using the second type of interface, models based on hyperbolic multiphase flows are usually constituted. There, we find two types of mixture models: considering total non-equilibrium and considering mechanical equilibrium. Afterward, one of theses mixture models is used to simulate phase change and mass transfer [91], [92], [98], [49].

As mentioned in Chapter 1, in this work the SPH-ALE method is used to model the cavitation erosion, where the emphasis is given in the representation of the bubble collapse phenomenon (i.e. pressure waves and micro jet event).

It is known that SPH method represents the physics of incompressible or weakly-compressible flows in a good way ([62], [68], [54], among others). However, few information concerning compressible flows modeled by SPH has been found, and the little information in this regard ([114], [115]) indicates the difficulty to treat the shock propagation problems present in compressible regimes. This exhibits one of the challenges of this thesis.

In relation to the interface treatment, since SPH-ALE is a meshless method following a Lagrangian approach, the interface is interpreted as a sharp discontinuity. Further information about the SPH-ALE method, including numerical considerations about compressibility and multiphase flow models is given in Chapter 4.

As we are interested in the study of the solid reaction due to the hydrodynamic impact caused by the bubble collapse phenomenon, coupling methods are addressed. Here, we present works related to the fluid-solid coupling of SPH methods. First, we present works about the coupling of SPH and Finite Element (FE) methods, where the fluid is represented by the SPH method and the solid by the FE method. We mention the work of Li [57] that couples in a non-intrusive and synchronized manner both solvers. By imposing the normal velocity continuity at the interface, this coupling method ensures that there is no energy dissipation nor energy production at the interface. The code has been developed for applications using the same time-step for the fluid and solid domain. Then, we present the work of Nunez et al. [69] developed in the frame of the PREDHYMA project and hence, it is the approach used in this thesis. The authors

propose an approach for transient nonlinear fluid structure interaction problems. They suggest that this coupling approach is suitable for the prediction of fluid-structure interaction phenomena occurring during a very short time. For example, authors present the case scenario of a rock immerse in a water jet that flows at high velocity and eventually the rock impacts against a steel plate. The strong point of their work is, similar to Li's contribution, that the energy exchange through the interface between fluid and solid is well controlled. In complement, Nunez et al. developed an approach capable of handling different time-steps in each domain. Second, we mention the coupling of fluid and solid, where both domains are represented by the SPH method, i.e. a fluid SPH - solid SPH coupling approach. In this frame, we found the work of Joshi et al. [42], whose authors main motivation is to develop a SPH cavitation erosion solver in order to estimate the structure reaction due to bubble collapses. The authors consider the fluid and solid within a same mathematical framework that allows to develop a single system for both domains (fluid and solid domain). The equations for both, fluid and solid, are fit into a stress stencil form, such that the interactions between fluid and solid can be considered within the kernel interaction itself.

In the next section a structural approach is presented in order to address the damage on solid walls caused by cavitation. The response of the material to cavitation impulsive loads and material properties most relevant to cavitation erosion are presented.

2.2 Cavitation erosion

The introduction about the general process of cavitation erosion given in this section comes from [45]. The collapse of bubbles is generally very violent. This is because the difference between the liquid pressure and the bubble inner pressure is quite large and it is able to provide a huge acceleration of the bubble surface. The bubble collapse comes with the compression of its content and the consequent emission of a large pressure wave. The impulsive pressure resulting from the impact of the micro-jet or from the impact of the pressure waves may exceed some appropriate material threshold (such as its yield stress) inducing local damage.

Material damage depends on the duration of exposure to cavitation. For metallic surfaces, there is an incubation period during which no measurable mass loss occurs [25]. During this period, damage takes the form of small permanent plastic deformations or pits.

These pits are present due to bubble collapses whose intensities exceed the elastic limit of the material [45]. Pit diameters are in the order of microns [10].

In general, when a material surface has received several cavitation impacts, failure and material removal usually occurs. This is the mass loss period. The erosion process involving these two period, i.e. incubation and mass loss, is the generalized process followed by most materials used in hydrodynamic applications [25]. Nevertheless, for brittle materials such as coating and composites, failure can occur before pits overlap.

2.2.1 General erosion process

The general erosion process describes the evolution of mass loss rate with exposure time. Normally, there are four stages in the material erosion process: incubation, acceleration, deceleration and steady-state periods [25], [45]. This stages can be observed in the weight or volume loss curve illustrated in Fig. 2.9.

Incubation period

Initially, the material surface deforms without material loss. In this phase the material surface follows a work hardening that makes the material more resistant to stress [45]. During this initial phase, permanent deformation may occur as well as the development of micro-cracks. This is a very short initial period that is difficult to observe, but its duration can be important to the determination of the material life under cavitation, as it is shown by some correlations between material incubation and lifetime [99].

Acceleration period

After the incubation phase, the erosion process accelerates. During the acceleration phase, the erosion rate increases until it attains a maximum value. In this phase, the material experiences weight loss and fractures. The duration of this phase depends on material properties. Normally, it ends once the surface properties have changed so much that it begins a different interaction between the new material surface shape and the cavitation field.

Deceleration period

The deceleration period starts with a new material surface shape. According to Chahine [45], entrapped gas and liquid in the deep craters of the new roughness can damp the incoming cavitation pressure waves, so attenuating the erosion process.

Steady-state period

Finally, equilibrium between the erosive power of the cavitation field and the response of the material occurs. The erosion process reaches the steady-state period (or terminal stage), where the weight loss rate reaches a quasi-constant value.

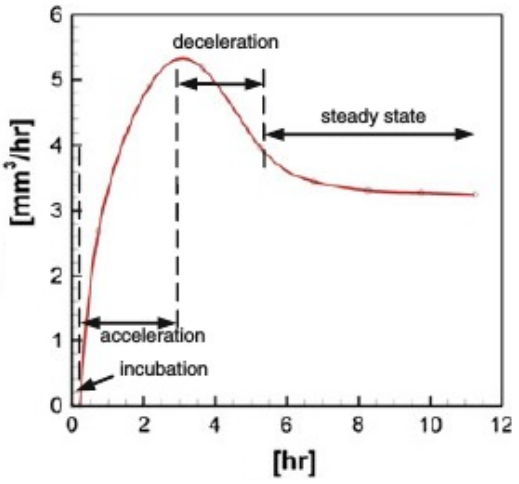

FIGURE 2.9: Rate of volume loss versus time curve [45].

The four stages described above depend on the type of materials and the erosive cavitation field. For some materials and test conditions, the erosion curve does not always show all four stages. For long duration tests, it has been observed a second attenuation period, in which erosion rate decreases. It arrives usually after the steady-state period [25].

2.2.2 Flow velocity influence

Cavitation erosion is greatly dependent on the flow velocity for two main reasons. First, it is linked to the bubble nucleation rate, which increases with flow velocity [25]. Second, it is because the impulsive pressure pulses induced by the bubble collapse increase with the flow velocity. A larger velocity results in a larger pressure drop, and so in larger pressure gradients. Thus, the bubble encounters greater pressure gradient at collapse. It results in an increment of the collapse intensity and pressure pulses [45].

Franc in his book [25] states that, in a general situation of hydraulic systems, the cavitation erosion damage increases with the liquid velocity. The material loss rate

increases as a power between 4 and 9 of the flow velocity. So, flow velocity could be an important factor in the hydrodynamic system suffering cavitation erosion.

2.2.3 Cavitation impact loads

Pressure pulses distributed in space and time characterize a cavitation flow field. They present high frequencies and high amplitudes producing a particular cavitation sound [45]. The pulse spectrum results from a statistical distribution of bubbles with violent dynamic behavior including explosive growth, collapse and rebound. An example of the pressure pulse can be observed in Fig 2.10, where the signal shows successive pulses of several amplitudes whose highest ones are suspected to be responsible for erosion damage [45].

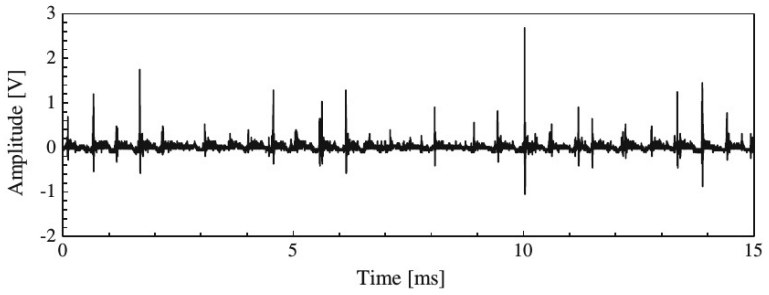

FIGURE 2.10: Typical pressure signal in a cavitation flow. The signal shows successive pulses of various amplitudes whose highest ones are likely responsible for erosion damage [45].

Therefore, a material placed in the vicinity of a cavitation field will be subjected to repeated impulsive loads distributed in space and time.

Another feature of the cavitation impulsive loads is the small size of the damaged area. Impacting microjets is only a portion of the maximum bubble size, approximately 1/10 of its maximum radius [33]. The characteristic size of the affected zone is of the same order of magnitude as the size of the cavitation erosion pits, i.e. few micrometers to several hundreds of micrometers [45].

Cavitation loads also have high amplitudes. Values on the order of GPa have been reported in the literature ([107], [99], [25]) for a load applied on a small surface area (i.e. of the order of micrometers). These high values might exceed the conventional yield stress of usual materials, explaining why cavitation impulsive loads can induce plastic deformations.

The characteristic values, such as duration, size, and amplitude, are difficult to measure accurately. In this regard two main experimental techniques have been reported in the literature [25], [45]. One is based on the use of small pressure sensors able to measure high frequency responses. The sensors may be directly exposed to the cavitating flow, so they may approach their limit of risk of damage [73], [45]. Another is based on controlled pitting tests carried out on materials. The method consists in estimating the impact load that is at the origin of each pit [25], [45]. The method uses the information from geometrical features of the pit and material properties. The pitting tests are limited to the incubation period during which pits do not overlap [25].

In the work of Okada et al. [73] is presented a pressure detector capable to measure impact loads and erosion damage (i.e. size of indents and volume loss) in order to study the relation between the load generated by the bubble collapse and the erosion. They express the impact energy as the accumulated summation of squares of impact loads. Then, using this definition, they conclude that there is a linear relationship between the impact energy and the material volume loss. Specially, in the stable period, it is found that the volume loss increases in proportion to the impact energy.

In addition, numerical methods have been used to estimate the violence of a cavitation flow. Simulations considering larger scales than the one followed in bubble dynamics approaches have been used in order to estimate the flow aggressiveness that causes material damage. Geometries such as hydrofoil profiles and venturi type sections have been simulated.

Among these models we have the erosion intensity model proposed by Fortes-Patella ([22], [47], [53]), where potential energy variations of the cavitation structures are considered as the main factor that produces erosion [53]. This model shows the influence of the flow velocity on the cavitation intensity and allows the prediction of the location of the damaged area.

The work of Ochiai et al. [70] proposes a new prediction method involving macro and micro scales. It is a one-way coupled analysis of the cavitating flow field (Eulerian approach) and of the bubble dynamics (Lagrangian approach) to treat different scale phenomena, such as the macroscopic phenomenon of a cavitating flow and the microscopic phenomenon of bubble collapse. They evaluated impulsive pressures acting on a material surface based on the bubble collapse features (i.e. position, time and intensity). On the other hand, they predicted the erosion rate using an existing material-dependent relationship between

the impulsive energy (square of the impulsive force) and the maximum erosion rate. Authors concluded that high impulsive pressures occur near the sheet cavity closure, the leading edge of the hydrofoil and the position of collapse of the cloud cavity. Also, the impulsive pressures are higher when the distance from a bubble collapse to the wall boundary decreases. Regarding the erosion rate, they found that the model over-predicts it if a constant bubble radius is considered. But, the model gives the same order of magnitude when the bubble nuclei distribution is considered. So, they concluded that considering the bubble nuclei distribution is important for the prediction of cavitation erosion.

2.2.4 Material response to impact loads

As discussed before, the material experiences pressure pulses of high intensity and short duration able to induce plastic deformation. The concentration of such mechanical energy, on small zones of the solid boundary, will then cause high stress levels that could exceed the material resistance (i.e. yield strength, ultimate strength and fatigue limit) [25] and ultimately produce mass loss of the material [45].

Aggressiveness power of cavitation flows was evaluated by Fortes-Patella et al. [23] in order to evaluate numerically the dynamic response and the surface deformation (i.e. pit profile and pit volume) of various materials exposed to pressure wave impacts. According to previous work [21], the main contribution to cavitation damage comes from the emission of pressure waves generated by spherical bubble collapses and by micro jet formation. The emitted pressure waves interact with neighboring solid surfaces, leading to material damage. In addition, the damage of material could be related to the energy of the pressure wave emitted by vapor structure collapses [21]. The authors characterized the pressure waves by the emitted energy, which is evaluated by an acoustic energy approach [23]. Further, the solid damage represented by the pit volume is found to be directly proportional to the pressure wave energy. The proportionality constant that relies the solid damage and the pressure wave energy is found to be a useful tool in the prediction of cavitation erosion because it depends strongly on the material properties, such as the yield limit, but it is almost independent on the impact amplitude.

Another consequence which follows from the energetic approach proposed by Fortes-Patella in [23] is the development of a erosion model, known as LEGI model [20]. In this

model the idea is to evaluate the erosion power of a cavitating flow, which depends on the surrounding pressure, the vapor pressure and the vapor volume during the emission of the pressure waves (i.e. during the collapse phenomenon). This numerical model was tested on a 2D hydrofoil geometry having good qualitative agreement between simulations and experiments. However, to obtain a better quantitative prediction of damage some numerical and model parameters have to be calibrated.

Choi and Chahine [11] studied the relationship between the impact pressure load and the resulting pit size through fluid structure interaction (FSI) simulations. They found out that the highest stresses are observed below the material surface, at a depth of the same order as the load radial extent. The effective strain also reaches a maximum at the same location below the surface. Authors explain that as the load increases during the impulsive loading, the compressive stress below the surface may reach the material yield point. From there on, plastic deformations continue to increase. If the load continues to rise, an increasing volume of the material undergoes plastic deformation. Later on, as the load amplitude decreases, unloading occurs and a permanent indentation or "pit" remains once the load is relaxed. Additionally, they found that the same impulsive pressure obtained from different bubble collapse conditions could produce very different pitting characteristics. Similarly, different values of loads produce the same pitting features. They explain that this response is because a pressure function shape linked to the same impulsive pressure peak level can vary significantly in space and time, for different bubble sizes, distance from the wall and collapse driving pressure functions.

A complementary approach to estimate the material loss due to cavitation is proposed by Fortes-Patella et al. [24]. This method uses data provided by pitting tests to estimate mass loss of a material that follows an elasto-plastic behavior. It is based on an oligocyclic fatigue approach, which is the process followed by a material when it is loaded between its elastic limit and its rupture limit. Since the material experiences plastification at each cycle, its rupture is produced after few cycles. This approach is able to simulate all the stages of the erosion process, i.e. incubation, acceleration, maximum rate, deceleration and terminal periods, highlighting the possibility of estimating the incubation and steady-state periods by numerical simulations. Similarly to Choi et al. [11], authors found the maximum of the residual internal stresses located below the material surface, at a depth depending on the loading shape.

These two works show promising results but also show the difficulties encountered in this type of analysis, such as the lack of material data (for example a criterion for fatigue damage). Consequently, specific tests should be done to get the required values.

The research about material reaction under high intensity loads constitutes an important aim in hydraulic applications. In particular, predicting the material response allows the improvement of surface treatment and coating selection. For example, experimental tests considering different metals and different coating materials have been done in order to select the proper coating for hydraulic machines, such as pumps and turbines. Recently, these tests involve also polymeric coating materials for ship applications because of polymers benefits in reducing noise and drag [12].

2.2.5 Cavitation erosion in Pelton turbines

Since this work is in the frame of PREDHYMA project, which seeks to predict the erosion in hydro-machines, particularly in Pelton turbines, the following description of cavitation erosion in Pelton turbines is given.

A pelton turbine is constituted mainly by nozzle injectors and a wheel containing buckets. Its working principle consists in the injection of high speed water jet, through a nozzle, to hit the buckets on the Pelton wheel in order to produce an impulsive force (see Fig. 2.11). This force makes the turbine rotate. The rotating shaft runs a generator and produces electricity.

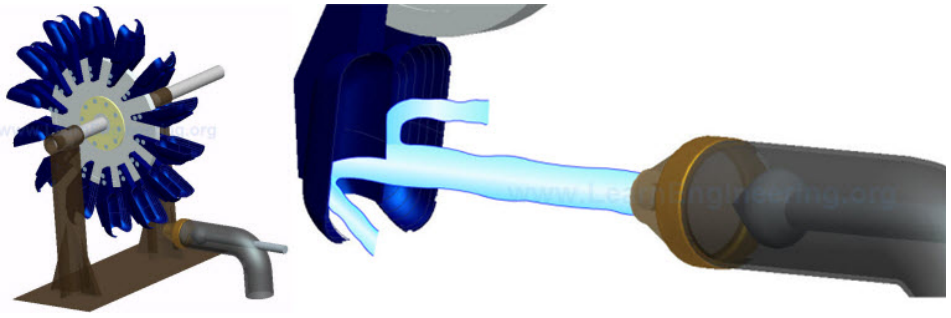

FIGURE 2.11: 3D model of a Pelton turbine and the water jet impinging on a Pelton bucket to develop the wheel rotation [52].

A work developed by Rossetti et al. [86] addresses the erosion on Pelton turbines through numerical simulations and experiment observations, showing the zones where hydraulic damage could occur. Fig. 2.12, which is taken from [86], shows seven locations of hydraulic damage on a Pelton bucket. Zone 1 is related to the presence of cavitation

in the last stages of the bucket-jet interaction. It is suggested that the zone 2 could be affected by droplet erosion in turbines having multi-jet configurations, when the discharged flow disturbs the next jet. This generates a droplet cloud that could hit and damage the back of the cutout. Zone 3 and 4 could be related to the presence of surface irregularities, which promote the flow detachment and cavitation. Zone 5 could be damaged by caviation and droplet erosion due to significant disturbance on the jet caused by the following bucket back. Cavitation pitting could be observed on zones 6 and 7 due to an improper bucket discharge angle.

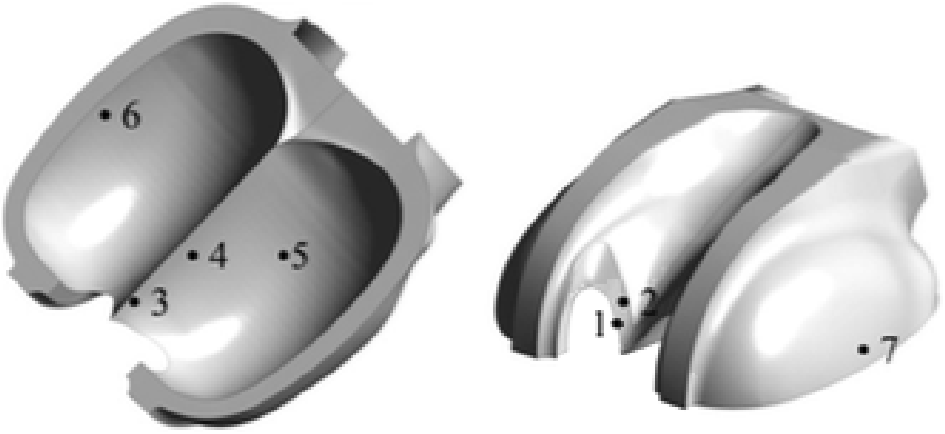

FIGURE 2.12: Location of hydraulic damage on a Pelton bucket [86]

Additionally, experimental essays carried out in ANDRITZ Hydro S.A. allow to observe cavitation erosion marks in Pelton turbines. Mainly, they are located on the buckets, near the cutout edge (zone 1 from Fig. 2.12) and at the bottom of the bucket (zone 5 from Fig. 2.12). Since Pelton turbines operate in power plants of high head ($\geq$ 800 m), strong pressure drop is expected in zone with change in curvature, like near the cutout edge. Additionally, jet disturbance due to high velocity might cause flow detachment, particularly at the bottom of the bucket. For visualization, Fig. 2.13 shows cavitation erosion at the cutout edge of the bucket.

In some configurations it is found "jet interference", which is a mechanism happening when water of a first jet is still in the bucket when water of the subsequent jet comes in. This two-way encounter may cause erosion. As mentioned before, another mechanism associated with cavitation erosion is the erosion by high-speed droplets. It occurs when a water drop hits the material surface: rarefaction waves are generated after the impact causing a pressure decrease inside the drop. This mechanism generates vapor structures that collapse and may produce cavitation erosion.

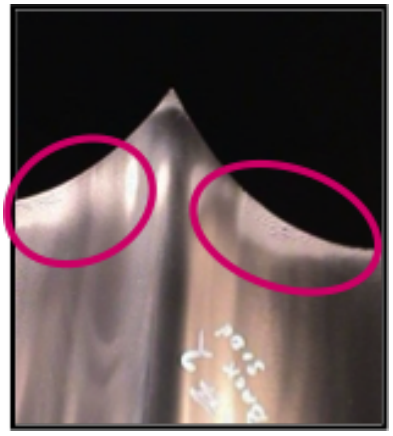

FIGURE 2.13: Cavitation erosion at the cutout edge of the bucket [ANDRITZ Hydro S.A.].

Characteristic times in Pelton turbines

An analysis about the characteristic time in Pelton turbines has been done in order to estimate if a bubble that travels in the water jet could collapse close to a bucket.

Two characteristic times are considered, t_1 which corresponds to the time taken by a fluid particle to go from the injector to the bucket, and t_2 which is the time that a fluid particle passes in the bucket (see Fig. 2.14(a)).

For the analysis, a turbine model and two prototypes are considered. Table 2.2 shows the associated values.

TABLE 2.2: Geometrical values for a Pelton turbine model and two prototypes, including the corresponding flow conditions. Values given by ANDRITZ Hydro S.A.

	Model	Prototype 1	Prototype 2
D_1 $[m]$	0.46	1.665	3.993
B_2 $[m]$	0.14	0.480	0.620
Number of jets	4	6	5
head $[m]$	93.5	437.50	1869.0
flow $[m^3/s]$	0.2	9.85	25.0

The distance B_2 is the width of the bucket, d is the distance between the injector and the bucket (when the water jet impinges perpendicularly to the bucket) and d_I the jet diameter (see Fig. 2.14). Then, the jet velocity can be estimated by Eq. (2.41),

$$V_I = \frac{(\frac{flow}{Number\ of\ jets})}{A_I}, \tag{2.41}$$

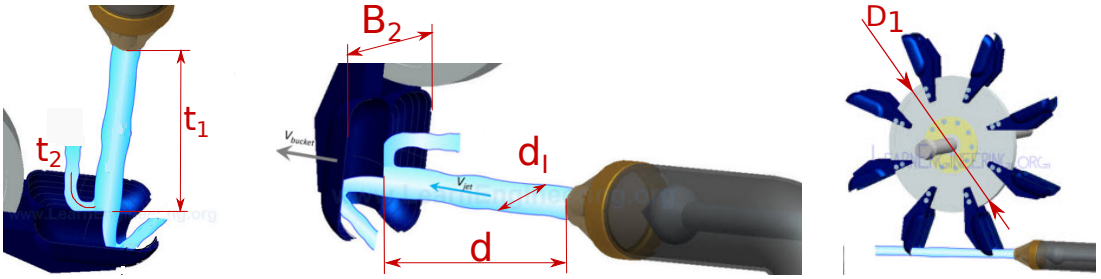

(a) Scheme of a water injector and a pelton bucket showing the characteristic times: t_1 and t_2

(b) Geometrical representation of the jet diameter d_I, bucket width B_2 and the distance between the injector outlet and the bucket d

(c) Geometrical representation of a Pelton wheel diameter D_1

FIGURE 2.14: Geometric representation of a wheel, bucket and injector of a Pelton turbine (Pictures taken from [52] to be then modified)

where A_I is the transversal area of the jet, i.e. $A_I = \frac{\pi}{4} d_I^2$.

The characteristic times, t_1 and t_2 are calculated through fundamental kinematic equations, i.e.

$$\begin{cases} t_1 = \dfrac{d}{V_I} \\ t_2 = \dfrac{\left(\frac{B_2}{2}\right)}{V_I} \end{cases} . \tag{2.42}$$

The characteristic times for each Pelton turbine are shown in Table 2.3. We remark that both times have the same order of magnitude, i.e. 10^{-4} $[s]$.

TABLE 2.3: Characteristic times for each Pelton turbine. t_1: time taken by a fluid particle to go from the injector to the bucket. t_2: time that a fluid particle passes in the bucket

	Model	Prototype 1	Prototype 2
t_1 $[s]$	$2.53 \cdot 10^{-4}$	$3.10 \cdot 10^{-4}$	$2.19 \cdot 10^{-4}$
t_2 $[s]$	$3.37 \cdot 10^{-4}$	$4.13 \cdot 10^{-4}$	$2.92 \cdot 10^{-4}$

These times are compared against the collapse time of a bubble filled only with non-condensable gas already formed. In this regard, it is considered a non-condensable gas bubble whose radius is set at $R_0 = 100$ $[\mu m]$ according to the literature ([49], [45], [25]). The bubble is submerged in water whose density is $\rho = 1000$ $[kg/m^3]$ and the water pressure is the atmospheric pressure, i.e. $p_{amb} = 10^5$ $[Pa]$. Using the Rayleigh equation

for estimating the collapse time (Eq. 2.12) considering only the non-condensable gas term and neglecting the surface tension and viscous term, it is obtained: $1 \cdot 10^{-5}[s]$.

During t_1, if the water jet contains bubble nuclei, they are translated along the flow. The water flow impinges the bucket and fluid detachment could occur due to the bucket displacement. This generates a zone of pressure drop favorable to the nuclei growth and to create vapor structures. When the bucket completes the transit through the jet, the pressure is again the atmospheric pressure. This increase of the local pressure may lead to a bubble collapse shortly after. Since t_2 is 10 times larger than the bubble collapse time, we can conclude that the bubbles formed during the fluid detachment will have the time necessary to collapse close to the bucket and more likely near the cutout edge.

Regarding the small sizes of the bubbles, ranging from 0.01 to 0.5 $[mm]$, and the bucket size, ranging from 140 to 700 $[mm]$, it is taken the hypothesis of considering the bucket as a flat plate with respect to the non-condensable gas bubble. So, the present research work is focused on predicting the erosion caused by a non-condensable gas bubble in the vicinity of a flat plate, neglecting any curvature effects.

2.3 Conclusion

The cavitation phenomenon has been presented showing its different stages in order to determine the predominant physical factors that could cause damage. It has been seen that the most severe stage is mainly represented by the bubble collapse since it is during this event that high-pressure levels are emitted. In particular, if the bubble collapses near a material, the high pressures emitted could damage it. In this frame, the bubble collapse near a wall represents our main target towards the prediction of cavitation erosion.

In order to properly model the physical events involved in the bubble collapse, such as pressure waves and micro jets, a compressible regime must be considered for the fluids. It has been seen that mass transfer does not play a relevant role during the collapse phase, so it is not modeled. Following this idea, since the phase change is not modeled, the bubble contains only non-condensable gas, which is modeled as ideal gas. The inclusion of ideal gas model brings in the temperature variable, which is considered for both fluids (i.e. water and gas). Although the liquid temperature does not change appreciably during cavitation, this consideration is taken because the compression process is not adiabatic and to be consistent in the modelisation of both fluids.

Mainly inertial forces control the bubble collapse; so the viscosity and surface tension effects are neglected.

With respect to the erosion process, the general stages have been described with emphasis in the material response under cavitation loading. Major characteristics, such as the distance between the bubble and the material surface, high pressure levels and a comparison against material properties (e.g. yield stress) have come in order to analyze the material response. These characteristics will be taken in consideration when studying the cavitation phenomenon near a solid boundary.

Additionally, we highlight the fact that the highest stress are observed below the material surface and that the fatigue mechanism is considered to explain the structural damage. All these inputs will be considered when estimating the material reaction due to cavitation.

Chapter 3

Physical model of cavitation flow

Cavitation phenomenon involves compressible flow in order to correctly represent the pressure waves present during the bubble collapse. It is called compressible flow when a fluid moves at speed comparable to its speed of sound, so generating significant density changes [108]. In this case, the temperature and pressure changes are also important.

The variables such as temperature, density, pressure and internal energy are known as state variables and their relation (e.g. $p = p(\rho, T)$ or $e = e(\rho, T)$) is given by equations of state. The equations of state are important in this work because they allow the description of properties of each fluid, i.e. water and gas. Therefore, an explanation following a thermodynamic approach is given to present the state variables and the equations of state concerned. As well, this chapter focuses on the physical definitions about compressible flow and the corresponding physical model used by the numerical method.

3.1 Thermodynamic variables in compressible flow

This part is devoted to explain the thermodynamic variables and concepts regarding compressible fluid flow before proposing any physical model.

First law of thermodynamics

The first law of thermodynamics gives a relation between the variation of the internal energy of a fluid, the heat exchanged with the environment and the work done by the

environment. If the pressure forces are the only forces acting on the system, this law can be expressed by,

$$de = dq - pd(1/\rho), \tag{3.1}$$

where e is the internal energy by mass unit, q is the heat transfer, also by mass unit.

The internal energy, pressure and density are related to define the enthalpy as,

$$\eta = e + p/\rho, \tag{3.2}$$

and in consequence,

$$d\eta = dq + (1/\rho)dp. \tag{3.3}$$

The Eq. (3.1) and Eq. (3.3) are thus equivalent.

The total derivatives of $e = e(\rho, T)$ and $\eta = \eta(p, T)$ can be expressed as,

$$de = \left[\frac{\partial e}{\partial T}\right]_{\rho} dT + \left[\frac{\partial e}{\partial \rho}\right]_{T} d\rho \tag{3.4}$$

and

$$d\eta = \left[\frac{\partial \eta}{\partial T}\right]_{p} dT + \left[\frac{\partial \eta}{\partial p}\right]_{T} dp. \tag{3.5}$$

Now, we address the specific heat concept, which is defined as the energy required to raise the temperature of a unit mass of a substance by one degree [8]. In general, this energy depends on how the process is executed. In thermodynamics, we are interested in two kinds of specific heats: specific heat at constant pressure C_p and specific heat at constant volume C_v. The specific heat at constant pressure is represented as the change of enthalpy with respect of temperature at constant pressure. Meanwhile, the specific heat at constant volume is represented as the change of internal energy with respect of temperature at constant volume.

So, in the frame of the first law of thermodynamics, both specific heats are found through Eq. (3.2), Eq. (3.4) and Eq. (3.5) as

$$C_p = \left[\frac{\partial \eta}{\partial T}\right]_p = \left[\frac{\partial e}{\partial T}\right]_\rho + \left(\left[\frac{\partial e}{\partial \rho}\right]_T - \frac{p}{\rho^2}\right)\left[\frac{\partial \rho}{\partial T}\right]_p, \tag{3.6}$$

$$C_v = \left[\frac{\partial e}{\partial T}\right]_\rho = \left[\frac{\partial \eta}{\partial T}\right]_p + \left(\left[\frac{\partial \eta}{\partial p}\right]_T - \frac{1}{\rho}\right)\left[\frac{\partial p}{\partial T}\right]_\rho. \tag{3.7}$$

Second law of thermodynamics

The second law of thermodynamics introduces another property known as entropy that is expressed for a reversible process by,

$$ds = dq/T, \tag{3.8}$$

where s defines the specific entropy of a fluid, i.e. entropy by mass unit.

Taking Eq. (3.1) and Eq. (3.3), we have the following relation for a reversible process,

$$Tds = de + pd(1/\rho) = d\eta - (1/\rho)dp. \tag{3.9}$$

Note that entropy is a property, in consequence it has fixed values at fixed states.

Now, the second law of thermodynamics is considered to obtain other relations for specific heats.

We take the total derivative of $s = s(p, T)$, i.e.

$$ds = \left[\frac{\partial s}{\partial T}\right]_p dT + \left[\frac{\partial s}{\partial p}\right]_T dp. \tag{3.10}$$

Then, using Eq. (3.5) and Eq. (3.9), we obtain:

$$ds = \frac{d\eta}{T} - \frac{dp}{\rho T} = \frac{1}{T}\left[\frac{\partial \eta}{\partial T}\right]_p dT + \frac{1}{T}\left(\left[\frac{\partial \eta}{\partial p}\right]_T - \frac{1}{\rho}\right) dp. \tag{3.11}$$

Comparing Eq. (3.10) and Eq. (3.11), we have the following relations between s and η:

$$\left[\frac{\partial s}{\partial T}\right]_p = \frac{1}{T}\left[\frac{\partial \eta}{\partial T}\right]_p = \frac{C_p}{T} \tag{3.12}$$

and

$$\left[\frac{\partial s}{\partial p}\right]_T = \frac{1}{T}\left(\left[\frac{\partial \eta}{\partial p}\right]_T - \frac{1}{\rho}\right), \tag{3.13}$$

where the derivative $\left[\frac{\partial \eta}{\partial p}\right]_T$ is [87]:

$$\left[\frac{\partial \eta}{\partial p}\right]_T = \frac{1}{\rho} + \frac{T}{\rho^2}\left(\frac{\partial \rho}{\partial T}\right)_p. \tag{3.14}$$

Following the same idea, but using the properties $e = e(\rho, T)$ and $s = s(\rho, T)$, two new expressions function of density (ρ), instead of pressure (p), and temperature (T) are obtained, i.e.

$$\left[\frac{\partial s}{\partial T}\right]_\rho = \frac{1}{T}\left[\frac{\partial e}{\partial T}\right]_\rho = \frac{C_v}{T} \tag{3.15}$$

and

$$\left[\frac{\partial s}{\partial \rho}\right]_T = \frac{1}{T}\left(\left[\frac{\partial e}{\partial \rho}\right]_T - \frac{p}{\rho^2}\right), \tag{3.16}$$

where the derivative $\left[\frac{\partial e}{\partial \rho}\right]_T$ is [87]:

$$\left[\frac{\partial e}{\partial \rho}\right]_T = \frac{1}{\rho^2}\left[p - T\left(\frac{\partial p}{\partial T}\right)_\rho\right]. \tag{3.17}$$

Eq. (3.14) and Eq. (3.17) are used in the development of the ideal gas model.

Change of entropy

The change of entropy can be calculated from Eq. (3.10) if the expressions for $\left[\frac{\partial s}{\partial T}\right]_p$ and $\left[\frac{\partial s}{\partial p}\right]_T$ are known.

So, we combine Eq. (3.13) and Eq. (3.14) to get:

$$\left[\frac{\partial s}{\partial p}\right]_T = \frac{1}{\rho^2}\left[\frac{\partial \rho}{\partial T}\right]_p \tag{3.18}$$

Finally, using Eq. (3.12) and Eq. (3.18), the change of entropy can be calculated as

$$ds = \frac{C_p}{T}dT + \frac{1}{\rho^2}\left[\frac{\partial \rho}{\partial T}\right]_p dp. \tag{3.19}$$

This last equation will be useful in the following section about equations of state.

Speed of sound

Another important quantity is the speed of sound, which is defined in Chapter 2 by Eq. (2.37). Since the equations of states are usually expressed in function of internal energy, density and pressure, and not in function of entropy, an equivalent expression for the speed of sound is searched. For that, we consider $p = p(\rho, s)$ and $e = e(p, \rho)$, so we have

$$dp = \left[\frac{\partial p}{\partial \rho}\right]_s d\rho + \left[\frac{\partial p}{\partial s}\right]_\rho ds \tag{3.20}$$

and

$$de = \left[\frac{\partial e}{\partial \rho}\right]_p d\rho + \left[\frac{\partial e}{\partial p}\right]_\rho dp. \tag{3.21}$$

Then, using Eq. (3.4) and the entropy relation (Eq. 3.9) it is obtained:

$$Tds = \left(\left[\frac{\partial e}{\partial \rho}\right]_p d\rho + \left[\frac{\partial e}{\partial p}\right]_\rho dp\right) - \frac{p}{\rho^2}d\rho. \tag{3.22}$$

Eq. (3.20) is substituted in Eq. (3.22) to give

$$Tds = \left(\left[\frac{\partial e}{\partial \rho}\right]_p d\rho + \left[\frac{\partial e}{\partial p}\right]_\rho \left(\left[\frac{\partial p}{\partial \rho}\right]_s d\rho + \left[\frac{\partial p}{\partial s}\right]_\rho ds\right)\right) - \frac{p}{\rho^2}d\rho. \tag{3.23}$$

Rearranging the Eq. (3.23) and because we search $\left[\frac{\partial p}{\partial \rho}\right]_s$, we impose $ds = 0$ to have

$$\left[\frac{\partial p}{\partial \rho}\right]_s = \frac{\frac{p}{\rho^2} - \left[\frac{\partial e}{\partial \rho}\right]_p}{\left[\frac{\partial e}{\partial p}\right]_\rho}. \tag{3.24}$$

Therefore, using the Eq. (2.37), the speed of sound expression is given by

$$c^2 = \frac{\frac{p}{\rho^2} - \left[\frac{\partial e}{\partial \rho}\right]_p}{\left[\frac{\partial e}{\partial p}\right]_\rho}. \tag{3.25}$$

3.2 Equations of state

In the previous section, a brief review about the thermodynamics variables and concepts involved in the compressible flow analysis has been exposed. Now, it is given a description about the equations of states, considering the physical model for each phase, i.e. gas and water.

An equation of state is a constitutive relation that provides a mathematical relationship between two or more state variables. This thermodynamic equation describes the state of a substance under a given set of physical conditions in order to describe the fluid properties.

3.2.1 Ideal gas

We start considering the gas phase, which models the bubble. As it was presented in Chapter 2, the mass transfer between liquid and gaseous phases is not expected to have an effect on the bubble collapse, so it is not modeled. Under this condition, it is assumed that the bubble contains only non-condensable gas, and thus the bubble medium is modeled as an ideal gas.

The thermodynamic equation of state for an ideal gas is given by [87],

$$p = \rho R_G T, \tag{3.26}$$

with R_G denoting the particular gas constant in $[J/(Kkg)]$, which is given by $R_G = \mathfrak{R}/\mathfrak{M}$, where $\mathfrak{M}$ is the molecular weight in $[kg/mol]$ and $\mathfrak{R}$ is the universal gas constant $(\mathfrak{R} = 8.31451[J/(molK)])$.

Applying Eq. (3.14) and Eq. (3.17) for an ideal gas, it is obtained that $\left[\frac{\partial \eta}{\partial p}\right]_T = 0$ and $\left[\frac{\partial e}{\partial \rho}\right]_T = 0$. This implies that the enthalpy and the internal energy for an ideal gas are only function of temperature T, i.e. $\eta = \eta(T)$ and $e = e(T)$. Then, following Eq. (3.6) and Eq. (3.7), the specific heats are also function only of temperature.

In consequence, the change of internal energy and enthalpy for an ideal gas can be expressed in a short form as,

$$de = C_v(T)\, dT, \tag{3.27}$$

$$d\eta = C_p(T)\, dT. \tag{3.28}$$

For all real gases, C_p and C_v vary with temperature, but only moderately; for example, C_p of air increases 30 % as temperature increases from 0 to 3000 K [108]. Since we do not deal with such large temperature changes, specific heats are assumed constant.

Hence, we have:

$$\Delta e = C_v \Delta T, \tag{3.29}$$

$$\Delta \eta = C_p \Delta T. \tag{3.30}$$

Next, Eq. (3.6), Eq. (3.7) and Eq. (3.26) are combined together to find a relation between both specific heats for an ideal gas, which is given as,

$$C_v = C_p - \frac{1}{\rho}\left[\frac{\partial p}{\partial T}\right]_\rho = C_p - R_G. \tag{3.31}$$

So, the relation $C_p - C_v = R_G$ that does not depend on temperature.

In addition, γ is defined as the ratio of specific heats $\gamma = C_p/C_v$. From experimental values of common gases, it is observed that γ lies between 1 and 1.7, and for air it is usually taken equal to 1.4 [108].

Regarding the change of entropy of an ideal gas, we can infer it using Eq. (3.19) and Eq. (3.26). Thus, the entropy for ideal gas is defined as:

$$s - s_{ref} = C_p\, ln\left(\frac{T}{T_{ref}}\right) - R_G\, ln\left(\frac{p}{p_{ref}}\right), \tag{3.32}$$

where the subscript "ref" indicates a reference state such that $s_{ref} = s(p_{ref}, T_{ref})$. Eq. (3.32) can be used to quantify entropy variations during non-isentropic transformations, such as shock waves.

In conclusion, the ideal gas model considers a dependency of density upon pressure and temperature, showing the requirements necessary to model compressibility. Thus, it can be used to model the compression of a non-condensable gas bubble.

3.2.2 Stiffened Gas equation of state

For liquid water, the compressibility must be taken in consideration in order to properly represent the pressure waves generated during the bubble collapse. The inclusion of compressibility brings in the consideration of temperature in the analysis, although the temperature does not change significantly during the cavitation phenomenon. In addition, the ideal gas equation of state is used for the gas phase; in this equation the density depends on temperature and pressure. So, the use of an equation of state involving the density, temperature and pressure for the liquid phase is recommended in order to guarantee the consistency of the physical model.

The equation of state considered for the liquid phase is the Stiffened Gas equation of state or sometimes called "Tammann Equation" [37]. It is expressed as,

$$p = p(\rho, e) = (\gamma - 1)\rho e - \gamma p_\infty, \tag{3.33}$$

where p_∞ denotes the stiffened constant pressure and it is fluid dependent as γ. The term γp_∞ corresponds to attractive effects leading to matter cohesion in liquids states [51].

To estimate the temperature, it is necessary to determine thermal expressions, such as $T(\rho, p)$ or $p(\rho, T)$, which are not yet available at this stage. In order to determine them, the fundamental relation expressed in Eq. (3.17) is used.

Determination of thermal expressions for the Stiffened Gas EOS

Here, the determination of thermal expressions (i.e. $T(\rho, p)$ and $p(\rho, T)$) for the Stiffened Gas EOS is in focus. The development presented hereafter is taken from [51].

Re-writing the Eq. (3.33), we get

$$e(\rho, T) = \frac{p(\rho, T) + \gamma p_\infty}{(\gamma - 1)\rho}, \tag{3.34}$$

where $p(\rho, T)$ is unknown at this stage.

The following partial derivatives are deduced from Eq. (3.34),

$$\left[\frac{\partial e}{\partial T}\right]_\rho = \frac{1}{(\gamma-1)\rho}\left[\frac{\partial p}{\partial T}\right]_\rho \tag{3.35}$$

and

$$\left[\frac{\partial e}{\partial \rho}\right]_T = \frac{1}{(\gamma-1)\rho}\left[\frac{\partial p}{\partial \rho}\right]_T - \frac{(p+\gamma p_\infty)}{(\gamma-1)\rho^2} \tag{3.36}$$

The Eq. (3.17) and the Eq. (3.36) are combined to give

$$\left[\frac{\partial p}{\partial \rho}\right]_T = \frac{\gamma(p+p_\infty)}{\rho} - \frac{(\gamma-1)T}{\rho}\left[\frac{\partial p}{\partial T}\right]_\rho. \tag{3.37}$$

Introducing the Eq. (3.7) in Eq. (3.35), it is obtained

$$\left[\frac{\partial p}{\partial T}\right]_\rho = C_v(\gamma-1)\rho. \tag{3.38}$$

Then, Eq. (3.38) is integrated over temperature T to give

$$p(\rho,T) = C_v(\gamma-1)\rho T + K(\rho), \tag{3.39}$$

where $K(\rho)$ is a function of the density ρ.

The Eq. (3.39) is derived over ρ at constant temperature T to give

$$\left[\frac{\partial p}{\partial \rho}\right]_T = C_v(\gamma-1)T + \frac{dK}{d\rho}. \tag{3.40}$$

Now, the Eq. (3.38) and the Eq. (3.39) are introduced in the Eq. (3.37), i.e.

$$\left[\frac{\partial p}{\partial \rho}\right]_T = C_v(\gamma-1)T + \frac{\gamma}{\rho}(K(\rho)+p_\infty). \tag{3.41}$$

The equality between Eq. (3.37) and Eq. (3.41) leads to the following first order differential equation,

$$\frac{dK}{d\rho} - \frac{\gamma}{\rho}K - \frac{\gamma}{\rho}p_\infty = 0, \tag{3.42}$$

whose solution is given by

$$K(\rho) = C\rho^\gamma - p_\infty, \tag{3.43}$$

where C is a constant to be determined. According to Le Métayer and Saurel in [51], the constant C must be imposed null in order to avoid nonphysical behavior.

Hence, the corresponding solutions is,

$$p(\rho, T) = C_v(\gamma - 1)\rho T - p_\infty. \tag{3.44}$$

Consequently, an expression for the temperature is given as,

$$T(\rho, p) = \frac{p + p_\infty}{C_v(\gamma - 1)\rho}. \tag{3.45}$$

Entropy for the Stiffened Gas EOS

As for the ideal gas equation, the entropy is considered for the Stiffened Gas EOS. From Eq. (3.19) and Eq. (3.45), it is obtained the entropy change as,

$$ds = \frac{C_p}{T}dT - \frac{1}{\rho T}dp, \tag{3.46}$$

and consequently,

$$s - s_{ref} = C_p\, ln\left(\frac{T}{T_{ref}}\right) - (\gamma - 1)C_v\, ln\left(\frac{p + p_\infty}{p_{ref} + p_\infty}\right), \tag{3.47}$$

where the subscript "ref" indicates a reference state.

Similar to the entropy of an ideal gas, Eq. (3.47) can be used to quantify entropy variations during non-isentropic process, like shock dynamics situations (e.g. underwater explosions and bubble compression [37], [91]) present in the phenomenon of interest.

Also, the Stiffened Gas EOS exhibits its resemblance with the ideal gas EOS when it is considered $p_\infty = 0$ and $1 < \gamma < 2$. This is an advantage in the numerical implementation.

In conclusion, the goal in using the Stiffened Gas EOS is to take in consideration the essential of the thermodynamics under a single formulation. Indeed, this equation of state contains the main properties of both fluids, as the repulsive and attractive effects in liquids, and repulsive effects in gases [50].

3.2.3 Additional consideration about the EOS for each phase

As it was presented, the Stiffened Gas EOS models the gas and liquid phases, because setting appropriate values for p_∞ and γ allows defining each phase.

In order to complete the model for each phase, the speed of sound expressions for liquid and gas are searched. Consequently, the Eq. (3.25) is used and the following expressions are obtained,

$$c_{liq}^2 = \frac{\gamma(p + p_\infty)}{\rho} \tag{3.48}$$

and

$$c_{gas}^2 = \frac{\gamma p}{\rho}. \tag{3.49}$$

Finally, the relations that describe both phases including the speed of sound expressions are established for the numerical implementation.

3.2.4 Comparative analysis of Tait and Stiffened Gas EOS

The Tait EOS relates the pressure and the density as,

$$p = p(\rho) = \frac{\rho_{ref} c_{ref}^2}{\gamma} \left[\left(\frac{\rho}{\rho_{ref}} \right)^\gamma - 1 \right] + p_{ref}, \tag{3.50}$$

where ρ_{ref}, c_{ref} and p_{ref} are constants depending of the fluid. They denote the reference density, reference speed of sound and reference pressure, respectively.

It is a quite accurate equation for water up to 25000 *bar* [94] and it has been successfully used for modeling engineering applications in the actual SPH solver ASPHODEL ([62], [68], [54]). However, it is not used in the current application since it describes a barotropic process, i.e. $p = p(\rho)$, where temperature dependence is neglected, so the equation of energy conservation is not considered.

This section presents an analysis between the Tait EOS and the Stiffened Gas EOS for the liquid phase in order to find a relation between both equations and to estimate the impact of the Stiffened Gas EOS implementation on the in-house SPH solver.

To develop the thermodynamic analysis, we consider both EOS and the associated entropy expressions. For the Stiffened Gas EOS, it is given by Eq. (3.47). Here, it is re-written to give:

$$\frac{1}{C_v}(s - s_{ref}) = \gamma ln\left(\frac{T}{T_{ref}}\right) - (\gamma - 1)ln\left(\frac{p + p_\infty}{p_{ref} + p_\infty}\right). \tag{3.51}$$

Now, considering the Tait EOS, since it does not depend on temperature, Eq. (3.19) leads to no entropy variations, $ds = 0$.

So, in order to compare both EOS, the change of entropy for the Stiffened Gas EOS is imposed to be zero also.

Introducing the Eq. (3.45) in the Eq. (3.51) and rearranging it, it is obtained

$$0 = \gamma ln\left(\frac{\rho_{ref}}{\rho}\right) + ln\left(\frac{p + p_\infty}{p_{ref} + p_\infty}\right). \tag{3.52}$$

Then, the Eq. (3.52) leads to:

$$\left(\frac{\rho}{\rho_{ref}}\right)^\gamma = \frac{p + p_\infty}{p_{ref} + p_\infty}. \tag{3.53}$$

And thus, it leads to:

$$p = p_{ref}\left[\frac{\rho}{\rho_{ref}}\right]^\gamma + p_\infty\left[\left(\frac{\rho}{\rho_{ref}}\right)^\gamma - 1\right]. \tag{3.54}$$

That can be written as

$$p = (p_{ref} + p_\infty)\left[\left(\frac{\rho}{\rho_{ref}}\right)^\gamma - 1\right] + p_{ref}. \tag{3.55}$$

Hence, the factor $(p_{ref} + p_\infty)$ for Stiffened Gas EOS equals to $\frac{\rho_{ref}c_{ref}^2}{\gamma}$ for the Tait EOS, and thus the Tait EOS is recovered, i.e.

$$p = \frac{\rho_{ref}c_{ref}^2}{\gamma}\left[\left(\frac{\rho}{\rho_{ref}}\right)^\gamma - 1\right] + p_{ref}. \tag{3.56}$$

In conclusion, the Stiffened Gas EOS reduces to the Tait EOS if an isentropic transformation is considered. This shows that equations of state relating the temperature,

density and pressure allow the calculation of reversible entropy changes; by cons it is not possible from barotropic equations. From a numerical point of view, the implementation of a more complete equation of state, i.e. $p = p(\rho, T)$, gives a wider range of applicability of the in-house solver, such as the simulation of compressible regimes. This last point is addressed below by introducing the Mach number, which is a useful dimensionless quantity for the analysis of compressible flow.

3.3 Mach number

In fluid dynamics, the Mach number is a dimensionless quantity representing the ratio of the fluid velocity and the speed of sound in the flow [108], i.e.

$$Ma = \frac{\|\mathbf{v}\|}{c}. \tag{3.57}$$

This dimensionless number is a criterion to determine when we could neglect the compressibility inherent in every real fluid. Under small Mach number conditions (e.g. $Ma \leq 0.3$), changes in fluid density are small everywhere in the flow field. The energy equation becomes uncoupled and temperature effects can be ignored. This means that the flow is considered as incompressible or only weakly-compressible. In the incompressible case, the density is considered constant and it is required to solve only the continuity and momentum equations. In the weakly-compressible case, the analysis requires to solve the continuity and momentum equations, as well as a barotropic equation of state (i.e. density varies only with pressure) to close the system. This latter approach has been used by ASPHODEL in many applications ([62], [68], [57], [54], [82]).

On the other hand, when Mach numbers are greater than 0.3, density variations are not negligible. This implies that pressure and internal energy vary. So, the energy equation can not be neglected and a system of four equations is solved: continuity, momentum, energy and equation of state (e.g. $p = p(\rho, e)$). This system is solved to find simultaneously four unknowns: density, flow velocity, internal energy and pressure.

In the applications of non-condensable gas bubble collapse, the Mach number reaches values of 0.5 during the micro jet event, justifying the consideration of a compressible approach.

3.4 Conclusion

In this chapter the equations of state considered to model the gas and liquid phases, together with thermodynamic concepts involved in compressible flows have been presented. It is highlighted the Stiffened Gas EOS to model the fluids due to its non-isentropic feature, i.e. it includes the density changes as function of pressure and temperature, and its single form to represent both phases, i.e. gas and liquid.

Then, it has been presented that the Tait EOS, the barotropic equation usually used to model weakly-compressible flows in ASPHODEL, can be interpreted as the isentropic expression of the Stiffened Gas EOS. So, basically because the temperature is not involved in the Tait EOS, it is not suitable to model the liquid compressibility and thus shock dynamics situations.

Chapter 4

Numerical Method: Compressible SPH-ALE

In this chapter the numerical method used for solving the Euler equations is introduced. The Smoothed Particle Hydrodynamics (SPH), a mesh-less method, is used to discretize the conservation of mass, momentum and energy equations in Arbitrary Lagrange Euler (ALE) formulation.

The calculation of flux exchanges between particles in multiphase flows and the numerical strategy to treat compressible flows are presented. In the end, it is given a set of validation cases for the compressible SPH solver. It is considered changes in fluid density, pressure and internal energy; fluid compressibility is also addressed through the Mach number.

4.1 Governing equations

The governing equations involved in inviscid flows are known as Euler equations, which are a set of non-linear equations based on the physical principles of conservation of mass, momentum and energy. They form a system of first-order partial differential equations hyperbolic in time [31].

These equations can be seen as particular Navier-Stokes equations without viscous and thermal diffusive effects (i.e. diffusion of heat in a medium, generally written as the law of heat conduction) [103]. In the following the system of partial differential equations is given in conservative form as

$$\begin{cases} \dfrac{\partial \rho}{\partial t} + \nabla \cdot (\rho \mathbf{v}) = 0 \\ \dfrac{\partial \rho \mathbf{v}}{\partial t} + \nabla \cdot (\rho \mathbf{v} \otimes \mathbf{v}) + \nabla \cdot (p\mathbf{I}) = \mathbf{S}_e \\ \dfrac{\partial \rho E}{\partial t} + \nabla \cdot (\rho \mathbf{v} E + p\mathbf{v}) = \mathbf{S}_e \cdot \mathbf{v} \end{cases} \tag{4.1}$$

where ρ is the density, p is the static pressure, $\mathbf{v}$ the velocity vector and $\mathbf{S}_e$ the vector of external forces. The total energy per mass unit, E, is defined by

$$E = e + \frac{1}{2}\mathbf{v}^2 \tag{4.2}$$

as sum of the internal energy e and the kinetic energy.

The symbol $\otimes$ denotes the outer product. Considering two column vectors $\mathbf{a} \in \mathbb{R}^m$ and $\mathbf{b} \in \mathbb{R}^n$, the outer product is

$$\mathbf{a} \otimes \mathbf{b} = \mathbf{a}\mathbf{b}^T \in \mathbb{R}^{m \times n}. \tag{4.3}$$

The system of equations (Eq. 4.1) has to be complemented by the constitutive laws, like the equation of state. It is used the Stiffened Gas EOS, already presented in Section 3.2.2.

Next, the Euler equation system (Eq. 4.1) is re-written in a flux vector form,

$$\frac{\partial \mathbf{\Phi}}{\partial t} + \nabla \cdot \mathbf{F}_C = \mathbf{S}_T \tag{4.4}$$

with

$$\mathbf{\Phi} = \begin{pmatrix} \rho \\ \rho \mathbf{v} \\ \rho E \end{pmatrix} \tag{4.5}$$

$$\mathbf{F}_C = \begin{pmatrix} \rho \mathbf{v} \\ \rho \mathbf{v} \otimes \mathbf{v} + p\mathbf{I} \\ \mathbf{v}(\rho E + p) \end{pmatrix}, \qquad \mathbf{S}_T = \begin{pmatrix} 0 \\ \mathbf{S}_e \\ \mathbf{S}_e \cdot \mathbf{v} \end{pmatrix}, \tag{4.6}$$

the vector $\mathbf{\Phi}$ is called the vector of conservative variables and $\mathbf{F}_C$ is the convective flux tensor. In our case, the vector of source terms, $\mathbf{S}_T$, contains the effect of the volume forces, i.e. gravity force.

4.2 Arbitrary Lagrange Euler

The Eulerian approach establishes that the fluid quantities are analyzed in a fixed frame of reference, meaning that the material fluid particles are passing through a fixed region in space. In contrary, the Lagrangian description establishes that the frame of reference follows the material fluid particles in their motion. In order to have a generalization of both approaches, the velocity of the frame of reference $\mathbf{v}_0$ is introduced [32]. The approach is called Arbitrary Lagrange Euler (ALE) because this velocity can be null to have the Eulerian formalism, it can be equal to the fluid velocity to obtain the Lagrangian approach, and it can also be arbitrary in order to move the calculation points in a way that is advantageous for certain numerical simulations [62], [68], [82].

Using the flux vector notation of equations (4.5) and (4.6), we have the Euler equations in conservative form and linked to the transport velocity $\mathbf{v}_0$ by

$$L_{vo}\left(\mathbf{\Phi}\right) + \nabla \cdot \left(\mathbf{F}_C - \mathbf{v}_0 \otimes \mathbf{\Phi}\right) = \mathbf{S}_T, \tag{4.7}$$

where L_{vo} is the transport operator linked to $\mathbf{v}_0$

$$L_{vo}\left(\mathbf{\Phi}\right) = \frac{\partial \mathbf{\Phi}}{\partial t} + \nabla \cdot \left(\mathbf{v}_0 \otimes \mathbf{\Phi}\right). \tag{4.8}$$

To simplify the notation, the flux tensor $\mathbf{F}$ is introduced as

$$\mathbf{F}(\mathbf{\Phi}, \mathbf{v}_0) = \mathbf{F}_C(\mathbf{\Phi}) - \left(\mathbf{v}_0 \otimes \mathbf{\Phi}\right). \tag{4.9}$$

Using the Reynolds transport theorem (also known as Leibniz − Reynolds transport theorem) for developing the volume integral in the moving frame of reference, and the Divergence or Gauss' theorem for passing from the volume integral to the surface integral of the flux vector, we have the corresponding integral representation by

$$\frac{d}{dt}\int_{\Omega}\mathbf{\Phi}dV+\int_{\partial\Omega}\mathbf{F}(\mathbf{\Phi},\mathbf{v}_0)\cdot dS=\int_{\Omega}\mathbf{S}_T dV, \tag{4.10}$$

where the time derivative is considered in the moving system and the boundary $\partial\Omega$ is moving at speed $\mathbf{v}_0$.

4.3 Smoothed Particle Hydrodynamics (SPH)

Smoothed Particle Hydrodynamics (SPH) is a numerical method to solve partial differential equations considering a group of calculation points $\mathbf{x}_i$ in a computational domain Ω. It was first introduced by Lucy [61] in the area of astronomy and astrophysics, and by Monaghan [64] in the area of fluid flows. It is known as a meshless method because there is no connectivity between the calculation points [68]. The calculation points are considered as particles that can describe the flow in Lagrangian motion.

An extensive introduction to SPH can be found in several publications ([106], [62], [54]). In the following sections an overview of the SPH method and its variant for SPH-ALE is presented with emphasis in the particle approximation, the SPH operators and its properties.

4.3.1 SPH approximation

In the following, a discrete representation of the equations is presented. The interpolation points ("particles") are moved with the local velocity ($\mathbf{v}$) and derivatives are calculated via a kernel approximation.

First, we consider a smooth scalar or vector field $f(\mathbf{x})$ in Ω written as a spatial convolution product with the Dirac delta function δ,

$$f(\mathbf{x})=\int_{\Omega}f(\mathbf{x}')\delta(\mathbf{x}-\mathbf{x}')dV'. \tag{4.11}$$

Then, the delta function is replaced by a smooth kernel function, which is the central feature of SPH. It gives the so-called *integral representation* or *kernel approximation* of a function f. That is

$$f(\mathbf{x}) \approx< f(\mathbf{x}) >_h = \int_\Omega f(\mathbf{x}')W(\mathbf{x}-\mathbf{x}', h)dV', \tag{4.12}$$

where $W(\mathbf{x}-\mathbf{x}', h)$ is the *smoothing kernel function* and h is the smoothing length [68]. The kernel function W is regular, continuous and differentiable, whose gradient can be calculated analytically.

For the approximation $f(\mathbf{x}) \approx< f(\mathbf{x}) >_h$ to be accurate to the first order, the two following conditions have to be verified [106]:

$$\int_\Omega W(\mathbf{x}-\mathbf{x}', h)dV' = 1 \tag{4.13}$$

and

$$\int_\Omega (\mathbf{x}-\mathbf{x}')W(\mathbf{x}-\mathbf{x}', h)dV' = 0. \tag{4.14}$$

The *normalization* condition (Eq. 4.13) designates that the kernel average should be equal to 1 (like the Dirac function) and it represents that the function can reproduce a constant field [106], [62]. The *symmetry* condition (Eq. 4.14) stipulates that the kernel function must be a symmetric (even) function, i.e. $W(\mathbf{x}-\mathbf{x}', h) = W(\mathbf{x}'-\mathbf{x}, h)$ [68].

Additionally, the kernel function $W(\mathbf{x}-\mathbf{x}', h)$ is positive in order to avoid non-physical approximations. It tends to the Dirac delta function if h tends to zero. It is monotonically decreasing when the distance between $\mathbf{x}$ and $\mathbf{x}'$ increases. Finally, it has a compact support, that depends on the smoothing length h, i.e.

$$W(\mathbf{x}-\mathbf{x}', h) = 0, \qquad if \ \ \|\mathbf{x}-\mathbf{x}'\| > \kappa h, \tag{4.15}$$

where κ is a constant related to the kernel function, e.g. $\kappa = 2$.

The kernel support of $\mathbf{x}$ is defined by [68]

$$D(\mathbf{x}) = \left\{\mathbf{x}' \in \Omega : W(\mathbf{x}-\mathbf{x}', h) \neq 0\right\} = \left\{\mathbf{x}' \in \Omega : \|\mathbf{x}-\mathbf{x}'\| \leq \kappa h\right\}. \tag{4.16}$$

Since the kernel function has a compact support, the kernel approximation (Eq. 4.12) is integrated, now, over the support $D(\mathbf{x})$. So, it depends on the compact sub domain that depends on the smoothing length h and not anymore on the whole computational domain. It is rewritten as

$$< f(\mathbf{x}) >_h = \int_{D(\mathbf{x})} f(\mathbf{x}')W(\mathbf{x}-\mathbf{x}', h)dV'. \tag{4.17}$$

It has been shown in previous works ([62], [68]) that linear consistency is obtained if kernel functions are chosen to be positive and following the conditions in Eq. (4.13) and Eq. (4.14). Therefore, it is guaranteed that linear functions are reproduced. However, this is only valid if $\mathbf{x}$ is located far away from the boundary of the numerical domain $\partial\Omega$, otherwise the support $D(\mathbf{x})$ is truncated by the boundary and the normalization condition is no longer satisfied. The subject about boundary truncation and its technique of treatment will not be addressed in the present document because it is out of the scope of this work. However additional information regarding this subject can be found in the work of Marongiu [62], Li [57], Neuhauser [68].

The gradient of the field ∇f can be also calculated using the kernel approximation, i.e.

$$< \nabla f(\mathbf{x}) >_h = \int_{D(\mathbf{x})} f(\mathbf{x}')\nabla W(\mathbf{x}-\mathbf{x}', h)dV' + \int_{\partial D(\mathbf{x})} f(\mathbf{x}')W(\mathbf{x}-\mathbf{x}', h)\mathbf{n}dS, \tag{4.18}$$

where the gradient of the kernel function $\nabla W(\mathbf{x}-\mathbf{x}', h)$ is calculated analytically. The boundary of the support $D(\mathbf{x})$ is denoted by $\partial D(\mathbf{x})$. The second integral is not zero only when the boundary of the domain intersects the kernel support.

From the symmetry condition of the kernel function it is stated that its gradient is anti-symmetric, i.e.

$$\nabla_{\mathbf{x}} W(\mathbf{x}-\mathbf{x}', h) = -\nabla_{\mathbf{x}'} W(\mathbf{x}-\mathbf{x}', h), \tag{4.19}$$

where $\nabla_{\mathbf{x}}$ is the gradient evaluated at $\mathbf{x}$.

4.3.2 Particle approximation

In SPH the domain of interest is populated with a finite amount of calculation points without any connectivity between them. The discrete equation equivalent to Eq. (4.17) represents the reconstructed value of f at the position $\mathbf{x}_i$, it is called *particle approximation* and it is defined by,

$$< f_i >= \sum_{j \in D_i} \omega_j f_j W_{ij}, \tag{4.20}$$

where $D_i = D(\mathbf{x}_i)$ is the kernel support of $\mathbf{x}_i$ and its boundary ∂D_i, ω_j is the integration weight of the calculation point j, and the discretized kernel is $W_{ij} = W(\mathbf{x}_j - \mathbf{x}_i, h_{ij})$ with $h_{ij} = \frac{h_i + hj}{2}$.

Congruently, the reconstructed value of the gradient ∇f at the position $\mathbf{x}_i$ is

$$< \nabla f_i >= \sum_{j \in D_i} \omega_j f_j \nabla_i W_{ij} + \sum_{j \in \partial D_i} \omega_j^{\partial} f_j W_{ij} \mathbf{n}_j, \tag{4.21}$$

where $\nabla_i W_{ij}$ is the gradient of the kernel function W_{ij} evaluated at the particle position $\mathbf{x}_i$. The second term in Eq. (4.21) corresponds to the discretization of the surface integral over the boundary of the support [62]. Consequently, it is needed to discretize the boundary in surface elements with surface area ω^{∂}.

The kernel function is still a symmetric function, i.e. $W_{ij} = W_{ji}$, and the gradient of the kernel function is anti-symmetric,

$$\nabla_i W_{ij} = -\nabla_j W_{ij}. \tag{4.22}$$

The anti-symmetric characteristic of the gradient is important to ensure conservation properties as will be seen in Section 4.3.4.

In practice, Eq. (4.21) is not able to calculate correctly the gradient of a constant function [68]. Consequently, zero consistency is not achieved. So, to enforce zero consistency for the computation of a gradient, the Eq. (4.21) is rewritten as [68],

$$< \nabla f_i >= \sum_{j \in D_i} \omega_j (f_j - f_i) \nabla_i W_{ij} + \sum_{j \in \partial D_i} \omega_j^{\partial} (f_j - f_i) W_{ij} \mathbf{n}_j. \tag{4.23}$$

Making a connection between the particle approximation with the physical quantities, the calculation points are interpreted as particles with a volume ω_i. The particle position is denoted by $\mathbf{x}_i$ and each particle brings its physical fields: pressure p_i, velocity $\mathbf{v}_i$, energy E_i. The surface elements are represented by a surface area in 3D, by a line segment in 2D and by a point in 1D.

4.3.3 Convergence in space of the SPH method

The SPH method has two parameters for the space discretization: Δx that is the distance between two particles and h that is the smoothing length. This last parameter is the size of the kernel function and it allows controlling the amount of neighbor particles used in the interpolation. These two parameters are shown in Fig. 4.1.

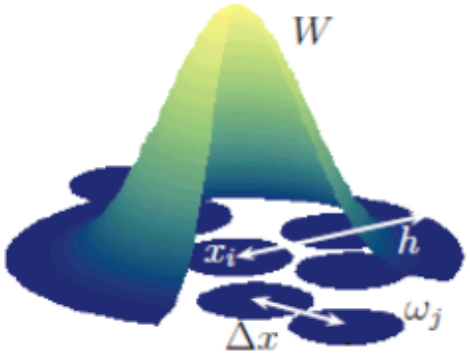

FIGURE 4.1: Spacial discretization parameters in the kernel function [82]

The SPH method converges if the numerical solution tends towards the exact solution when the space discretization tends to zero. Since the SPH method has two space discretization parameters, it is necessary that the distance between particles and the integration volume tend to zero to have convergence in space ([62], [82]),

$$\begin{cases} \Delta x \to 0 \\ h \to 0 \, . \\ \dfrac{h}{\Delta x} \to \infty \end{cases} \tag{4.24}$$

The limit of the ratio $\frac{h}{\Delta x}$ means that the distance between particles decreases faster than the kernel length.

Because we search finite ratios of $\frac{h}{\Delta x}$, it is found in the literature ([105], [62], [82]) a suitable ratio value, i.e.

$$\frac{h}{\Delta x} = 1.23. \tag{4.25}$$

This ratio corresponds to have approximately twenty neighbor particles inside the kernel function for a 2D domain.

4.3.4 SPH-ALE

The SPH-ALE method was introduced by Vila in 1999 [105] in order to give a contribution towards the design of SPH methods for conservation laws.

First, to get a particle approximation of the Euler equations in ALE form (Eq. 4.7), we take a set of moving particles considering its geometric properties: the position of the particle $\mathbf{x}_i$ and its volume or weight ω_i [105]. The particles move along the field $\mathbf{v}_0$ describing the temporal evolution of the particle position in ALE form:

$$\frac{d(\mathbf{x}_i)}{dt} = \mathbf{v}_0(\mathbf{x}_i, t). \tag{4.26}$$

As well, the evolution of the particle volume is considered in order to take into account its deformations due to the field $\mathbf{v}_0$:

$$\frac{d(\omega_i)}{dt} = \omega_i \nabla \cdot (\mathbf{v}_0(\mathbf{x}_i, t)). \tag{4.27}$$

As the particle approximation expression (Eq. 4.23) can be applied to the gradient or divergence of a function [57], the previous expression is discretized as

$$\begin{aligned} \frac{d(\omega_i)}{dt} = \omega_i \sum_{j \in D_i} \omega_j (\mathbf{v}_0(\mathbf{x}_j, t) - \mathbf{v}_0(\mathbf{x}_i, t)) \cdot \nabla_i W_{ij} \\ + \omega_i \sum_{j \in \partial D_i} \omega_j^{\partial} (\mathbf{v}_0(\mathbf{x}_j, t) - \mathbf{v}_0(\mathbf{x}_i, t)) \cdot \mathbf{n}_j W_{ij}. \end{aligned} \tag{4.28}$$

Next, the Euler equations in ALE approach expressed in integral form (Eq. 4.10) are re-written using the Divergence theorem,

$$\frac{d}{dt}\int_{\Omega}\mathbf{\Phi}dV+\int_{\Omega}\nabla\cdot\mathbf{F}(\mathbf{\Phi},\mathbf{v}_0)dV=\int_{\Omega}\mathbf{S}_T dV. \tag{4.29}$$

Then, considering the local equations for the particle i, we have

$$\frac{d}{dt}\int_{D_i}\mathbf{\Phi}dV+\int_{D_i}\nabla\cdot\mathbf{F}(\mathbf{\Phi},\mathbf{v}_0)dV=\int_{D_i}\mathbf{S}_T dV. \tag{4.30}$$

The evaluation of volume integrals needs the definition of the average value of the field $\mathbf{\Phi}$ in a volume D_i. Because SPH-ALE is a method centered on the particles i, the volume D_i is taken as the volume of the particle, i.e. $D_i=\omega_i$. So, it is given [82]

$$\mathbf{\Phi}_i=\frac{1}{\omega_i}\int_{D_i}\mathbf{\Phi}dV. \tag{4.31}$$

In consequence, Eq. (4.30) becomes

$$\frac{d}{dt}(\omega_i\mathbf{\Phi}_i)+\omega_i\nabla_i\cdot\mathbf{F}(\mathbf{\Phi},\mathbf{v}_0)=\omega_i\mathbf{S}_{Ti}. \tag{4.32}$$

Now, to obtain the ALE formulation for the Euler system, we focus on the second term of Eq. (4.32). This term is discretized using the Eq. (4.21), to give [105]:

$$\omega_i\nabla_i\cdot\mathbf{F}(\mathbf{\Phi},\mathbf{v}_0)\approx\omega_i\sum_{j\in D_i}\omega_j\mathbf{F}_j\cdot\nabla_i W_{ij}+\omega_i\sum_{j\in\partial D_i}\omega_j^{\partial}\mathbf{F}_j\cdot\mathbf{n}_j W_{ij} \tag{4.33}$$

However, the Eq. (4.33) does not ensure to be a conservative formulation. This statement can be explained by recalling that the kernel function is anti-symmetric (i.e. $\nabla_i W_{ij}=-\nabla_j W_{ij}$). So, the following relation:

$$\omega_i\omega_j(\mathbf{F}_j)\cdot\nabla_i W_{ij}=-\omega_j\omega_i(\mathbf{F}_i)\cdot\nabla_j W_{ij} \tag{4.34}$$

is not satisfied because usually $\mathbf{F}_j\neq\mathbf{F}_i$.

So, following the mathematical development explained by Vila [105], an additional term is introduced in order to ensure the conservation. It is taken an unit function $H(x)=1$,

so $\nabla H(x) = 0$. Later, it is introduced $\mathbf{F}_i \cdot \nabla H(x)$ into Eq. (4.29) to give

$$\frac{d}{dt}\int_\Omega \mathbf{\Phi} dV + \int_\Omega (\nabla \cdot \mathbf{F}(\mathbf{\Phi}, \mathbf{v}_0) + \mathbf{F}_i \cdot \nabla H) dV = \int_\Omega \mathbf{S}_T dV. \tag{4.35}$$

Since $\mathbf{F}_i \cdot \nabla H = 0$, equations (4.35) and (4.29) are equivalent.

Next, it is used the SPH approximation on this additional term,

$$\begin{aligned}\int_\Omega \mathbf{F}_i \cdot \nabla H dV = \mathbf{F}_i \cdot \int_\Omega \nabla H dV &\approx \mathbf{F}_i \cdot \left(\omega_i \sum_{j \in D_i} \omega_j H_j \nabla_i W_{ij} + \omega_i \sum_{j \in \partial D_i} \omega_j^\partial H_j \mathbf{n}_j W_{ij} \right) \\ &= \omega_i \sum_{j \in D_i} \omega_j \mathbf{F}_i \cdot \nabla_i W_{ij} + \omega_i \sum_{j \in \partial D_i} \omega_j^\partial \mathbf{F}_i \cdot \mathbf{n}_j W_{ij},\end{aligned} \tag{4.36}$$

where $H_j = H(\mathbf{x}_j) = 1$.

Finally, with Eq. (4.36), it is obtained the particle approximation for the Euler system in ALE formulation,

$$\begin{aligned}\frac{d\left(\omega_i \mathbf{\Phi}_i\right)}{dt} + \omega_i \sum_{j \in D_i} \omega_j (\mathbf{F}_i(\mathbf{\Phi}_i, \mathbf{v}_0) + \mathbf{F}_j(\mathbf{\Phi}_j, \mathbf{v}_0)) \cdot \nabla_i W_{ij} \\ + \omega_i \sum_{j \in \partial D_i} \omega_j^\partial (\mathbf{F}_i(\mathbf{\Phi}_i, \mathbf{v}_0) + \mathbf{F}_j(\mathbf{\Phi}_j, \mathbf{v}_0)) \cdot \mathbf{n}_j W_{ij} \\ = \omega_i \mathbf{S}_{Ti}.\end{aligned} \tag{4.37}$$

where $\mathbf{F}_i$ and $\mathbf{F}_j$ correspond to the flux vector $\mathbf{F}$ given in Eq. (4.9), evaluated at $\mathbf{x}_i$ and $\mathbf{x}_j$ respectively. The first sum for $j \in D_i$ is computed for the fluid particles, and the second sum computed for $j \in \partial D_i$ represents the boundary term, which is zero far away from the boundaries of the domain $\partial\Omega$.

Because

$$\omega_i \omega_j (\mathbf{F}_i + \mathbf{F}_j) \cdot \nabla_i W_{ij} = -\omega_j \omega_i (\mathbf{F}_j + \mathbf{F}_i) \cdot \nabla_j W_{ij}, \tag{4.38}$$

Eq. (4.37) is a conservative formulation.

The centered discretization in space present in Eq. (4.37) is not stable [55], so a decentered scheme should be used. Vila [105] proposed to replace the term $(\mathbf{F}_i + \mathbf{F}_j)$ by two times

a decentered numerical flux computed at $\mathbf{x}_{ij} = \frac{\mathbf{x}_i + \mathbf{x}_j}{2}$ in order to stabilized it, i.e.

$$\mathbf{F}_i(\mathbf{\Phi}_i, \mathbf{v}_0) + \mathbf{F}_j(\mathbf{\Phi}_j, \mathbf{v}_0) \approx 2\mathbf{F}_{ij}(\mathbf{\Phi}_{ij}, \mathbf{v}_0). \tag{4.39}$$

The decentered scheme (4.39) is applied to Eq. (4.37) to give the ALE discretization of the conservation of mass, momentum and energy. Assembling it with the temporal evolution of the particle position (Eq. 4.26) and particle volume (Eq. 4.28), it is obtained the discrete SPH-ALE formulation of the Euler equations, i.e.

$$\begin{cases} \dfrac{d(\mathbf{x}_i)}{dt} = \mathbf{v}_0(\mathbf{x}_i, t) \\ \dfrac{d(\omega_i)}{dt} = \omega_i \displaystyle\sum_{j \in D_i} \omega_j (\mathbf{v}_0(\mathbf{x}_j, t) - \mathbf{v}_0(\mathbf{x}_i, t)) \cdot \nabla_i W_{ij} \\ + \omega_i \displaystyle\sum_{j \in \partial D_i} \omega_j^{\partial} (\mathbf{v}_0(\mathbf{x}_j, t) - \mathbf{v}_0(\mathbf{x}_i, t)) \cdot \mathbf{n}_j W_{ij} \\ \dfrac{d(\omega_i \mathbf{\Phi}_i)}{dt} = -\omega_i \displaystyle\sum_{j \in D_i} \omega_j 2\mathbf{F}_{ij}(\mathbf{\Phi}, \mathbf{v}_0) \cdot \nabla_i W_{ij} - \omega_i \sum_{j \in \partial D_i} \omega_j^{\partial} 2\mathbf{F}_{ij}(\mathbf{\Phi}, \mathbf{v}_0) \cdot \mathbf{n}_j W_{ij} + \omega_i \mathbf{S}_{Ti}. \end{cases} \tag{4.40}$$

The two first equations are related to the ALE feature of the method and the last equation represents the conservation equations. The calculation of the fluxes ($\mathbf{F}_{ij}$) requires to solve Riemann problems between fluid particles in the fluid domain D_i [105], and to solve partial Riemann problems between fluid particles and boundary elements along ∂D_i [62].

4.4 Computation of the numerical fluxes

4.4.1 Classical Riemann problem

The Riemann problem is the initial value problem for a hyperbolic system of conservation equations [37], i.e. the Euler system (Eq. 4.4).

From a numerical point of view the Riemann problem is considered in the direction of the connecting line between two fluid particles, and the initial discontinuity is located at the midpoint of this connecting line [68].

A direction of observation ($\mathbf{n}_k$) is considered with origin at $\mathbf{x}_k$ (see Fig. 4.2). The direction of interest is the unit vector between two fluid particles and it is parallel to

the $x-direction$. Then, the one-dimensional Riemann problem for the time dependent Euler equations (Eq. 4.4) in the $\mathbf{n}_k$ direction is given as,

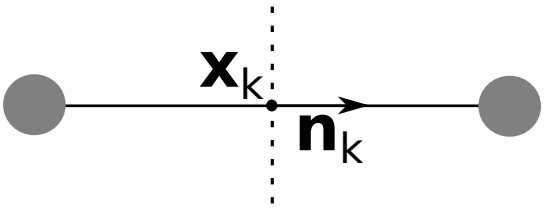

FIGURE 4.2: One-dimensional Riemann problem between fluid particles (in grey) showing the initial discontinuity

$$\frac{\partial(\mathbf{\Phi})}{\partial t}+\frac{\partial(\mathbf{F}\cdot\mathbf{n}_k)}{\partial x}=0,\quad \mathbf{\Phi}(x,0)=\begin{cases}\mathbf{\Phi}_L & if\ x<0\\ \mathbf{\Phi}_R & if\ x>0\end{cases}, \tag{4.41}$$

with initial conditions consisting in two constant states ($\mathbf{\Phi}_L$ and $\mathbf{\Phi}_R$) separated by a discontinuity defined at the interface. Here, $\mathbf{\Phi}_L$ and $\mathbf{\Phi}_R$ are the vectors written in conservative variables for each particle.

In the ALE formulation, $\mathbf{F}$ is given by Eq. (4.9), i.e. $\mathbf{F}=\mathbf{F}(\mathbf{\Phi},\mathbf{v}_0)=\mathbf{F}_C(\mathbf{\Phi})-(\mathbf{v}_0\otimes\mathbf{\Phi})$. So, considering this expression in the one-dimensional Riemann problem formulation, we obtained a moving Riemann problem,

$$\frac{\partial(\mathbf{\Phi})}{\partial t}+\frac{\partial}{\partial x}\left(\mathbf{F}_C(\mathbf{\Phi})\cdot\mathbf{n}_k-\mathbf{v}_0\cdot\mathbf{n}_k\mathbf{\Phi}\right)=0,\quad \mathbf{\Phi}(x,0)=\begin{cases}\mathbf{\Phi}_L & if\ x<0\\ \mathbf{\Phi}_R & if\ x>0\end{cases}. \tag{4.42}$$

In this case, the interface moves with the ALE velocity $\mathbf{v}_0(\mathbf{x}_k,t)$.

Hence, the solution of the Riemann problem, i.e. $\mathbf{\Phi}_k^E=(\rho_k^E,\ \rho_k^E\mathbf{v}_k^E,\ \rho_k^E E_k^E)^T$, is obtained with the following relation,

$$\begin{cases}x/t=\lambda_k=\mathbf{v}_0(\mathbf{x}_k,t)\cdot\mathbf{n}_k\\ \mathbf{\Phi}_k^E=\mathbf{\Phi}_k^E(\lambda_k)\end{cases}. \tag{4.43}$$

The solution of the moving Riemann problem is thus inserted into the flux vector to calculate the numerical flux, i.e.

$$\mathbf{F}(\mathbf{\Phi},\mathbf{v}_0)=\mathbf{F}_C(\mathbf{\Phi}_k^E)-\left(\mathbf{v}_0(\mathbf{x}_k,t)\otimes\mathbf{\Phi}_k^E\right). \tag{4.44}$$

To solve the Riemann problem, it is usually preferable to use the vector of primitive variables $\mathbf{W}$ rather than the vector of conservative variables $\mathbf{\Phi}$ [103]. For the Stiffened Gas EOS, the primitive variable vector in one-dimension is $\mathbf{W} = (\rho, u, p)^T$, with p given by the equation of state ($p = p(\rho, e)$).

Instead of Eq. (4.41), the new system of equations has the form

$$\frac{\partial \mathbf{W}}{\partial t} + \mathbf{A}\frac{\partial \mathbf{W}}{\partial x} = 0, \tag{4.45}$$

where $\mathbf{A}$ is the Jacobian matrix of the system in Eq. (4.45), i.e.

$$\mathbf{A} = \left(\frac{\partial(\mathbf{\Phi})}{\partial W}\right)^{-1} \frac{\partial(\mathbf{F}\cdot\mathbf{n}_k)}{\partial W}. \tag{4.46}$$

Using the expression for the speed of sound Eq. 3.48, $c^2 = \frac{\gamma}{\rho}(p + p_\infty)$, the coefficients of $\mathbf{A}$ in 1D for the Stiffened Gas EOS are

$$\mathbf{A} = \begin{bmatrix} u & \rho & 0 \\ 0 & u & 1/\rho \\ 0 & \rho c^2 & u \end{bmatrix}. \tag{4.47}$$

This system has three real eigenvalues: $\lambda_1 = u - c$, $\lambda_2 = u$, $\lambda_3 = u + c$, with corresponding right eigenvectors:

$$\begin{cases} \mathbf{R}^1 = (1, -c/\rho, c^2)^T \\ \mathbf{R}^2 = (1, 0, 0)^T \\ \mathbf{R}^3 = (1, c/\rho, c^2)^T \end{cases}, \tag{4.48}$$

and left eigenvectors:

$$\begin{cases} \mathbf{L}^1 = (0, 1, -1/(\rho c)) \\ \mathbf{L}^2 = (1, 0, -1/(c^2)) \\ \mathbf{L}^3 = (0, 1, 1/(\rho c)) \end{cases}. \tag{4.49}$$

Following Ivings [37] and Toro [103], Fig. 4.3 shows the structure of the Riemann problem for Stiffened Gas EOS. There are three waves associated with the eigenvalues ($\lambda_i, i = 1, 2, 3$), two non-linear waves which are either shock or rarefaction waves, and the

middle wave which is a contact wave. In the case of two and three dimensions in space, the contact wave is associated to the repeated eigenvalue $\lambda = u$. The *Star Region* is the zone that lies in between the two waves λ_1 and λ_3 (see Fig. 4.3). The density varies discontinuously across the contact wave, from ρ_L^* to ρ_R^*. On the contrary, the pressure p^* and the particle velocity u^* that lie in the *Star Region* are constant.

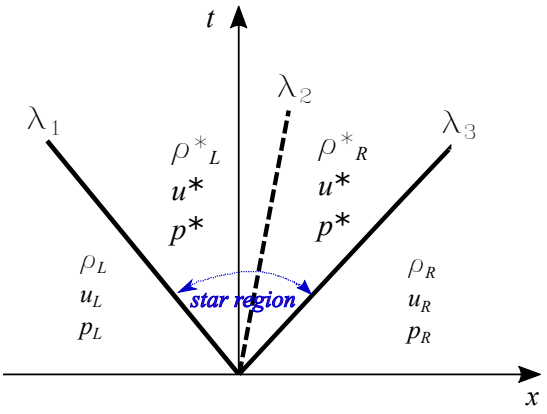

FIGURE 4.3: Structure of a one-dimensional Riemann problem along a direction of observation parallel to the $x - axis$ for the Euler equations using Stiffened Gas EOS

Next, it is presented a procedure to derive a solution for the *Star Region* in order to have an expression for the physical quantities $p^*, u^*, \rho_L^*, \rho_R^*$.

4.4.2 Riemann solvers

The purpose is to find an approximate solution of the Riemann problem. A linearized Riemann solver, often known as the primitive variable Riemann solver (PVRS) ([37], [103]) is explained thereafter.

Previously, the Riemann solver with the Tait equation of state has been used to solve the Euler system using the SPH-ALE method. Supplementary information regarding this Riemann solver can be found in the work of Marongiu [62], Leduc [54], Neuhauser [68] and Renaut[82]. In addition, we have seen that in order to solve the non-isentropic Euler equations another equation of state must be considered, thus another Riemann solver must be regarded. Continuing with this idea, we present first the PVRS for Stiffened Gas EOS, and at the end some comments comparing both solvers are done.

Instead of PVRS, another way of obtaining the approximate solution for the star region is also described. It is about the use of characteristic equations in the direction of

the eigenvalues. This method, known as acoustic solver, is especially helpful for the calculation of multi-phase flow.

Primitive Variable Riemann Solver (PVRS)

In order to solve the system of Eq. (4.45), we assume that the initial data $\mathbf{W}_L$, $\mathbf{W}_R$ and the solution $\mathbf{W}$ are close to a constant state $\bar{\mathbf{W}}$ [103]. So, the primitive variable system (Eq. 4.45) is linearized about some average state [103] i.e. $\bar{\mathbf{W}} = (\bar{\rho}, \bar{u}, \bar{p})^T$.

Then, by setting $\bar{\mathbf{A}} = \mathbf{A}(\bar{\mathbf{W}})$ i.e.

$$\bar{\mathbf{A}} = \begin{bmatrix} \bar{u} & \bar{\rho} & 0 \\ 0 & \bar{u} & 1/\bar{\rho} \\ 0 & \bar{\rho}\bar{c}^2 & \bar{u} \end{bmatrix}, \tag{4.50}$$

we have the Riemann problem for the linear hyperbolic system with constant coefficients,

$$\frac{\partial \mathbf{W}}{\partial t} + \bar{\mathbf{A}} \frac{\partial \mathbf{W}}{\partial x} = 0. \tag{4.51}$$

The eigenvalues $\bar{\lambda}_i$ associated to the matrix $\bar{\mathbf{A}}$ for the Stiffened Gas EOS represent each wave speed. They are given by,

$$\begin{cases} \bar{\lambda}_1 = \bar{u} - \bar{c} \\ \bar{\lambda}_2 = \bar{u} \\ \bar{\lambda}_3 = \bar{u} + \bar{c} \end{cases}. \tag{4.52}$$

Then, across a wave of speed $\bar{\lambda}_i$ we have

$$\bar{\mathbf{A}} \Delta \mathbf{W} = \bar{\lambda}_i \Delta \mathbf{W}. \tag{4.53}$$

After solving Eq. (4.53), the solution in the star region is:

$$\begin{cases} p^* = 1/2(p_L + p_R) + 1/2(u_L - u_R)(\bar{\rho}\bar{c}) \\ u^* = 1/2(u_L + u_R) + 1/2(p_L - p_R)/(\bar{\rho}\bar{c}) \\ \rho_L^* = \rho_L + (u_L - u^*)(\bar{\rho}/\bar{c}) \\ \rho_R^* = \rho_R + (u^* - u_R)(\bar{\rho}/\bar{c}) \end{cases}. \tag{4.54}$$

Because we are dealing with a linearized solution, we specify constant values for the density $\bar{\rho}$ and the speed of sound $\bar{c}$, given by

$$\begin{cases} \bar{\rho} = 1/2(\rho_L + \rho_R) \\ \bar{c} = 1/2(c_L + c_R) \end{cases}. \tag{4.55}$$

In the case of two dimensions, the tangential velocity component v across the contact wave is given by ([37], [103]),

$$v = \begin{cases} v_L & if \quad x/t < u^* \\ v_R & if \quad x/t > u^* \end{cases}. \tag{4.56}$$

The main difference between the Riemann solver for the Tait EOS and for the Stiffened Gas EOS lies in calculating the solution in the star region. For the Tait EOS only ρ^* and u^* are searched. Differently, for the Stiffened Gas EOS, there are calculated the pressure p^* and the densities ρ_L^* and ρ_R^*, in addition to the velocity u^*.

Acoustic Riemann Solver

In the PVRS solver, we assume a linearized solution, so the density and the speed of sound are calculated as an average between each state (Eq. 4.55). However, this assumption can not be taken when considering multiphase flows involving fluids with high density ratio. So, another way to obtain the approximate solution for the star values is presented thereafter. In this case, the characteristic equations in the direction of the eigenvalues are used.

The left eigenvectors (Eq. 4.49) associated to the mentioned eigenvalues are used in order to obtain the characteristic equations,

$$\begin{cases} dp - \rho c du = 0 & along \; u - c \\ dp - c^2 d\rho = 0 & along \; u \\ dp + \rho c du = 0 & along \; u + c \end{cases}. \tag{4.57}$$

These expressions are valid along characteristic directions [103]. Then, in order to find the star values, we connect the state $\mathbf{W}_L^*$ to the state $\mathbf{W}_L$ by integrating the characteristic equation along $u + c$. Similarly, we connect $\mathbf{W}_R^*$ to the state $\mathbf{W}_R$ by integrating along

$u - c$. Finally, to obtain the expressions for ρ_L^* and ρ_R^* we connect $\mathbf{W}_L^*$ to $\mathbf{W}_L$ and $\mathbf{W}_R^*$ to $\mathbf{W}_R$ along u, respectively.

With $Z = \rho c$ evaluated for each state L and R, the complete solution is [103]:

$$\begin{cases} p^* = \dfrac{1}{Z_L + Z_R}[Z_R p_L + Z_L p_R + Z_L Z_R (u_L - u_R)] \\ u^* = \dfrac{1}{Z_L + Z_R}[Z_L u_L + Z_R u_R + (p_L - p_R)] \\ \rho_L^* = \rho_L + (p^* - p_L)/c_L^2 \\ \rho_R^* = \rho_R + (p^* - p_R)/c_R^2 \end{cases} . \tag{4.58}$$

Different with the PVRS solver, it is noted that the density is not calculated as the average between two control volumes. So, this solver is adapted for multi-phase flow simulations.

Strategy to compute the solution state for the numerical fluxes

Considering the structure of the Riemann problem, there are four possible wave patterns of shock and rarefaction waves, see Figure 4.4. Theses regions are delimited by the wave speed, denoted by $x/t = \mu$ and $\mu_i \leq \mu_{i+1}$. For the case of two shock waves, there are three lines $x/t = \mu_1 = \mu_2$, $x/t = \mu_3$ and $x/t = \mu_4 = \mu_5$, so four regions. For the case of two rarefaction waves, two additional lines are added considering the speeds of the head and tail of each rarefaction wave, giving six regions and having five different wave speeds. Additionally, for the case of one shock and one rarefaction wave, there are five regions. In the following, we develop the general case of one shock and one rarefaction wave (Fig. 4.4(c) and Fig. 4.4(d)).

To determine in which zone the solution has to be picked using Eq. 4.43, the wave speeds are computed. We know that the contact wave associated to μ_3 travels at speed u^*. Pursuing, the other wave speeds are presented.

- The left wave is a rarefaction wave if $p^* \leq p_L$ (Fig. 4.4(b) and Fig. 4.4(d))

$$\begin{cases} \mu_1 = u_L - c_L \\ \mu_2 = u^* - c^* \end{cases} . \tag{4.59}$$

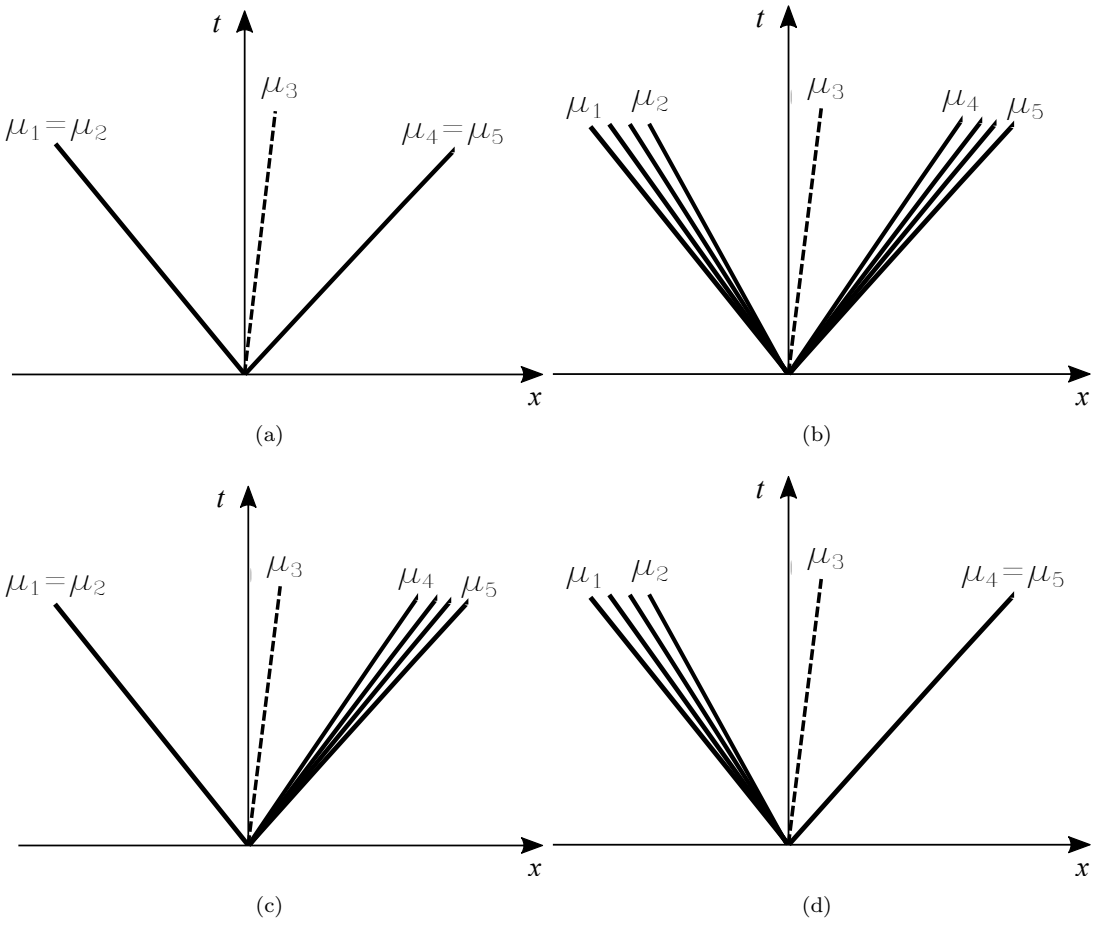

FIGURE 4.4: Possible wave patterns in the solution of the Riemann problem: (a) left shock, contact, right shock (b) left rarefaction, contact, right rarefaction (c) left shock, contact, right rarefaction (d) left rarefaction, contact, right shock

- The left wave is a shock wave if $p^* > p_L$ (Fig. 4.4(a) and Fig. 4.4(c))

$$\left\{ \mu_1 = \mu_2 = u_L - \frac{Q_L}{\rho_L} \right. . \tag{4.60}$$

with

$$Q_L = \left[[(p^* + p_{\infty L})(\gamma_L + 1) + (p_L + p_{\infty L})(\gamma_L - 1)] \frac{\rho_L}{2} \right]^{1/2} . \tag{4.61}$$

- The right wave is a rarefaction wave if $p^* \leq p_R$ (Fig. 4.4(b) and Fig. 4.4(c))

$$\begin{cases} \mu_4 = u^* + c^* \\ \mu_5 = u_R + c_R \end{cases} . \tag{4.62}$$

- The right wave is a shock wave if $p^* > p_R$ (Fig. 4.4(a) and Fig. 4.4(d))

$$\begin{cases} \mu_4 = \mu_5 = u_R + \dfrac{Q_R}{\rho_R} \end{cases}. \tag{4.63}$$

with

$$Q_R = \left[[(p^* + p_{\infty R})(\gamma_R + 1) + (p_R + p_{\infty R})(\gamma_R - 1)] \frac{\rho_R}{2} \right]^{1/2}. \tag{4.64}$$

It is to notice that $Q_{L/R}$ is calculated using the Stiffened Gas EOS constants, γ and p_∞.

Once we have the solution for the star region using the primitive variable solver (Eq. 4.54) or the acoustic one (Eq. 4.58) and the nature of the left and right waves, we are able to compute the solution state ($\mathbf{\Phi}_k^E$) needed for the calculation of the numerical fluxes. This solution is searched in the direction $x/t = \lambda_k = \mathbf{v}_0(\mathbf{x}_k, t) \cdot \mathbf{n}_k$.

To determine in which region the sought solution lies, we evaluate where is located the wave speed λ_k with respect to the other wave speeds $\mu_\alpha, \alpha = 1, ..., 5$.

First, we introduce the most probable cases that correspond to the cases where the solution lies in the *Star Region*.

- $\mu_2 < \lambda_k \leq \mu_3$

$$\begin{cases} \rho_k^E = \rho_L^* \\ \mathbf{v}_k^E = \mathbf{v}_L + [u^* - \mathbf{v}_L \cdot \mathbf{n}_k] \cdot \mathbf{n}_k \\ p_k^E = p^* \\ e_k^E = \dfrac{p_k^E + \gamma_L p_{\infty L}}{\rho_k^E (\gamma_L - 1)} \end{cases}. \tag{4.65}$$

- $\mu_3 < \lambda_k \leq \mu_4$

$$\begin{cases} \rho_k^E = \rho_R^* \\ \mathbf{v}_k^E = \mathbf{v}_R + [u^* - \mathbf{v}_R \cdot \mathbf{n}_k] \cdot \mathbf{n}_k \\ p_k^E = p^* \\ e_k^E = \dfrac{p_k^E + \gamma_R p_{\infty R}}{\rho_k^E (\gamma_R - 1)} \end{cases}. \tag{4.66}$$

Next, we have the cases where the solution lies in a rarefaction wave.

- $\mu_1 < \lambda_k \leq \mu_2$

$$\begin{cases} \rho_k^E = \rho_L \left[\dfrac{u_{normal} - \lambda_k}{c_L} \right]^{2/(\gamma_L - 1)} \\ \mathbf{v}_k^E = \mathbf{v}_L + [u_{normal} - \mathbf{v}_L \cdot \mathbf{n}_k] \cdot \mathbf{n}_k \\ p_k^E = (p_L + p_{\infty L}) \left[\dfrac{u_{normal} - \lambda_k}{c_L} \right]^{(2\gamma_L)/(\gamma_L - 1)} - p_{\infty L} \\ e_k^E = \dfrac{p_k^E + \gamma_L p_{\infty L}}{\rho_k^E (\gamma_L - 1)} \end{cases} . \tag{4.67}$$

  with $u_{normal} = \frac{2}{\gamma_L + 1}(c_L + 0.5 u_L(\gamma_L - 1) + \lambda_k)$.

- $\mu_4 < \lambda_k \leq \mu_5$

$$\begin{cases} \rho_k^E = \rho_R \left[\dfrac{\lambda_k - u_{normal}}{c_R} \right]^{2/(\gamma_R - 1)} \\ \mathbf{v}_k^E = \mathbf{v}_R + [u_{normal} - \mathbf{v}_R \cdot \mathbf{n}_k] \cdot \mathbf{n}_k \\ p_k^E = (p_R + p_{\infty R}) \left[\dfrac{\lambda_k - u_{normal}}{c_R} \right]^{(2\gamma_R)/(\gamma_R - 1)} - p_{\infty R} \\ e_k^E = \dfrac{p_k^E + \gamma_R p_{\infty R}}{\rho_k^E (\gamma_R - 1)} \end{cases} . \tag{4.68}$$

  with $u_{normal} = \frac{2}{\gamma_R + 1}(-c_R + 0.5 u_R(\gamma_R - 1) + \lambda_k)$.

Finally, extreme cases are presented.

- $\lambda_k \leq \mu_1$ The solution state is equal to the left initial state, i.e.

$$\begin{cases} \mathbf{W}_k^E = \mathbf{W}_L \\ e_k^E = \dfrac{p_k^E + \gamma_L p_{\infty L}}{\rho_k^E (\gamma_L - 1)} \end{cases} . \tag{4.69}$$

- $\lambda_k > \mu_5$ The solution state is equal to the right initial state, i.e.

$$\begin{cases} \mathbf{W}_k^E = \mathbf{W}_R \\ e_k^E = \dfrac{p_k^E + \gamma_R p_{\infty R}}{\rho_k^E (\gamma_R - 1)} \end{cases} . \tag{4.70}$$

It is important to highlight that the calculation of the internal energy for each case is done using the equation of state given in Eq. (3.33) and paying attention to the physical parameters in the case of multi-phase simulations, e.g. γ and p_∞ values. Next, the

calculation of the total energy, also needed for the computation of the numerical fluxes, is done using the Eq. (4.2).

4.4.3 Discrete SPH-ALE equations

Using the computed solution of the states $\mathbf{W}_k^E = (\rho_k^E, u_k^E, p_k^E)^T$, we are able to calculate the sought solution for the numerical fluxes $\mathbf{\Phi}_k^E$, and afterwards to obtain the numerical fluxes for the system of discrete equations (4.40). Hence, the resulting system of discrete SPH-ALE equations is given by

$$
\begin{cases}
\dfrac{d(\mathbf{x}_i)}{dt} = \mathbf{v}_0(\mathbf{x}_i, t) \\
\dfrac{d(\omega_i)}{dt} = \omega_i \displaystyle\sum_{j \in D_i} \omega_j (\mathbf{v}_0(\mathbf{x}_j, t) - \mathbf{v}_0(\mathbf{x}_i, t)) \cdot \nabla_i W_{ij} \\
+ \omega_i \displaystyle\sum_{j \in \partial D_i} \omega_j^{\partial} (\mathbf{v}_0(\mathbf{x}_j, t) - \mathbf{v}_0(\mathbf{x}_i, t)) \cdot \mathbf{n}_j W_{ij} \\
\dfrac{d(\omega_i \rho_i)}{dt} + \omega_i \displaystyle\sum_{j \in D_i} \omega_j 2\rho_{ij}^E (\mathbf{v}_{ij}^E - \mathbf{v}_0(\mathbf{x}_{ij}, t)) \cdot \nabla_i W_{ij} \\
+ \omega_i \displaystyle\sum_{j \in \partial D_i} \omega_j^{\partial} 2\rho_{ij}^E (\mathbf{v}_{ij}^E - \mathbf{v}_0(\mathbf{x}_{ij}, t)) \cdot \mathbf{n}_j W_{ij} = 0 \\
\dfrac{d(\omega_i \rho_i \mathbf{v}_i)}{dt} + \omega_i \displaystyle\sum_{j \in D_i} \omega_j 2[\rho_{ij}^E \mathbf{v}_{ij}^E \otimes (\mathbf{v}_{ij}^E - \mathbf{v}_0(\mathbf{x}_{ij}, t)) + p_{ij}^E] \cdot \nabla_i W_{ij} \\
+ \omega_i \displaystyle\sum_{j \in \partial D_i} \omega_j^{\partial} 2[\rho_{ij}^E \mathbf{v}_{ij}^E \otimes (\mathbf{v}_{ij}^E - \mathbf{v}_0(\mathbf{x}_{ij}, t)) + p_{ij}^E] \cdot \mathbf{n}_j W_{ij} = \omega_i \mathbf{S}_{ei} \\
\dfrac{d(\omega_i \rho_i E_i)}{dt} + \omega_i \displaystyle\sum_{j \in D_i} \omega_j 2[\rho_{ij}^E E_{ij}^E (\mathbf{v}_{ij}^E - \mathbf{v}_0(\mathbf{x}_{ij}, t)) + p_{ij}^E \mathbf{v}_{ij}^E] \cdot \nabla_i W_{ij} \\
+ \omega_i \displaystyle\sum_{j \in \partial D_i} \omega_j^{\partial} 2[\rho_{ij}^E E_{ij}^E (\mathbf{v}_{ij}^E - \mathbf{v}_0(\mathbf{x}_{ij}, t)) + p_{ij}^E \mathbf{v}_{ij}^E] \cdot \mathbf{n}_j W_{ij} = \omega_i \mathbf{S}_{ei} \mathbf{v}_{ij}^E
\end{cases} . \tag{4.71}
$$

The two first equations are related to the feature of the ALE method, computing the particle position and updating the particle volume. The three last equations represent the conservation of mass, momentum and energy. This discrete equation system includes the boundary and source terms.

Interface velocity in the volume evolution equation

In the discrete SPH-ALE system (Eq. 4.71) the equation to compute the volume evolution considers the difference between the velocities of two particles i and j, i.e. $\mathbf{v}_0(\mathbf{x}_j, t) - \mathbf{v}_0(\mathbf{x}_i, t)$, and not the average of both velocities, i.e.

$$\mathbf{v}_0(\mathbf{x}_{ij}, t) = \frac{\mathbf{v}_0(\mathbf{x}_j, t) + \mathbf{v}_0(\mathbf{x}_i, t)}{2}, \tag{4.72}$$

like in the discretization of the conservation equations (mass, momentum and energy equations). Hence, the idea is to introduce the average of velocities (Eq. 4.72) into the discretization of the volume evolution (Eq. 4.28), so it will be consistent with the other equations.

We start the analysis by considering the Eq. (4.72) that is re-written as

$$\mathbf{v}_0(\mathbf{x}_j, t) = 2\mathbf{v}_0(\mathbf{x}_{ij}, t) - \mathbf{v}_0(\mathbf{x}_i, t). \tag{4.73}$$

Then, the term $\mathbf{v}_0(\mathbf{x}_i, t)$ is subtracted on both sides, i.e.

$$\mathbf{v}_0(\mathbf{x}_j, t) - \mathbf{v}_0(\mathbf{x}_i, t) = 2\left(\mathbf{v}_0(\mathbf{x}_{ij}, t) - \mathbf{v}_0(\mathbf{x}_i, t)\right). \tag{4.74}$$

Hence, we obtain the expression for the term $\mathbf{v}_0(\mathbf{x}_j, t) - \mathbf{v}_0(\mathbf{x}_i, t)$ in the volume evolution equation in order to be consistent in the use of an arbitrary interface velocity among the SPH-ALE equations.

Finally, it is presented the set of discretized equations used for the numerical simulations developed in the frame of this work, i.e.

$$
\begin{cases}
\dfrac{d(\mathbf{x}_i)}{dt} = \mathbf{v}_0(\mathbf{x}_i, t) \\
\dfrac{d(\omega_i)}{dt} = \omega_i \displaystyle\sum_{j \in D_i} \omega_j 2(\mathbf{v}_0(\mathbf{x}_{ij}, t) - \mathbf{v}_0(\mathbf{x}_i, t)) \cdot \nabla_i W_{ij} \\
+ \omega_i \displaystyle\sum_{j \in \partial D_i} \omega_j^{\partial} 2(\mathbf{v}_0(\mathbf{x}_{ij}, t) - \mathbf{v}_0(\mathbf{x}_i, t)) \cdot \mathbf{n}_j W_{ij} \\
\dfrac{d(\omega_i \rho_i)}{dt} + \omega_i \displaystyle\sum_{j \in D_i} \omega_j 2\rho_{ij}^E (\mathbf{v}_{ij}^E - \mathbf{v}_0(\mathbf{x}_{ij}, t)) \cdot \nabla_i W_{ij} \\
+ \omega_i \displaystyle\sum_{j \in \partial D_i} \omega_j^{\partial} 2\rho_{ij}^E (\mathbf{v}_{ij}^E - \mathbf{v}_0(\mathbf{x}_{ij}, t)) \cdot \mathbf{n}_j W_{ij} = 0 \\
\dfrac{d(\omega_i \rho_i \mathbf{v}_i)}{dt} + \omega_i \displaystyle\sum_{j \in D_i} \omega_j 2[\rho_{ij}^E \mathbf{v}_{ij}^E \otimes (\mathbf{v}_{ij}^E - \mathbf{v}_0(\mathbf{x}_{ij}, t)) + p_{ij}^E] \cdot \nabla_i W_{ij} \\
+ \omega_i \displaystyle\sum_{j \in \partial D_i} \omega_j^{\partial} 2[\rho_{ij}^E \mathbf{v}_{ij}^E \otimes (\mathbf{v}_{ij}^E - \mathbf{v}_0(\mathbf{x}_{ij}, t)) + p_{ij}^E] \cdot \mathbf{n}_j W_{ij} = \omega_i \mathbf{S}_{ei} \\
\dfrac{d(\omega_i \rho_i E_i)}{dt} + \omega_i \displaystyle\sum_{j \in D_i} \omega_j 2[\rho_{ij}^E E_{ij}^E (\mathbf{v}_{ij}^E - \mathbf{v}_0(\mathbf{x}_{ij}, t)) + p_{ij}^E \mathbf{v}_{ij}^E] \cdot \nabla_i W_{ij} \\
+ \omega_i \displaystyle\sum_{j \in \partial D_i} \omega_j^{\partial} 2[\rho_{ij}^E E_{ij}^E (\mathbf{v}_{ij}^E - \mathbf{v}_0(\mathbf{x}_{ij}, t)) + p_{ij}^E \mathbf{v}_{ij}^E] \cdot \mathbf{n}_j W_{ij} = \omega_i \mathbf{S}_{ei} \mathbf{v}_{ij}^E
\end{cases} . \tag{4.75}
$$

4.4.4 Reconstruction strategy: MUSCL

The Godunov scheme is a first order conservative scheme where the initial states of primitive variables for the Riemann solver, $\mathbf{W}_L$ and $\mathbf{W}_R$, are taken to be equal to the states of the corresponding particles, i.e. $\mathbf{W}_L = \mathbf{W}_i$ and $\mathbf{W}_R = \mathbf{W}_j$. It has been shown that this method presents numerical dissipation in the Riemann solver [62], [83]. So, a reconstruction strategy, such as MUSCL [62], has been implemented in order to reduce it.

The idea is to replace the constant approximation of the Riemann problem states by linear approximation at the midpoint between particles i and j. It means to interpolate the interface states $\mathbf{W}_L$ and $\mathbf{W}_R$ by the following expression:

$$
\begin{cases}
\mathbf{W}_L = \mathbf{W}_i + \alpha(\mathbf{W}_i, \mathbf{W}_j, \nabla_i \mathbf{W}) \nabla_i \mathbf{W} \cdot (\dfrac{\mathbf{x}_j - \mathbf{x}_i}{2}) \\
\mathbf{W}_R = \mathbf{W}_j - \alpha(\mathbf{W}_i, \mathbf{W}_j, \nabla_j \mathbf{W}) \nabla_j \mathbf{W} \cdot (\dfrac{\mathbf{x}_j - \mathbf{x}_i}{2})
\end{cases} , \tag{4.76}
$$

where the local gradients $\nabla_i \mathbf{W}$ and $\nabla_j \mathbf{W}$ are estimated following a SPH gradient approximation (Eq. 4.21) [82]. A limiter function α is needed to prevent spurius oscillations to appear at discontinuities [68]. For all the simulations presented in this work, we have used the minmod limiter.

It is to notice that the vector of primitive variables for the non-isentropic model, i.e. $\mathbf{W} = (\rho, u, p)^T$ includes an additional variable with respect to the barotropic case, i.e $\mathbf{W} = (\rho, u)^T$ ([62], [68], [83]). Hence, it is mandatory to do the reconstruction for the density, velocity and pressure.

4.5 Boundary conditions

In SPH, a particle close to the boundary of the computational domain has a kernel support truncated, so a special treatment must be done in order to deal with boundary conditions.

For solid boundaries like walls, the boundary conditions are calculated using the technique based on the work of Marongiu [62], where partial Riemann solvers on surface elements are solved. At the wall boundary, one initial state is missing, so the missing information is calculated using the fluid information. For the Stiffened Gas EOS, the fluid information includes density, pressure and velocity. For inlets and outlets boundaries, an analysis of eigenvalues is done in order to establish the fluid information required to impose the conditions. These boundary condition analyses were already presented by Marongiu [62], Li [57] and Neuhauser [68] for the Tait EOS case, but thereafter they are presented for the Stiffened Gas EOS emphasizing the differences with respect to the previous EOS.

4.5.1 Solid wall

In the SPH method, the treatment of solid wall boundary condition is a difficult subject. In the literature we can find several approaches to treat it, like the fictive particle method [66] and the ghost particle method [30]. However these methods present difficulties when handling complex geometries. In this work we treat the solid boundary conditions following the work of Marongiu (2010) [62] where partial Riemann solvers on surface elements are solved. That is suitable for complex geometries [68].

Because the fluid is assumed to be inviscid, the solid wall boundary is treated with the so-called *slip* condition, which establishes the equality of velocities in the normal direction of the solid boundary. This condition is translated into the following equation

$$(\mathbf{v}(\mathbf{x}_k, t) - \mathbf{v}_w(\mathbf{x}_k, t)) \cdot \mathbf{n}_k = 0, \tag{4.77}$$

where $\mathbf{x}_k$ denotes a point at the wall and $\mathbf{v}_w$ the velocity of the solid boundary. The purpose here is to consider partial Riemann problems on boundaries where the interface is located at the solid wall (e.g. at $\mathbf{x}_k$) [18], [62].

Partial Riemann problem

For the classical Riemann problem, we have seen that it consists in two non-linear waves associated with the eigenvalues $\lambda_1 = u - c$ and $\lambda_3 = u + c$, and a contact wave associated with the eigenvalue $\lambda_2 = u$. Then, an analysis of the characteristic fields considering the eigenvalues $\lambda_i, i = 1, 2, 3$ is developed in order to relate the state in the star region with the states in the left and the right zones (see Section about Riemann solvers 4.4.2). However, at the boundary, one initial state is missing because there is no fluid particle inside the solid. We assume that the missing state that comes from the boundary is $\mathbf{W}_R$ and the fluid state is $\mathbf{W}_L$. So, we have only one relation across the wave associated with the eigenvalue $\lambda_1 = u - c$. This is called the partial Riemann solver and its structure is given in Fig. 4.5 to be compared to Fig. 4.3.

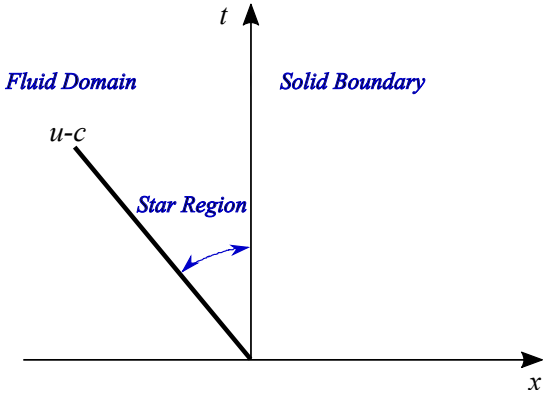

FIGURE 4.5: Structure of a one-dimensional Partial Riemann problem along a direction of observation parallel to the $x - axis$ for the Euler equations using Stiffened Gas EOS

Then, across the wave of speed $u - c$ we solve the following relation,

$$\mathbf{A}\Delta\mathbf{W} = \lambda_1 \Delta\mathbf{W}, \tag{4.78}$$

in order to calculate the solution in the star region.

Since the interface of the partial Riemann problem is located at the solid wall, the velocity of the interface, $\mathbf{v}_0(\mathbf{x}_k, t)$, is equal to the solid velocity, $\mathbf{v}_w(\mathbf{x}_k, t)$, along the normal direction $\mathbf{n}_k$, i.e. $\mathbf{v}_0(\mathbf{x}_k, t) \cdot \mathbf{n}_k = \mathbf{v}_w(\mathbf{x}_k, t) \cdot \mathbf{n}_k$. Thus, the velocity in the Star Region (u^*) from the partial Riemann solver is already known and it is the velocity of the solid wall projected on the normal direction,

$$u^* = \mathbf{v}_w \cdot \mathbf{n}_k. \tag{4.79}$$

Continuing, the solution from the partial Riemann solver is given by,

$$\begin{cases} p^* = p_L + (u_L - u^*)(\rho_L c_L) \\ \rho_L^* = \rho_L + (u_L - u^*)(\rho_L / c_L) \end{cases}, \tag{4.80}$$

where p_L, ρ_L and c_L are the pressure, density and speed of sound of the fluid particle, respectively. And u_L is the normal component of the fluid velocity, i.e. $u_L = \mathbf{v}_L \cdot \mathbf{n}_k$.

Then, the state solution useful for computing the boundary flux is given by,

$$\begin{cases} \rho_k^E = \rho_L^* \\ \mathbf{v}_k^E = \mathbf{v}_L + [u^* - \mathbf{v}_L \cdot \mathbf{n}_k] \cdot \mathbf{n}_k \\ p_k^E = p^* \\ e_k^E = \dfrac{p_k^E + \gamma_L p_{\infty L}}{\rho_k^E (\gamma_L - 1)} \end{cases}. \tag{4.81}$$

From the expressions above, we can obviously observe that the fluid and solid velocities in the normal direction are equal, i.e. $(\mathbf{v}_k^E - \mathbf{v}_w(\mathbf{x}_k, t)) \cdot \mathbf{n}_k = 0$, according to Eq. (4.77).

Subsequently, it results that $(\mathbf{v}_k^E - \mathbf{v}_0(\mathbf{x}_k, t)) \cdot \mathbf{n}_k = 0$. This cancels the convective part of the boundary flux in Eq. (4.75) and it establishes that the mass transfer between the fluid and the wall is null.

4.5.2 Inlet and outlet

In the frame of this work, we consider subsonic conditions because the fluid velocity is smaller than the speed of sound, $\|\mathbf{v}\| < c$. It is considered a 2D numerical domain where the normal vectors at the inlet and outlet point inside the fluid domain.

The Riemann problem in primitive variables in 2D is given by

$$\frac{\partial \mathbf{W}}{\partial t} + \mathbf{A}\frac{\partial \mathbf{W}}{\partial x} + \mathbf{B}\frac{\partial \mathbf{W}}{\partial y} = 0, \tag{4.82}$$

with,

$$\mathbf{W} = \begin{pmatrix} \rho \\ u \\ v \\ p \end{pmatrix}, \qquad \mathbf{A} = \begin{bmatrix} u & \rho & 0 & 0 \\ 0 & u & 0 & 1/\rho \\ 0 & 0 & u & 0 \\ 0 & \rho c^2 & 0 & u \end{bmatrix}, \qquad \mathbf{B} = \begin{bmatrix} v & \rho & 0 & 0 \\ 0 & v & 0 & 0 \\ 0 & 0 & v & 1/\rho \\ 0 & 0 & \rho c^2 & v \end{bmatrix}. \tag{4.83}$$

This system has the following four eigenvalues:

$$\begin{cases} \lambda_1 = \mathbf{v} \cdot \mathbf{n}_k - c \\ \lambda_2 = \lambda_3 = \mathbf{v} \cdot \mathbf{n}_k \\ \lambda_4 = \mathbf{v} \cdot \mathbf{n}_k + c \end{cases}, \tag{4.84}$$

where $\mathbf{n}_k$ is the unit vector in the direction of interest when considering the Riemann problem solution, which is usually chosen to be the normal vector when studying boundary conditions.

For the following analysis, it is assumed that the normal vector $\mathbf{n}_k$ for inlet and outlet boundaries lies on the $x - axis$. For inlet, $\mathbf{n}_k$ is pointing towards the positive direction of the $x - axis$, and for outlet $\mathbf{n}_k$ is pointing towards the negative direction of the $x - axis$. In consequence, the fluid velocity in the $x - direction$ is $\mathbf{v} \cdot \mathbf{n}_k = u$.

So, the eigenvalues for analyzing inlet and outlet boundary conditions are:

$$\begin{cases} \lambda_1 = \mathbf{v} \cdot \mathbf{n}_k - c = u - c \\ \lambda_2 = \lambda_3 = \mathbf{v} \cdot \mathbf{n}_k = u \\ \lambda_4 = \mathbf{v} \cdot \mathbf{n}_k + c = u + c \end{cases}. \tag{4.85}$$

At the inlet, the eigenvalues fulfill $\lambda_1 < 0 < \lambda_2 = \lambda_3 < \lambda_4$, showing three positive eigenvalues and one negative eigenvalue. The positive eigenvalues correspond to information that come in from the outside, and the negative ones correspond to information going outside of the domain. Hence, for the inlet, there are imposed three components of the vector of primitive variables $\mathbf{W}$, usually the fluid density ρ, and the two velocity components, i.e. (ρ, u, v). In contrary, the Tait EOS implementation requires two components of the primitive vector and in this case is usually imposed the two components of the velocity (u, v).

For the outlet, the eigenvalues satisfy $\lambda_1 < \lambda_2 = \lambda_3 < 0 < \lambda_4$, giving one positive eigenvalue. Hence, for the outlet, the same as for the Tait EOS case, it is usually imposed the pressure p.

4.5.3 Symmetry and periodic boundary conditions

To apply periodic and symmetry boundary conditions, SPH particles are added to complete the numerical stencil or kernel support. Physical fields of each added particle are taken equal to the physical fields from the "real" particle, excepting the velocity field for symmetry conditions. In this regard, only the velocity component in the perpendicular direction to the symmetry plane is taken in the opposite direction with respect to the "real" particle.

4.6 Time integration

The time integration scheme used is an explicit Runge-Kutta method implemented for the hyperbolic Euler system. In particular, the following schemes were implemented: Euler scheme, Heun scheme and the Runge-Kutta methods for second, third and fourth orders. They can be found in books about numerical computation, e.g. [32].

The time step is subjected to the Courant-Friedriech-Levy (CFL) condition,

$$\Delta t_{CFL} = K_{CFL} \cdot min_{i \in \Omega} \frac{h_i}{c_i + \|\mathbf{v}_i\|}, \tag{4.86}$$

where h_i, c_i, $\mathbf{v}_i$ are the smoothing length, the speed of sound and the velocity of particle i. The constant K_{CFL} is less than one for explicit schemes. Δt_{CFL} is calculated at each time step.

This condition establishes that an acoustic wave does not cross a characteristic size of the discretized domain during one time step. One consequence of this relation is that it is computationally expensive because the real physical speed of sound for water and gas must be used. In consequence, the use of the numerical speed of sound to decrease the computational cost usually employed for the barotropic simulations (i.e. using Tait EOS [68], [82]) can not be used for non-isentropic simulations (i.e. using Stiffened Gas EOS).

4.7 Correction method for the compressible SPH

It is well known that SPH has a lack of consistency due to the discretization of the kernel approximation [68]. In literature, different methods can be found to correct the kernel function and/or its gradient satisfying the consistency conditions for the particle approximation. For example we mention the Shepard correction that ensures the normalization condition [84], the renormalization that corrects the kernel gradient to increase the order of consistency of the particle approximation [80] and the work of Neuhauser [68] about a novel correction method that ensures zeroth order consistency for the computation of the divergence of the flux vector.

It is interesting to point out that the SPH method fails to satisfy the consistency conditions not only because of the discretization of the kernel approximation. Following Colagrossi [13], the particles position setting at the beginning of a numerical simulation has a crucial role in order to simulate correctly the fluid flow. Otherwise particles may resettle, causing spurious motions which can create non-physical momentum.

If the particle distribution is not adequate for the SPH operators, an error term is introduced, thus generating an artificial velocity. The error term has been defined by Neuhauser [68] as,

$$\mathbf{b}_i = \sum_{j \in Di} \omega_j \nabla_i W_{ij} + \sum_{j \in \partial Di} \omega_j^{\partial} W_{ij} \mathbf{n}_j \tag{4.87}$$

and it is called the closed box error. $\mathbf{b}_i$ should be zero according to Eq. (4.21) with $f = 1$, what is false in practical configurations.

It is found that the particles distribution is an issue especially for compressible flows with large Mach number, e.g. 0.5, as we are interested in. This could be further explained, stating that the Lagrangian displacement of a particle in a time step becomes equivalent to the transport of information to the neighborhood through acoustic waves. So, the usual particle resettlement observed in low Mach number applications can no longer "efficiently" take place for applications involving Mach number higher than 0.3.

In consequence, the ALE feature of the scheme is exploited through a specific correction of the motion of the particles. Hence, adapting the particles distribution itself using a corrected particle velocity can reduce the errors introduced by an unacceptable distribution of particles.

The main idea is, without generating an artificial fluid velocity, to use the intrinsic re-meshing capacity of SPH ([13], [68]) in order to correct the particle velocity at every time step throughout the simulation. So, we shift the particles in the adequate direction in order to improve the particles distribution. For that purpose, a pressure field is applied to all particles with,

$$\forall i \in \Omega : \quad p_{ci} = \beta \rho_i c_c^2, \tag{4.88}$$

where ρ_i is the corresponding density of each particle, c_c is the speed of sound for the correction and β is a numerical parameter. c_c is established equal to the speed of sound of the fluid in monophase simulations and, for multiphase simulations, it is established equal to the speed of sound of the heaviest fluid, ergo, the fluid having the highest speed of sound. The transport of information to the neighborhood is done following the same speed of sound for multiphase applications. When $\beta = 100$, the correction of movement behaves properly for the cases presented thereafter and it is the value used for all the cases presented in this thesis. This value of β was established by trial and error. Nevertheless additional research should be done in order to establish a link between this parameter and the flow conditions, such as the Mach number.

The pressure p_{ci} only acts on the particle velocity $\mathbf{v}_0(\mathbf{x}_i)$ and the particle position $\mathbf{x}_i$. Hence, the correction on the particle velocity is computed by

$$\left(\frac{d\mathbf{v}_0(\mathbf{x}_i)}{dt}\right)_c = \sum_{j\in D_i} \omega_j \left[\frac{p_{ci}}{\rho_i} + \frac{c_c}{2}\left(\mathbf{v}_0(\mathbf{x}_i) - \mathbf{v}_0(\mathbf{x}_j)\right)\cdot \mathbf{n}_{ij}\right]\nabla_i W_{ij} + \sum_{j\in \partial D_i} \omega_j^{\partial} \left[\frac{p_{ci}}{\rho_i} + \frac{c_c}{2}\left(\mathbf{v}_0(\mathbf{x}_i) - \mathbf{v}_0(\mathbf{x}_j)\right)\cdot \mathbf{n}_{j}\right] W_{ij}\mathbf{n}_j. \tag{4.89}$$

When Eq. (4.88) is introduced in Eq. (4.89), it is observed that the correction $\frac{p_{ci}}{\rho_i}$ is uniform and constant for all the particles.

Equation (4.89) is used to correct the particle kinematic.

For illustration purpose, we employ the Euler time integration scheme. It has been shown by Neuhauser [68] that correcting also the particle position improves the numerical results. Hence, the particle position is also corrected using the computed value from Eq. (4.89).

Then, the particle velocity is calculated as:

$$\mathbf{v}_0^{n+1}(\mathbf{x}_i) = \mathbf{v}_0^{n}(\mathbf{x}_i) - \Delta t \left(\frac{d\mathbf{v}_0(\mathbf{x}_i)}{dt}\right)_c, \tag{4.90}$$

noting that at the initial time, $\mathbf{v}_0^{n=0}(\mathbf{x}_i)$ is the initial fluid velocity, i.e. $\mathbf{v}_0^{n=0}(\mathbf{x}_i) = \mathbf{v}^{n=0}(\mathbf{x}_i)$.

And the particle position is updated as follows:

$$\mathbf{x}_i^{n+1} = \mathbf{x}_i^{n} + \mathbf{v}_0^{n}(\mathbf{x}_i)\Delta t - 0.5(\Delta t)^2 \left(\frac{d\mathbf{v}_0(\mathbf{x}_i)}{dt}\right)_c. \tag{4.91}$$

Additionally, the closed box error (Eq. 4.87) is calculated at each time step in order to verify that the ALE velocity correction is well implemented.

As a consequence of using the velocity particle correction, the time step is affected. It is reduced due to the term βc_c^2, and thus it reaches values of 10^{-10} s for multiphase cases. Of course this value depends on the particle size. The time step becomes more restrictive in cases involving smaller particle sizes. Also, it is important to mention that multiphase

simulations without correction do not behave properly because the particles distribution is not adequate and so this correction is mandatory to have satisfactory results.

4.8 Multi-phase model

The multi-phase model implemented in the frame of this work allows the simulation of flow with strong density variation without diffusion at the interface. It was taken from the work of Leduc [54] where the main idea is to cancel the mass flux between two particles associated to different fluids. To do so, the interface velocity between these two particles is chosen to be not arbitrary.

Choice of the interface velocity for the multi-phase model

In agreement with the approach of Leduc [54], in order to cancel the mass flux between two particles associated to different fluids, the interface velocity between these two particles is imposed to be equal to the velocity from the Riemann solver solution, i.e.

$$\mathbf{v}_0(\mathbf{x}_{ij}, t) = \mathbf{v}_{ij}^E. \tag{4.92}$$

In consequence and for the case involving two particles associated to different fluids, the velocity from the Riemann solver solution is substituted into the discretized system of equations (Eq. 4.75). Then, it is obtained that the mass transfer and the convective flux are zeroed.

In consequence, the interface between two different fluids is not diffused during the advance in time of the simulation.

Along with this assumption, it is used a suitable Riemann solver that takes in consideration the physical discontinuities between both fluids, as the acoustic Riemann solver presented in Section 4.4.2. For calculating the solution, this Riemann solver relies on p^* and u^*, which are continuous through the interface in absence of surface tension. In addition, it does not take into account an average state, because the solution is calculated along characteristic equations associated to each fluid (Eq. 4.57).

4.9 Validation cases

In this work we are focused on developing two phase flow simulations considering the interactions of liquid and gas.

We choose the shock tube configuration because it allows us to test the correct evolution of shock and rarefaction waves, since these waves are present in the collapse phenomenon of a non-condensable gas bubble and its correct calculation is important in the erosion estimation. First, we present a mono-phase shock tube for validation purpose of the Riemann solver for the Stiffened Gas EOS. Then, a two-phase (liquid-gas) shock tube is presented to show the capabilities of the multi-phase model in the numerical resolution of interface problems. Additionally, a comparison between the actual model in SPH (i.e. a non-isentropic model) and the previous model (i.e. a barotropic model) is presented for a mono-phase dam break case in the Appendix A.

4.9.1 Mono-phase shock tube

It is considered the monophasic shock tube test case proposed by Ivings [37]. It consists in a flow reaching a Mach number of 0.2. We consider a shock tube of unity length with a discontinuity at $x = 0.5$ separating two liquid states. Table 4.1 shows the initial left and right states data. The constant values for the Stiffened Gas EOS are $\gamma = 7.15$, $p_\infty = 300\ MPa$ and $C_v = 587\ J/(kgK)$. At $t = 0.0\ s$ both fluids are instantaneously in contact.

TABLE 4.1: Initial states for mono-phase shock tube validation case

Initial data states		
Primitive variables	*Left*	*Right*
Density [kg/m3]	1100.0	1000.0
Velocity x [m/s]	500.0	0.0
Velocity y [m/s]	0.0	0.0
Pressure [MPa]	5000.0	0.1

TABLE 4.2: Numerical parameters for mono-phase shock tube validation case

Reconstruction scheme	MUSCL
Limitor	minmod
SPH particles in the length of the domain	500

The results presented were obtained using the PVRS Riemann solver developed for the Stiffened Gas EOS (see Section 4.4.2). The numerical parameters for this validation case are shown in Table 4.2. It is mentioned that the particle distribution correction is not used because the Mach number is lower than 0.3.

Fig. 4.6 presents the spatial distribution of density, velocity, pressure and internal energy. The results are shown at time $t = 7 \cdot 10^{-5}\ s$ and consist in three conventional waves: a shock wave and a contact wave travelling to the right and a rarefaction wave going to the left. The SPH-ALE numerical solution is compared to the exact solution taken from the work of Ivings in [37] and good agreement is obtained.

Fig. 4.7 shows the temperature profile throughout the shock tube. The temperature profile is smooth and as expected the temperature and the internal energy curves have the same shape. This similarity in the shape is due to the equation of state used (i.e. the Stiffened Gas EOS). Indeed according to Eq. 3.33 and Eq. 3.45, we can write

$$T = \frac{e}{C_v} - \frac{p_\infty}{\rho C_v}. \tag{4.93}$$

So, if density does not vary significantly, the temperature curve is proportional to the internal energy curve but shifted of $\frac{p_\infty}{\rho C_v}$.

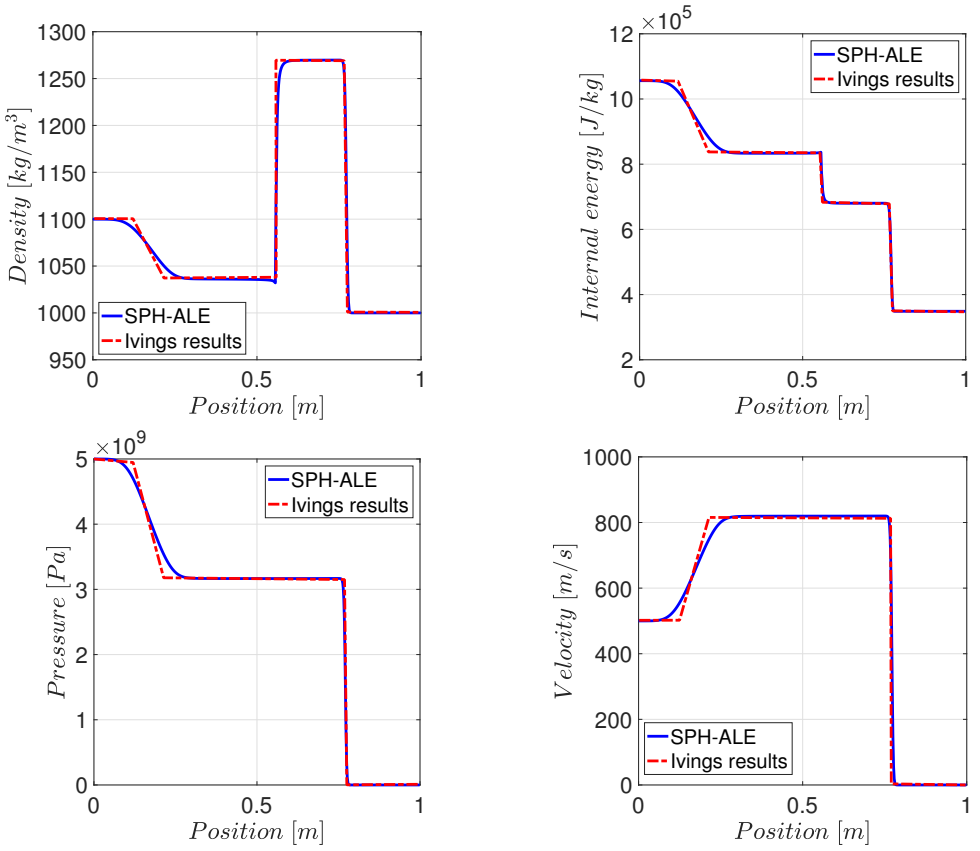

FIGURE 4.6: Shock tube test case. Flow fields in spatial distribution at $t = 7 \cdot 10^{-5}$ s. Comparison between SPH-ALE numerical results (solid lines) and the exact solution from Ivings in [37] (dashed lines)

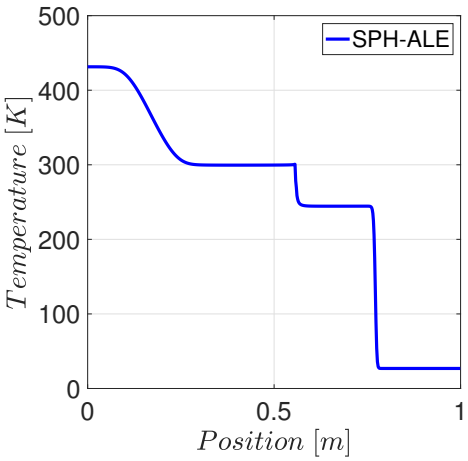

FIGURE 4.7: Shock tube test case. SPH numerical results of temperature at $t = 7{\cdot}10^{-5}$ s.

4.9.2 Multi-phase shock tube

The multiphase shock-tube test case without mass transfer presented in [91] is used for validation purpose. In this example, the left part of a shock tube is filled with liquid dodecane at high pressure and the right side is filled with vapor dodecane at atmospheric pressure. The initial discontinuity is located at $x = 0.75$ of a 1 m long tube. Table 4.3 shows the initial left and right states data. The suitable parameters for the Stiffened Gas EOS are taken from Saurel [91] and they are presented in Table 4.4.

TABLE 4.3: Initial states for multi-phase shock tube validation case

Initial data states		
	Liquid - left side	*Vapor - right side*
Density [kg/m3]	500.0	2.0
Velocity x [m/s]	0.0	0.0
Velocity y [m/s]	0.0	0.0
Pressure [MPa]	100.0	0.1

TABLE 4.4: Stiffened Gas EOS parameters for liquid and vapor dodecane

Dodecane	p_∞ $[Pa]$	C_p $[Jkg^{-1}K^{-1}]$	C_v $[Jkg^{-1}K^{-1}]$	γ
liquid	$4 \,.\, 10^8$	2534	1076	2.35
vapor	0	2005	1956	1.025

The numerical parameters for the multiphase validation case are shown in Table 4.5. Because the flow has a Mach number of 0.6 in the gas side of the tube, the particle motion correction is used imperatively in order to have a good numerical estimation of the flow fields. The results were obtained using the acoustic solver developed for the Stiffened Gas EOS (see Section 4.4.2).

TABLE 4.5: Numerical parameters for multiphase shock tube validation case

Reconstruction scheme	MUSCL
Limitor	minmod
SPH particles in the length of the domain	1000
Parameter for particle distribution correction β	100

The liquid-gas interface is solved as a contact discontinuity. At $t = 0.0\ s$ both fluids are instantaneously in contact. The results are shown at time $t = 473\ \mu s$ and consists of three conventional waves. A rarefaction wave propagates through the liquid to the left, the contact discontinuity is moving from left to right and a shock propagates through the vapor to the right.

Fig. 4.8 presents the spatial distribution of density, velocity, pressure and vapor fraction. The SPH-ALE numerical solution is compared to the one from Saurel in [91] and good agreement is observed. The model is able to reproduce the density variations in the liquid and gas sides. The velocity distribution is well described also, although the head and tail of the rarefaction wave present a smooth behavior that we could link to the numerical dissipation associated to the method. Fig. 4.8(d) shows the vapor fraction where 0 represents liquid and 1 vapor. Because we do not use a mixture model, the vapor fraction value is either 0 or 1, there are not intermediate values. This graph also presents the interface position showing very good agreement with respect to the reference solution. For validation purpose the pressure distribution is shown in Fig. 4.8(c). Likewise, it has very good agreement with the reference solution; nevertheless the pressure variations are not appreciated here. So, Fig. 4.9(a) shows the same pressure distribution in log scale. There, we observe the pressure changes along the shock tube; the pressure profile is very smooth even in the liquid-gas interface, where normally the numerical problems are located. The Mach number calculated in each fluid along the shock tube is plotted in Fig. 4.9(b). We observe the maximal value in the gas side, i.e. $Ma = 0.62$, specifically for the gas particles that are close to the liquid ones, which represent the gas particles that suffer compression.

Fig. 4.10 shows the temperature profile throughout the multiphase shock tube. The temperature profile is smooth in the liquid and gas side. However a discontinuity at the liquid-gas interface is observed. This discontinuity is due to the density discontinuity also observed through the interface and to the fluid parameters (i.e. γ and p_∞) that are different for each fluid. It is important to highlight that the pressure and velocity profiles trough the interface are smooth and continuous. So, in multiphase simulations, there is a pressure equilibrium between both fluids, but there is a discontinuity in the temperature profile trough the liquid-gas interface.

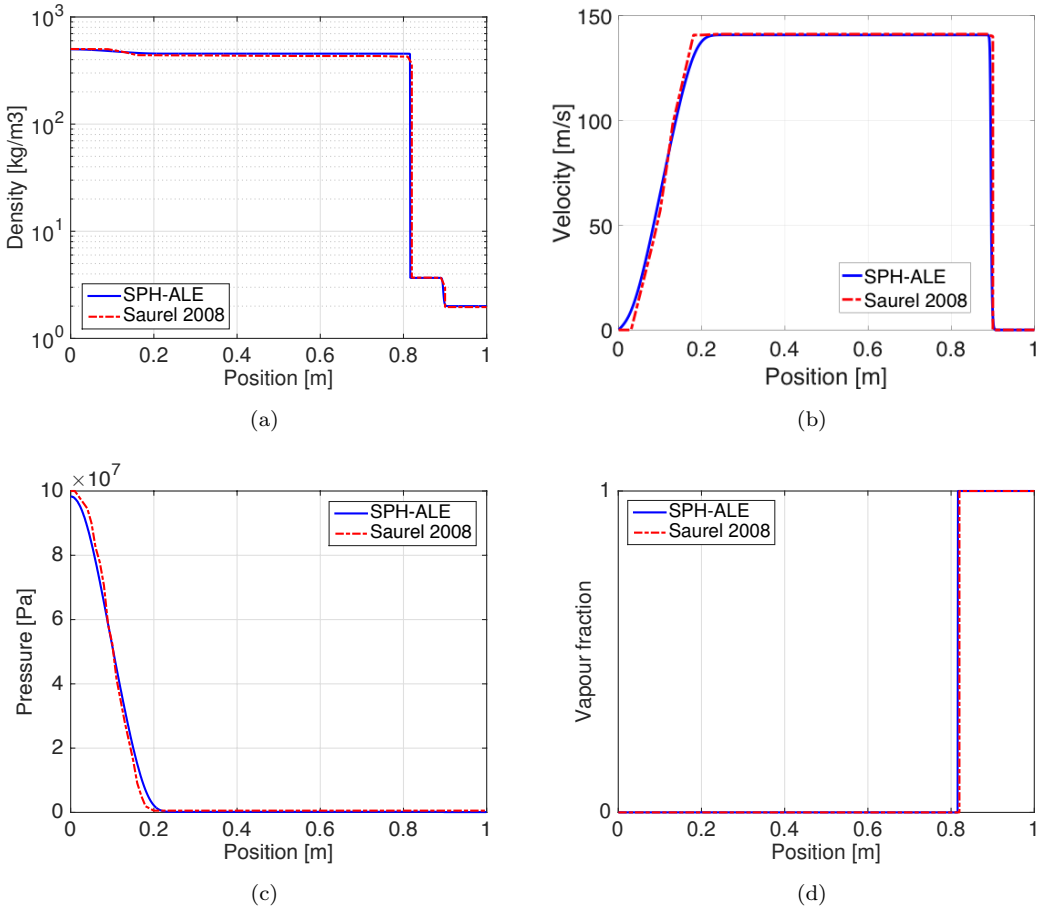

FIGURE 4.8: Multiphase shock tube test case. Numerical results in spatial distribution at $t = 473\ \mu s$. Comparison between SPH-ALE results (solid line) and results from Saurel in [91] (dashed lines)

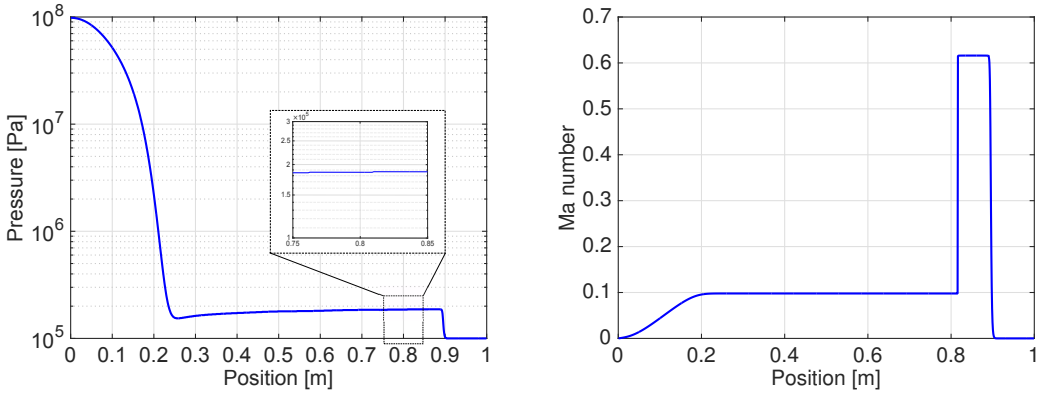

(a) Pressure vs. position in log scale, with a zoom around the interface position showing the continuity and smoothness of the solution

(b) Mach number vs. position

FIGURE 4.9: Multiphase shock tube test case. SPH numerical results at $t = 473\ \mu s$. Pressure in log scale and Mach number

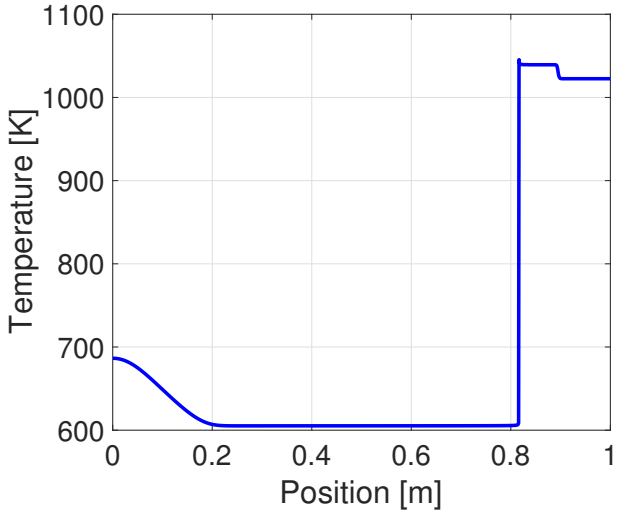

FIGURE 4.10: Multiphase shock tube test case. SPH numerical results of temperature at $t = 473\ \mu s$.

4.10 Conclusion

Since the fluid flow is assumed inviscid and the heat transfer is not considered, this section has addressed the Euler system and the numerical method used to solve it. It is the SPH-ALE, a mesh-less numerical method widely used to model weakly-compressible flows. In this regard, some modifications have been done in order to make SPH-ALE suitable to simulate compressible flows. Firstly, we have considered the energy equation among the Euler system, and in consequence it is involved another variable, such as the internal energy. This additional variable affects the calculation of fluxes (i.e. Riemann solvers) and the reconstruction strategy (i.e. the MUSCL approach). Regarding the flux calculation, two Riemann solvers were implemented and validated for compressible flows. One of them is the acoustic Riemann solver, which is specially developed for multiphase flows. On this subject, it has been presented the use of a particular velocity for solving the Riemann solver between particles of different fluids (e.g. liquid and gas) in order to cancel the mass flux between them, and thus to guarantee no diffusion of the interface.

As well, it has been presented that the particles distribution resettlement does not efficiently work anymore for compressible flows. For that reason, a correction strategy is implemented through the ALE particle velocity. It exploits the ALE feature of the method to improve the particles distribution, which is crucial for flows of large Mach number, e.g. 0.5.

To summarize, in order to simulate the collapse of a non-condensable gas bubble in liquid, it is solved the Euler equations, i.e. conservation of mass, momentum and energy equations. For that, it is used the compressible SPH-ALE method, considering the acoustic Riemann solver to model multiphase flows, the particle velocity correction for compressible flows and the MUSCL reconstruction to improve the accuracy of the numerical results and to reduce the numerical diffusion.

Chapter 5

Simulation of the collapse of a non-condensable gas bubble

The dynamics of a non-condensable gas bubble during compression in a free field is studied and compared against the analytic solution from Rayleigh-Plesset equation (Eq. 2.17 considering only non-condensable gas inside the bubble and neglecting viscosity and surface tension effects) in order to show the capabilities of the numerical model to represent the bubble collapse phenomenon. Then, the dynamics and the loading caused by the bubble collapse near a surface is analyzed and characterized.

5.1 General considerations about simulations of non-condensable gas bubble compression

This section is intended to present the general considerations applied to all simulations about the collapse of a non-condensable gas bubble, i.e. simulations in free field and near a solid boundary (rigid and non rigid).

Particularly, for all the numerical simulations, it is considered the following assumptions:

- The bubble contains only non-condensable gas;
- the bubble pressure is initially smaller than the uniform pressure of the surroundings;
- the collapse starts from the bubble's maximum radius, i.e. the initial condition corresponds to the maximum radius of the bubble.

Additionally, the calculations were carried out following a two dimensional approach due to computational cost issues. As it was explained in Section 2.1.2.2, the pressure field is qualitatively comparable between the 3D and 2D descriptions. As well, the fluid dynamics is well represented by the 2D simplification.

5.1.1 Physical considerations on the compression of a non-condensable gas bubble

As explained in Chapter 3, the gas inside the bubble is modeled as ideal gas and the liquid as water following the Stiffened Gas EOS. The dynamics of gas and liquid phases are modeled using compressible multiphase flows, in which the two fluids are assumed immiscible. Then, following Chapter 2, surface tension and phase change are not expected to affect significantly the bubble dynamics during the compression phase and are therefore neglected. Additionally, body forces are ignored. The appropriate parameters for the equation of state are taken from Saurel [91] and are shown in Table 5.1.

TABLE 5.1: Stiffened Gas EOS parameters for water and gas

	$p_\infty\ [Pa]$	$C_p\ [Jkg^{-1}K^{-1}]$	$C_v\ [Jkg^{-1}K^{-1}]$	γ
water	$1 \cdot 10^9$	4267	1816	2.35
gas	0	1487	1040	1.43

Since the fluid components are considered immiscible, there is no mixture and the meshless feature of the SPH-ALE method is exploited to model sharp interfaces. Each SPH particle contains the information associated to one fluid phase, i.e. there are particles representing only the water and particles that represent only the non-condensable gas.

The collapse is driven by the pressure ratio between the liquid (p_w) and the gas (p_b). The subscripts w and b denote water and gas respectively. The bubble pressure is set initially as atmospheric (i.e. $1 \cdot 10^5\ [Pa]$). So, this quantity (i.e. $\frac{p_w}{p_b}$) will be used to characterize each simulated case.

The initial water density (ρ_w), the initial speed of sound on the water (c_w) and the initial bubble radius (R_0) are used to non-dimensionalize the variables. From the equation of motion we have the following non-dimensional groups: x/R_0, y/R_0, z/R_0, u/c_w, v/c_w, w/c_w, $p/(\rho_w c_w^2)$, $t(c_w/R_0)$ and from the problem description we can add p_w/p_b.

The initial conditions used for all the simulations about the compression of a non-condensable gas bubble are presented in Table 5.2. It is highlighted the initial pressure for water, its value is used to characterized each simulation, so the initial pressure for water will be mentioned for each simulation. On the other hand, the initial bubble radius presented in Table 5.2 is used for most of the simulations, but in cases where this initial value does not correspond to the one displayed, the new value will be explicitly mentioned.

TABLE 5.2: Initial conditions for simulations of the compression of a non-condensable gas bubble

	$p_{initial}\ [Pa]$	$\mathbf{v}_{initial}\ [m/s]$	$\rho_{initial}\ [kgm^{-3}]$	$R_0[mm]$
water	$*$	0	1000	-
gas	$1 \cdot 10^5$	0	1	$10**$

$*$ this value will be given in the set up of each simulation
$**$ this value is used for most of the cases and when exception, the new value will be mentioned

In the next section, it is analyzed the influence on the numerical results of the particle refining, the reconstruction strategies (i.e. Godunov and MUSCL) and the kernel length variation. Precisely, it is about changing the kernel size of particles when the particle size varies. This situation can be encountered along the simulation when the gas particles have reduced their volume due to the compression effect. This volume reduction is more important on gas particles than on water particles. So, the variation of the kernel size may not be the same for gas and water particles and this may cause instabilities.

5.1.2 Numerical considerations on simulations about the compression of a non-condensable gas bubble

For all the bubble collapse simulations, a numerical limit is estimated in order to guarantee that the SPH particles represent accurately the bubble, especially in the last stages of compression. This limit is established at 5 times the initial SPH particle size. This means that the minimum bubble radius corresponds to 5 times the initial SPH particle size. In percentage, the allowed minimum radius corresponds to 12.5% of the initial radius.

Numerical techniques to reduce the numerical dissipation

To reduce the numerical dissipation, it is usually used the refining technique. In meshless methods, this technique is addressed by the discretization of the computational domain introducing more and more particles. For these simulations, the particle refining is addressed as the number of particles in the bubble radius, i.e. more particles in the bubble radius indicates more particles in the whole numerical domain, and thus a better refining. However, the computational cost is a drawback of this technique. Another technique used to reduce the numerical dissipation is the implementation of reconstruction methods, like the MUSCL method, which was implemented to improve the results obtained by the Godunov scheme.

Figure 5.1(a) shows the history of the bubble volume until the bubble achieves the minimum volume, for different amount of SPH particles in the bubble radius (i.e. 20 and 40) and two reconstruction strategies (Godunov and MUSCL). The bubble volume is calculated by summing the volume in each gas particle. As expected, the bubble volume tends to converge in a global sense as the amount of particles in the radius increases and for the reconstruction method of higher order, i.e. MUSCL method.

In conclusion, for the numerical simulations of the bubble collapse, it is chosen to use the MUSCL method and 40 SPH particles in the bubble radius, satisfying good discretization of the numerical domain, a reduction of numerical dissipation and an acceptable computational cost.

Kernel size variation

It has been presented in Section 4.3.3 that the kernel size (h) allows controlling the amount of neighbor particles used in the interpolation. So, its possible variation along the simulation may have an influence on the numerical results.

When the initial kernel length of each SPH particle is maintained constant during the entire time of the simulation, a minimum number of neighbor particles is guaranteed. It corresponds to the amount of neighbor particles at the beginning. Otherwise, when the kernel length varies along the simulation, the amount of neighbor particles may change. Then, we may find a situation where a particle is having less or more neighbors than another particle. We may think that a gas particle would have fewer neighbors than a liquid particle, because its kernel becomes smaller than the one for liquid particles. However, this situation is not straightforward because the gas particle also reduces its

volume in a more important way than the liquid particle, so more gas particles may be part of the kernel.

For the case of maintaining constant the kernel size, we consider the gas and close-to-interface particles. For them, the amount of neighbor particles increases gradually with the compression of gas particles. In consequence, the interpolation inside the kernel is improved, however the CPU calculation time is raised. On contrary, allowing the kernel variation may introduce instabilities due to its frequent update. This situation is found, particularly, in the last stages of the calculation, where the gas particle has a reduced volume in comparison with the liquid particles.

To analyze this effect, it is considered the case involving the MUSCL method. Fig. 5.1(b) shows the evolution of the bubble volume. There, three simulation results are presented. To compare the kernel variation influence two simulations of 20 SPH particles in the bubble radius are considered, one allowing the kernel variation and the other one forbidding its variation. The third numerical result corresponds to the case of 40 SPH particles in the bubble radius (red dashed line) and it is presented just as a reference.

The three numerical results are very similar, but a small difference in the last stages is found for the simulation allowing the kernel variation (green dot-dashed line). This difference can be an indication of numerical dissipation, however it is not conclusive. On the other hand, for the case maintaining constant the kernel size (blue dashed line), the numerical dissipation is less marked and the curve behavior is in agreement with the less-diffusive result (red dashed line).

Although the kernel variation along the simulation does not significantly affect the numerical results of the bubble collapse, it is chosen to maintain the kernel size constant in order to have results with less numerical dissipation and to guarantee good interpolation in the interface between both fluids.

To summarize, the numerical parameters taken for all the simulations about the compression of a non-condensable gas bubble in water are shown in Table 5.3.

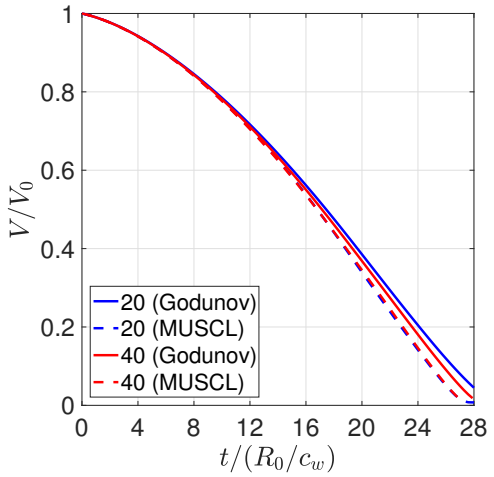

(a) History of the bubble volume using two amount of SPH particles in the bubble radius (20 and 40) and two reconstruction schemes (Godunov and MUSCL)

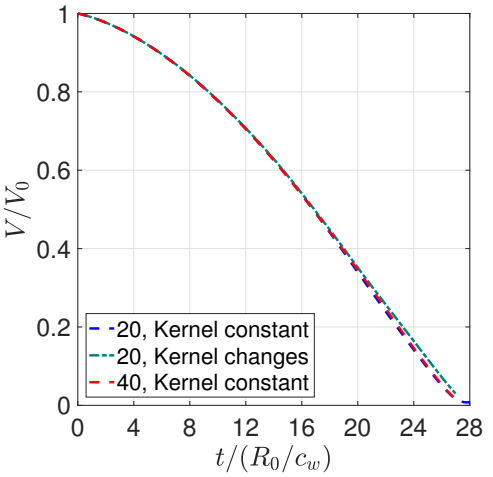

(b) History of the bubble volume using the MUSCL method, two amount of SPH particles in the bubble radius (20 and 40) and allowing the kernel variation

FIGURE 5.1: History of the bubble volume for free-field collapse ($p_w/p_b = 100$)

TABLE 5.3: Numerical parameters for simulations of a non-condensable gas bubble in water

Reconstruction scheme	MUSCL
Limitor	minmod
SPH particles in the bubble radius	40
Parameter for particle distribution correction β	100

Kernel size is constant throughout the whole simulation.

5.2 Compression of a non-condensable gas bubble in free field

The compression of a non-condensable gas bubble in free field corresponds to the collapse driven by the ratio between the water pressure and the one inside the bubble. This problem is the classical example of the bubble collapse and occurs in most cavitation situations [40].

The known *Rayleigh collapse* (already presented in Chapter 2) makes reference to the symmetric collapse of an empty cavity in an infinite-incompressible-irrotational field [40]. Because of its resemblances with the bubble collapse in free field, a comparison of our numerical results is made with respect to the analytic solution of the *Rayleigh collapse*.

5.2.1 Simulation description about the non-condensable gas bubble compression in free field

The set-up problem consists in a square where the two-dimensional bubble of initial radius R_0 is located at the center. The square side is 40 times the bubble radius R_0, in order to guarantee that the possible wave reflections on domain boundaries do not influence the region of interest (close to the bubble) throughout the whole time period covered by the simulations. In addition, boundary conditions are set periodic.

Figure 5.2 shows the scheme of the computational domain, noting that it is not at scale.

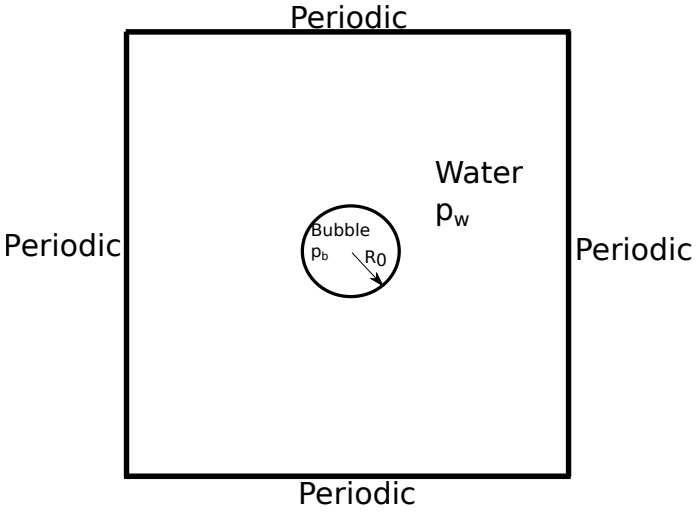

FIGURE 5.2: Scheme of the computation domain for free-field simulations. Not at scale

The collapse is driven by the pressure ratio between the liquid (p_w) and the non-condensable gas (p_b). For this section, two cases linked to two pressure ratios are considered, i.e. $p_w/p_b = 100$, which is a pressure ratio usually taken in the literature ([45], [43]) and $p_w/p_b = 353$, which corresponds to lithotripsy conditions [39] and it is chosen for comparison purpose.

5.2.2 Rayleigh collapse comparison

Since the numerical simulations are set-up in two dimensions, the comparison against theanalytical solution of the 2D Rayleigh-Plesset equation (Eq. 2.17), considering that the bubble is filled only with non-condensable gas and ignoring viscous and surface tension effects, is done.

It is reminded that R_∞ is the distance at which the velocity in the fluid has dropped to zero. In the following numerical simulations, R_∞ is identified with the computational domain boundaries. The bubble is located in the center and the limits of the computational domain are situated at 20 times its radius, so $R_\infty = 20R_0$.

Special attention is taken in terms of initial conditions in order to correctly compare the Rayleigh problem and the one simulated. In the simulations, at the beginning, both fluids are at rest and the movement is caused by the pressure difference between the gas and liquid, leading to a Riemann problem at the interface. Hence, for the numerical results, the initial velocity corresponds to the velocity of the Riemann problem at the interface liquid-gas, i.e. u^*, which is calculated from the Eq. (4.58). Following this idea, the 2D Rayleigh equation is integrated using u^* as the initial velocity, and R_0 as the initial bubble radius.

Figure 5.3 shows the behavior of the bubble radius R and the interface velocity $\dot{R}$ (i.e. the derivative of the bubble radius) as a function of time. The radius is non-dimensionalized with respect to R_0 and the time with respect to t_c, which is the analytic Rayleigh collapse time obtained after solving Eq. (2.17). The bubble radius is calculated from the bubble volume, which has been determined by summing the volume in each gas particle. In terms of physical assumptions, the liquid compressibility is taken into account for the numerical solution. In contrary, it is not considered in the Rayleigh model (Eq. 2.17).

Figure 5.3 shows good agreement between the analytic and numerical results. The difference in the last stages may be attributed to the liquid compressibility assumptions. It is known from Fuster [27] that the liquid compressibility causes a delay in the bubble collapse, particularly for collapses of high intensity (e.g. $\frac{p_w}{p_b} = 100$), like the one simulated. Similarly as Fuster et al., we found a difference of 5% between the collapse time estimated by the Rayleigh-Plesset model and the one calculated by our compressible model.

In conclusion, we can say that the compressible SPH-ALE method predicts satisfactorily the bubble collapse of high intensity.

5.2.3 Evolution of the non-condensable gas bubble compression

The behavior of the free-field collapse is represented qualitatively in Fig. 5.4. The phenomenon is started by a pressure difference between the liquid and the non-condensable gas, where the liquid pressure is higher than the one of gas. This pressure difference

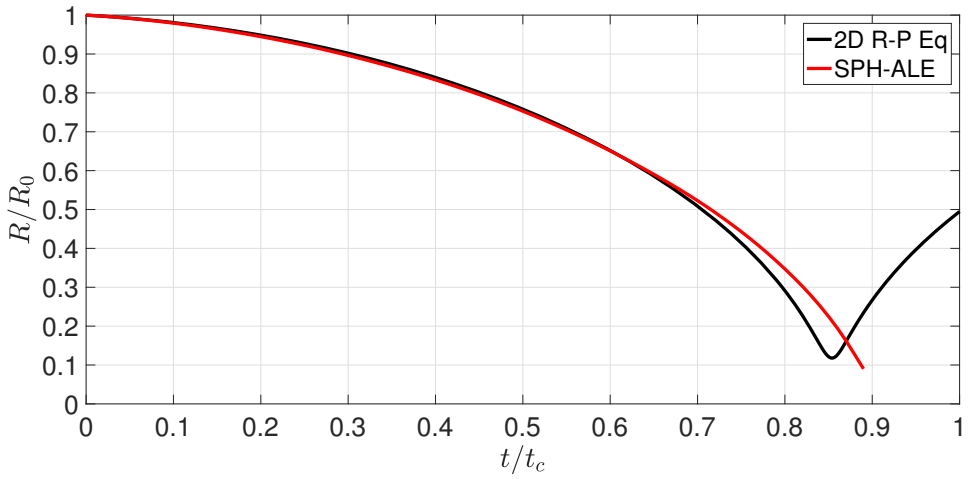

FIGURE 5.3: Comparison between numerical and analytic results of the Rayleigh collapse in free-field ($p_w/p_b = 100$). (a) Non-dimensional radius vs. non-dimensional time. t_c is the analytic Rayleigh collapse time determined from the 2D Rayleigh-Plesset equation (Eq. 2.17)

leads to a Riemann problem across the interface. A shock wave converges in the bubble and an expansion wave travels inside the liquid. This Riemann problem is found during the first instants of the non-condensable gas bubble compression, the velocity of the liquid-gas interface increases and the liquid pressure near the non-condensable gas bubble decreases. Then over the final stages of compression, another phenomenon is observed. As the bubble radius decreases, the liquid pressure close to the interface increases. This pressure behavior can be explained as the result of the conservation of the liquid volume that tends to concentrate liquid motion into a smaller region. Continuously, the bubble volume decreases until collapse.

The temperature field along with the interface contour are presented in Fig. 5.5. As explained in Section 4.9.2, it is observed a discontinuity in the temperature through the liquid-gas interface during the whole compression phenomenon, which is due to the difference in fluid properties, i.e. both fluids have different densities and different specific heats. It is observed that water temperature does not significantly vary during the bubble compression. However the non-condensable gas temperature notably increases in the last stages of compression due to the high pressure levels that the bubble attains.

In the last stages of compression the bubble shape does not remain circular. This could be the consequence of numerical or physical instabilities. In terms of the physical instabilities for this type of problems, it is found the Taylor instabilities, which are short-wave instabilities of the Hadamard type [41]. They are found particularly when

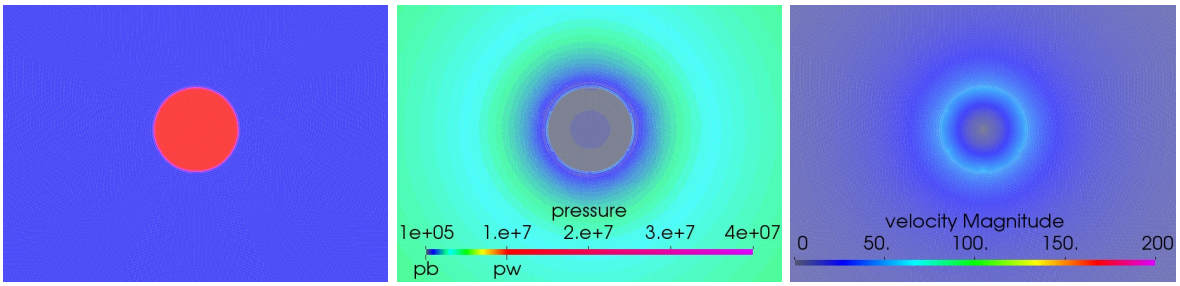

(a) Interface, $t/(R_0/c_w) = 16$ (b) Pressure (Pa), $t/(R_0/c_w) = 16$ (c) Velocity (m/s), $t/(R_0/c_w) = 16$

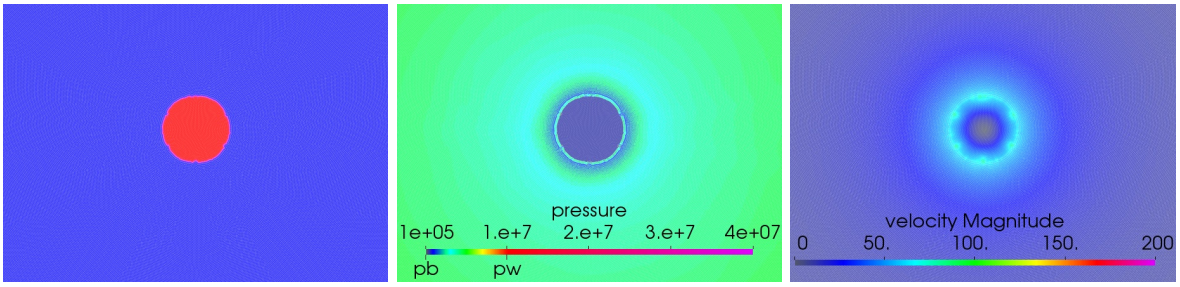

(d) Interface, $t/(R_0/c_w) = 20$ (e) Pressure (Pa), $t/(R_0/c_w) = 20$ (f) Velocity (m/s), $t/(R_0/c_w) = 20$

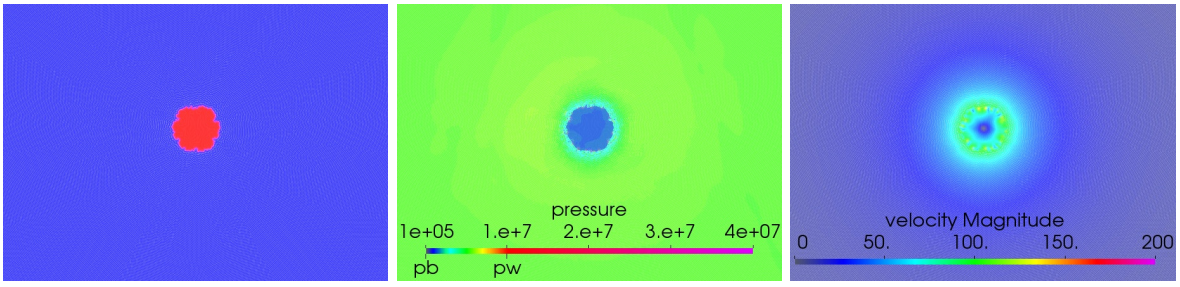

(g) Interface, $t/(R_0/c_w) = 24$ (h) Pressure (Pa), $t/(R_0/c_w) = 24$ (i) Velocity (m/s), $t/(R_0/c_w) = 24$

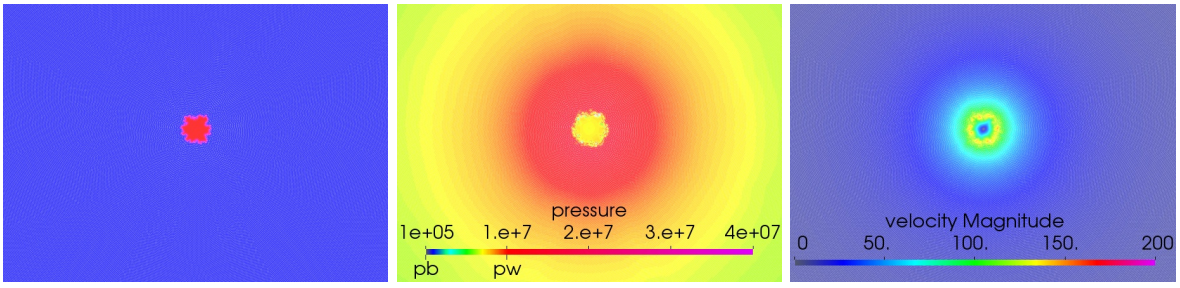

(j) Interface, $t/(R_0/c_w) = 26$ (k) Pressure (Pa), $t/(R_0/c_w) = 26$ (l) Velocity (m/s), $t/(R_0/c_w) = 26$

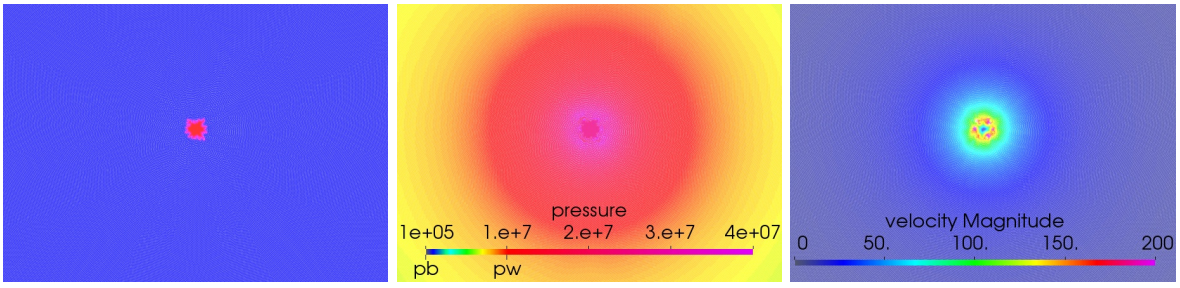

(m) Interface, $t/(R_0/c_w) = 26.8$ (n) Pressure (Pa), $t/(R_0/c_w) = 26.8$ (o) Velocity (m/s), $t/(R_0/c_w) = 26.8$

FIGURE 5.4: Evolution of free field collapse ($p_w/p_b = 100$). At times: (a),(b) and (c) $t/(R_0/c_w) = 16$; (d),(e) and (f) $t/(R_0/c_w) = 20$; (g),(h) and (i) $t/(R_0/c_w) = 24$; (j), (k) and (l) $t/(R_0/c_w) = 26$; (m), (n) and (o) $t/(R_0/c_w) = 26.8$. Left: interface contour (red: gas, blue: liquid), center: pressure, right: velocity

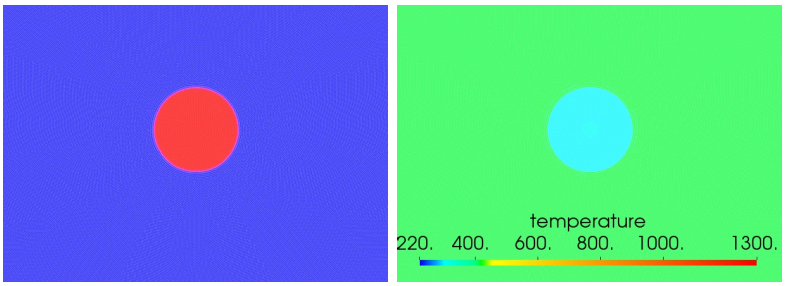

(a) Interface, $t/(R_0/c_w) = 16$

(b) Temperature (K), $t/(R_0/c_w) = 16$

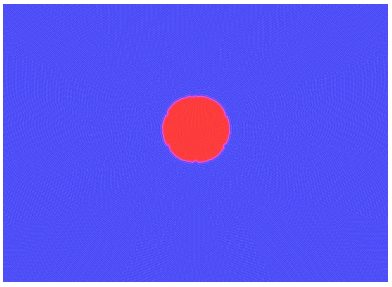

(c) Interface, $t/(R_0/c_w) = 20$

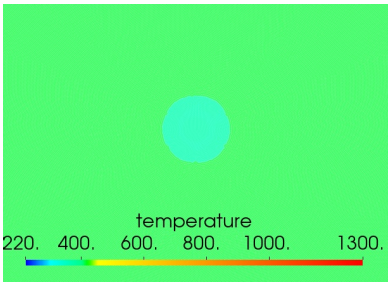

(d) Temperature (K), $t/(R_0/c_w) = 20$

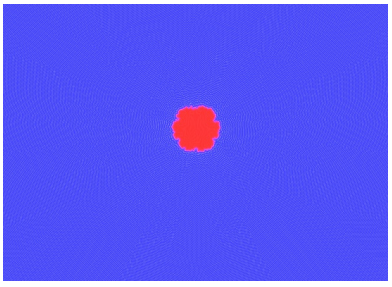

(e) Interface, $t/(R_0/c_w) = 24$

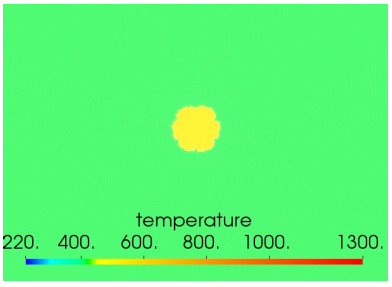

(f) Temperature (K), $t/(R_0/c_w) = 24$

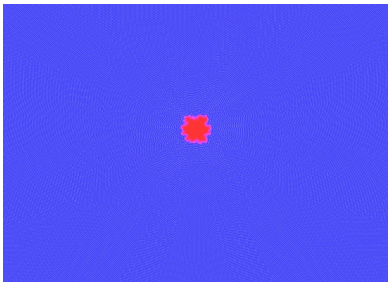

(g) Interface, $t/(R_0/c_w) = 26$

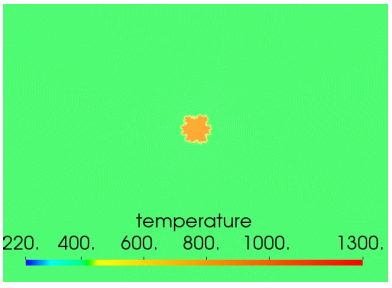

(h) Temperature (K), $t/(R_0/c_w) = 26$

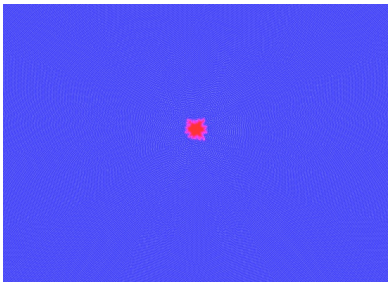

(i) Interface, $t/(R_0/c_w) = 26.8$

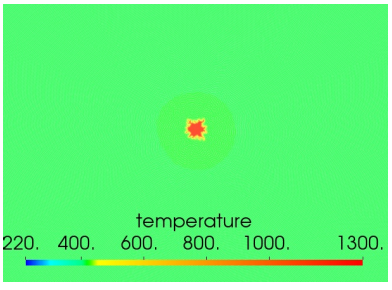

(j) Temperature (K), $t/(R_0/c_w) = 26.8$

FIGURE 5.5: Evolution of free field collapse ($p_w/p_b = 100$). At times: (a),(b) and (c) $t/(R_0/c_w) = 16$; (d),(e) and (f) $t/(R_0/c_w) = 20$; (g),(h) and (i) $t/(R_0/c_w) = 24$; (j), (k) and (l) $t/(R_0/c_w) = 26$; (m), (n) and (o) $t/(R_0/c_w) = 26.8$. Left: interface contour (red: gas, blue: liquid), right: temperature

collapsing bubbles reach the minimum radius [40], [41]. On the other hand, numerical instabilities can be present when diffusive effects like surface tension are neglected [41]. Since we do not considered the surface tension effects and the liquid SPH particles located on the interface are relatively large for the bubble size found in the last stages of collapse, we can assume that our numerical results present numerical instabilities at this stage. They are observed only in the case of free-field collapse, because it is in this case where the bubble achieves such a small size. Using an adaptive refining method for SPH-ALE, where the refining is done around the liquid-gas interface, could solve this issue. Actually, smaller SPH particles can help improving the simulations because they allow going down to smaller limit bubble sizes (see Section 5.1.2).

For this case of $p_w/p_b = 100$, the relation between both dimensionless times (i.e. t_c and R_0/c_w) is given by $\frac{t_c}{(R_0/c_w)} = 27.1$.

Fig. 5.6 represents the evolution of geometrical features of the collapsing bubble. It shows the history of the bubble volume V/V_0, the bubble circularity and the displacement of the bubble centroid X_C with respect to its initial position X_0. The centroid (X_C) is calculated as the arithmetic mean (i.e. average) position of all SPH particles located at the interface liquid-gas.

A quantitative measure of the bubble circularity is given by the ratio of the radius calculated from the volume V and the average radius calculated from the position of each particle located on the interface, i.e.

$$circularity = \frac{radius\ calculated\ from\ volume}{2 \times (average\ radius)}. \tag{5.1}$$

A value of 0.5 corresponds to a bubble whose interface is not deformed, while a value of zero indicates that the bubble interface is highly deformed.

In agreement with a symmetric phenomenon, the bubble displacement is null and the liquid-gas interface during the collapse remains circular. It is important to mention that the simulations are done without imposing the symmetry condition. This shows that the numerical method represents well the symmetric feature of the phenomenon without additional conditions, and so this highlights its robustness.

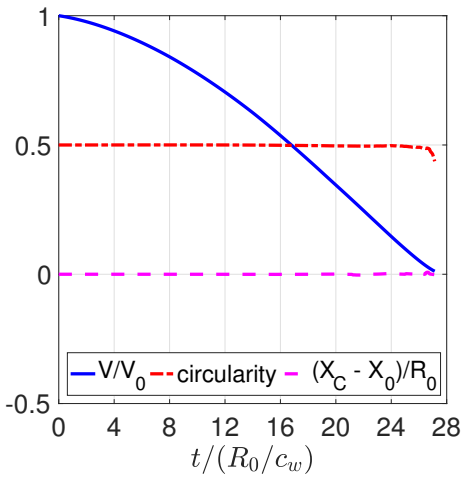

FIGURE 5.6: Rayleigh collapse in free-field ($p_w/p_b = 100$). History of the normalized volume V/V_0 (blue solid line), circularity (red dashed-dotted line) and displacement $(X_C - X_0)/R_0$ (magenta dashed line).

5.2.4 Pressure field

Fig. 5.7 shows the pressure as a function of the radial coordinate at different times. For verification purpose, three different radial lines were taken, these lines can be seen as horizontal, vertical and oblique. The data extracted from these three lines are the same, which is congruent with the symmetry feature of this phenomenon. Fig. 5.7 shows then the pressure values extracted from the radial line placed horizontally. Each curve shows the pressure evolution inside the bubble and in the liquid phase along a radial coordinate. Then, each curve is linked to a specific time during the simulation, i.e. each curve represents the pressure distribution along a radial coordinate for a given instant, and thus for a given bubble radius.

The pressure profile is uniform when r/R_0 is close to zero. This part corresponds to the pressure inside the bubble. Then, the pressure profile changes abruptly, increasing its value. This part corresponds to the pressure in the liquid phase. It is observed that the bubble pressure also increases with time due to the compression.

As explained before, during the final stages of bubble compression, the velocity and pressure at the interface increase because of the concentration of liquid motion into a small region. As a consequence the liquid pressure near the bubble rises and eventually becomes higher than the pressure far away from the bubble. This high pressure behavior has been also presented when analyzing the analytic model in 2D and 3D configurations, see Section 2.1.2.2.

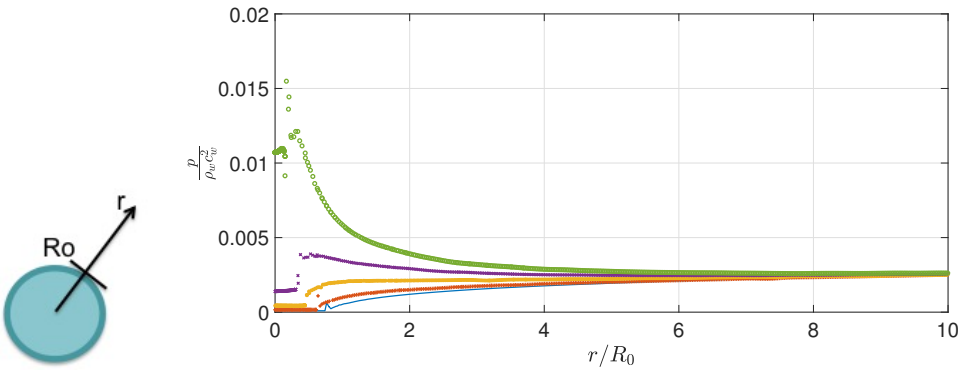

(a) (b)

FIGURE 5.7: Pressure profile along a radial coordinate at different times, for free field collapse ($p_w/p_b = 100$). At times: blue $t/(R_0/c_w) = 15$; red $t/(R_0/c_w) = 18.75$; yellow $t/(R_0/c_w) = 22.5$; violet $t/(R_0/c_w) = 24.75$; green $t/(R_0/c_w) = 26.25$. (a) scheme and representation of the radial coordinate; (b) pressure as a function of radial coordinate

5.2.5 Pressure and velocity at the interface

Figures 5.8 and 5.9 show the evolution of the velocity and the pressure at the interface in order to better understand the local details during the compression. These two quantities (i.e. velocity and pressure) are calculated as the average among the SPH particles, that model the liquid, located at the interface. The standard deviation is also presented in the figures as a shaded envelop around the main curve, showing that the data points tend to be close to the mean value and so, the dispersion of the numerical results is low.

In general, the interface moves towards the bubble center. The velocity interface increases with time, presenting acceleration in the final instants of the bubble compression (e.g. after $t/(R_0/c_w) \approx 20$ and after $t/(R_0/c_w) \approx 10$ for $p_w/p_b = 100$ and $p_w/p_b = 353$, respectively). Later, the velocity presents a maximum value. After this velocity peak, the interface decelerates and the bubble undergoes the collapse.

Respecting the continuity of pressure at the interface, it is first observed the wave expansion effects, so the pressure value goes down. Then, the inter-facial pressure slowly increases until it reaches a value higher than the pressure far away from the bubble (e.g. at $t/(R_0/c_w) \approx 26$ and at $t/(R_0/c_w) \approx 12.5$ for $p_w/p_b = 100$ and $p_w/p_b = 353$, respectively). Finally, the pressure at the interface greatly increases until the bubble collapses. It is noted that the liquid concentration into a region creates an increase of pressure. If we consider the divergence of the transport velocity of liquid particles, it

is negative, so their volume decreases, and because the mass remains constant, their pressure increases.

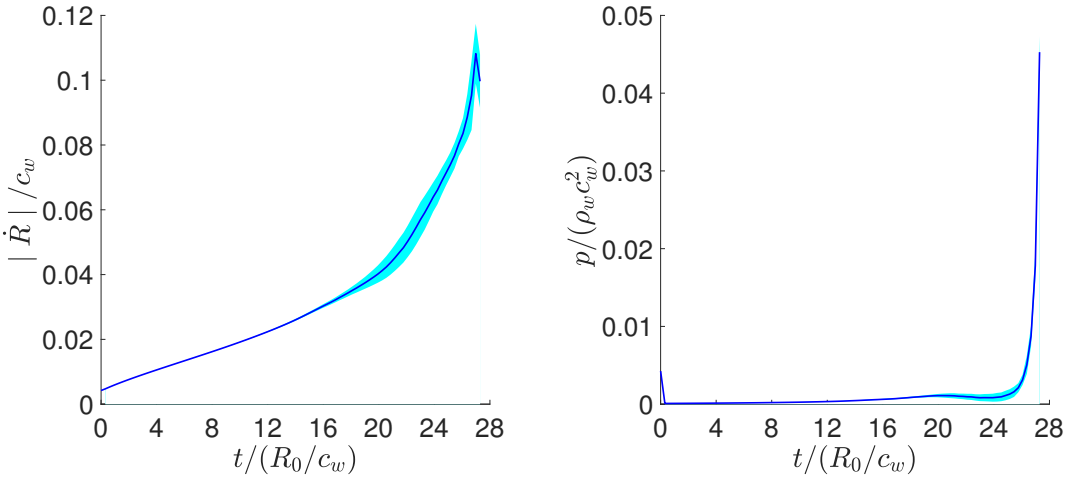

FIGURE 5.8: Rayleigh collapse in free-field ($p_w/p_b = 100$). History of the velocity and pressure at the interface. (a) velocity at the interface, (b) pressure at the interface. The standard deviation is shown by the shaded area

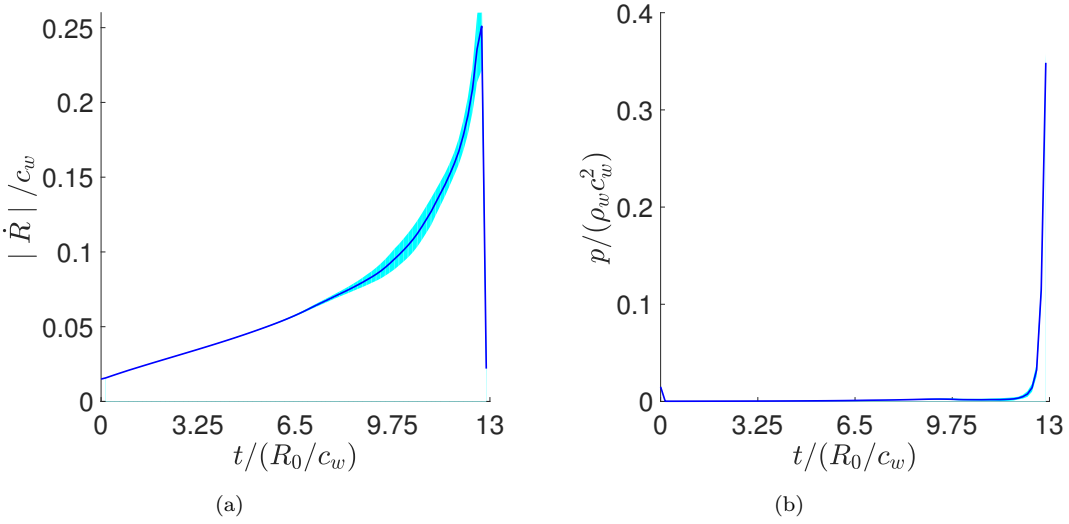

FIGURE 5.9: Rayleigh collapse in free-field ($p_w/p_b = 353$). History of the velocity and pressure at the interface. (a) velocity at the interface, (b) pressure at the interface. The standard deviation is shown by the shaded area

Regarding the collapse time, it depends on the pressure ratio driving the collapse [3] and it is observed that the phenomenon is faster for the case of larger pressure ratio. Additionally, it can be observed in Fig. 5.10 that the collapse time estimated in the numerical simulations and the analytic Rayleigh-Plesset collapse time are in agreement. It is to notice that the analytic equation (Eq. 2.17) is solved considering that there is only non-condensable gas inside the bubble and neglecting the surface tension and

viscous effects. The difference between simulated and analytic results is attributed to the physical considerations followed in our simulation that are not present in the analytic model, i.e. liquid compressibility, as already explained in Section 5.2.2.

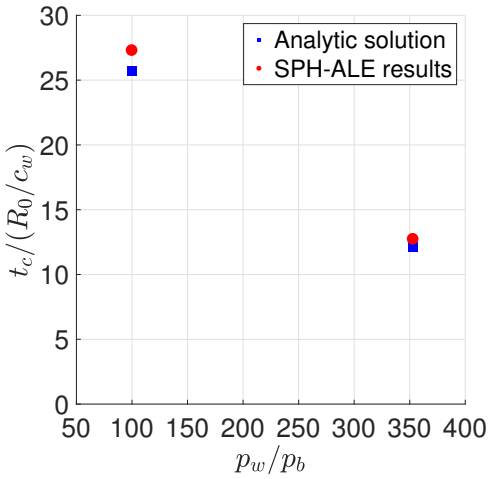

FIGURE 5.10: Collapse time for free field collapse. Squares: analytic solution from the 2D Rayleigh equation, Circles: SPH-ALE numerical results

5.2.6 Comparison against numerical results

With the idea of comparing our results and estimating a link between 2D and 3D solutions, a comparison against the axisymmetric numerical results of Johnsen and Colonius (2009) [40] is presented. These authors use a mesh method with a high order interface-capturing WENO scheme. Both numerical simulations present the same pressure ratio, $p_w/p_b = 353$.

Fig. 5.11 shows that the overall behavior of the bubble volume evolution is similar in both cases. The bubble remains symmetric and it does not move with respect to its initial centroid position. So, from a qualitative point of view, the 2D simulations allow us to capture and to understand correctly the bubble dynamics. However, they overestimate the bubble collapse time. For the same pressure ratio, this effect was addressed through the simplified model presented in Section 2.1.2.2. The collapse time is shorter when considering three-dimensional effects, which is reasonable. Therefore, the bubble collapse will occur faster than in the 2D simulations.

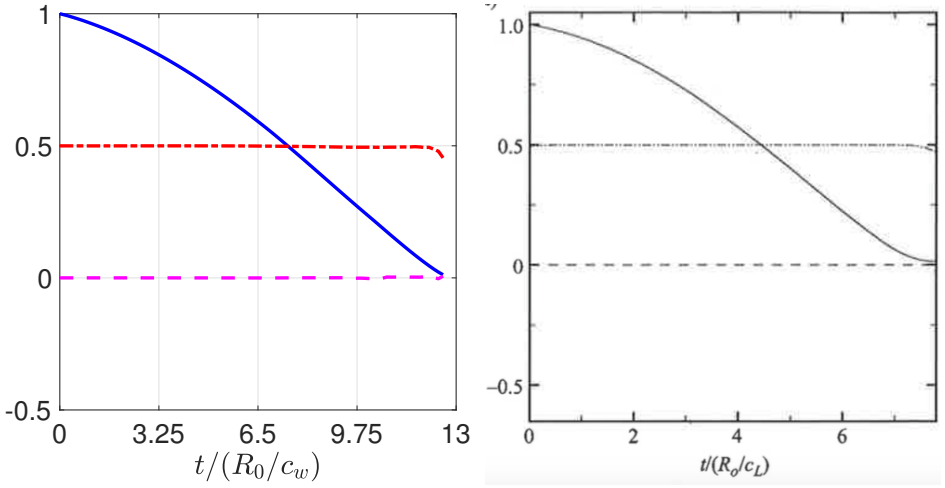

(a) SPH-ALE Numerical results in 2D

(b) Axisymmetric numerical results from Johnsen and Colonius [40]

FIGURE 5.11: Rayleigh collapse in free-field ($p_w/p_b = 353$). (a) SPH-ALE Numerical results in 2D, history of the normalized volume V/V_0 (blue solid line), circularity (red dashed-dotted line) and displacement $(X_C - X_0)/R_0$ (magenta dashed line). (b) Axisymmetric numerical results from [40], history of the normalized volume V/V_0 (solid line), circularity (dashed-dotted line) and displacement $(X_C - X_0)/R_0$ (dashed line)

5.3 Compression of a non-condensable gas bubble near a rigid surface

The non-spherical collapse of a non-condensable gas bubble near a wall is simulated in order to study the micro jet formation, the emission of pressure waves and eventually the loading on the nearby surface. In this section, the effects of the major parameters governing the bubble collapse dynamics are presented, analyzing the effect of the initial distance between the bubble center and the wall (H_0), the bubble size (R_0), and the pressure ratio (p_w/p_b) driving the collapse.

5.3.1 Simulation description

For the collapse near a wall, the domain is rectangular whose largest side measures 50 times the bubble radius, the bottom side represents the rigid wall and the bubble is initially circular and situated close to it at a distance H_0, which is the initial distance between the bubble center and the wall. The upper side is located at 20 times the bubble radius in order to guarantee as before, that the numerical results are not influenced by the eventually reflection of waves against the boundaries. The wall is assumed rigid, so all waves are reflected there. The geometric configuration (not at scale) is shown in Fig. 5.12.

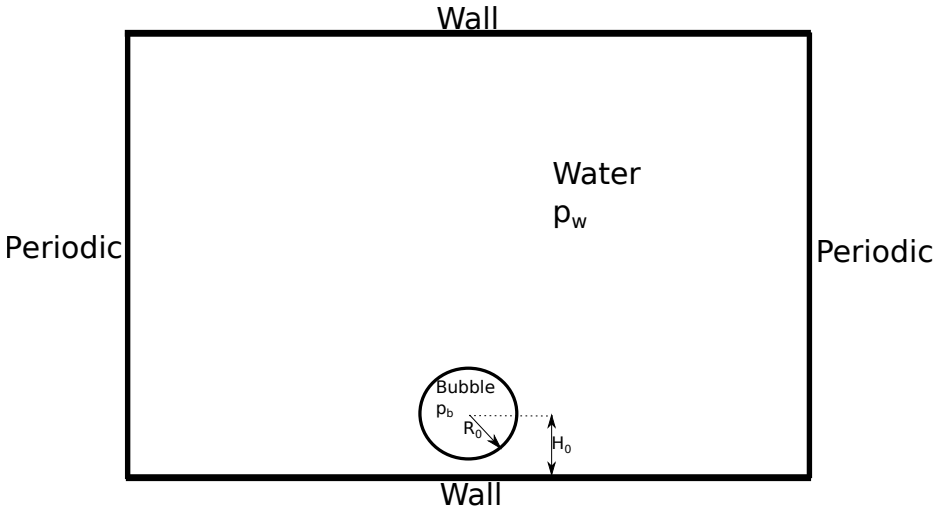

FIGURE 5.12: Scheme of the computation domain for bubble collapse near a wall case. Not at scale

The numerical simulations are conducted using the physical parameters and the assumptions already explained in Section 5.1. In short, the bubble is modeled as ideal gas and

the liquid as water, the physical parameters for the equation of state are shown in Table 5.1.

The initial standoff distance between the bubble center and the wall is non-dimensionalized with respect to the bubble radius (H_0/R_0), and it is part of the dimensionless variables of the problem, which are the same as before (see Section 5.1).

The dependence of the results to the pressure ratio that controls the collapse is investigated by considering two pressure ratios: $p_w/p_b = 34$ and $p_w/p_b = 353$. The pressure ratio of $p_w/p_b = 34$ corresponds to the cavitation conditions ($p_{atm}/p_v \approx 34$, where p_v is the saturation pressure for water at $T = 25\ ^\circ C$) and the pressure ratio of $p_w/p_b = 353$ corresponds to lithotripsy conditions [39]. The latter is done in order to compare the results from this new configuration with the results obtained in free field. In addition, the effect of the initial standoff distance is considered by varying it in the range $1.1 \leq H_0/R_0 \leq 5$, keeping R_0 constant.

5.3.2 Evolution of the non-condensable gas bubble compression near a wall

The compression of a non-condensable gas bubble near the wall starts by suddenly subjecting the bubble to a high ambient pressure. This produces a rarefaction wave that expands in the liquid. Fig. 5.13 shows a qualitative description of events; the pressure and velocity are shown, along with a representation of the interface. It illustrates the propagation of an expansion wave travelling in the liquid. The rarefaction wave reflects from the rigid wall, and then it goes towards the bubble interacting with the bubble in a complex way as the number of reflections increases. Afterwards, as the bubble is compressed due to the pressure difference, its farther side with respect to the wall flattens, thus leading to a displacement of its centroid towards the rigid surface. As the compression continues, the farther side involutes to form a micro jet. In Fig. 5.13(i) the micro jet is observed and in Fig. 5.13(l) it is completely developed. Later, when the collapse is imminent, the bubble shape is highly non-cylindrical. The numerical results presented are in agreement with previous works [40], [45], [43].

In Figures 5.13(j), 5.13(k) and 5.13(l) is observed the moment when the micro jet impacts the bubble side the closest to the wall. The high velocity present at this moment can be translated into a water-hammer pressure.

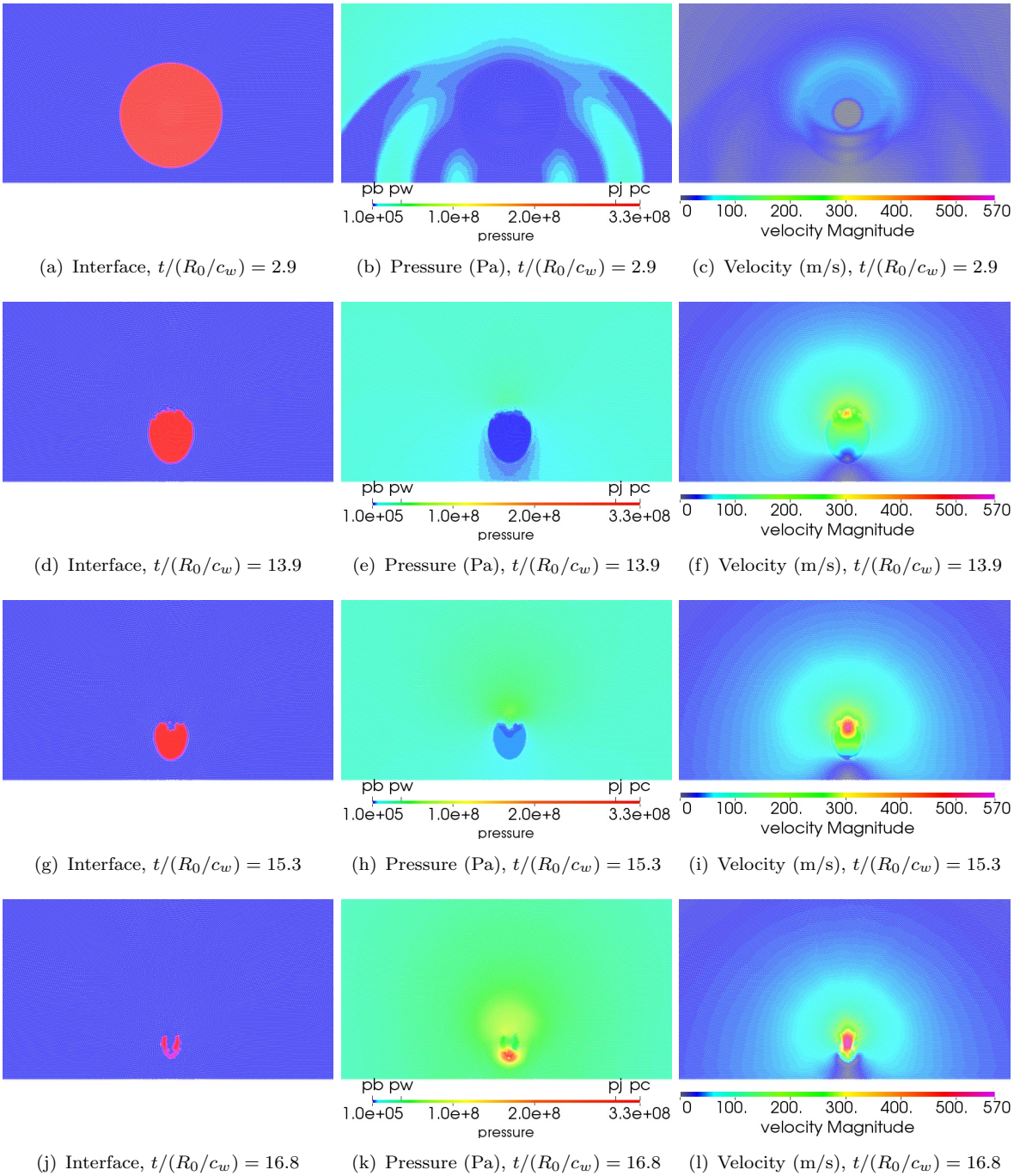

(a) Interface, $t/(R_0/c_w) = 2.9$ (b) Pressure (Pa), $t/(R_0/c_w) = 2.9$ (c) Velocity (m/s), $t/(R_0/c_w) = 2.9$

(d) Interface, $t/(R_0/c_w) = 13.9$ (e) Pressure (Pa), $t/(R_0/c_w) = 13.9$ (f) Velocity (m/s), $t/(R_0/c_w) = 13.9$

(g) Interface, $t/(R_0/c_w) = 15.3$ (h) Pressure (Pa), $t/(R_0/c_w) = 15.3$ (i) Velocity (m/s), $t/(R_0/c_w) = 15.3$

(j) Interface, $t/(R_0/c_w) = 16.8$ (k) Pressure (Pa), $t/(R_0/c_w) = 16.8$ (l) Velocity (m/s), $t/(R_0/c_w) = 16.8$

FIGURE 5.13: Evolution of collapse near a wall ($p_w/p_b = 353$ and $H_0/R_0 = 1.25$). At times: (a),(b) and (c) $t/(R_0/c_w) = 2.9$; (d),(e) and (f) $t/(R_0/c_w) = 13.9$; (g),(h) and (i) $t/(R_0/c_w) = 15.3$ (j),(k) and (l) $t/(R_0/c_w) = 16.8$. Left: interface contour (red: gas, blue: liquid), center: pressure, right: velocity

Then, Fig. 5.14 shows three close instants after the bubble is impacted by the micro jet in order to analyze what happens afterwards. Fig. 5.14(b) shows the moment when the pressure wave emitted due to the impact of the micro jet hits the wall. Fig. 5.14(e) presents the pressure wave traveling and impacting the wall. We also observed a high pressure at the bubble-liquid interface, which corresponds to the collapse of the bubble by itself. This generates a second pressure wave. Afterwards, this second pressure wave hits the wall (Fig. 5.14(h)). Hence, two pressure waves are observed, one produced by the micro jet and a second one generated by the bubble collapse.

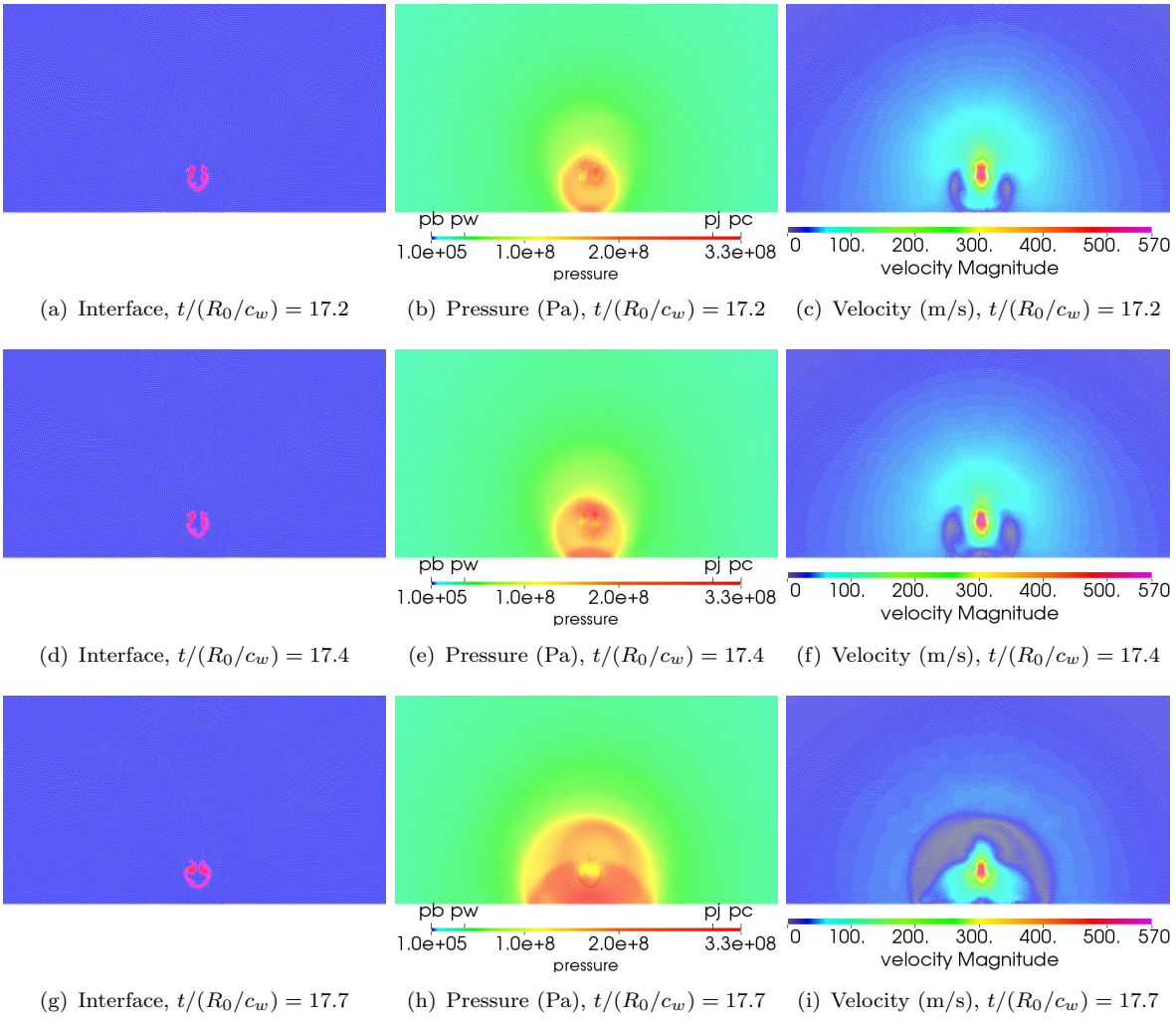

(a) Interface, $t/(R_0/c_w) = 17.2$ (b) Pressure (Pa), $t/(R_0/c_w) = 17.2$ (c) Velocity (m/s), $t/(R_0/c_w) = 17.2$

(d) Interface, $t/(R_0/c_w) = 17.4$ (e) Pressure (Pa), $t/(R_0/c_w) = 17.4$ (f) Velocity (m/s), $t/(R_0/c_w) = 17.4$

(g) Interface, $t/(R_0/c_w) = 17.7$ (h) Pressure (Pa), $t/(R_0/c_w) = 17.7$ (i) Velocity (m/s), $t/(R_0/c_w) = 17.7$

FIGURE 5.14: Evolution of collapse near a wall after the bubble collapse ($p_w/p_b = 353$ and $H_0/R_0 = 1.25$). At times: (a),(b) and (c) $t/(R_0/c_w) = 17.2$; (d),(e) and (f) $t/(R_0/c_w) = 17.4$; (g),(h) and (i) $t/(R_0/c_w) = 17.7$. Left: interface contour (red: gas, blue: liquid), center: pressure, right: velocity

The temperature field and the interface contours are represented in figures 5.15 and 5.16. Similarly as the bubble compression in free field, the water temperature does not vary significantly. On the contrary, the non-condensable gas temperature greatly increases

during the last stages of the bubble compression. The non-condensable gas temperature slightly increases during the first instants of compression (Fig. 5.15(b), 5.15(d) and 5.15(f)). Later, when the water jet is developed and hits the bottom side of the bubble, the non-condensable gas temperature greatly increases there (see Fig. 5.15(h)). As the bubble compression continues, the high temperature is distributed throughout the whole bubble as a consequence of the high pressure levels attained by the non-condensable gas as the bubble collapses (Fig. 5.16(d)).

For the case involving a pressure ratio of 353, we show an overview of the phenomenon for all the standoff distances, i.e. H_0/R_0. Fig. 5.17 shows the evolution of the normalized bubble volume, the bubble circularity and the displacement of its centroid. As a reminder, the quantitative measure of circularity indicates the interface deformity. A value of 0.5 indicates that the bubble interface is circular, while a value of 0 implies that the interface has deformed. Particular times of the phenomenon are also shown. In black vertical lines are shown the times related to the fluid flow and in red vertical lines are presented the times related to the solid reaction. From the bubble dynamics we highlight the time when the jet impacts the bubble (left most black vertical line) and the time when the bubble collapses (right most black vertical line). From the solid side, we show the time when the solid wall is impacted by the first pressure wave (left most red vertical line) and the time when the wall is hit by the second pressure wave (right most red vertical line).

In order to relate specific images to these instants, we take the $H_0/R_0 = 1.25$ case, which was already presented in figures 5.13 and 5.14. It is observed in Fig. 5.17(b) the four instants of interest. The left most black line corresponds to the moment when the jet impacts the bubble at $t/(R_0/c_w) = 16.8$, which correspond to figures 5.13(j), 5.13(k) and 5.13(l). The second vertical line (i.e. left most red vertical line) in Fig. 5.17(b) is linked to the moment when the solid is impacted by the pressure wave at $t/(R_0/c_w) = 17.2$; this event is observed in figures 5.14(a), 5.14(b) and 5.14(c). The third vertical line corresponds to the moment when the bubble collapses at $t/(R_0/c_w) = 17.4$; it is shown in figures 5.14(d), 5.14(e) and 5.14(f). Finally, the moment when the wall is hit by the second pressure wave is shown by the right most red line and in figures 5.14(g), 5.14(h) and 5.14(i).

It is observed for all the values of H_0/R_0 that the bubble remains circular during a certain time; then at a particular moment its shape starts to deform until to achieve its maximal non-circular shape at collapse. As seen in previous works ([40], [107], [39])

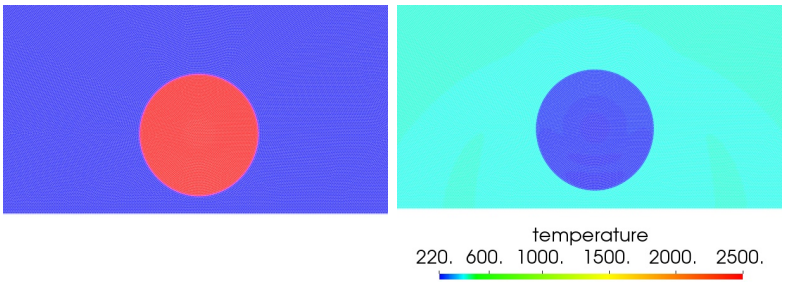

(a) Interface, $t/(R_0/c_w) = 2.9$

(b) Temperature (K) , $t/(R_0/c_w) = 2.9$

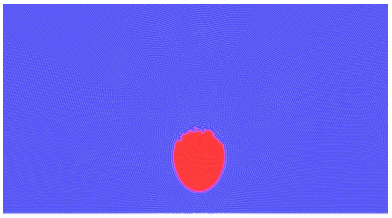

(c) interface, $t/(R_0/c_w) = 13.9$

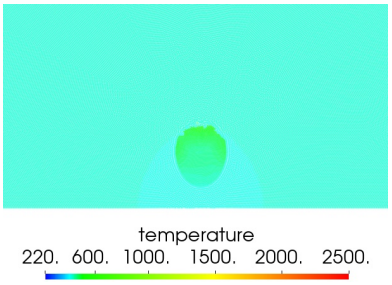

(d) Temperature (K), $t/(R_0/c_w) = 13.9$

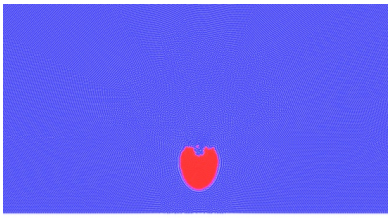

(e) interface, $t/(R_0/c_w) = 15.3$

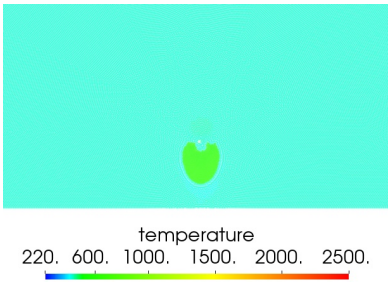

(f) Temperature (K), $t/(R_0/c_w) = 15.3$

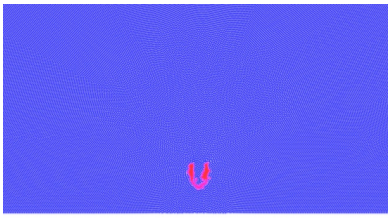

(g) interface, $t/(R_0/c_w) = 16.8$

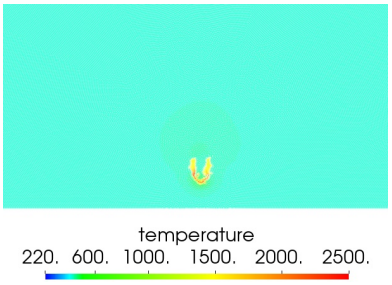

(h) Temperature (K), $t/(R_0/c_w) = 16.8$

FIGURE 5.15: Evolution of collapse near a wall ($p_w/p_b = 353$ and $H_0/R_0 = 1.25$). At times: (a),(b) and (c) $t/(R_0/c_w) = 2.9$; (d),(e) and (f) $t/(R_0/c_w) = 13.9$; (g),(h) and (i) $t/(R_0/c_w) = 15.3$ (j),(k) and (l) $t/(R_0/c_w) = 16.8$. Left: interface contour (red: gas, blue: liquid), right: temperature

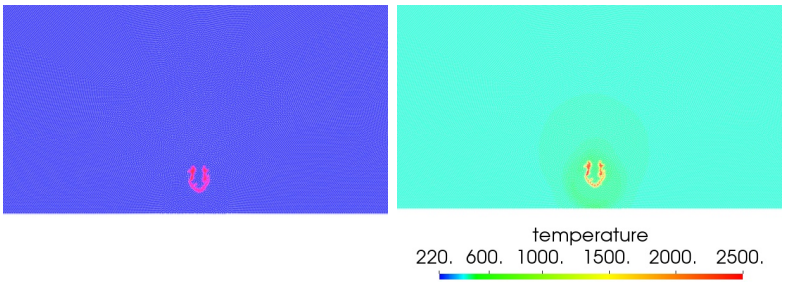

(a) Interface, $t/(R_0/c_w) = 17.2$ (b) Temperature (K), $t/(R_0/c_w) = 17.2$

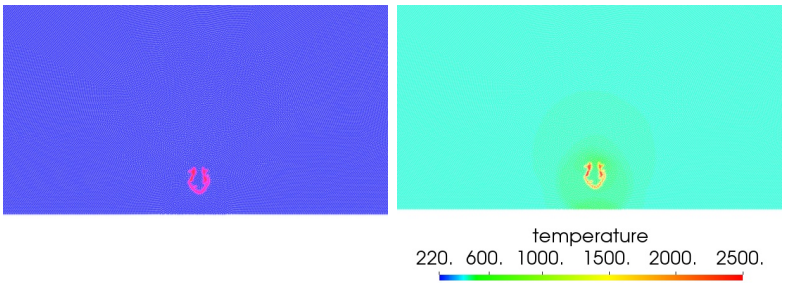

(c) Interface, $t/(R_0/c_w) = 17.4$ (d) Temperature (K), $t/(R_0/c_w) = 17.4$

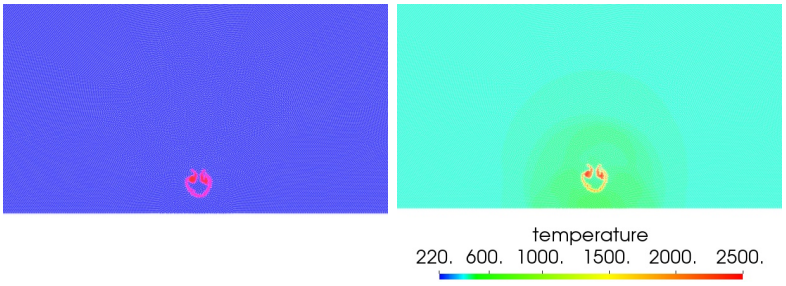

(e) Interface, $t/(R_0/c_w) = 17.7$ (f) Temperature (K), $t/(R_0/c_w) = 17.7$

FIGURE 5.16: Evolution of collapse near a wall after the bubble collapse ($p_w/p_b = 353$ and $H_0/R_0 = 1.25$). At times: (a),(b) and (c) $t/(R_0/c_w) = 17.2$; (d),(e) and (f) $t/(R_0/c_w) = 17.4$; (g),(h) and (i) $t/(R_0/c_w) = 17.7$. Left: interface contour (red: gas, blue: liquid), right: temperature

the bubble migrates towards the wall ($X_C - X_0 < 0$). Evidently, the bubble volume decreases during the compression until to achieve the minimum volume at collapse.

Two bubble dynamics are observed. For the standoff distances between $1.1 \leq H_0/R_0 \leq 1.85$, the bubble dynamics presents two events generating high pressure peaks, firstly the moment when the jet impacts the bubble and secondly the moment when the bubble collapses. These two events produce two pressure peaks on the solid wall (i.e. two red vertical lines in Fig. 5.17). On the other hand, for cases of $H_0/R_0 \geq 2$, only one high-pressure-peak event is registered, producing only one pressure peak on the solid surface. This phenomenon could be explained considering the standoff distance. As the standoff distance increases, the difference between the bubble collapse time and the time

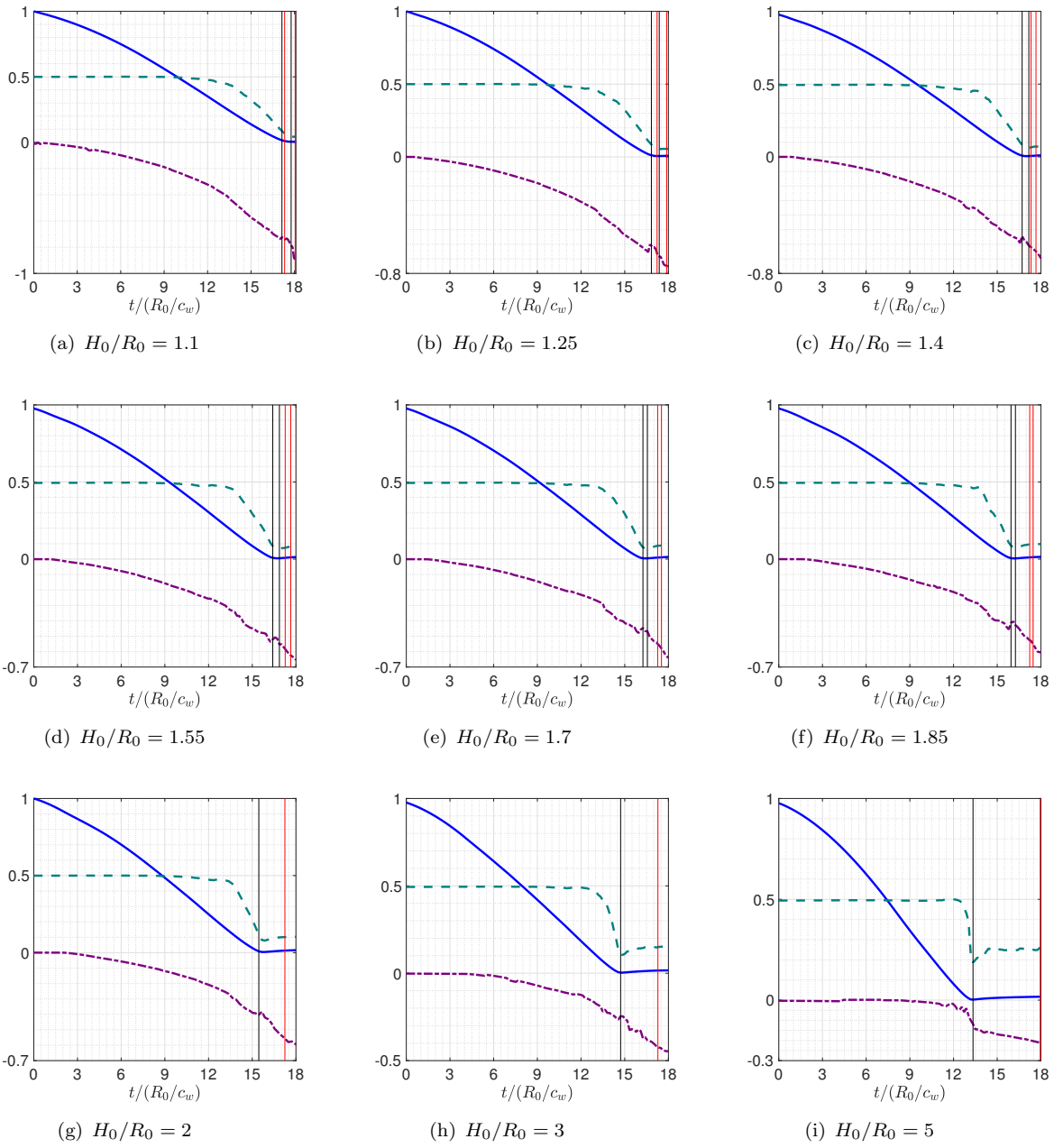

(a) $H_0/R_0 = 1.1$ (b) $H_0/R_0 = 1.25$ (c) $H_0/R_0 = 1.4$

(d) $H_0/R_0 = 1.55$ (e) $H_0/R_0 = 1.7$ (f) $H_0/R_0 = 1.85$

(g) $H_0/R_0 = 2$ (h) $H_0/R_0 = 3$ (i) $H_0/R_0 = 5$

FIGURE 5.17: History of the normalized volume V/V_0 (blue solid line), circularity (green dashed line) and displacement $(X_C - X_0)/R_0$ (violet dashed-dotted line) of collapse near a wall for $p_w/p_b = 353$. Jet impact time (first black vertical line), bubble collapse time (second black vertical line), pressure peaks on the wall (two red vertical lines)

when the micro jet hits the bubble is shorter (see the shift between the two black vertical lines in Fig. 5.17). Hence, both wave emissions are getting closer until the moment when both waves are emitted at the same time. Thus, only one pressure wave impacts the wall. For the particular case of $H_0/R_0 = 5$, a micro jet is not even clearly observed, what indicates that the influence of the wall in the collapse is not so important anymore, so the bubble collapses by itself and it does not experiences the micro jet phenomenon.

The difference between the time of the bubble collapse and the one of the jet impact is presented in Fig 5.18 in order to support this explanation. The case $H_0/R_0 = 5$ is excluded from this figure because the micro jet is not clearly observed.

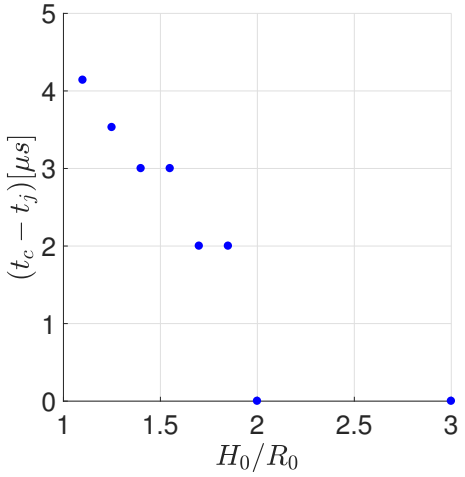

FIGURE 5.18: Difference between the jet impacting time and the collapse time for case of $p_w/p_b = 353$ and $1.1 \leq H_0/R_0 \leq 3$

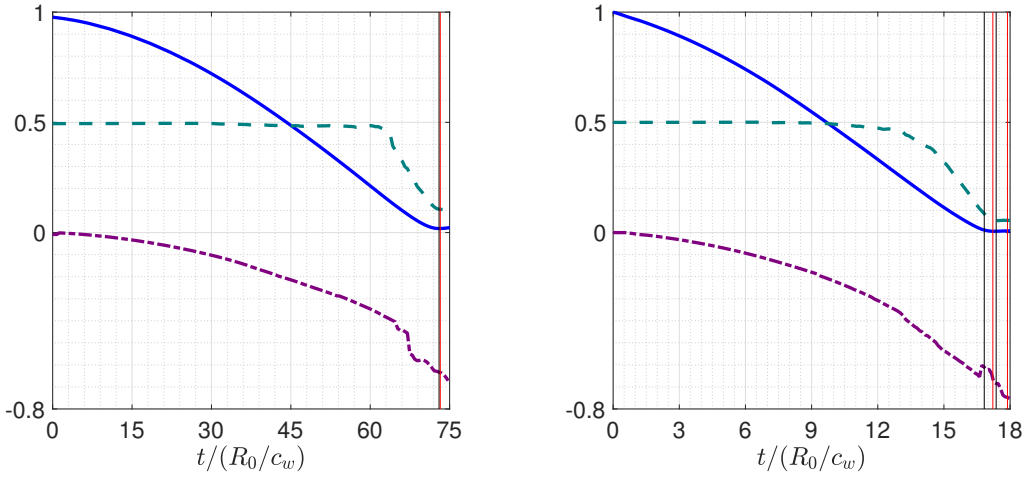

(a) $p_w/p_b = 34$ (b) $p_w/p_b = 353$

FIGURE 5.19: History of the normalized volume V/V_0 (blue solid line), circularity (green dashed line) and displacement $(X_C - X_0)/R_0$ (violet dashed-dotted line) of collapse near a wall ($H_0/R_0 = 1.25$). (a) $p_w/p_b = 34$, (b) $p_w/p_b = 353$

Additionally, the influence of the pressure ratio driving the collapse is analyzed. It is considered $p_w/p_b = 34$ and $p_w/p_b = 353$. Fig. 5.19 shows the evolution of the bubble volume, circularity and centroid displacement, as well as the four particular times (i.e. jet impact time, bubble collapse time, first and second solid impact times) for each case. It is observed that the general behavior is alike. However, the two-peaks episode is

not observed for the smaller pressure ratio (i.e. $p_w/p_b = 34$), for which only one high-pressure-peak event is observed, and consequently, only one pressure peak is recorded on the wall.

In addition, from figures 5.17 and 5.19, it is concluded that the bubble displacement towards the wall depends mainly on the standoff distance and not on the pressure ratio driving the collapse.

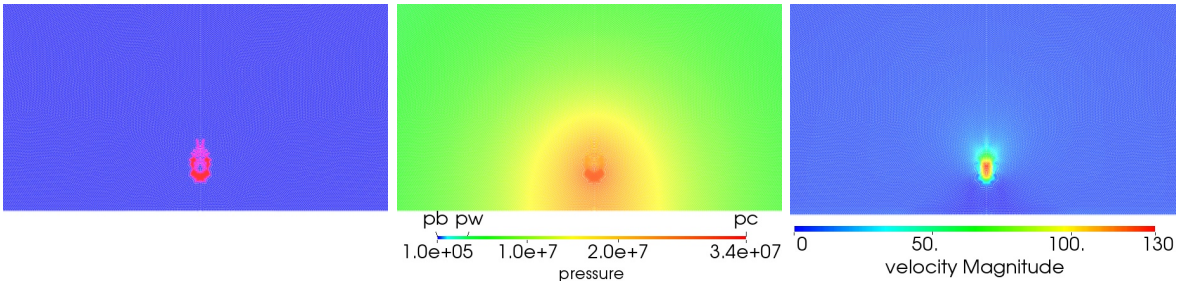

(a) interface, $t/(R_0/c_w) = 70.5$ (b) Pressure (Pa), $t/(R_0/c_w) = 70.5$ (c) Velocity (m/s), $t/(R_0/c_w) = 70.5$

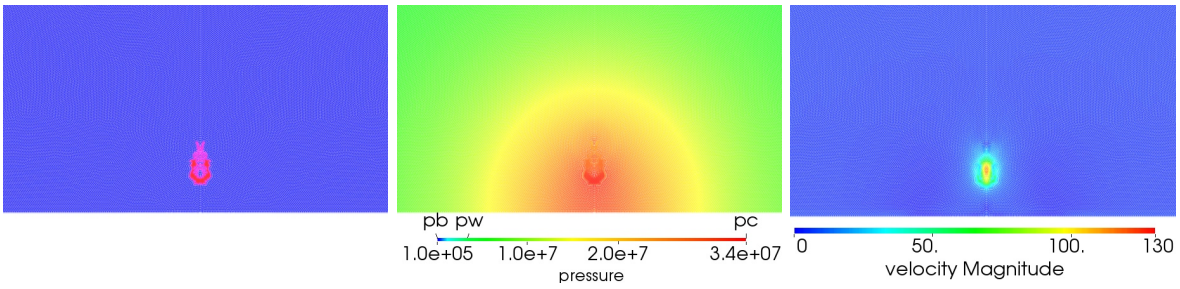

(d) interface, $t/(R_0/c_w) = 73$ (e) Pressure (Pa), $t/(R_0/c_w) = 73$ (f) Velocity (m/s), $t/(R_0/c_w) = 73$

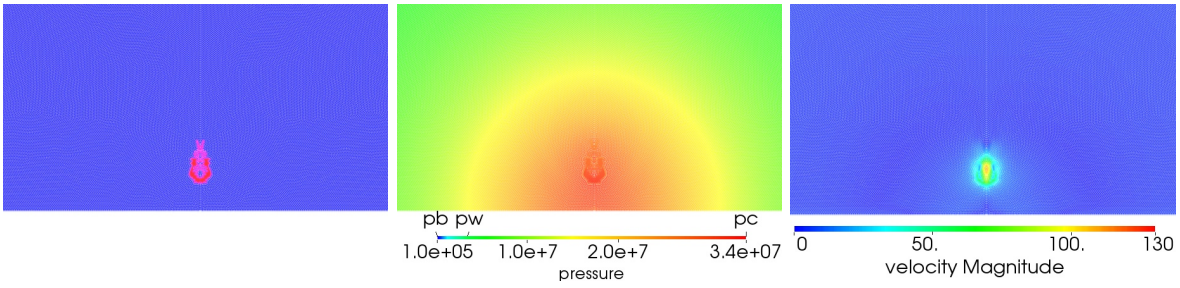

(g) interface, $t/(R_0/c_w) = 73.2$ (h) Pressure (Pa), $t/(R_0/c_w) = 73.2$ (i) Velocity (m/s), $t/(R_0/c_w) = 73.2$

FIGURE 5.20: Evolution of collapse near a wall after the bubble collapse ($p_w/p_b = 34$ and $H_0/R_0 = 1.25$). At times: (a),(b) and (c) $t/(R_0/c_w) = 70.5$; (d),(e) and (f) $t/(R_0/c_w) = 73$; (g),(h) and (i) $t/(R_0/c_w) = 73.2$. Left: interface contours (red: gas, blue: liquid), center: pressure, right: velocity

This one-pressure-peak episode is discussed following the sequence of the bubble compression for $p_w/p_b = 34$, shown in Fig. 5.20. The bubble shape becomes elongated as it is compressed, similarly to the case of higher-pressure ratio (i.e. $p_w/p_b = 353$). However, a difference in shape with respect to the case of $p_w/p_b = 353$ is observed when the micro jet is developed. The "U" shape that the bubble adopts due to the micro jet development

is less pronounced. This might be the consequence of a slower micro jet, i.e. the jet velocity is smaller than the jet velocity in the case of $p_w/p_b = 353$. Therefore, the bubble collapses by itself before the micro jet hits its bottom side. This moment happens at $t/(R_0/c_w) = 73$ and it is observed in figures 5.20(d), 5.20(e) and 5.20(f). Later, the pressure wave impacts the wall at $t/(R_0/c_w) = 73.2$ as shown in figures 5.20(g), 5.20(h) and 5.20(i). This result suggests that the intensity of the micro jet depends also on the pressure ratio that drives the collapse and not only on the standoff distance with respect to the wall.

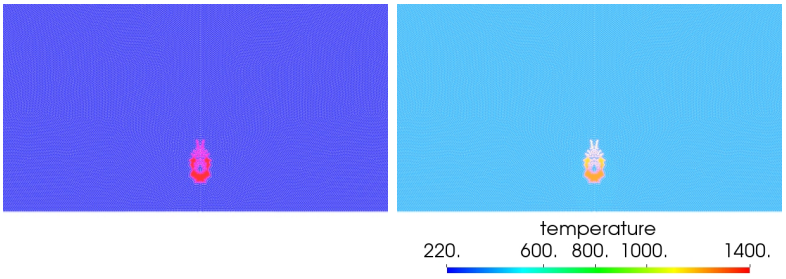

(a) interface, $t/(R_0/c_w) = 70.5$ (b) Temperature (K), $t/(R_0/c_w) = 70.5$

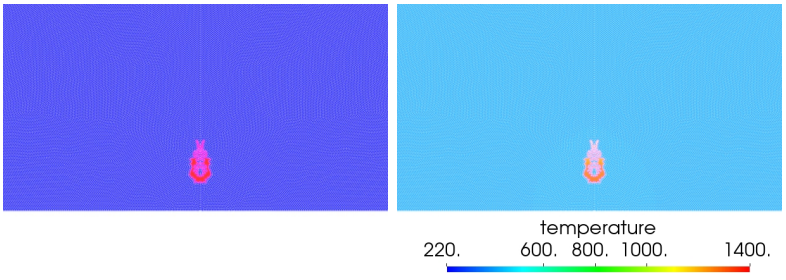

(c) interface, $t/(R_0/c_w) = 73$ (d) Temperature (K), $t/(R_0/c_w) = 73$

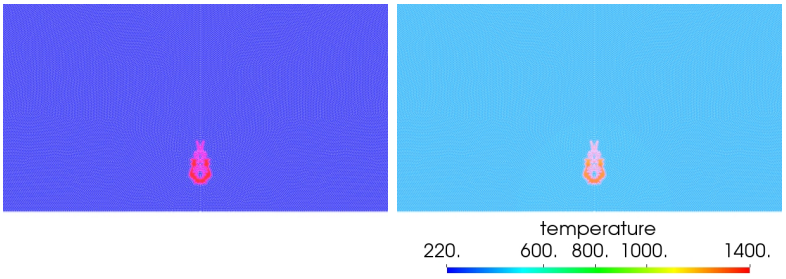

(e) interface, $t/(R_0/c_w) = 73.2$ (f) Temperature (K), $t/(R_0/c_w) = 73.2$

FIGURE 5.21: Evolution of collapse near a wall after the bubble collapse ($p_w/p_b = 34$ and $H_0/R_0 = 1.25$). At times: (a),(b) and (c) $t/(R_0/c_w) = 70.5$; (d),(e) and (f) $t/(R_0/c_w) = 73$; (g),(h) and (i) $t/(R_0/c_w) = 73.2$. Left: interface contour (red: gas, blue: liquid), right: temperature

The temperature field and the interface contours are represented in Fig. 5.21. Similarly as the case of higher pressure ratio, the non-condensable gas temperature greatly increases during the last stages of the bubble compression. When the water jet is developed and

goes through the bubble, the non-condensable gas temperature greatly increases due to the high pressure levels attained. It is important to mention that the temperature levels attained are lower than the ones attained in the case where the pressure ratio is larger ($p_w/p_b = 353$). This is another consequence of a lower initial pressure ratio and so, a slower micro jet. Therefore, for this case of $p_w/p_b = 34$, the pressure levels attained by the non-condensable gas produce a lower increment of the non-condensable gas temperature with respect the previous case (i.e. $p_w/p_b = 353$).

5.3.3 Bubble properties at collapse

Fig. 5.22(a) shows the displacement of the bubble's centroid at the moment when the micro jet impacts the lower side of the bubble, for different standoff distances. It shows that the bubble displacement depends on the wall position (i.e. H_0/R_0). This effect of attraction created by the wall is explained analyzing the flow locally. The wall creates a restriction of the fluid flow in the region between the bubble and the wall. It generates a higher pressure on the top of the bubble with respect to its bottom side, and so a pressure gradient is directed towards the wall. This pressure gradient pushes the bubble towards the wall generating its displacement. When the wall is farther from the bubble, the wall effect is less noticeable.

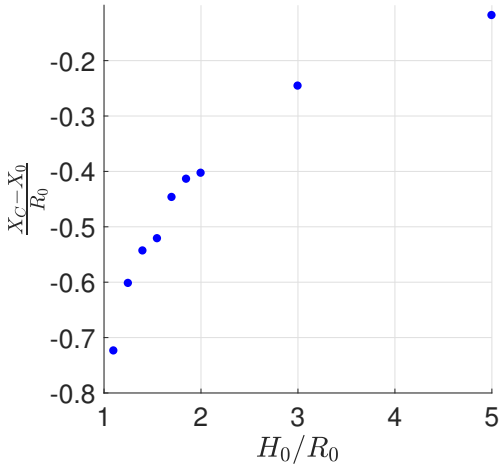

(a) Displacement of the bubble when the micro jet impacts its lower side as a function of the standoff distance

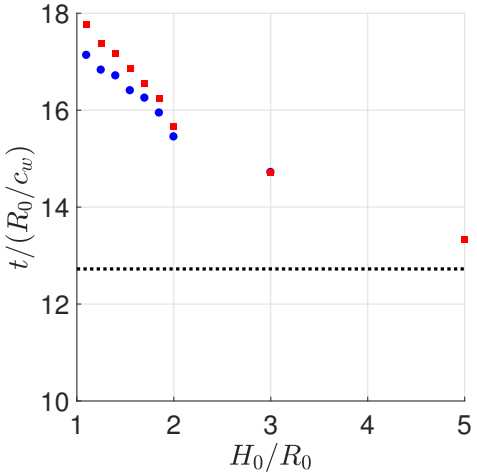

(b) Times of interest during the bubble collapse as a function of the standoff distance. Blue circle: time when the re-entrant jet impacts the bubble bottom side. Red square: time when the bubble collapses

FIGURE 5.22: Collapse features as a function of the standoff distance H_0/R_0 for $p_w/p_b = 353$. (a) Displacement of the bubble at collapse and (b) times of interest during the bubble collapse, dotted line represents the collapse time for free-field configuration

Regarding the collapse time, Fig. 5.22(b) shows the dimensionless times corresponding to the impact of the micro jet on the bubble and to the bubble collapse by itself as a function of the standoff distance. Also, the collapse time for the bubble in free-field is presented in dotted line as a reference. It is observed that these times decrease if H_0/R_0 increases, showing an asymptotical tendency towards the collapse time of the free-field configuration. This result can be explained by describing the bubble collapse. When the compression starts, the bubble shape becomes elongated in the direction normal to the wall (see Fig. 5.13(d)). The compression of the lower part of the bubble is affected by the presence of the wall, because it retards the flow filling the space between the lower part of the bubble and the wall. So, the overall collapse is slower. In addition, the wall reflects back the expansion waves released by the initial Riemann problem. This reflection reduces locally the pressure in the liquid, increasing thus the collapse time. In conclusion, the closer the bubble is to the wall, the longer is its collapse time. This behavior has been observed in experimental and numerical works ([111], [107], [46], [40], [45]).

With respect to the pressure ratio driving the collapse, it is noted that as the bubble is subjected to a higher pressure in the surrounding, its collapse arrives sooner, as expected. For example, the collapse time is reported at $t/(R_0/c_w) = 73$ for the case of $p_w/p_b = 34$, and at $t/(R_0/c_w) = 17.4$ for the case $p_w/p_b = 353$.

5.3.4 Jet velocity and water-hammer pressure

During the bubble compression, a micro jet is generated. When the jet impacts the lower part of the bubble, which moves at some velocity, v_d, a water-hammer pressure is generated. The value of jet velocity, v_j, and v_d are important because they determine the water-hammer pressure, which is an indicator of potential loading of the surface.

First, we start the analysis by explaining the jet formation. As observed previously, the solid boundary retards the fluid flow towards the space between the bubble and the wall. This produces a difference in the liquid pressure above and below the bubble, causing an acceleration of the upper bubble-liquid interface with respect to the lower one, and thus, a displacement of the bubble centroid towards the wall. This pressure gradient normal to the wall increases with time, creating a gain in the velocity of the bubble's centroid. Thus, the velocity of the upper bubble-liquid interface becomes much more important than the one of the lower part, and it generates the liquid jet pointing to the wall.

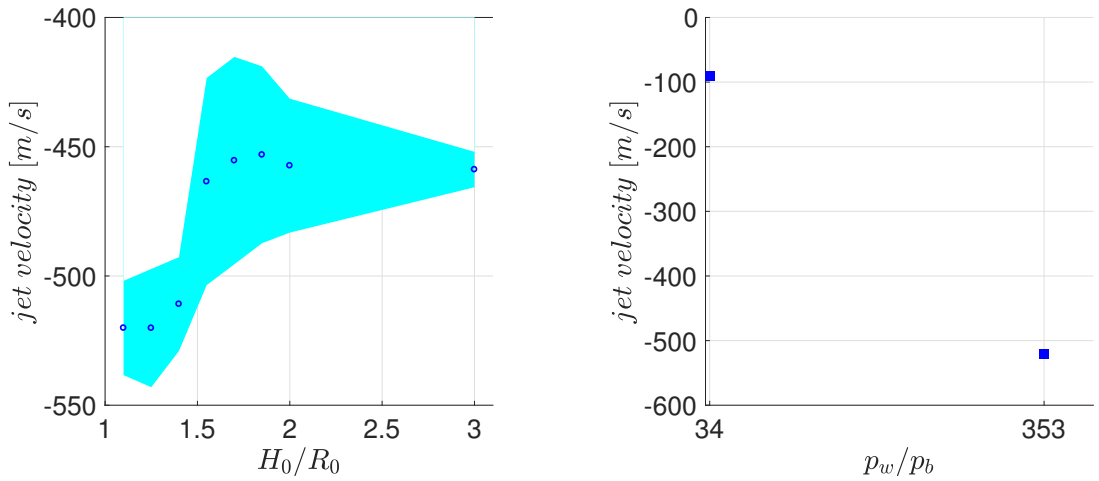

(a) Jet velocity as a function of H_0/R_0 for $p_w/p_b = 353$. The standard deviation is shown by the shaded area.

(b) Jet velocity as a function of p_w/p_b for $H_0/R_0 = 1.25$

FIGURE 5.23: Jet velocity as a function of the standoff distance H_0/R_0 for $p_w/p_b = 353$ and as a function of the pressure ratio driven the collapse p_w/p_b for $H_0/R_0 = 1.25$.

Fig. 5.23(a) shows the jet velocity as a function of H_0/R_0 for a pressure ratio driving the collapse of 353. The jet velocity is calculated as the average of the vertical component of the velocity of all the SPH particles located along the axis of symmetry at each instant considered. There are taken in consideration for the average calculation four instants around the moment when the micro jet impacts the bottom side of the bubble. It is observed that the standard deviation is larger for the cases ($H_0/R_0 = 1.55,\ 1.7,\ 1.85,\ 2$) where the four numerical instants considered for the average are saved more distantly relative to one another.

For decreasing values of H_0/R_0, the jet velocity increases until it attains values around 520 m/s for $p_w/p_b = 353$. An increase of jet velocity with decreasing standoff distance was also reported in the numerical studies by Johnsen and Colonius [40]. When comparing our 2D results against 3D simulations, it is found that our results, for this pressure ratio ($p_w/p_b = 353$), underestimate the jet velocity. Chahine [45] reports values of 800 m/s for $p_w/p_b = 353$ in 3D.

Fig. 5.23(b) shows the influence of the pressure ratio driving the collapse on the jet velocity. It is observed that as the pressure ratio increases, the jet velocity also increases. This behavior has also been presented in experimental and numerical works ([40], [43], [45]). For the case of pressure ratio of 34 (cavitation conditions), we have found values of 90 m/s. As expected, our results understimate the jet velocity. For example, Vogel et al. [107] reported values up to 130 m/s for $H_0/R_0 = 1$ in cavitation conditions.

In free-field collapse there is no jetting. As expected, the velocities of the lower and upper part of the bubble increase with the initial pressure ratio symmetrically. So, the jet is created by the non-symmetry caused by the wall.

For our case, the water-hammer pressure is generated when the liquid at high velocity (v_j) impacts the lower part of the bubble, which moves at a certain velocity v_d. Therefore, the water hammer pressure is calculated following the expression [39]:

$$p_{wh} = \rho_w c_w \frac{|v_j - v_d|}{2}. \tag{5.2}$$

The jet may hit the wall afterwards but its velocity is reduced by the impact with the bubble interface. Fig. 5.24 shows the water hammer-pressure computed by Eq. 5.2 (using the average of v_j and v_d) as a function of the standoff distance and as a function of the pressure ratio. Fig. 5.24(a) shows that the highest values of the water hammer pressure are achieved for small values of H_0/R_0, because the velocity difference is the largest. These observations suggest that the bubbles that cause an important damage would be the bubbles the nearest to the wall. For example, if we consider a bubble attached to the wall ($H_0/R_0 = 1$), in this case the jet would hit the wall directly.

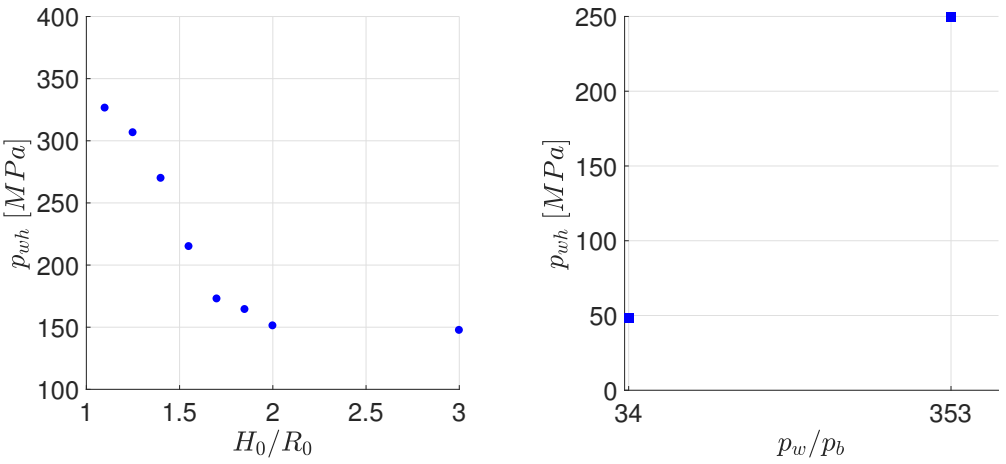

(a) Water hammer pressure as a function of the standoff distance H_0/R_0 for $p_w/p_b = 353$.

(b) Water hammer pressure as a function of p_w/p_b for $H_0/R_0 = 1.25$.

FIGURE 5.24: Water hammer pressure as a function of the standoff distance H_0/R_0 for $p_w/p_b = 353$ and as a function of p_w/p_b for $H_0/R_0 = 1.25$.

As explained before, the micro jet is observed in cases where $H_0/R_0 \leq 3$; beyond this standoff distance, the jet is not clearly formed. This suggests that the jet does not penetrates the bubble enough to impact its lower side. And therefore, the emitted pressure wave is due only to the compression of the gas bubble at collapse.

Regarding the pressure ratio driving the collapse (see Fig. 5.24(b)), consistently it is noted that for a smaller pressure ratio, the water-hammer pressure calculated is also less important. We report pressure values of 50 [MPa] for $p_w/p_b = 34$ and 250 [MPa] for $p_w/p_b = 353$, both cases having a standoff distance (H_0/R_0) of 1.25.

5.3.5 Pressure on the wall

The pressure along the wall is considered as a measure of the potential damage induced by the bubble collapse. Fig. 5.25 shows the history of the wall pressure registered at the center of the wall for several standoff distances ($1.1 \leq H_0/R_0 \leq 5$) and for $p_w/p_b = 353$. All situations show similar features. Initially, the pressure value registered corresponds to the surrounding pressure ($p_w = 35.3[MPa]$). Then, during the first moments, the pressure wave reflects against the wall creating pressure pulses on the wall. After this transitory phenomenon has passed, the pressure on the wall is uniform. This behavior is also present when the bubble is located farther from the wall, but the oscillations are more distant (see Fig. 5.25(i)).

For $t/(R_0/c_w) > 15$, the pressure on the wall suddenly increases. Two peaks of pressure are noted in cases where the standoff distance (H_0/R_0) is lower than 2. The first peak is related to the pressure wave emitted due to the impact of the micro jet to the lower side of the bubble, and the second one is linked to the pressure wave emitted by the collapse of the bubble.

When the standoff distance increases, the two pressure peaks get closer in time and in amplitude. Eventually, in cases where the standoff distance is equal or larger than 2, the micro jet and the bubble collapse events happen within a time window that suggests that the two phenomena occur at the same time. This indicates that both phenomena (jet impact and bubble collapse) are superposed, as explained in previous sections. In consequence, the only peak observed on the wall is due to the superposition effect of both waves traveling together towards the wall.

Fig. 5.26 shows the history of the wall pressure at different locations along the wall ($x/R_0 = 0,\quad 0.5,\quad 1,\quad 2$) for two standoff distances ($H_0/R_0 = 1.1$ and 3) and the pressure ratio driving the collapse set to $p_w/p_b = 353$. For small standoff distance (see Fig. 5.26(a)) the bottom side of the bubble barely moves because it is very close to the wall. Thus, the pressure wave impacts the wall shortly after the wave has been emitted.

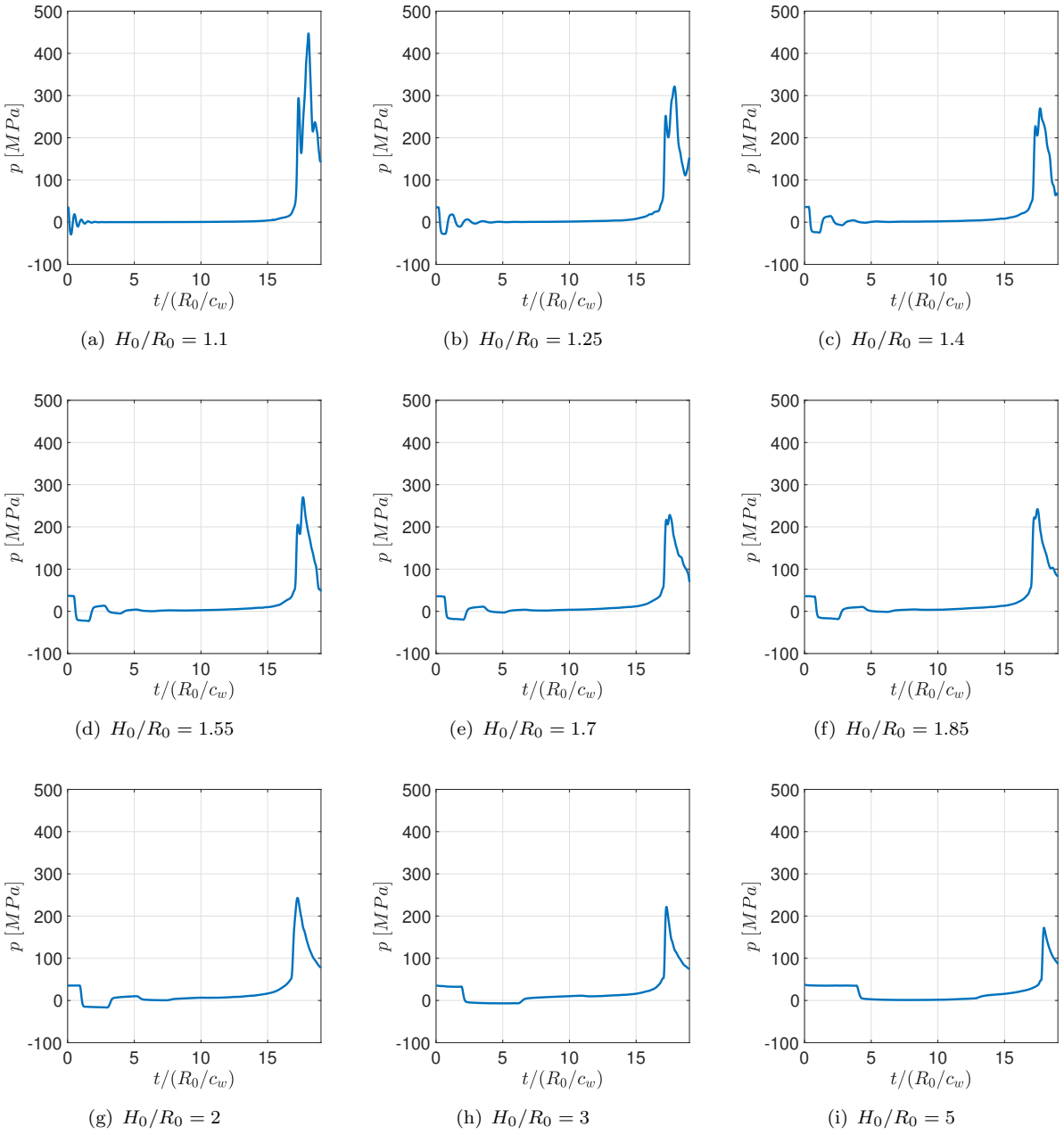

(a) $H_0/R_0 = 1.1$ (b) $H_0/R_0 = 1.25$ (c) $H_0/R_0 = 1.4$

(d) $H_0/R_0 = 1.55$ (e) $H_0/R_0 = 1.7$ (f) $H_0/R_0 = 1.85$

(g) $H_0/R_0 = 2$ (h) $H_0/R_0 = 3$ (i) $H_0/R_0 = 5$

FIGURE 5.25: Pressure on the center of the wall over time for collapse near a wall ($p_w/p_b = 353$) for several standoff distances ($1.1 \leq H_0/R_0 \leq 5$)

Consequently, the wall pressure strongly increases along the center-line ($x/R_0 = 0$), but off-axis the pressure values quickly decrease. On the other hand, when the bubble is initially farther from the wall (see Fig. 5.26(b)), the decrease in the pressure values off-axis is slower. It is even noted that the pressure behavior at $x/R_0 = 0.5$ and $x/R_0 = 1$ are very similar as both curves overlap. This behavior is explained below.

The pressure waves emitted during the bubble compression propagate radially from its origin. Hence, the curvature radius of the wavefront increases with its propagation.

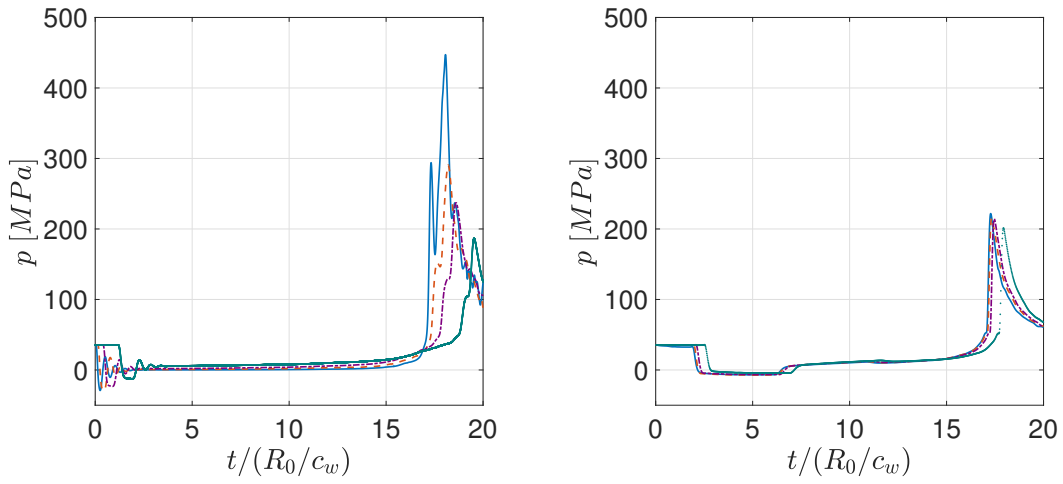

(a) $H_0/R_0 = 1.1$ (b) $H_0/R_0 = 3$

FIGURE 5.26: History of the wall pressure at different locations along the wall for $p_w/p_b = 353$. (a) $H_0/R_0 = 1.1$ and (b) $H_0/R_0 = 3$. Blue ($x/R_0 = 0$), red ($x/R_0 = 0.5$), violet ($x/R_0 = 1$) and green ($x/R_0 = 2$)

When the wavefront arrives to the wall, the curvature radius of a wave emitted farther from the wall is larger than the curvature radius of a wave emitted closer to the wall. In consequence, for cases where the wave emission occurs at a large distance with respect to the wall, the front propagation behaves like a planar wave at the moment it arrives at the wall. So, the wave arrives at the same time at all the points near the centerline.

Fig. 5.27 shows the water-hammer pressure computed by Eq. (5.2) and the pressure values related to the first pressure peak on the wall. For $H_0/R_0 \leq 1.55$, the values of the pressure peak are lower than the water-hammer pressure calculated. This result is due to the radial attenuation of the pressure wave while it travels into the liquid. For $H_0/R_0 \geq 1.7$, the superposition effect is present. Pressure values higher than the water-hammer pressure values are registered. Since the wavefront can only be attenuated in the liquid, these higher values are reached due to the contribution of the bubble collapse (i.e. the second pressure peak), whose wave emission occurs shortly after the wave emission of the micro jet. Therefore, the pressure values at the wall are higher than the water-hammer pressure values alone.

5.3.5.1 Bubble size effect on the wall pressure

The bubble size effect on the wall pressure is analyzed by considering two bubble radii, $R_0 = 1\ mm$ and $R_0 = 10\ mm$, located at a standoff distance H_0/R_0 of 1.25 and

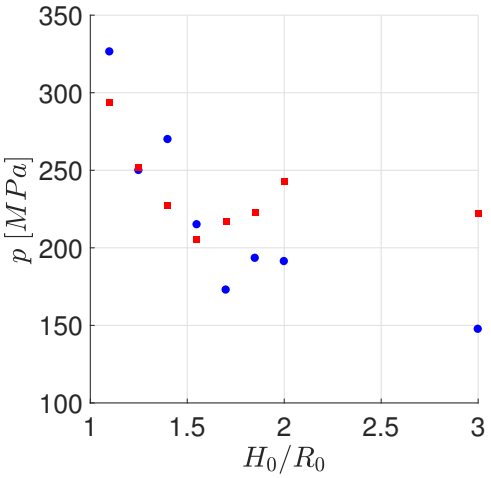

FIGURE 5.27: Pressure as a function of the standoff distance H_0/R_0 for $p_w/p_b = 353$. Blue circle: water hammer pressure calculated by Eq. 5.2, red square: First pressure peak on the wall measured in the simulations

experiencing a pressure ratio driving the collapse p_w/p_b of 353. Fig. 5.28 shows the evolution of the pressure at the center of the wall for these two cases. A zoom in the scale is presented in Fig. 5.28(b). It is illustrated that for a given standoff distance, the pressure peak value and the pressure curve behavior agree quite well between both bubble sizes, showing that the pressure generated on the wall does not depend on the bubble size.

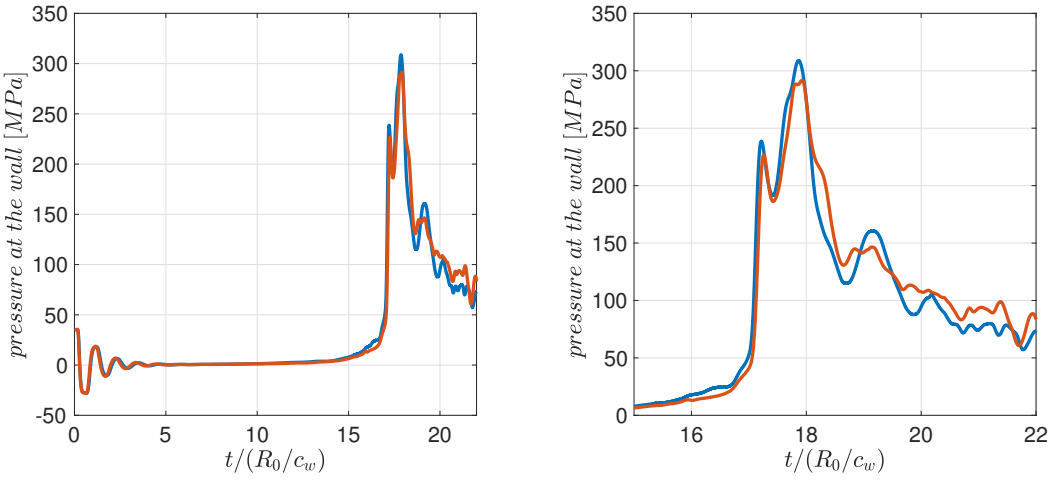

FIGURE 5.28: History of the wall pressure at the center of the wall for $p_w/p_b = 353$ and $H_0/R_0 = 1.25$ considering two bubble radius: blue line $R_0 = 10\ mm$ and red line $R_0 = 1\ mm$.

Regarding the bubble collapse period, it is obtained a shorter collapse time for the case involving the smaller bubble, i.e. for the bubble of $R_0 = 1\ mm$ the collapse time is

$1.1 \cdot 10^{-5}$ $[s]$ and for the bubble of $R_0 = 10\ mm$ the collapse time is $1.1 \cdot 10^{-4}$ $[s]$. So, comparing these two cases, it is observed that the bubble with a radius 10 times larger has a collapse time 10 times longer. This shows a direct relation with respect to the bubble initial radius.

It is interesting to note that for a given standoff distance, the jet velocity estimated for both bubble radii are similar. For both cases ($R_0 = 1\ mm$ and $R_0 = 10\ mm$), it is obtained a jet velocity of about 520 m/s. This shows that the jet velocity is mostly controlled by the standoff distance and the pressure ratio, as we have seen before, and not by the bubble size.

5.3.5.2 Pressure ratio driving the collapse effect on the wall pressure

The influence of the initial pressure ratio on the pressure at the wall is regarded by considering two scenarios, the one linked to the cavitation condition ($p_w/p_b = 34$) and the other one related to the lithotripsy ($p_w/p_b = 353$). Fig. 5.29 shows the evolution of the pressure at the center of the wall. In both cases, the standoff distance (H_0/R_0) is 1.25 and the initial bubble radius is the same ($R_0 = 10\ [mm]$). In general, both results show that the pressure suddenly increases due to the bubble collapse and a well-defined peak of pressure is present. For the cavitation conditions, only one peak of pressure is observed, suggesting that the two peaks feature is mostly linked to cases of higher-pressure ratios because in those cases, the bubble collapses after the water jet has gone through it. However, it is not conclusive and additional simulations considering several standoff distance and pressure ratio in between these two limits (i.e. 34 and 353) are suggested.

Another feature to consider is the phase change. In reality, during the compression of a vapor bubble, the vapor may condense. This mechanism may influence the amplitude of the pressure wave for cases where the driving pressure ratio is low, because in those cases the inertial effects are less important than in high-pressure ratio situations. It may be interesting to consider the bubble filled with vapor and to consider the phase change phenomenon in order to simulate a more realistic case.

Otherwise, as expected, the pressure peak value is lower when the pressure ratio is smaller, and the collapse time is shorter when increasing the pressure ratio.

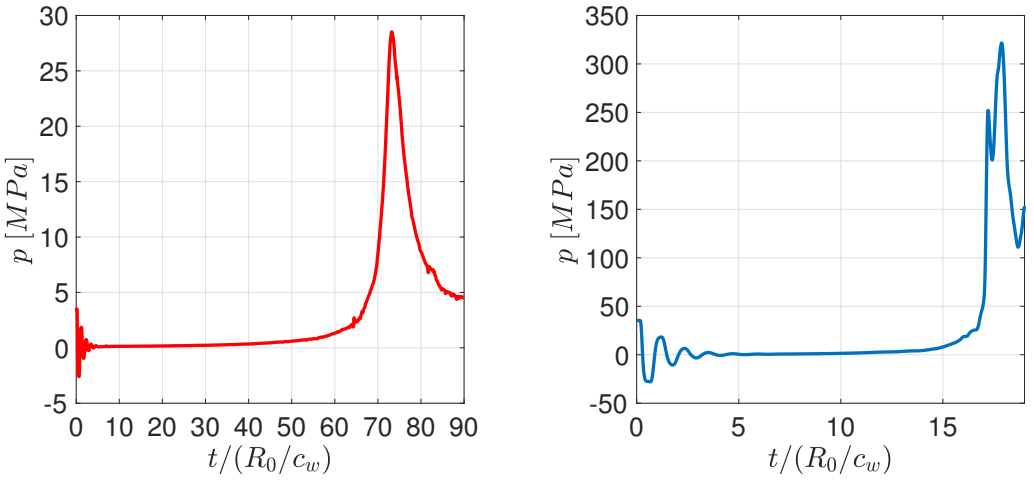

(a) $p_w/p_b = 34$ (b) $p_w/p_b = 353$

FIGURE 5.29: History of the wall pressure at the center of the wall for $H_0/R_0 = 1.25$. (a) $p_w/p_b = 34$ and (b) $p_w/p_b = 353$

5.3.5.3 Estimation of potential damage

For estimating the potential damage, the maximum value of the pressure on the wall is important, but also it is important to consider the time during which the pressure pulse is applied. This magnitude is called impulse and it is calculated as the integral of the pressure during a certain amount of time, 20 μs, around the peak of pressure. Thus, the impulse is a better indicator of the energy exchanged between the fluid and the solid because it considers the transient characteristic of the problem. So, the important quantity to estimate the loading on the solid is the impulse and not the maximum values of pressure that might be brief in time.

As the impulse value is high, the potential damage on the solid wall may be also important. Nevertheless, it is just an indicator and further solid analyses involving the material properties are required. Fig. 5.30 shows the maximum value of the wall pressure and the impulse as a function of the standoff distance H_0/R_0, for a pressure ratio of 353. It is interesting to mention that for the cases considered in this work, both indicators present the same tendency.

For the bubble located initially close to the wall, we obtain values of impulse and wall pressures higher than when the bubble is farther. This is consistent with the velocity jet values and water-hammer pressure values found. This also suggests that the collapse of bubbles close to the wall present more potential to damage the material.

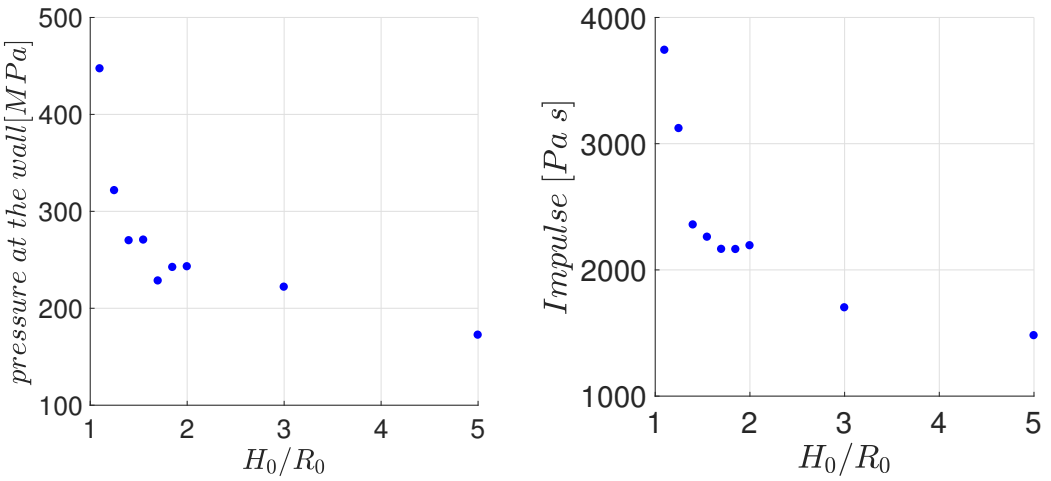

(a) (b)

FIGURE 5.30: Maximum wall pressure (a) and impulse (b) as a function of the standoff distance (H_0/R_0) for $p_w/p_b = 353$.

Regarding the pressure ratio driving the collapse, we obtain, for the impulse, values of 500 [Pa s] for $p_w/p_b = 34$ and 3120 [Pa s] for $p_w/p_b = 353$, both cases with a standoff distance of 1.25. This suggests that cases having high pressure ratio will produce more damage.

In the literature, material properties values are found, i.e. yield stress. These material properties allow estimating if a load can damage the material and actually wear it. Comparing standard values for steel (i.e. yield stress $\approx 500[MPa]$ [88]) and the pressure values found in our caculations (i.e. $450[MPa]$), it may be said at first sight that the maximum pressure values seem to be too small to actually wear the material. Nevertheless, a parallel work on material resistance for these type of fluid phenomenon has shown that one main cause of material damage is fatigue [15], [14], i.e. the localized structural damage caused by a repeated and localized applied load. In this case, the load comes from the pressure waves emitted during the compression of the non-condensable gas bubble. Thus, several bubbles or a cloud of bubbles collapsing during a certain time in a localized region may cause structural damage. The structural response is studied in the next chapter through the execution of fluid-structure interaction simulations of the bubble collapse near a non-rigid surface, towards the prediction of structural damage.

5.4 Conclusion

The simulation of the bubble collapse in free field has been compared with the Rayleigh-Plesset analytic solution and with existing numerical results, showing good agreement. These comparisons indicate that the compressible SPH-ALE is able to model the bubble dynamics.

The collapse of a non-condensable gas bubble close to the wall has been addressed as an approximation of the fundamental mechanism producing damage in cavitation applications. The general behavior of the non-condensable gas bubble dynamics near the wall is characterized by the formation of a micro jet and by the collapse of the bubble by itself. These two phenomena are responsible of generating high-pressure levels on the solid boundary. It is obtained that the intensity of the collapse depends mainly on the pressure ratio between the liquid and the bubble. As the pressure ratio is larger, the pressure levels on the wall are higher and the collapse time is shorter.

The influence of the distance between the bubble and the wall has been examined. In this regard, it is obtained that the higher wall pressure and the higher impulse values belong to bubbles located initially close to the wall. The bubble size was also analyzed, concluding that it does not influence the wall pressure. In summary, the pressure signal registered on the wall depends on the pressure driving the collapse and the standoff distance, but not on the bubble size.

Regarding the velocity of the micro jet, it is linked to the water-hammer pressure. As well, the highest values of the micro jet velocity and of the water-hammer pressure are also associated to the bubbles collapsing near the wall. Specifically, for all these loading indicators (pressure at the wall, impulse, water-hammer pressure and micro jet velocity), it is found that the bubbles with high potential loading are initially located at a distance lower than $H_0/R_0 = 2$.

Chapter 6

Fluid-structure interaction simulations of the collapse of a non-condensable gas bubble near a solid material

Previous chapter focused on presenting and interpreting the fluid dynamics involved in the bubble collapse phenomenon in order to predict the potential load that impacts on a solid boundary. This analysis can be enlarged by considering a fluid-structure interaction approach in order to take into account the material reaction over time.

This chapter presents numerical simulations of the non-symmetric dynamics of a non-condensable gas bubble near a deformable solid in order to analyze the response of the material to the loads generated during the last stages of bubble compression. Since the nearest non-condensable gas bubbles to the wall present more potential to wear the material, we have considered only two configurations associated to the smallest value of H_0/R_0 to conduct this study. The aim is then to estimate the material response to the impulsive pressures resulting from the bubble dynamics.

6.1 Structural model and coupling approach

In this work, the fluid-structure interaction involves the simulation of the material response due to the dynamics of two-fluid flows (liquid-gas) highly compressible. A robust and accurate coupling technique developed by Nunez-Ramirez [69], in the frame of the PREDHYMA Project, is used to simulate these fluid-structure interactions. In this part of the work, we consider a technique that couples, in a synchronized way, two solvers: one based on the finite element method to model the solid and another one following the compressible SPH-ALE method to model the fluid. By imposing the normal velocity continuity at the interface, this coupling method ensures the energy conservation at the fluid-solid interface, thus guaranteeing coupling simulation's stability over time [69].

The computations of each domain are performed with specialized solvers. The Europlexus code [89] is used for the solid domain. It is developed by the French office of atomic energy (Commissariat à l'Énergie Atomique) and the European Commission Joint Research Centre. This code is suitable for the simulation of transient fast dynamic phenomena involving strong nonlinearities. The compressible SPH-ALE fluid solver Asphodel, presented in Chapter 4, is employed for simulating the fluid. These codes are linked by an external coupling software, managing only the interface computation considering the normal velocity continuity at the interface between the fluid and solid domains. For solving the interface problem, the method uses the pressure exerted by the fluid on the interface as input for each solver (fluid and solid) to complete their computations for a given time-step [69]. Each code uses different time integrators, i.e. second-order Runge-Kutta scheme for the fluid and an explicit Newmark time integrator for the solid.

6.1.1 Stress tensor

The stress tensor is a representation used in the mechanics of continuous medium to characterize the stress state of a material, i.e. the internal forces involved.

If we take an orthonormal base $\mathbf{x}_i$, the stress tensor is represented by a matrix of elements σ_{ij} $(i, j = 1, 2, 3)$ [97], [19], i.e.

$$\sigma = \begin{bmatrix} \sigma_{11} & \sigma_{12} & \sigma_{13} \\ \sigma_{21} & \sigma_{22} & \sigma_{23} \\ \sigma_{31} & \sigma_{32} & \sigma_{33} \end{bmatrix}.$$

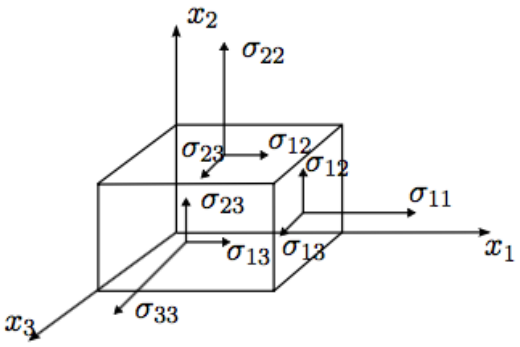

FIGURE 6.1: General stress tensor [97]

The diagonal components (i.e. $\sigma_{11}, \sigma_{22}, \sigma_{33}$) are therefore normal stresses, while the non-diagonal components (i.e. $\sigma_{12}, \sigma_{13}, \sigma_{23}$, $\sigma_{21}, \sigma_{31}, \sigma_{21}$) are shear stresses (see Fig. 6.1). The symmetry of the stress tensor, e.g. $\sigma_{12} = \sigma_{21}$, expresses the equality of the shear stress associated with two perpendicular faces.

Dimensionally, a stress is homogeneous to a force per unit area, and therefore to a pressure. In the SI unit, the unit is Pascal ($1Pa = 1N/m^2$).

Hydrostatic pressure

The hydrostatic pressure, p_h, is defined as the third of the trace of the stress matrix, that is to say as the average of the diagonal terms, i.e.

$$p_h = \frac{\sigma_{11} + \sigma_{22} + \sigma_{33}}{3}. \tag{6.1}$$

If the hydrostatic pressure is negative, the material is under a compression stress; otherwise it is under a tension stress [97].

von Mises stress

The von Mises stress, σ_v, is an equivalent stress used in estimating whether an isotropic and ductile material will yield when subjected to a loading condition. A material starts yielding when the von Mises stress reaches a value known as the material yield strength, σ_y.

The von Mises stress is calculated through the components of the stress tensor as

$$\sigma_v = \left[\frac{1}{2}\left[(\sigma_{11}-\sigma_{22})^2 + (\sigma_{22}-\sigma_{33})^2 + (\sigma_{33}-\sigma_{11})^2 + 6(\sigma_{23}^2+\sigma_{31}^2+\sigma_{12}^2)\right]\right]^{1/2}. \quad (6.2)$$

6.1.2 Europlexus

Europlexus is able to simulate fast dynamic problems, such as explosions and impacts. It takes into account geometric non-linearity (i.e. large displacement, large rotations and large strains) and material non-linearity (i.e. plasticity) [89].

The spatial discretization is based on the Finite Element Method adopting the Lagrangian scheme to discretize the governing equations. An external Computer-aided-design (CAD) solver, called Salome, enables conducting the pre-processing stage, which involves the development of the geometry and the meshing. Later, the post-treatment stage is done using Paraview.

6.1.3 Coupling solver

In this section a brief description of the coupling method is developed. The fundamental elements are taken from Nunez-Ramirez [69] in order to have the basics for understanding this coupling approach. Three main parts of the numerical treatment are identified: the fluid, the solid and the coupling treatment.

6.1.3.1 Strategy for fluid domain

The numerical approach followed for the fluid domain considers the solution of the partial Riemann problem already presented in Section 4.5.1. The term p_{ij}^E is established as the pressure solution of a partial Riemann problem that can be expressed between a fluid particle i and the boundary element j in its neighborhood.

In order to obtain the expression of the pressure value on a solid wall element j, the boundary term of the momentum equation in Eq. (**??**) must be considered. Hence, this momentum equation is re-written taking only the boundary term:

$$\frac{d(\omega_i \rho_i \mathbf{v}_i)}{dt} = -\omega_i \sum_{j \in \partial D_i} \omega_j^{\partial} 2p_{ij}^E \cdot \mathbf{n}_j W_{ij}, \quad (6.3)$$

where we consider, for a solid wall element j, all the fluid particles i whose support domain (i.e. kernel support) is truncated by j. $\mathbf{n}_j$ is the normal direction pointing-outward the fluid domain.

For the fluid particle i, the force exerted by the solid wall element j is

$$\mathbb{F}_{j\to i} = -\omega_i 2p_{ij}^E \mathbf{n}_j W_{ij}\omega_j^\partial. \tag{6.4}$$

Inversely, the force applied to the solid wall element j by the fluid particle i is

$$\mathbb{F}_{i\to j} = -\mathbb{F}_{j\to i} = \omega_i 2p_{ij}^E \mathbf{n}_j W_{ij}\omega_j^\partial. \tag{6.5}$$

Then, the force exerted to the solid wall element j by the fluid can be calculated by

$$\sum_{i\in\partial D_j} \mathbb{F}_{i\to j} = \sum_{i\in\partial D_j} \omega_i 2p_{ij}^E \mathbf{n}_j W_{ij}\omega_j^\partial. \tag{6.6}$$

The hydrodynamic force exerted by the fluid on the solid wall element j is given by $p_j\mathbf{n}_j\omega_j^\partial$, where p_j is the fluid pressure at the solid wall element. So, we can write

$$p_j\mathbf{n}_j\omega_j^\partial = \sum_{i\in\partial D_j} \omega_i 2p_{ij}^E \mathbf{n}_j W_{ij}\omega_j^\partial. \tag{6.7}$$

Then, the fluid pressure is calculated by

$$p_j = \sum_{i\in\partial D_j} \omega_i 2p_{ij}^E W_{ij}. \tag{6.8}$$

From the pressure expressions in Eq. (4.79), Eq. (4.80) and Eq. (4.81), the solution for the pressure p_{ij}^E can be derived as a function of the wall velocity $\mathbf{v}_j$ and it is written as

$$p_{ij}^E = p_i - \rho_i c_i(\mathbf{v}_j - \mathbf{v}_i)\cdot\mathbf{n}_j. \tag{6.9}$$

Eq. (6.9) is substituted in Eq. (6.8) to have:

$$\left(\sum_{i\in\partial D_j} 2\omega_i\rho_i c_i W_{ij}\right) v_{fj} + p_j = \sum_{i\in\partial D_j} 2\omega_i(p_i + \rho_i c_i \mathbf{v}_i\cdot\mathbf{n}_j)W_{ij}, \tag{6.10}$$

where $v_{fj} = \mathbf{v}_j \cdot \mathbf{n}_j$ and it corresponds to the solid element velocity in the normal direction pointing outward the fluid domain.

Eq. (6.10) can be written in matrix form as

$$\mathbf{M}_f \mathbf{v}_{fj} + \mathbf{\Lambda} = \mathbf{G}_f, \tag{6.11}$$

where $\mathbf{M}_f$ is a square diagonal matrix of dimensions (N_j, N_j) and N_j is the total number of solid wall elements. The vectors $\mathbf{v}_{fj}$, $\mathbf{\Lambda}$ and $\mathbf{G}_f$ are of dimensions $(1, N_f)$. The respective coefficients are given by [69]

$$\begin{cases} \mathbf{M}_f(j,j) = \displaystyle\sum_{i \in \partial D_j} 2\omega_i \rho_i c_i W_{ij} \\ \mathbf{v}_{fj}(j) = v_{fj} = \mathbf{v}_j \cdot \mathbf{n}_j \\ \mathbf{\Lambda}(j) = p_j \\ \mathbf{G}_f(j) = \displaystyle\sum_{i \in \partial D_j} 2\omega_i (p_i + \rho_i c_i \mathbf{v}_i \cdot \mathbf{n}_j) W_{ij} \end{cases}. \tag{6.12}$$

In order to integrate in time the fluid status, it is used the second-order accurate Runge-Kutta 2 mid-point scheme. To find the solution at $(n+1)$ it is required to have the prediction solution at $(n+1/2)$. So, the system (Eq. 6.11) is expressed at both time stages as

$$\begin{cases} \mathbf{M}_f^{n+1/2} \mathbf{v}_{fj}^{n+1/2} + \mathbf{\Lambda}^{n+1/2} = \mathbf{G}_f^{n+1/2} \\ \mathbf{M}_f^{n+1} \mathbf{v}_{fj}^{n+1} + \mathbf{\Lambda}^{n+1} = \mathbf{G}_f^{n+1} \end{cases}. \tag{6.13}$$

Finally, Eq. (6.13) is the first equation of interest for the coupling scheme. It gives the relation between the solid boundary velocity ($\mathbf{v}_{fj}^{n+1}$) and the pressure ($\mathbf{\Lambda}^{n+1}$) at the solid-fluid interface. They correspond to the unknowns of the system for the fluid domain.

6.1.3.2 Strategy for solid domain

The solid domain is discretized using the FEM where $\mathbf{u}_s$, $\mathbf{v}_s$ and $\mathbf{a}_s$ are the displacement, velocity and acceleration vectors, respectively. In an explicit scheme, the matrix $\mathbf{M}_s$

is the positive diagonal mass matrix whose components are related to the degrees of freedom of the system.

According to [69], the equilibrium equation for the coupled solid domain is expressed in Eq. (6.14)

$$\mathbf{M}_s\mathbf{a}_s + \mathbf{f}_s^{int} + \mathbf{L}_p\mathbf{\Lambda} - \mathbf{f}_s^{ext} = 0, \tag{6.14}$$

where the internal and external forces of the solid material are illustrated by $\mathbf{f}_s^{int}$ and $\mathbf{f}_s^{ext}$, respectively. And $\mathbf{L}_p\mathbf{\Lambda}$ is interpreted as an interface force acting on the solid domain.

As seen in Section 6.1.3.1, $\mathbf{\Lambda}$ is homogeneous to a pressure applied by the fluid on the solid domain. The matrix $\mathbf{L}_p$ contains information about the surface area of each element along the interface. In this way, the force vector related to the fluid pressure on the solid is found when the product $\mathbf{L}_p\mathbf{\Lambda}$ is operated.

To compute the unknowns for the solid domain, Eq. (6.14) is discretized with the central difference explicit Newmark algorithm,

$$\begin{cases} \mathbf{a}_s^{n+1} = [\mathbf{M_s}]^{-1}(\mathbf{f}_s^{ext^{n+1}} - \mathbf{f}_s^{int^{n+1}} - \mathbf{L}_p^{n+1}\mathbf{\Lambda}^{n+1}) \\ \mathbf{v}_s^{n+1} = {}^p\mathbf{v}_s^{n+1} + \dfrac{1}{2}\Delta t_s\mathbf{a}_s^{n+1} \\ \mathbf{u}_s^{n+1} = {}^p\mathbf{u}_s^{n+1} \end{cases}, \tag{6.15}$$

where ${}^p\mathbf{v}_s^{n+1}$ and ${}^p\mathbf{u}_s^{n+1}$ depend exclusively on the expression of the kinematic vectors from the known (initial) condition, and they are called the predictors for the velocity and displacement vector, respectively.

The expression for the predictors is given by

$$\begin{cases} {}^p\mathbf{v}_s^{n+1} = \mathbf{v}_s^n + \dfrac{1}{2}\Delta t_s\mathbf{a}_s^n \\ {}^p\mathbf{u}_s^{n+1} = \mathbf{u}_s^n + \Delta t_s\mathbf{v}_s^n + \dfrac{1}{2}\Delta t_s^2\mathbf{a}_s^n \end{cases}. \tag{6.16}$$

So, from Eq. (6.15) and Eq. (6.16), the unknowns are the solid acceleration $\mathbf{a}_s^{n+1}$ and the pressure $\mathbf{\Lambda}^{n+1}$ at the solid-fluid interface. Finally, Eq. (6.15) gives the second equation needed for solving the coupled system along Eq. (6.13).

6.1.3.3 Coupling strategy

The coupling strategy establishes the kinematic continuity at the interface in terms of normal velocities, guaranteeing the energy conservation at the interface. So, the normal velocity equilibrium at the fluid-solid interface is established by

$$\mathbf{L}_s\mathbf{v}_s + \mathbf{L}_f\mathbf{v}_f = 0, \tag{6.17}$$

where the subscript s denotes solid and f denotes fluid.

As explained in [69], $\mathbf{L}_s$ and $\mathbf{L}_f$ are matrices that extract the interface velocity of the degrees of freedom of the system and project them along the normal direction.

For any solid element j, let $\mathbf{x}_j$ be at the geometrical barycenter of the interface element. It is considered that the normal direction pointing outward the solid domain $\mathbf{n}_s(\mathbf{x}_j)$ is opposite in sign to the outward pointing normal of the fluid domain $\mathbf{n}_f(\mathbf{x}_j)$. Then, it is introduced that $\mathbf{n}_{js}(\mathbf{x}_j) = -\mathbf{n}_{jf}(\mathbf{x}_j) = \mathbf{n}_j$ (see Fig. 6.2).

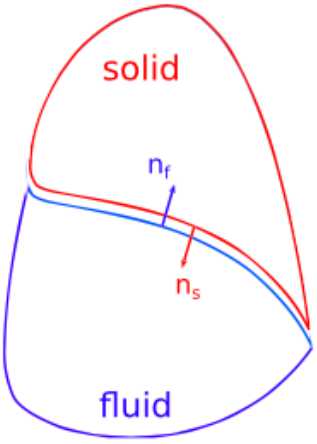

FIGURE 6.2: Illustration of the outward pointing normals, $\mathbf{n}_s$ and $\mathbf{n}_f$, for each domain (solid and fluid) [69]

This condition is applied to Eq. (6.17) to have

$$\mathbf{n}_j \cdot (\mathbf{v}_s(\mathbf{x}_j) - \mathbf{v}_f(\mathbf{x}_j)) = 0, \tag{6.18}$$

getting in mind that $\mathbf{n}_j \cdot \mathbf{v}_f(j) = \mathbf{v}_{fj}(j)$ for j an element at the interface.

Then, the Eq. (6.17) can be written in matrix notation for the whole domain as

$$\mathbf{L}_s\mathbf{v}_s + \mathbf{v}_{fj} = 0. \tag{6.19}$$

Taking into account the time integration aspects, it is presented the discretization of Eq. (6.19) using a two-step Runge-Kutta scheme, to be in agreement with the fluid integration. Hence, it is given as

$$\begin{cases} \mathbf{L}_s^{n+1/2}\mathbf{v}_s^{n+1/2} + \mathbf{v}_{fj}^{n+1/2} = 0 \\ \mathbf{L}_s^{n+1}\mathbf{v}_s^{n+1} + \mathbf{v}_{fj}^{n+1} = 0 \end{cases}. \tag{6.20}$$

Eq. (6.20) represents the third equation needed for solving the coupled system along Eq. (6.13) and Eq. (6.15). In geometrically nonlinear cases, it is not possible to consider the reference geometry for the whole duration of the simulation. Therefore, the operators $\mathbf{L}_s$ and $\mathbf{L}_p$ have to be updated at each time-step [69].

6.1.3.4 Explicit solver

The system of coupled equations to be solved at each time step in order to obtain the values of the unknown quantities, $\mathbf{a}_s^{n+1}$, $\mathbf{v}_{fj}^{n+1}$, $\mathbf{\Lambda}^{n+1}$, at time $t = t^{n+1}$ from the configuration known at $t = t^n$, can be expressed as:

$$\begin{cases} \mathbf{M}_f^{n+1}\ \mathbf{v}_{f_j}^{n+1} + \mathbf{\Lambda}^{n+1} = \mathbf{G}_f^{n+1} \\ \mathbf{M}_s\mathbf{a}_s^{n+1} + \mathbf{L}_p^{n+1}\mathbf{\Lambda}^{n+1} = \mathbf{f}_s^{ext^{n+1}} - \mathbf{f}_s^{int^{n+1}} \\ \mathbf{L}_s^{n+1}\left({}^{p}\mathbf{v}_s^{n+1} + \dfrac{\Delta t_s}{2}\mathbf{a}_s^{n+1}\right) + \mathbf{v}_{f_j}^{n+1} = 0 \end{cases} \tag{6.21}$$

where $(n+1)$-superscripted quantities indicate values that need to be updated at each time-step. In the third equation of Eq. (6.21) which imposes normal velocity continuity at the interface, the solid velocity vector $\mathbf{v}_s^{n+1}$ is expressed in terms of the solid acceleration vector $\mathbf{a}_s^{n+1}$ and a predictor of the velocity vector ${}^{p}\mathbf{v}_s^{n+1}$ by using Newmark's explicit central difference scheme. The whole solution process is detailed by Nunez-Ramirez in [69].

6.2 Material deformation due to hydrodynamic impulsive loads

The simulation approach presented in Section 5.3.5 enables the analysis of impulsive loads on a solid-rigid wall, without considering the material response. This corresponds to the one-way coupled approach. A more accurate analysis involves a two-way coupled simulation. This means the development of two computations simultaneously, one involving the bubble dynamics within the fluid domain and another one considering the structural mechanics of the solid response. With this goal in mind, this section shows numerical simulations of fluid-structure interactions about a non-condensable gas bubble that undergoes compression in the vicinity of a deformable solid plate taking into account material properties.

6.2.1 Simulation set-up of the fluid-structure interaction simulations

In this section, it is presented the numerical and physical considerations followed in the development of FSI simulations.

6.2.1.1 Time step selection

Regarding the time-step selection for the coupled simulation, we remind that both solvers use explicit time integrators, avoiding the need of executing iterative procedures to update the fluid and solid status. However, these schemes are known to present numerical instabilities if the stability condition (i.e. Courant-Friedrich-Lewy (CFL)) is violated. Thus, when working with explicit time integrators, the CFL condition has to be considered for each domain. In a general way, the CFL condition can be written as [69],

$$\Delta t \leq K_{CFL} \cdot min \frac{\Delta_{xi}}{c_{wp}}, \tag{6.22}$$

where Δt is the required time-step, Δ_{xi} is the characteristic size of the SPH distribution or the FEM mesh elements, c_{wp} is the speed of wave propagation in the domain, and $K_{CFL} \in]0, 1]$.

For similar initial characteristic sizes in the SPH distribution and FEM elements, the application of the CFL condition requires a smaller time-step for the domain where

the wave propagation is the fastest. Hence, at first sight, for the domains considered, fluid (i.e. water and gas) and steel, the smaller time-step is usually related to the solid. Nevertheless, in our case, the fluid SPH domain presents a numerical correction (see Section 4.7) that causes a reduction in the fluid time step. So, the fluid time step is actually lower than the solid time step. For that reason, it was chosen the same time step for both domains, the fluid time step being the decisive value.

6.2.1.2 Meshing and boundary conditions

A finite element mesh for a rectangular plate is generated using the CAD solver Salome. The plate is $40R_0$ wide and $18R_0$ thick. The mesh was generated using quadrangular elements and a linear refining method in the vertical direction in order to have smaller elements close to the fluid-solid interface. It is obtained 256000 cells and 257761 nodes. The elements close to the interface are squares measuring the same size as the SPH particle radius. The mesh is illustrated in Fig. 6.3 showing the whole mesh (Fig. 6.3(a)), a zoom near the fluid-solid interface (Fig. 6.3(b)) and a second zoom to highlight the vertical refinement (Fig. 6.3(c)). The thickness of the solid domain was selected to be sufficiently large to not have reflected waves in the material that could affect the results.

(a) FEM domain

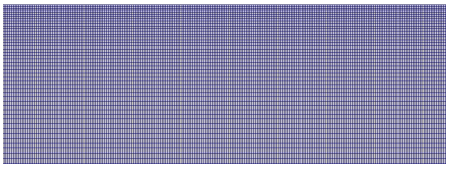

(b) First zoom near the fluid-solid interface (at the top)

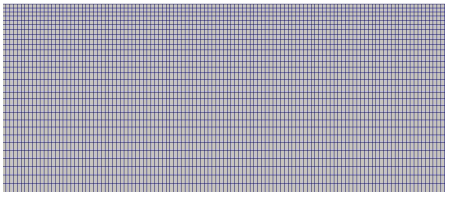

(c) Second zoom showing the vertical refinement at the top

FIGURE 6.3: Mesh for the solid domain. Quadrangular elements. Whole and zoomed mesh representations near the fluid-solid interface

The most significant impulsive loads on the material occur when the pressure waves emitted by the water jet and the bubble collapse phenomena impact the solid. Therefore, the coupled simulations start when the micro water jet begins its formation. For that, a

not coupled fluid simulation was done in order to have the initial condition of velocity, density and pressure fields for the coupled simulations.

Fig. 6.4 illustrates the coupled (fluid + solid) domain. It shows the initial conditions for the coupled simulation, which corresponds to the beginning of the compression phase. In the fluid SPH domain, the blue particles represent the water and the red ones the gas. The solid SPH wall and the solid FEM wall are shown in green.

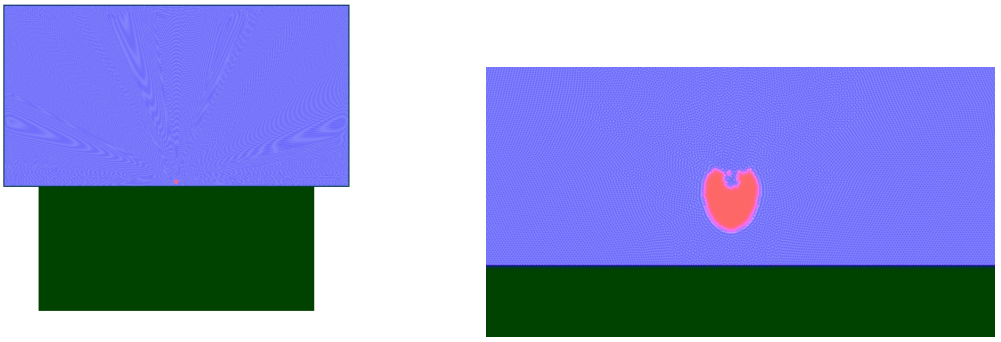

(a) Coupled (fluid + solid) domain

(b) Closer view of the bubble initial condition for the coupled simulation

FIGURE 6.4: Coupled (fluid + solid) domain. Initial conditions for the fluid SPH domain, the solid SPH wall and the solid FEM wall in green. Case $H_0/R_0 = 1.25$ $p_w/p_b = 353$.

The coupled simulations are done in two-dimensions considering a Cartesian coordinate system for simplicity, where the domain is located on the $x - y$ plane and z direction is the outward axis. For the structural model, it is considered the plane strain calculation assumption. This assumption considers that the strain in the outward direction is null. It means that the stress tensor in 2D has all the components non-null (i.e. $\sigma_x,\ \sigma_y,\ \sigma_z,\ \sigma_{xy}$) and the strain tensor in 2D only presents zero for the normal strains on the outward axis (i.e. $\epsilon_x,\ \epsilon_y,\ \epsilon_z = 0,\ \gamma_{xy}$).

In addition, the boundary conditions imposed on the solid domain are non-reflecting boundary condition on the three edges of the plate (i.e. two vertical and the bottom edges), except at the fluid-solid interface.

6.2.1.3 Physical considerations

Two materials are considered for this study, a standard steel and a stainless steel (SS) whose properties have been estimated by an internal study developed by ANDRITZ Hydro and the Stuttgart University [88]. Material properties, such as Young's modulus, yield stress and density, are presented in Table 6.1 and are specified as input in the

calculations. Fig. 6.5 shows the relation between the strain and the stress for both materials.

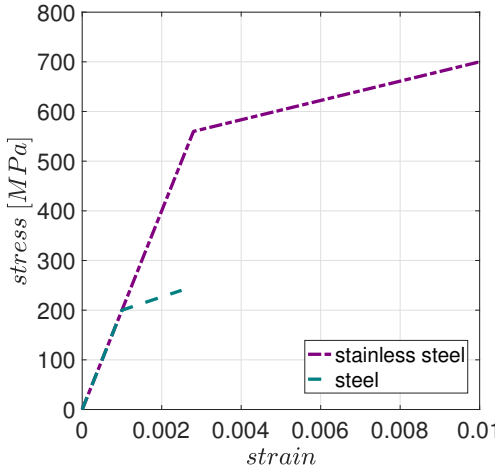

FIGURE 6.5: Stress-strain curves used in Europlexus to model elasto-plastic behavior of the two materials considered

TABLE 6.1: Material properties used for Europlexus simulations

Material	Yield stress [MPa]	Young's Modulus [GPa]	Poisson Modulus	Density $[Kg/m^3]$
steel	200	200	0.3	7800
SS CrNi13 4 [88]	560	200	0.288	7700

It is used an isotropic elasto-plastic law to model the material. This law means that as long as the local stresses do not exceed the Yield stress, the material deforms elastically during the loading, and then it returns to its initial state once the load is not longer applied. However, permanent deformation occurs if the Yield stress is surpassed.

For the fluid domain, it is considered the most severe cases. The pressure ratio driving the collapse corresponds to 353 and the standoff distances considered are $H_0/R_0 = 1.1$ and $H_0/R_0 = 1.25$.

6.2.2 Analysis of FSI simulations

The response of the solid material to impulsive loads from a non-condensable gas bubble has been studied through FSI simulations.

6.2.2.1 Pressure field in the fluid and the stresses in the solid domain

The FSI simulations are analyzed considering the pressure field in the fluid and the hydrostatic stress in the solid. According to the Cartesian coordinate system considered in the calculations, the domain is located in the $x-y$ plane and z direction is the outward axis, so the hydrostatic pressure involves the following stress components: σ_x, σ_y, σ_z. Since the plain strain calculation assumption is used, the three normal stress components are *a priori* non-zero.

In this section, we consider the hydrostatic pressure, which is a measurement of the normal stresses.

Fig. 6.6 shows the hydrostatic pressure evolution inside the solid due to pressure wave impacts. It shows the instants when the solid is impacted by the pressure waves. The first instant corresponds to the impact of the pressure wave emitted by the hit of the water jet against the bottom side of the bubble (Fig. 6.7(a)), while the second impact is due to the pressure wave emitted by the bubble collapse (Fig. 6.7(b)). The third instant is shortly after.

The hydrostatic pressure in the solid results from the pressure exerted by the fluid and it is transmitted through the fluid-solid interface. Color contours show negative and positive values of the hydrostatic pressure. The positive values indicate that the solid is under traction and the negative ones indicate that the solid is under compression.

The highest pressure in the fluid arrives to the solid as a loading that causes compression on the material at the impact zone. Then, the compression wave generated inside the material travels causing traction zones. Also, since the waves travel faster in the solid than in the water (i.e. the speed of sound is larger in the steel than in the water), the waves inside the material reach a larger zone than in the fluid.

In practice, an impulsion load generates two waves in the solid material, a normal wave and a shear wave. The normal wave can be represented by the hydrostatic pressure, while the shear wave can be addressed by the von Mises stress because it involves the shear components of the stress tensor. So, when the hydrostatic pressure is non-null, the material experiences normal waves. Otherwise, when the hydrostatic pressure is zero, it just means that the material does not experience normal waves, but it can undergo shear waves.

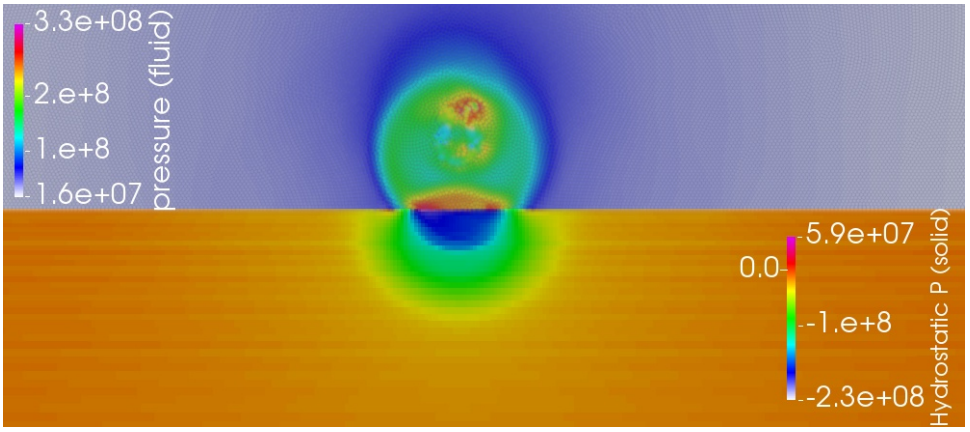

(a) $t/(R_0/c_w) = 17.2$

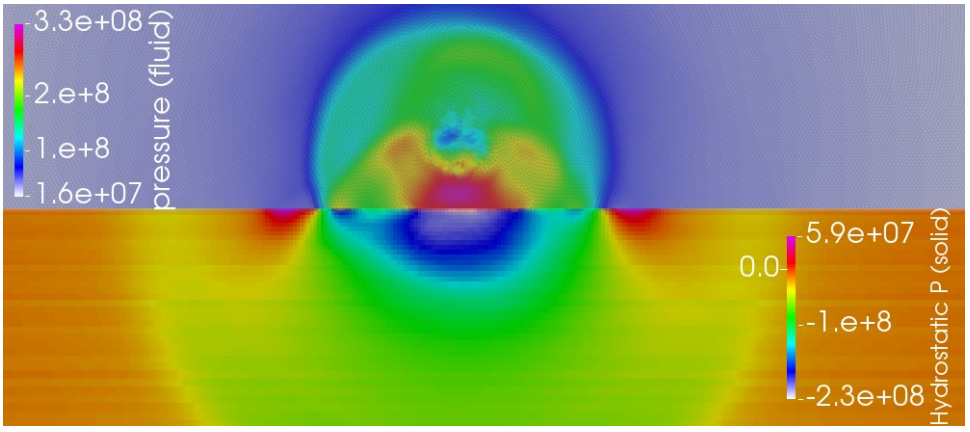

(b) $t/(R_0/c_w) = 17.7$

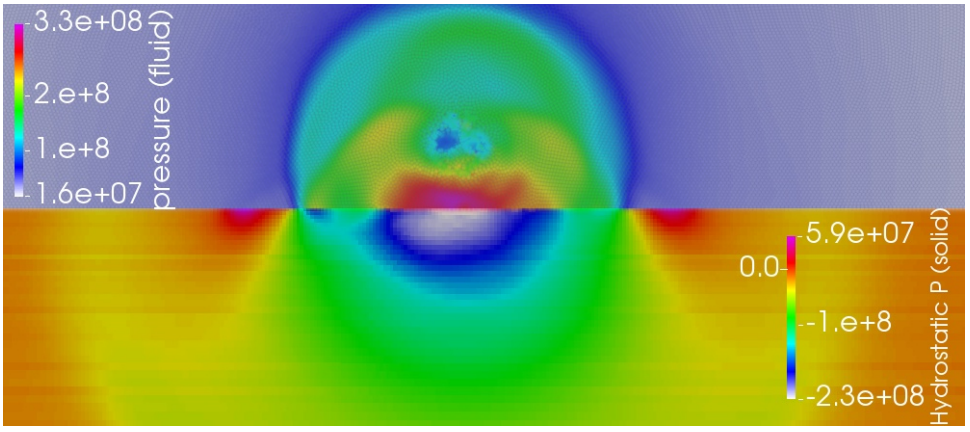

(c) $t/(R_0/c_w) = 17.8$

FIGURE 6.6: Evolution of pressure field $[Pa]$ in the fluid and solid domain due to the bubble collapse ($p_w/p_b = 353$ and $H_0/R_0 = 1.25$). Material: steel. (a) shows the instant of first impact on the wall ($t/(R_0/c_w) = 17.2$); (b) shows the instant of second impact on the wall ($t/(R_0/c_w) = 17.7$); (c) shows a moment after the second impact ($t/(R_0/c_w) = 17.8$).

Actually, the load produced by the fluid dynamics generates a compression stress in the normal direction with respect to the solid-fluid interface. The stress component normal to the solid-fluid interface (in this case σ_y) is the reaction to the fluid pressure. So, the

value of this stress component (σ_y), at the solid-fluid interface, is the fluid pressure at the interface with negative sign. The negative sign indicates that the material is under compression at this zone.

The evolution of σ_y is observed in Fig. 6.7. The instants are the same as represented in Fig. 6.6. The color palette in the solid domain has been inverted in order to compare σ_y with the fluid pressure. It is shown that the material reaction in the y-direction corresponds to the fluid pressure at the interface.

The components σ_x and σ_z are considered in order to show their contribution in the hydrostatic stress. Fig. 6.8 shows the evolution of σ_x and σ_z at the same three instants as in figures 6.6 and 6.7.

The stress component σ_x corresponds to the parallel direction with respect to the solid-fluid interface and σ_z corresponds to the stress in the outward direction with respect to the domain. It is observed that the material reacts to the fluid impulses by generating stress in all the directions. In the two direction considered here (x and z), compression waves are present in the material near the pressure pulse location, generating thus traction waves. It is noted that the compression and traction waves are less important in the z-direction than in the x-direction. Nonetheless, the three stress components σ_x, σ_y and σ_z present the same order of magnitude. Then, all these normal stress components contribute to the calculation of the hydrostatic pressure.

6.2.2.2 Material response: Hydrostatic pressure and von Mises stress

To analyze the material reaction under the impulsive load, the hydrostatic pressure and the von Mises stress are considered. Fig. 6.9 presents the hydrostatic pressure and the von Mises stress of the stainless steel CrNi13 4 subjected to the loading caused by a non-condensable gas bubble. This bubble is initially located at $H_0/R_0 = 1.25$ and its collapse is driven by a pressure ratio of $p_w/p_b = 353$.

Initially, pressure waves travel inside the solid due to the rarefaction waves emitted along the bubble compression. Then, the solid receives two impulsing loads, the first one comes from the micro jet event (Fig. 6.9(a)) and the second one develops from the bubble collapse event (Fig. 6.9(c)). So, the material experiences compression in a concentrated zone. The material reacts to these loads by generating pressure waves that travel inside it. Traction zones moving along the surface followed by compression

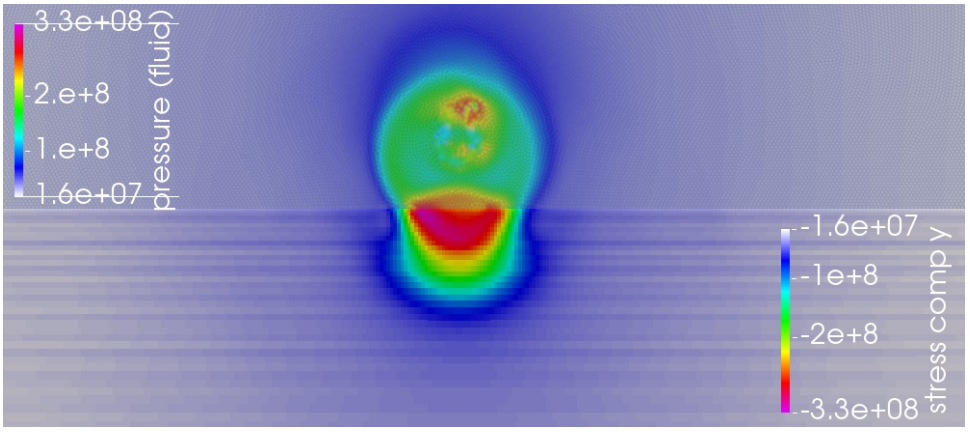

(a) $t/(R_0/c_w) = 17.2$

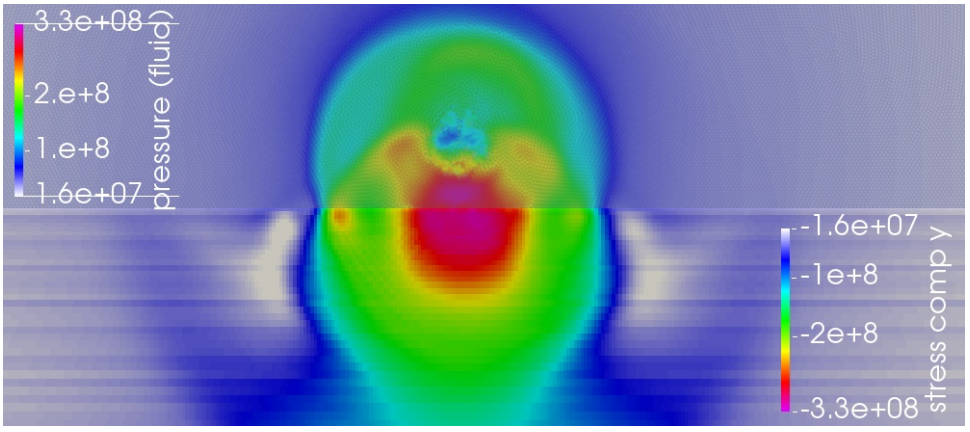

(b) $t/(R_0/c_w) = 17.7$

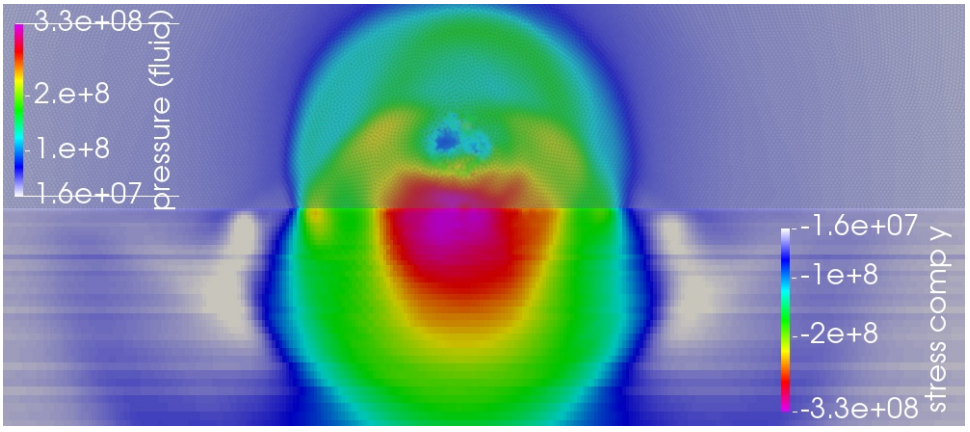

(c) $t/(R_0/c_w) = 17.8$

FIGURE 6.7: Evolution of pressure field $[Pa]$ in the fluid and the stress component σ_y in the solid domain due to the bubble collapse ($p_w/p_b = 353$ and $H_0/R_0 = 1.25$). Material: steel. (a) shows the instant of first impact on the wall ($t/(R_0/c_w) = 17.2$); (b) shows the instant of second impact on the wall ($t/(R_0/c_w) = 17.7$); (c) shows a moment after the second impact ($t/(R_0/c_w) = 17.8$).

zones are observed in figures 6.9(c) and 6.9(e). At the end, the material has experienced traction and compression states.

It is interesting to point out that during the hydrodynamic loading, several bubbles

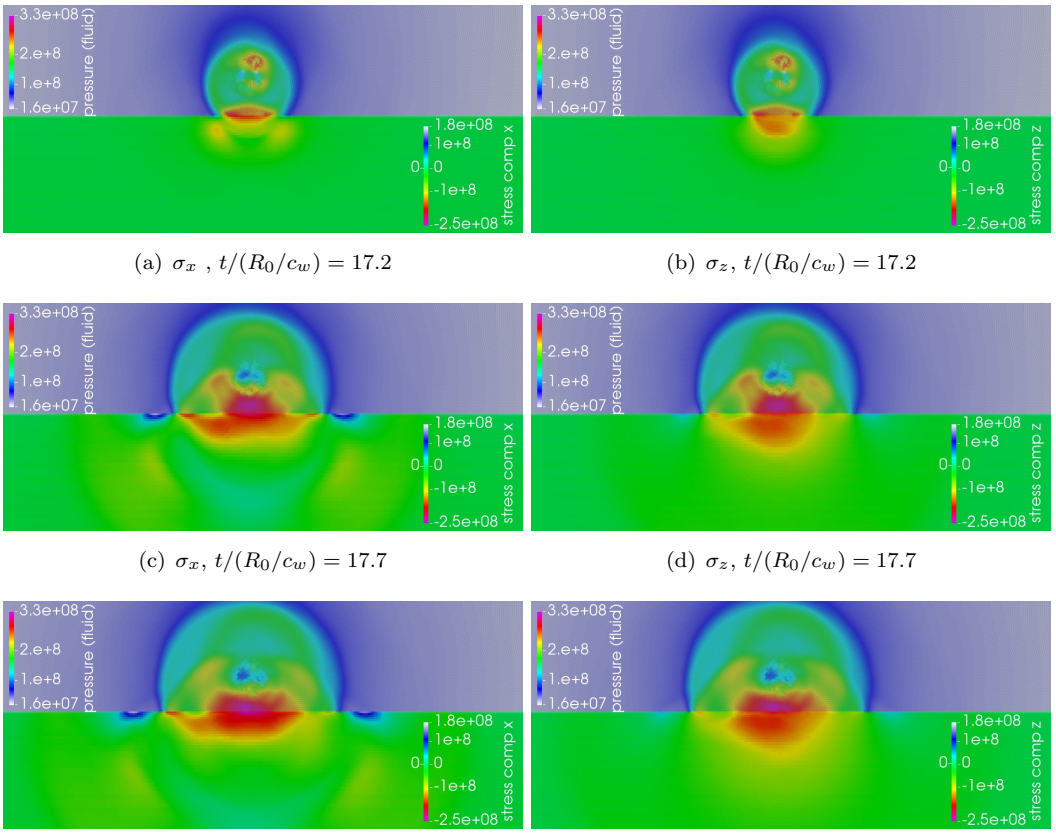

(a) σ_x , $t/(R_0/c_w) = 17.2$

(b) σ_z, $t/(R_0/c_w) = 17.2$

(c) σ_x, $t/(R_0/c_w) = 17.7$

(d) σ_z, $t/(R_0/c_w) = 17.7$

(e) σ_x, $t/(R_0/c_w) = 17.8$

(f) σ_z, $t/(R_0/c_w) = 17.8$

FIGURE 6.8: Evolution of pressure field $[Pa]$ in the fluid and the stress components σ_x and $\sigma_z$in the solid domain due to the bubble collapse ($p_w/p_b = 353$ and $H_0/R_0 = 1.25$). Material: steel. (a, b) shows the instant of first impact on the wall ($t/(R_0/c_w) = 17.2$); (c, d) shows the instant of second impact on the wall ($t/(R_0/c_w) = 17.7$); (e, f) shows a moment after the second impact ($t/(R_0/c_w) = 17.8$).

implode near the solid material causing that the material is under this repeated mechanism (i.e. the material passes from traction to compression states). In consequence and according to the literature ([24], [15], [14]), this repeated mechanism can produce fatigue failure in the material.

It is also observed the contours of the effective stress distribution or von Mises stress, which allow the estimation of zones where the stresses are concentrated. The effective stress appears when the material receives the impacts. The stressed zone is enlarged deeper in the material when the impacts are frequent and repeated (the material receives two loads, one from the micro jet event and the second one from the bubble collapse) as it is observed in figures 6.9(b) and 6.9(d). Then, Fig. 6.9(f) shows an instant shortly after the second load to exhibit that the load is still applied. Finally, the stress dissipates after the loading has passed.

For all the cases simulated, the highest stresses are observed below the material surface (see Fig. 6.9(f)), which is in agreement with previous works ([10], [24]).

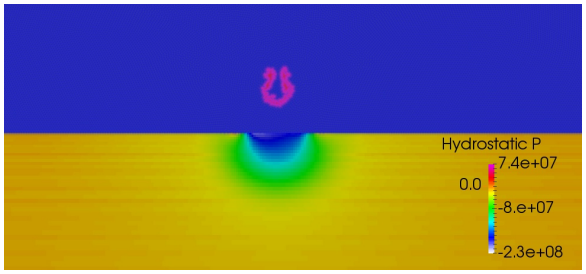

(a) Hydrostatic pressure (Pa) at $t/(R_0/c_w) = 17.2$

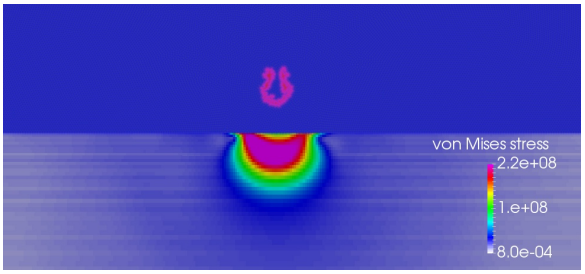

(b) Von Mises stress (Pa) at $t/(R_0/c_w) = 17.2$

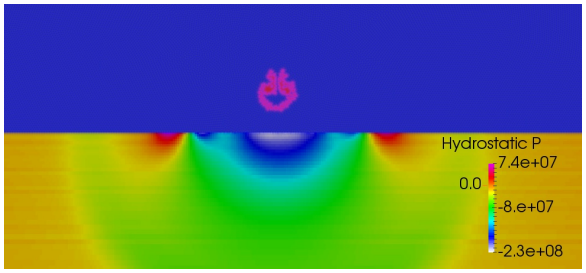

(c) Hydrostatic pressure (Pa) at $t/(R_0/c_w) = 17.7$

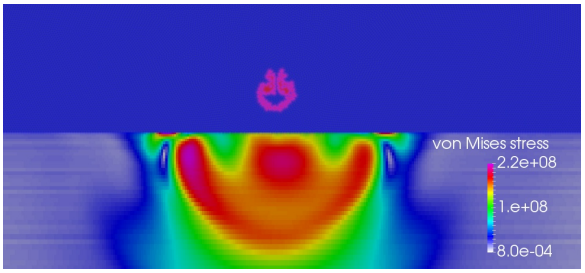

(d) Von Mises stress (Pa) at $t/(R_0/c_w) = 17.7$

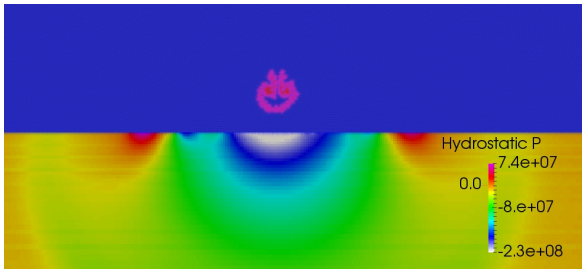

(e) Hydrostatic pressure (Pa) at $t/(R_0/c_w) = 17.8$

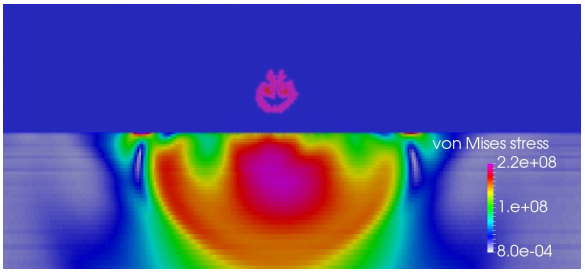

(f) Von Mises stress (Pa) at $t/(R_0/c_w) = 17.8$

FIGURE 6.9: Evolution of the material response due to the bubble collapse ($p_w/p_b = 353$ $H_0/R_0 = 1.25$). Material: stainless steel. (a) and (b) show the moment of the first wave impact on the wall (at $t/(R_0/c_w) = 17.2$)); (c) and (d) show the moment of the second wave impact on the wall (at $t/(R_0/c_w) = 17.7$)); (e) and (f) show a moment after the second impact ($t/(R_0/c_w) = 17.8$)).

It is considered thereafter the instant when the highest stress is registered in order to compare the standoff distance influence. Fig. 6.10 presents the stainless steel material reaction for standoff distances of $H_0/R_0 = 1.1$ and $H_0/R_0 = 1.25$. The color palette is the same for both cases in order to compare them.

Fig. 6.10 shows that the case of $H_0/R_0 = 1.1$ presents the highest compression and the highest von Mises stress values. This result is consistent with the one-way coupled results where the severe case corresponds to the bubble nearest to the wall. Additionally, the stress value increases as the amplitude value of the loading increase. This can be taken

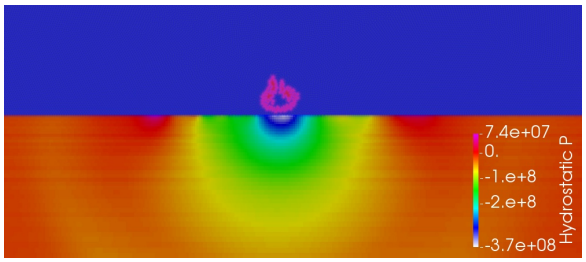

(a) Hydrostatic pressure (Pa) for $H_0/R_0 = 1.1$ at $t/(R_0/c_w) = 18$

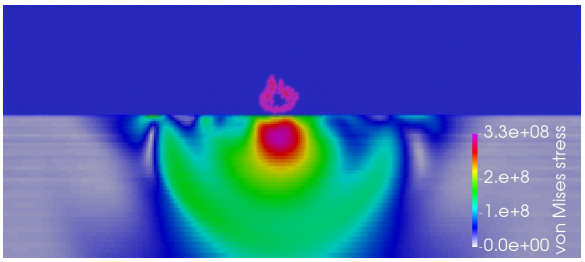

(b) Von Mises stress (Pa) for $H_0/R_0 = 1.1$ at $t/(R_0/c_w) = 18$

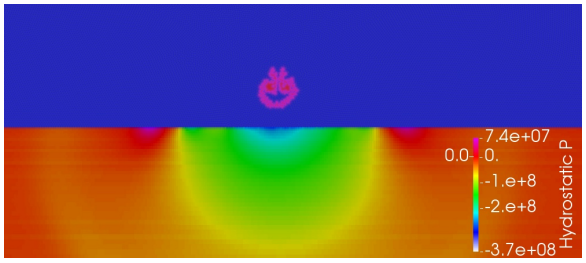

(c) Hydrostatic pressure (Pa) for $H_0/R_0 = 1.25$ at $t/(R_0/c_w) = 17.8$

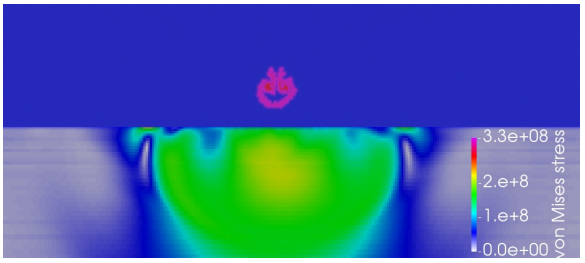

(d) Von Mises stress (Pa) for $H_0/R_0 = 1.25$ at $t/(R_0/c_w) = 17.8$

FIGURE 6.10: Material response at the moment of the highest stress due to the bubble collapse ($p_w/p_b = 353$ for two H_0/R_0 values). Material: stainless steel.

from figures 6.10(b) and 6.10(d), because it is known that higher loads are registered from the bubbles initially located closer to the solid (see Section 5.3.5).

Since the simulation domain is dimentionalized with respect to the bubble radius, we are able to give some orders of magnitude (see Fig. 6.11(a)). Firstly, it is chosen the case involving the stainless steel; it is found that the location of the maximum stress depends on the standoff distance between the bubble and the wall. The maximum stress location from the material surface is at $0.2R_0$ for $H_0/R_0 = 1.1$ and $0.4R_0$ for $H_0/R_0 = 1.25$. So, the maximum stress location is closer to the material surface when the bubble implodes closer to the solid. Secondly, the material effect is also addressed by analyzing the results obtained with steel. In this case, the stress location is at $0.5R_0$ for $H_0/R_0 = 1.25$. This shows that material properties also affect the maximum stress location. The potential damage would be placed deeper in the material for materials having weaker stress yield.

In addition, it is known from the literature [45] that the range of a real cavitation bubble radius is between 50 μm and 500 μm. Thus for the estimation, a value of 300 μm for the bubble radius is taken. With this value, we estimate that the maximum stresses are located at 60 μm for the case where $H_0/R_0 = 1.1$ and at 120 μm for the case $H_0/R_0 = 1.25$, these results corresponding to the stainless steel (see Fig. 6.11(b)). For the steel, we found the maximum stress location at 150 μm for $H_0/R_0 = 1.25$. These

results highlight the stress location dependency to the standoff distance and the material. Of course, these stress locations varies with the bubble size.

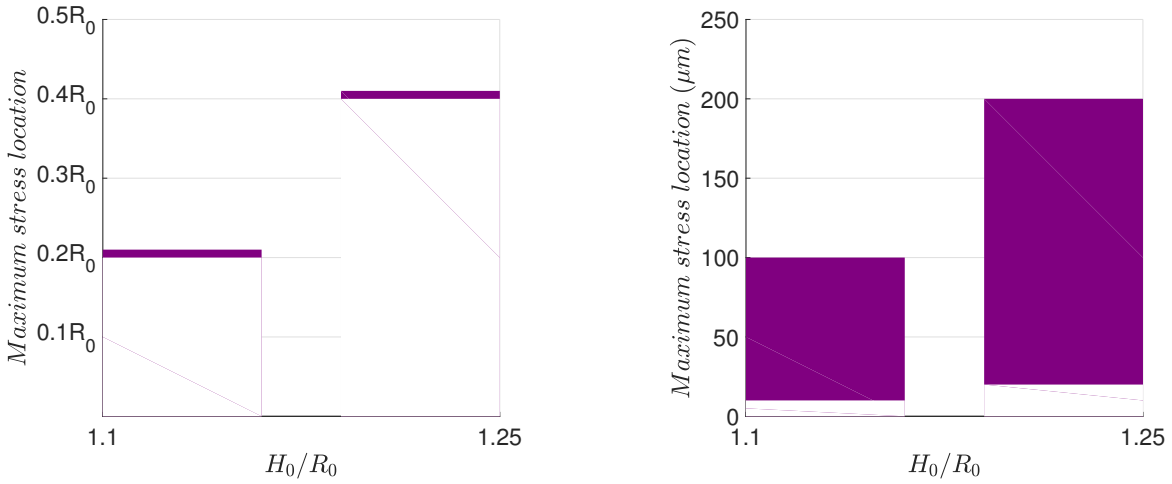

(a) Maximum stress location expressed in function of R_0

(b) Estimation of the maximum stress location considering $R_0 = 300\ \mu m$

FIGURE 6.11: Maximum stress location in the material for $p_w/p_b = 353$ and for two H_0/R_0 values. Material: stainless steel.

Additionally, from an industrial point of view, the material surface is usually coated. The coating thickness is between 100 μm and 500 μm. So, these findings suggest that the concentrated stresses may be located in the vicinity of the interface between the material and the coating. However, an extended study considering the coating and the material in the FSI simulations is recommended in order to go deeper in this regard.

6.2.2.3 Material response: von Mises stress and strain

Strain characterizes a deformation that could happen when the material is under a certain stress. When the stress is removed and the material returns to its initial shape, the deformation is non permanent, so the material has an elastic strain. On the other hand, when the stress is removed and the material does not return to its initial shape, the material experiences a plastic strain. Hence, we are interested in analyzing the cases where plastic strain has been reached as an indicator of damage.

The plastic strain is only registered in the simulation where the steel material is considered, in which stress values are higher than the steel Yield stress. Fig. 6.12 shows the von Mises stress and the strain at the instant when the highest stress is registered. This moment arrives shortly after the second pressure wave coming from the bubble collapse

impacts the wall. This figure corresponds to the case of $H_0/R_0 = 1.25$ and $p_w/p_b = 353$. For stainless steel cases, plastic strain values are not observed, basically because the stress values do not exceed the stainless steel Yield stress.

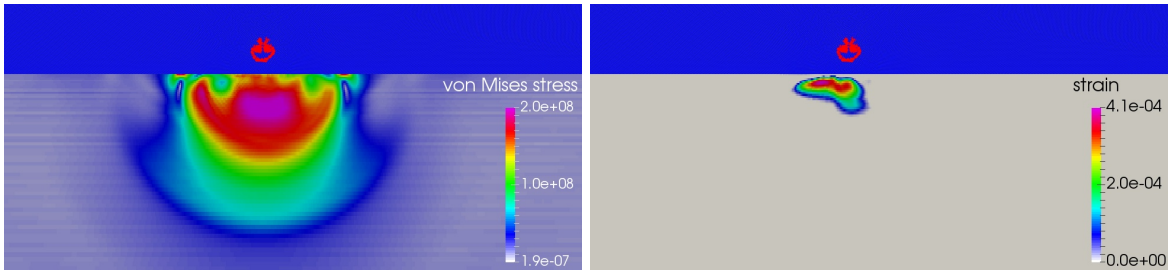

(a) von Mises stress (Pa) (b) strain

FIGURE 6.12: Material response at $t/(R_0/c_w) = 17.8$, moment of highest stress due to the bubble collapse for $p_w/p_b = 353$ and $H_0/R_0 = 1.25$. Material: steel.

The plastic strain maximum value is observed around the same location where the maximum stress is registered, i.e. below the surface. It is important to mention that the plastic strain value is just an indicator of material plasticity. Hence, we can argue that during several impulsive loads, the compression stress below the surface may reach the material yield, generating a zone of plastic strain. From there on, the plastic strain region continues to grow inducing a progressive hardening. The material gradually becomes more fragile and the probability of micro-ruptures increases, leading to the material erosion.

6.3 Conclusion

The fluid-structure interaction approach has been addressed through out this Chapter. The solver (Europlexus) used for the solid domain has been described, as well as the coupling solver developed by Nunez-Ramirez [69]. Two materials, i.e. steel and stainless steel, are considered to study the material response under the bubble dynamics. The materials are considered as isotropic and they follow the elasto-plastic law.

There are two main impulsive loads that could damage the material. The first one comes from the micro jet event and the second one develops from the bubble collapse event. The material reacts to these loads by having compression and traction zones that travel inside the material. Since the material passes from traction to compression states in a repeatedly way, a fatigue mechanism could drive the damage phenomenon.

The highest stresses are located below the material surface indicating that the damage starts under the material surface, making this region more fragile, and thus, more subjected to micro-ruptures. This location depends on the bubble size, the standoff distance and the material properties. This result suggests that under certain conditions, the highest-stress location may coincide with the coating-steel interface. However further investigation in this regard is suggested.

Chapter 7

Conclusion and perspectives

7.1 Conclusions

The first objective of this thesis is the development of a numerical model able to simulate the compression of non-condensable gas bubble and to estimate the pressure loads emitted during this phenomenon near a solid boundary. For this purpose, a two-phase model in the SPH-ALE method able to deal with fully compressible fluids was developed and validated. It solves the mass, momentum and energy conservation equations of the Euler system using the Stiffened Gas EOS for water and the ideal gas EOS for the gas bubble.

The meshless feature of the SPH-ALE method allows the calculation of two-phase flow defining a sharp interface and avoiding special mesh treatments near the interface zone, typically present in mesh-based methods. However, for this type of applications where the Mach number is around 0.5, the Lagrangian motion of SPH particles is not adequate. In consequence, the ALE scheme was exploited through the implementation of a proper algorithm to correct the motion of particles for compressible flows. This implementation allows the simulation of compressible flows and the propagation of pressure waves in order to take into account the compression of a non-condensable gas bubble.

The compression of a non-condensable gas bubble in free field was simulated to study the fluid dynamics and validated against analytic and numerical results. Then, the bubble dynamics near a wall was simulated in order to investigate the bubble dynamics and the loading caused by its collapse. Characteristic quantities, such as collapse times, bubble displacements, velocities and pressures, were analyzed as a function of time and with

respect to the initial-standoff distance between the bubble and the wall. As well, these quantities were compared against available theories and numerical simulations showing good agreement.

Due to computational cost issues, the simulations were carried out following a 2D configuration. In consequence, an analytic comparison between 3D and 2D configurations was conducted showing that the 2D configuration allows the description of the fluid dynamics. Nevertheless, some difference between the 2D and 3D models are encountered and discussed. Particularly, there is a difference in the pressure peak and the pressure profile in the liquid during the bubble compression. The pressure decay described by the 2D simulation is slower than the one described by the 3D simulation. This difference is due to the law used for the description of each configuration, i.e. the inverse-square law is used in the 3D configuration and the inverse-law used in the 2D assumption. Although, the pressure peak and the decreasing rate is affected by the 2D assumption, the liquid pressure tendency is comparable qualitatively in both configuration.

In the case of the bubble compression near a wall, a micro jet directed towards the surface is observed. This micro jet is developed due to the non-symmetric configuration given by the solid boundary. It impacts the bottom side of the bubble generating a pressure wave that propagates radially outwards. Additionally, high velocities are linked to the micro water jet formation, producing a water-hammer phenomenon in the liquid. Afterwards, the bubble collapses by itself emitting a second pressure wave that also propagates radially inside the liquid. These two phenomena lead to high pressures pulses on the wall.

The pressure waves generated by the water jet and the bubble collapse propagate in the liquid and eventually impact the solid wall. The wall is thus affected by the loading generated during the bubble compression. The wall receives a loading characterized by two pressure peaks that are linked to the two pressure waves emitted in the fluid. In consequence, one or two pressure peaks are observed depending on the standoff distance. For bubbles initially located at relatively short distance with respect to the wall (e.g. $H_0/R_0 < 2$), two pressure waves well separated are observed. On the other hand, for bubbles initially located at $H_0/R_0 = 2$ and $H_0/R_0 = 3$, only one pressure peak is observed. This occurs because as the standoff distance increases, the two pressure wave emissions get closer until the case where both wave emissions occur at the same time. Consequently, only one pressure peak is registered on the wall. For bubbles far away

from the wall (e.g. $H_0/R_0 = 5$) the micro jet is not clearly formed and only the pressure wave generated by the collapse of the bubble itself is present.

In cases where the water jet is observed (e.g. $H_0/R_0 \leq 3$), the water-hammer event is present, the corresponding pressure wave is generated and thus, it arrives to the wall. This wavefront is attenuated while it travels inside the liquid, producing pressure pulse of less amplitude for cases where the wave emission happens farther away from the wall.

It is to remark that as the initial standoff distance is shorter, the pressure amplitudes registered on the wall increase. Hence, the bubbles that can cause more damage are the ones located initially closer to the wall. This is also shown through the impulse calculation, which is an indicator of the potential loading by considering not only the pressure value but also the applied time of the pulse.

The second objective of this thesis is to have an insight towards the erosion by cavitation through fluid-structure interaction simulations. Two materials (steel and stainless steel) are considered to study the material response under the non-condensable gas bubble dynamics. Both materials are considered as isotropic and they follow the elasto-plastic law.

The response of the solid material to these impulsive loads is described as an alternating behavior that involves compression and traction mechanisms on the material. This material reaction can lead to fatigue as a damage phenomenon.

Additionally, it was found that the zones of highest stress are located below the material surface, indicating that the damage starts there, making this region more fragile, and thus, more subjected to micro-ruptures. The stress location was determined in function of the bubble size, the standoff distance and the material properties. This result suggests that under certain conditions, the highest-stress location may coincide with the coating-steel interface.

7.2 Perspectives

In order to simulate real bubbles and be able to do a direct comparison against existing experiments, a numerical tool that allows the running of 3D simulations must be implemented. To do so, an adaptive particle refinement for SPH-ALE method is contemplated in order to reduce the amount of particles in the liquid domain and to make possible 3D

calculations in a acceptable computational time. Additionally, it would be interesting to carry out an extended study considering pressure ratios around the cavitation pressure ratio, i.e. 34, in order to analyze if there are changes in the fluid flow and what is the influence on the pressure profile on the wall.

In nature, a cavitation bubble that undergoes compression contains mainly vapor and only a small amount of non-condensable gas. During the collapse, the vapor may condense. Hence, for the same initial radius, the minimum radius attained is smaller for a vapor bubble than for the simulated non-condensable gas bubble. In consequence, the pressure amplitudes may be influenced by the phase change phenomenon. This suggests that the consideration of vapor inside the bubble and the inclusion of phase change phenomenon seem necessary in the simulation of cavitation bubble collapse.

Another phenomenon that may influence the bubble dynamics is the flow velocity. Then, it can be interesting to analyze the dynamics of a bubble subjected to a velocity field parallel to the wall. The velocity field may increase the flow aggressiveness and so change the pressure profile on the wall.

Simulations of the interaction between several bubbles can be considered because it is believed that their interaction increases the aggressiveness of the fluid flow and thus increases the material damage. In this regard, it is proposed to take advantage of the mesh-less feature of the compressible SPH-ALE method to simulate the interaction of several bubble without the inconvenient of constant re-meshing.

It has been suggested that the fatigue could be the erosion mechanism followed by the material when a cavitating flow is present. So, a fatigue analysis must be included in order to predict the material life cycle under a repeated hydrodynamic load.

Additionally in terms of material response, the coating that is used to protect the material of Pelton turbines should be considered in the FSI simulation in order to determine its influence in the material response. Actually, the coating properties are different than the stainless steel ones. So, its behavior face to hydrodynamic loading might not be exactly the same as the behavior followed by the stainless steel. As well, the contact between the stainless steel and the coating may change the material behavior, for example by changing the location of maximum stresses. Hence, the interaction between both materials (i.e. coating and stainless steel) should be evaluated in order to determine its influence on the material response.

Below, it is given the publication list from this thesis work:

Pineda S.; Marongiu J.-C.; Aubert S.; Lance M. Comparison of numerical results using a barotropic and a non-isentropic EOS in SPH-ALE method. In 11th international SPHERIC workshop, Munich, Germany, June 2016.

Pineda S.; Marongiu J.-C.; Aubert S.; Lance M. Multiphase model in SPH-ALE for modeling a fully compressible multiphase flow. In 11th international SPHERIC workshop, Munich, Germany, June 2016.

Appendix A

Comparison between Tait and Stiffened Gas EOS

The dam break flow is a typical free surface problem often used as a benchmark for SPH implementations [54]. It is considered a 2D simulation. The fluid is confined between two vertical walls. After a sudden removal of one of these barriers holding the water at rest, the fluid can flow. The initial fluid column is 1 m wide and 2 m high that is contained in a square box of 4 m. The water column is represented with 5000 fluid particles.

In this test case, the flow using the Stiffened Gas EOS is simulated and the idea is to compare it with respect to the Tait EOS results already presented and validated [83], [54]. Both numerical results were solved using the SPH-ALE method with a MUSCL reconstruction scheme. The Tait and the Stiffened Gas EOS simulations use the same initial particle configuration.

Table A.1 shows the fluid parameters for the simulation using Tait EOS and the one using Stiffened Gas EOS. The constant parameters γ and p_∞ for the Stiffened Gas EOS are chosen to have the same speed of sound value that the one used in Tait EOS. Hence both simulations can be compared for the same Mach number. The maximum Mach number along the simulation is 0.13.

Regarding stability limits, it has been observed a lower limit in the CFL condition using the Stiffened Gas EOS. Considering the Heun method for numerical integration, we have seen that the CFL condition is 0.2 with the Tait EOS, but using the Stiffened Gas

TABLE A.1: Fluid parameters for 2D dam break simulation

Tait EOS		**Stiffened Gas EOS**	
γ	7.15	γ	1.86
ρ_{ref} $[kg/m^3]$	1000	ρ $[kg/m^3]$	1000
p_{ref} $[MPa]$	0	p_∞ $[MPa]$	3
c_{ref} $[m/s]$	75	c $[ms]$	75

EOS the CFL condition is 0.1. This restriction in the stability condition increments the computational time and the CPU workload when using the Stiffened Gas EOS.

For comparative purposes, figures (A.1) and (A.2) show the velocity and pressure fields for $t = 0.70\ s$ and $t = 1.5\ s$. We observe that the particles have a good spatial distribution along the simulation. These fields are in good agreement between both simulations.

The computed water depth as a function of time is compared for the Tait EOS, the Stiffened Gas EOS and experimental values from [96]. The dimensionless parameters are given by $h^* = h/(2L)$ and $t^* = t\sqrt{2g/L}$, where L and h are the initial length and height of the water column respectively, in this case $L = 1$ and $h = 2$.

Figure A.3 shows the water height evolution. First, we observe the numerical results using Tait and Stiffened Gas EOS are in very good agreement. Both results predict similarly the water height evolution for the time recorded. Second, comparing the numerical results to the experimental one, we observe that the numerical results roughly predict the experimental behavior; differences can be due to the numerical viscosity that is not fully reduced.

The main topic here is the comparison of the same numerical method using different equations of state. So, focusing on this subject, the results from both models are analyzed. It is obtained that both results are equivalent. This is because the fluid flow behaves like a weakly-compressible flow, i.e. the density variations are very small. Consequently, the non-isentropic model reduces to the barotropic model, and thus they are equivalent (see Section 3.2.4). To demonstrate the weakly compressible feature, Fig. A.4 shows that negligible variations (less than 0.1%) in density and internal energy in the system are recorded.

About the numerical viscosity, it is linked to the numerical method, in this case SPH-ALE, and it does not depend on the equation of state. Therefore, both approaches present equal numerical dissipations.

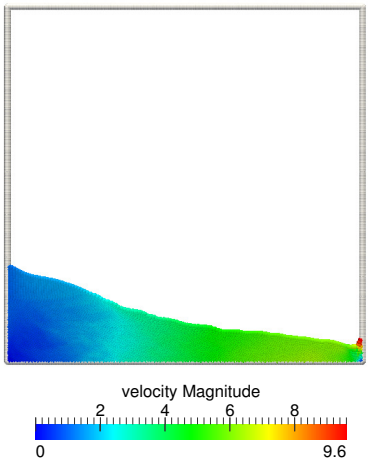

(a) Tait EOS

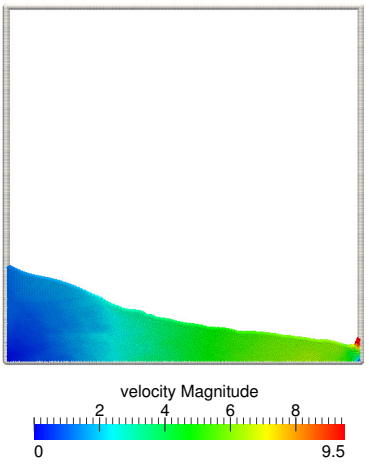

(b) Stiffened Gas EOS

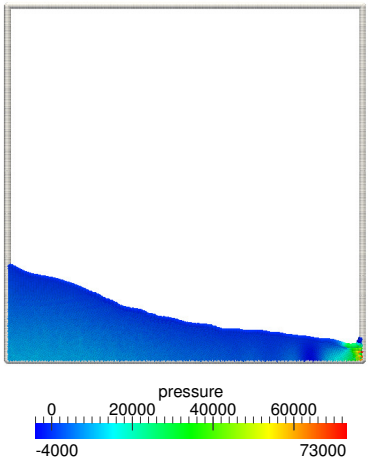

(c) Tait EOS

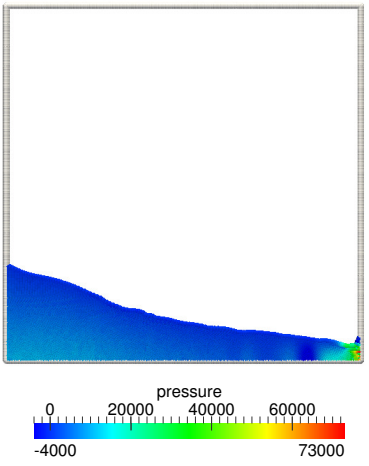

(d) Stiffened Gas EOS

FIGURE A.1: Dam break test case. Numerical results for the Tait EOS and the Stiffened Gas EOS. Numerical results at $t = 0.70\ s$

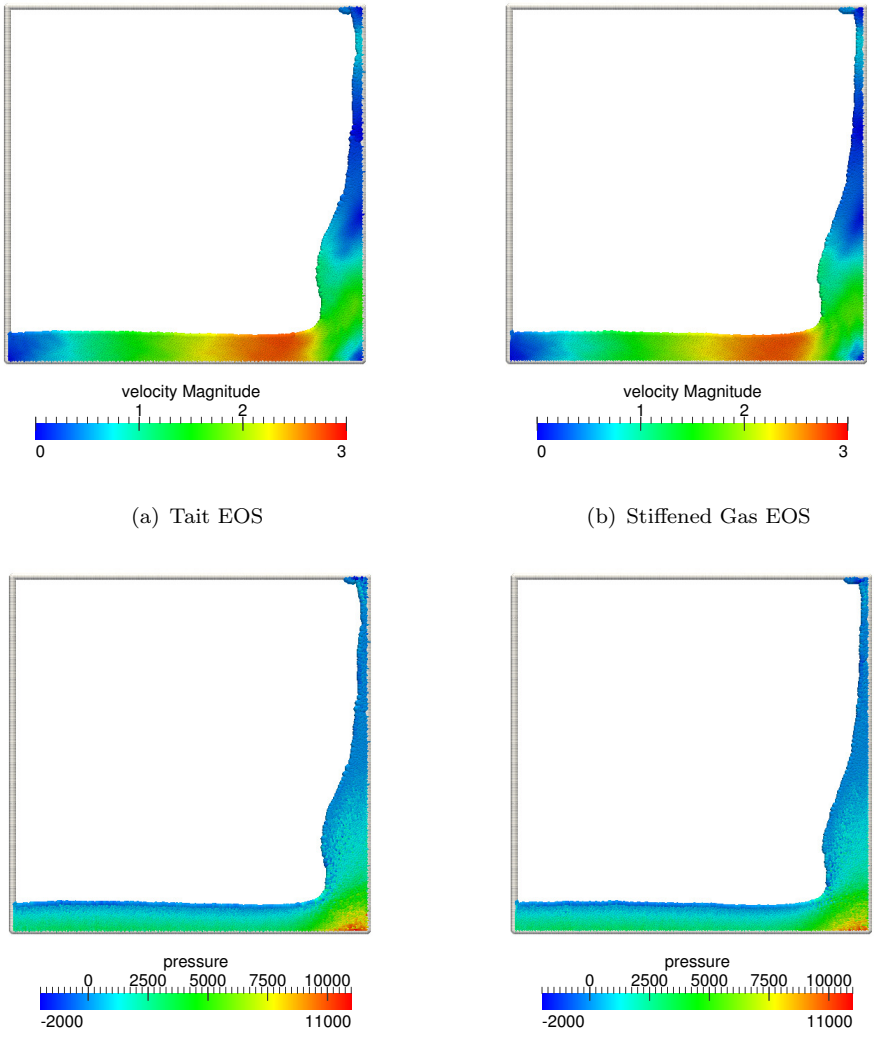

(a) Tait EOS

(b) Stiffened Gas EOS

(c) Tait EOS

(d) Stiffened Gas EOS

FIGURE A.2: Dam break test case. Numerical results for the Tait EOS and the Stiffened Gas EOS. Numerical results at $t = 1.50\ s$

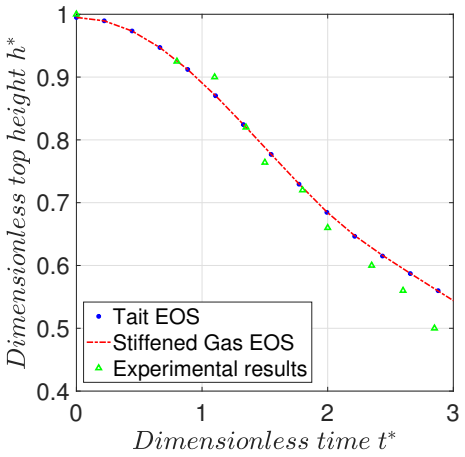

FIGURE A.3: Dam break test case. Water height evolution. Comparison between numerical results obtained from the Tait EOS (circle), the Stiffened Gas EOS (dashed lines) and experimental results [96] (triangle)

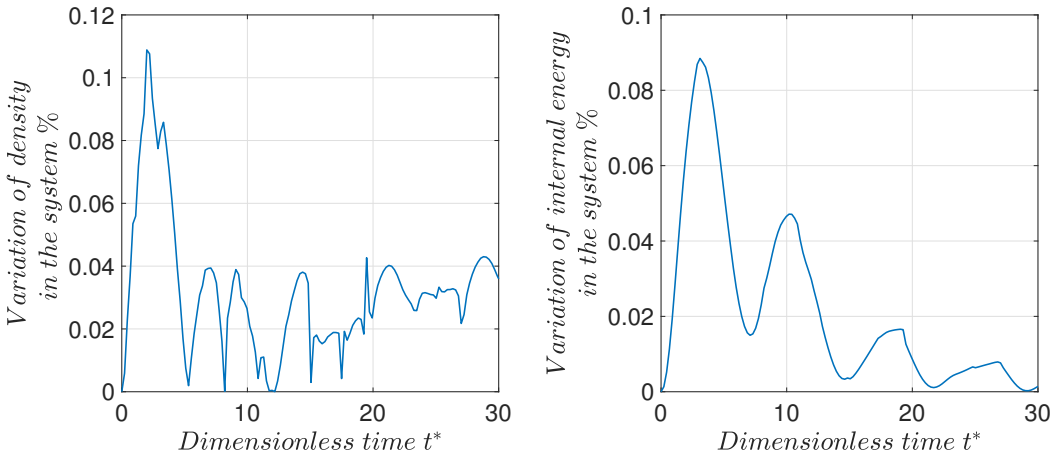

FIGURE A.4: Dam break test case. Evolution of density and internal energy of the system using Stiffened Gas EOS. Average calculated among the SPH particles for each time

Bibliography

[1] Bergerat, L. (2012). *Développement dune méthode numérique compressible pour la simulation de la cavitation en géométrie complexe.* PhD thesis, Ecole Nationale Supérieure d'Arts et Métiers.

[2] Bogoyavlenskiy, V. (1999). Differential criterion of a bubble collapse in viscous liquids. *Physical Review E*, 60(1):504–508.

[3] Brennen, C. E. (1995). *Cavitation and bubble dynamics.* Oxford University Press.

[4] Brujan, E., Ikeda, T., and Matsumoto, Y. (2008). On the pressure of cavitation bubbles. *Experimental Thermal and Fluid Science*, 32:1188–1191.

[5] Brujan, E., Ikeda, T., Yoshinaka, K., and Matsumoto, Y. (2011). The final stage of the collapse of a cloud of bubbles close to a rigid boundary. *Ultrasonics Sonochemistry*, 18:59–64.

[6] Campos-Amezcua, R. (2012). *Analyse des écoulements cavitants stationaires et instationaires dans les turbomachines.* PhD thesis, Ecole Nationale Supérieure d'Arts et Métiers.

[7] Can, E. and Prosperetti, A. (2012). A level set method for vapor bubble dynamics. *Journal of Computational Physics*, 231:1533–1552.

[8] Cengel, Y. A. and Boles, M. A. (2006). *Thermodynamics: an engineering approach.* McGraw-Hill, fifth edition edition.

[9] Chahine, G. (1984). Pressures generated by a bubble cloud collapse. *Chem. Eng. Commun*, 28:355–367.

[10] Chahine, G., Kapahi, A., Choi, J., and Hsiao, C. (2016). Modeling of surface cleaning by cavitation bubble dynamics and collapse. *Ultrasonic Sonochemistry*, 29:528–542.

[11] Choi, J. and Chahine, G. (2016). Relationship between material pitting and cavitation field impulsive pressures. *Wear*, 352-353:42–53.

[12] Choi, J.-K. and Chahine, G. (2015). Experimental and numerical study of cavitation erosion resistance of a polyurea coating layer. In *Fourth International Symposium on Marine Propulsors SMP 15*, USA.

[13] Colagrossi, A. (2012). Particle packing algorithm for sph schemes. *Computer Physics Communications*, 183.8:1641–1653.

[14] Coudouel, G., Combescure, A., and Marongiu, J.-C. (2017a). Numerical simulation of droplet impact erosion : Dang van fatigue approach. In *VII International Conference on Computational Methods for Coupled Problems in Science and Engineering*, Greece.

[15] Coudouel, G., Combescure, A., and Marongiu, J.-C. (2017b). Prédiction du dommage par impacts de gouttes deau sur une structure métallique. In *13eme Colloque National en Calcul des Structures*, France.

[16] Cummins, S. and Rudman, M. (1999). An sph projection method. *Computer Physics Communications*, 152.2:584–607.

[17] Cussler, E. L. (1997). *Diffusion: Mass transfer in fluid systems.* Cambridge university press, second edition edition.

[18] Dubois, F. (2001). *Partial Riemann problem, boundary conditions and gas dynamics. In Absorbing Boundaries and Layers, Domain decomposition methods: Applications to large scale computations.* Nora Science publishers, Inc.

[19] Eringen, A. C. (1967). *Mechanics of Continua.* Jhon Wiley and Sons, Inc.

[20] Flageuil, C., Fortes-Patella, R., and Archer, A. (2012). Cavitation erosion prediction by numerical simulations. In *14th International Symposium on Transport Phenomena and Dynamics od Rotating Machinery ISROMMAC-14*, Honolulu, USA.

[21] Fortes-Patella, R. (1994). *Analyse de l'erosion de cavitation par simulations numériques d'impacts.* PhD thesis, Institut National Polytechnique de Grenoble.

[22] Fortes-Patella, R., Archer, A., and Flageul, C. (2012). Numerical and experimental investigations on cavitation erosion. In *26th IAHR Symposium on Hydraulic Machinery and Systems.*

[23] Fortes-Patella, R., Challier, G., Reboud, J., and Archer, A. (2001). Cavitation erosion mechanism: Numerical simulations of the interaction between pressure waves and solid boundaries. In *CAV 2001*.

[24] Fortes-Patella, R., Choffat, T., Reboud, J., and Archer, A. (2013). Mass loss simulation in cavitation erosion: Fatigue criterion approach. *Wear*, 300:205–215.

[25] Franc, J.-P. and Michel, J.-M. (2006). *Fundamentals of cavitation*. Kluwer Academic Publisher.

[26] Fujikawa, S. and Akamatsu, T. (1978). Experimental investigation of cavitation bubble. *Bulletin of the JSME*, 21(152):223–230.

[27] Fuster, D., Dopazo, C., and Hauke, G. (2011). Liquid compressibility effects during the collapse of a single cavitating bubble. *Journal Acoustical Society of America*, 129:122–131.

[28] Grekula, M. and Bark, G. (2001). Experimental study of cavitation in a kaplan model turbine. In *Fourth international symposium on cavitation (CAV 2001)*.

[29] Gueyffier, D., Li, J., Nadim, A., Scardovelli, R., and Zaleski, S. (1999). Volume-of-fluid interface tracking with smoothed surface stress methods for three-dimensional flows. *Journal of Computational Physics*, 152:423–456.

[30] Guilcher, P. (2008). *Contribution au développement d'une méthode SPH pour la simulation d'interaction houle-structure*. PhD thesis, Ecole centrale de Nantes.

[31] Hirsch, C. (1988a). *Numerical Computation of Internal and External Flows*, volume 2. John Wiley and Sons.

[32] Hirsch, C. (1988b). *Numerical Computation of Internal and External Flows*, volume 1. John Wiley and Sons.

[33] Hsiao, G. C. R. A. C. and Harris, G. (2006). Scaling rules for the prediction on undex bubble re-entering jet parameters. *SAVIAC Critical Technologies in Shock and Vibration*, 4(1):1–12.

[34] Hu, X. and Khoo, B. (2004). An interface interaction method for compressible multifluids. *Journal of Computational Physics*, 198:35–64.

[35] Hydrolink (2009). Small hydro power. http://www.hydrolink.cz/en/pelton-turbines/hhp-h-type-horizontal-compact-pelton-turbine-4.html.

[36] Inanc, S. and Wei, S. (2002). Evaluation of cavitation models for navier-stokes computations. In *ASME 2002 Fluid Engineering Division Summer Meeting*.

[37] Ivings, M., Causon, D., and Toro, E. (1998). On riemann solvers for compressible liquids. *International Journal for Numerical Methods in Fluids*, 28.3:395–418.

[38] Johnsen, E. and Colonius, T. (2006). Implementation of weno schemes in compressible multicomponent flow problems. *Journal of Computational Physics*, pages 1–18.

[39] Johnsen, E. and Colonius, T. (2008). Shock-induced collapse of a gas bubble in shockwave lithotripsy. *L. Acoustical Society of America*, 124(4):2011–2020.

[40] Johnsen, E. and Colonius, T. (2009). Numerical simulations of non-spherical bubble collapse. *Journal of Fluid Mech.*, 629:231–262.

[41] Joseph, D. and Saut, J.-C. (1990). Short-wave instabilities and ill-posed initial-value problems. *Theoret. Comput. Fluid Dynamics*, 1:191–227.

[42] Joshi, S., Ghigilotti, G., Franc, J.-P., and Fivel, M. (2017). Development of solid sph solver with fluid-structure interaction within sphysics: Application to cavitation erosion. In *12th international SPHERIC workshop*, Ourense, Spain.

[43] Kapahi, Hsiao, C., and Chahine, G. (2015). Shock-induced bubble collapse versus rayleigh collapse. In *9th International Symposium on Cavitation (CAV 2015)*.

[44] Keller, J. and Miksis, M. (1980). Bubble oscillations of large amplitude. *The Journal of the Acoustical Society of America*, 68(2):628–633.

[45] Ki-Han Kim, Georges Chahine, J.-P. F. and Karimi, A. (2014). *Advanced experimental and numerical techniques for cavitation erosion prediction.*, volume 106. Springer.

[46] Krieger, J. and Chaine, G. (2005). Acoustic signal of underwater explosions near surfaces. *J. Acoust. Soc. Am.*, 118:2961–2974.

[47] Krumenacker, L., Fortes-Patella, R., and Archer, A. (2014). Numerical estimation of cavitation intensity. In *27th IAHR Symposium on Hydraulic Machinery and Systems (IAHR 2014)*.

[48] Kunz, R. (2000). A preconditioned navierstokes method for two-phase flows with application to cavitation prediction. *Computers and Fluids*, 29:849–875.

[49] Lauer, E. (2012). Numerical modelling and investigation of symmetric and asymmetric cavitation bubble dynamics. *Computers and Fluids*, 69:1–19.

[50] Le-Metayer, O., Massoni, J., and Saurel, R. (2005). Modelling evaporation fronts with reactive riemann solvers. *Journal of Computational Physics*, 205:567–610.

[51] Le-Metayer, O. and Saurel, R. (2016). The noble-able stiffened gas equation of state. *Physics of fluids, American Institute of Physics*, 28:046102.

[52] LearnEngineering and Ltd, I. C. E. P. (2011). Pelton turbine - working and design aspects.

[53] Leclercq, C., Archer, A., and Fortes-Patella, R. (2016). Numerical investigations on cavitation intensity for 3d homogeneous unsteady viscous flows. In *28th IAHR symposium on Hydraulic Machinery and Systems (IAHR 2016)*.

[54] Leduc, J. (2010). *Etude physique et numérique de l'écoulement dans un dispositif d'injection de turbine Pelton.* PhD thesis, Ecole centrale de Lyon.

[55] LeVeque, R. (1992). *Numerical Methods for Conservation Laws.* Birkhauser.

[56] Li, J. and Rong, J. (2011). Bubble and free surface dynamics in shallow underwater explosion. *Ocean Engineering*, 38:1861–1868.

[57] Li, Z. (2013). *Développement d'une méthode de simulation de couplage fluide-structure à l'aide de la méthode SPH.* PhD thesis, Ecole centrale de Lyon.

[58] Lind, S. and Phillips, T. (2010). Spherical bubble collapse in viscoelastic fluids. *Journal of Non-Newtonian Fluid Mechanics*, 165:56–64.

[59] Lind, S. and Phillips, T. (2012). The effect of viscoelasticity on the dynamics of two gas bubbles near a rigid boundary. *IMA Journal of Applied Mathematics*, 77:652–677.

[60] Lohse (2004). Impact on soft sand: Void collapse and jet formation. *Physical review letters. The American Physical Society*, 93, 19:198003–1 – 198003–4.

[61] Lucy, L. (1977). A numerical approach to the testing of the fission hypothesis. *Astronomical Journal*, 82:1013–1024.

[62] Marongiu, J.-C. (2007). *Méthode numérique lagrangienne pour la simulation d'écoulements à surface libre: application aux turbines Pelton.* PhD thesis, Ecole centrale de Lyon.

[63] McDonald, J. (1962). Homogeneous nucleation of vapor condensation. i. thermodynamic aspects. *American Journal of Physics*, pages 870–877.

[64] Monaghan, J. and Pongracic, H. (1985). Artificial viscosity for particle methods. *Applied Numerical Mathematics*, 1.3:187–194.

[65] Morgut, M., Nobile, E., and Bilus, I. (2011). Comparison of mass transfer models for the numerical prediction of sheet cavitation around a hydrofoil. *International Journal of Multiphase Flow*, 37:620–626.

[66] Morris, J., Fox, P., and Zhu, Y. (1997). Modeling low reynolds number incompressible flows using sph. *Journal of Computational Physics*, 136:214–226.

[67] Nagahara, T., Sato, T., and Okamura, T. (2003). Measurement of the flow around the submerged vortex cavitation in a pump intake by means of piv. In *Fifth International Symposium on Cavitation (CAV 2003).*

[68] Neuhauser, M. (2014). *Development of a coupled SPH-ALE/Finite Volume method for the simulation of transient flows in hydraulic machines.* PhD thesis, Ecole centrale de Lyon.

[69] Nunez-Ramirez, J., Marongiu, J.-C., Brun, M., and Combescure, A. (1997). A partitioned approach for the coupling of sph and fe methods for transient nonlinear fsi problems with incompatible time-steps. *Journal of Computational Physics*, 136:214–226.

[70] Ochiai, N., Iga, Y., Nohmi, M., and Toshiaki, I. (2013). Study of quantitative numerical prediction of cavitation erosion in cavitating flow. *Journal of Fluids Engineering*, 135:011302–1.

[71] Oguz, H. and Prosperetti, A. (1993). Dynamics of bubble growth and detachment from a needle. *J. Fluid Mech.*, 257:111–145.

[72] Oguz, H. and Zeng, J. (1997). Axisymmetric and three-dimensional boundary integral simulations of bubble growth from an underwater orifice. *Engineering Analysis with Boundary Elements*, 19:319–330.

[73] Okada, ., Iwai, Y., Hattori, S., and Tanimura, N. (1995). Relation between impact load and the damage produced by cavitation bubble collapse. *Wear*, 184:231–239.

[74] Pearson, A., Cox, E., Blake, J., and Otto, S. (2004). Bubble interactions near a free surface. *Engineering analysis with boundary elements*, 28:295–313.

[75] Philipp, A., Delius, M., Scheffczyk, C., Vogel, A., and Lauterborn, W. (1993). Interaction of lithotripter-generated shock waves with air bubbles. *J. Acoust. Soc. Am.*, 93:2496–2509.

[76] Pineda, S., Marongiu, J.-C., Aubert, S., and Lance, M. (2016a). Comparison of numerical results using a barotropic and a non-isentropic eos in sph-ale method. In *11th international SPHERIC workshop*, Munich, Germany.

[77] Pineda, S., Marongiu, J.-C., Aubert, S., and Lance, M. (2016b). Multiphase model in sph-ale for modeling a fully compressible multiphase flow. In *11th international SPHERIC workshop*, Munich, Germany.

[78] Plesset, M. (1949). The dynamics of cavitation bubbles. *Journal of Applied Mechanics*, 48:277–282.

[79] Plesset, M. and Chapman, R. (1971). Collapse of an initially spherical vapour cavity in the neighbourhood of a solid boundary. *Journal of Fluid Mechanics*, 47:283–290.

[80] Randles, P. and Libersky, L. (1996). Smoothed particle hydrodynamics: Some recent improvements and applications. *Comput. Methods Appl.*, 139:375–408.

[81] Rayleigh, L. (1917). On the pressure developed in a liquid during the collapse of a spherical cavity. *Philosophical Magazine Series 6*, 34:200:94–98.

[82] Renaut, G.-A. (2015). *Schemas d'ordre élévé pour la méthode SPH-ALE appliquée à des siulations sur machines hydrauliques.* PhD thesis, Ecole centrale de Lyon.

[83] Renaut, G.-A., Marongiu, J.-C., and Aubert, S. (2014). Towards a higher order sph-ale method based on moving least squares method. In *9th international SPHERIC workshop.*

[84] Robb, D., Gaskin, S., Marongiu, J.-C., and Villeneuve, M. (2013). Smoothed particle hydrodynamics simulations of freely moving solid objects in a free-surface flow with applications to river ice dynamics. In *21st Canadian Hydrotechnical Conference.*

[85] Robert Knapp, J. D. and Hammitt, F. (1970). *Cavitation.* McGraw-Hill Book Company.

[86] Rossetti, A., Pavesi, G., Ardizzon, G., and Santolin, A. (2014). Numerical analyses of cavitating flow in a pelton turbine. *Journal of Fluids Engineering*, 136(081304):1–10.

[87] Ryhming, I. (1991). *Dynamique des fluides*. Presses polytechniques et universitaires romandes, deuxième edition edition.

[88] S.A., A. H. (2012). *Materialprufungsanstalt Universitat Stuttgartl*.

[89] Saclay, C. (2016). *EuroPlexus, A Computer Program for the Finite Element Simulation of Fluid-Structure Systems under Transient Dynamic Loading, User's manual*.

[90] Saurel, R., Boivin, P., and Métayer, O. L. (2016). A general formulation for cavitating, boiling and evaporating flows. *Computers and Fluids*, 128:53–64.

[91] Saurel, R., Petitpas, F., and Abgrall, R. (2008). Modelling phase transition in metastable liquids: application to cavitating and flashing flows. *Journal of Fluid Mechanics*, 607:313–350.

[92] Saurel, R., Petitpas, F., and Berry, R. (2009). Simple and efficient relaxation methods for interfaces separating compressible fluids, cavitating flows and shocks in multiphase mixtures. *Journal of Computational Physics*, 228:1678–1712.

[93] Schrage, R. W. (1953). *A theoretical study of interphase mass transfer*. Columbia University Press.

[94] Sezal, I. (2009). *Compressible Dynamics of Cavitating 3-D Multi-Phase Flows*. PhD thesis, Technische Universitat Munchen.

[95] Shima, A. and Fujiwara, T. (1980). The collapse of bubbles in compressible hydraulic oils. *Journal Acoust. Soc. Am.*, 68:1509–1515.

[96] Shobeyri, G. and Afshar, M. (2010). Simulating free surface problems using discrete least squares meshless method. *Computers and Fluids*, 39.3:461–470.

[97] Sidoroff, F. (1980). *Mécanique des milieux continus.* Engineering school. Ecole Centrale de Lyon.

[98] Silva, E. G. D. and Charriere, B. (2014). Modelling for isothermal cavitation with a four-equation model. *International Journal of Multiphase Flow*, 59:54–72.

[99] Soyama, H. and Futakawa, M. (2004). Estimation of incubation time of cavitation erosion for various cavitating conditions. *Tribology Letters*, 17(1):27–30.

[100] Stride, E. (2015). Key note: Cavitation enhanced drug delivery. In *9th International Symposium on Cavitation*.

[101] Supponen, O., Kobel, P., Obreschkow, D., and Farhat, M. (2015a). The inner worl of a collapsing bubble. *Physics of Fluids*, 27(091113):1–2.

[102] Supponen, O., Obreschkow, D., Kobel, P., and Farhat, M. (2015b). Detailed jet dynamics in a collapsing bubble. In *9th International Symposium on cavitation CAV2015*.

[103] Toro, E. F. (2009). *Riemann solvers and numerical methods for fluid dynamics: a practical introduction.* Springer Science and Business Media.

[104] Van-Wijngaarden, E., Bosschers, J., and Kuiper, G. (2005). Aspects of the cavitating propeller tip vortex as a source of inboard noise and vibration. In *2005 ASME Fluids Engineering Division Summer Meeting and Exhibition*.

[105] Vila, J. (1999). On particle weighted methods and smooth particle hydrodynamics. *Mathematical models and methods in applied sciences*, 9:161–209.

[106] Violeau, D. (2012). *Fluid Mechanics and the SPH method: theory and applications.* Oxford University Press, sixth edition edition.

[107] Vogel, A., Lauterborn, W., and Timm, R. (1989). Optical and acoustic investigations of the dynamics of laser-produced cavitation bubbles near a solid boundary. *J. Fluid Mech.*, 206:299–338.

[108] White, F. M. (2008). *Fluid Mechanics.* McGraw-Hill Companies.

[109] Williams, P., Williams, P., and Brown, S. (1997). A technique for studying liquid jets by cavitation bubble collapse under shockwaves, near a free surface. *J. Non-Newtonian Fluid Mech.*, 72:101–110.

[110] Williams, P., Williams, P., and Brown, S. (1998). A study of liquid jets formed by bubble collapse under shock waves in elastic and newtonian liquids. *J. Non-Newtonian Fluid Mech.*, 76:307–325.

[111] Zhang, A., Yao, X., and Feng, L. (2009). The dynamic behavior of a gas bubble near a wall. *Ocean engineering*, 36:295305.

[112] Zhang, Y., Yeo, K., Khoo, B., and Chong, W. (1998). Three-dimensional computation of bubbles near a free surface. *Journal of computational physics*, 146:105–123.

[113] Zhang, Y., Yeo, K., Khoo, B., and Wang, C. (2001). 3d jet impact and toroidal bubbles. *Journal of computational physics*, 166:336–360.

[114] Zisis, I., Messahel, R., Mhamed, S., van-der Liden, B., and Koren, B. (2014). Two-phase benchmarks for sph multiphase fully compressible schemes. In *9th international SPHERIC workshop*, Paris, France.

[115] Zisis, I., Messahel, R., Mhamed, S., van-der Liden, B., and Koren, B. (2015). Validation of robust sph schemes for fully compressible multiphase flows. In *10th international SPHERIC workshop*, Parma, Italy.